DEVELOPMENT OF PEPTIDE-BASED ^{19}F MRI TRACERS AND MR-BASED THERMOMETRY SENSORS

A DISSERTATION

SUBMITTED TO THE FACULTY OF

THE UNIVERSITY OF MINNESOTA

BY

JIAQIAN LI

IN PARTIAL FULFILLMENT OF THE REQUIREMENTS

FOR THE DEGREE OF

DOCTOR OF PHILOSOPHY

ADVISOR:

DR. WILLIAM C.K. POMERANTZ

JULY 2023

Acknowledgments

Dr. William Pomerantz – I can be asked about ‘Did you ever regret to join the Pomerantz’s Group?’ over and over, and the answer would always be the same ‘Never’. Will is the best mentor I can ask for. Will is the one motivates me all the time with his unparralled enthusiasm in research; Will is the one that never give up on me even when I was down so bad; Will is the one always try his best to help whenever I need him; and Will is the one cares about his students so greatly. I enjoy every conversation with Will about the projects and I enjoy turning myself into a better researcher under Will. Appreciation and gratitude are always in my heart. Always.

My Family – My mom is the greatest mom in the world! Cheers me up all the time with her optimistic spirit. I want to thank my uncle for trying his best to get be a bright furture since I was young. His is preachy but he is my role model. I would thank my dad for the financial support all the years to make sure I never need to get bothered by the rent. I want to thank my grandparents for shaping me into who I am. I am so happy that I can have them both as my grandparents and I am so so sorry I can’t be with them in the last couple of years.

Dr. Huarui Cui – I am very very very happy to have Huarui as my girl friend, my lab mate, and my soul mate. Huarui is the one highly recommend me to join the Pomerantz’s group; Huarui is the one give me so many advises on my research projects; Huarui is the one guide me into a real man, a more mature man. I can’t say who is the funnier one between Huarui and my mom, but Huarui definitely is my source of joy.

Dr. Philippe Buhlmann – I would like to thank Dr. Philippe Buhlmann for that life-changing chat with me. Phil helped me reflect on myself and see the world in a brand new way.

Dr. Michel Andrey Joaqui – Andrey and I have been friends since the first week in graduate school and it’s so great! We shared with each other the happy moments as well as the struggles. We backed up each other all the times. I cheerish the friendship with Andrey and I wish the friendship would last for many many years. Gracias mi amigo!

Dr. Yiao Wang – I would like to thank Dr. Yiao Wang for his help for my CSAN projects. Yiao was so helpful for my project, sharing many tricks and tips to me. Thanks to Yiao, I saved myself lots of headache from troubleshooting.

Dr. Dan Yang – I would like to thank Dr. Dan Yang for giving me the opportunity to work in your lab when I was an undergraduate student. There, I felt the happiness of doing research. And thanks for all the help and advise in my graduate school study.

Dr. Yu Chen – I would like to thank Dr. Yu Chen for all the help and advise during my undergraduate study and graduate school study.

Dr. Yingchun Zhao – I would like to thank Dr. Yingchun Zhao for the help with MS experiments all the years. Dr. Zhao was always there whenever I needed him. I truly appreciate him for all the help and I enjoy every chat with him.

Dr. Thomas Smith – I would like to thank Dr. Thomas Smith for helping me with all the NMR experiments. Thomas helped me understand the NMR at a different level. I am so glad to know Thomas.

Dr. Angela Perkins – I would like to thank Dr. Perkins for having me work as life-science TA for 5 semesters. It's a great pleasure to work for her and I had lots of fun teaching freshmen and sophomore.

Tuotuo and Barnaby – FYI, Tuotuo and Barnaby are my cats. I am very happy with my time with them. Thanks for bring me and Huarui so much happiness.

Lab mates – I would like to thank my lab mates for the fun, help, and respect – Dr. Steven Kirberger, Dr. Peter Ycas, Dr. Noelle Olson, Dr. Prakriti Kalra, Kayla Vinh, Dr. Sai Giridhar Sarma Kandanur, Nora Vail, Brandon Paul Datuin, Kerstin Peterson, Molly Vittengl, Richard Ede, Joe McPherson, Nayan Banerjee, Saba Samreen, Elliott Peterson, Pete Gabriel Ledesma, and Ruoqi Jiang.

Friends – Thanks for the happiness from you all, Auld Lang Syne - Dr. Lei Chen, Dr. Xiaoyu Bai, Dr. Yi Sui, Qian Xu, Dr. Mengyuan Jin, Sibin Shen, Bingfa Miao, Hao Li, Yanqing Gu, Jianxiong Sanhao.

Dedication

I would like to dedicate this thesis to my beloved grandpa, Rongting Che. All the great memories between my grandpa and I will always be in my heart. I knew he would be very proud of me.

Abstract

Molecular imaging is defined as the visualization, characterization, quantification of biological processes at the cellular and subcellular level in living subjects. To conduct molecular imaging on specific target, a molecular imaging agent is needed, which is composed of a specific recognition group for a molecular target and an imaging domain. Of various molecular imaging modalities, ^{19}F MRI is gaining increasing attention with its favorable imaging properties. However, the low sensitivity of ^{19}F MRI remains a major challenge.

The design of imaging agents with high fluorine content is essential for overcoming the challenge associated with signal detection limits. In addition to perfluorocarbon and fluorinated polymers, fluorinated peptides offer an additional strategy for creating sequence-defined ^{19}F MRI imaging agents with high fluorine signal.

The first part of this dissertation gives a general introduction of ^{19}F MRI as one molecular imaging modality. Major categories of ^{19}F MRI imaging agents are covered with individual strength and weaknesses highlighted. A complementary category of fluorinated peptide is also discussed in detail. The constructs of those peptides were where the designs of my ^{19}F MRI molecular tracers originated. A brief introduction of the biomarker of choice for molecular imaging and the multivalent CSAN construct for signal amplification follows, both of which were important in the design of my molecular tracers. As other important applications of ^{19}F MRI, thermometry and oximetry with ^{19}F MRI is also covered with the challenges in the design of the sensors.

The second part of this dissertation focused on the development of peptide-based imaging agents. The designs were based on the unstructured peptides previously reported by our group. Chapter 2 focuses on addressing the challenges of those reported peptides through developing new fluorinated amino acids to improve the peptides' detection limits and modifying the peptide structures to remove the undesired non-specific cellular interactions. Chapter 3 focused on addressing the challenge of limited signal in cell-based ^{19}F NMR with the molecular imaging agent prepared in previous chapter. Efforts were made by engineering the molecular imaging agent into multivalent nanoring to further increase the fluorine content while maintain the favorable cellular interactions.

Apart from molecular imaging, ^{19}F MRI is also utilized in thermometry applications. Accurate temperature measurement via magnetic resonance is valuable for both *in vitro* and *in vivo* analysis of local tissue for evaluating disease pathology and medical interventions.

The third part of this dissertation focused on the development of ^{19}F MRI temperature sensors. Those temperature sensors were developed in Chapter 4 with the goals to improve the temperature sensitivity, being ready for encapsulation, and addressing the environmental persistence concerns.

The last part of this dissertation covered the projects on stapled peptides. One is about the cellular interaction on stapled peptides to albumin under the collaboration with Ratmir Derda group; the other one is about the macrocyclization of MLL fragments on their interaction with KIX domain.

Table of Contents

List of Tables

List of Figures

List of Abbreviations

^{18}F-FDG	[^{18}F]Fluorodeoxyglucose
Alloc	allyoxycarbonyl
bisMTX	bis-methotrexate
CSAN	chemically self-assembled nanorings
CT	computerized tomography
EGF	epidermal growth factor
Fmoc	fluorenylmethoxycarbonyl
FWHM	full width at half maximum
HFB	hexafluorobenzene
HSA	human serum albumin
IFABP	intestinal fatty acid binding protein
KIX	kinase-inducible domain interacting domain
MRI	magnetic resonance imaging
MRS	magnetic resonance spectroscopy
MFI	mean fluorescence intensity
mAbs	monoclonal antibodies
NSCLC	non-small cell lung cancer
NMR	nuclear magnetic resonance
PFCE	perfluoro-15-crown-5-ether
PFPE	perfluoro(polyethylene glycol dimethyl ether)
PFC	perfluorocarbon
PFOB	perfluorooctyl bromide
PFTBA	perfluorotributylamine
PEI	polyethylenimine
PET	positron emission tomography

PPI	protein-protein interaction
PRF	proton-resonance frequencey
SNR	signal to noise ratio
SPECT	single photon emission computed tomography
SEC	size exclusive chromatography
SPPS	solid phase peptide synthesis
Boc	tert-Butyloxycarbonyl
Trt	trityl
US	ultrasound
wt%	weight percentage

Chapter 1

Intro

1.1 Molecular imaging

Molecular imaging enables the visualization, characterization, and quantification of biological processes at the cellular and subcellular level in intact living subjects.[1] While conventional imaging delineates anatomical changes in tissues for diagnosis, surgical guidance and follow-up, and treatment monitoring, molecular imaging, due to the ability to quantify specific biomolecular target levels in vivo, offers the potentials for specific and quantitative screening, early diagnosis, personalized therapy, as well as early treatment follow-up.

To conduct molecular imaging, a molecular tracer is introduced to probe biological targets in living subjects. The molecular tracer is composed of an imaging agent and a targeting agent. The targeting moiety is designed to enable the molecular tracer to bind specifically to the molecular markers of interest. Following intravenous administration, the molecular tracer would accumulate at tissue sites overexpressing specific molecular markers, and therefore enhancing the imaging signal. (**Fig. 1-1**) The main advantage of molecular imaging over conventional imaging is that molecular imaging can be performed in the intact organism non-invasively with sufficient spatial and temporal resolution.[2]

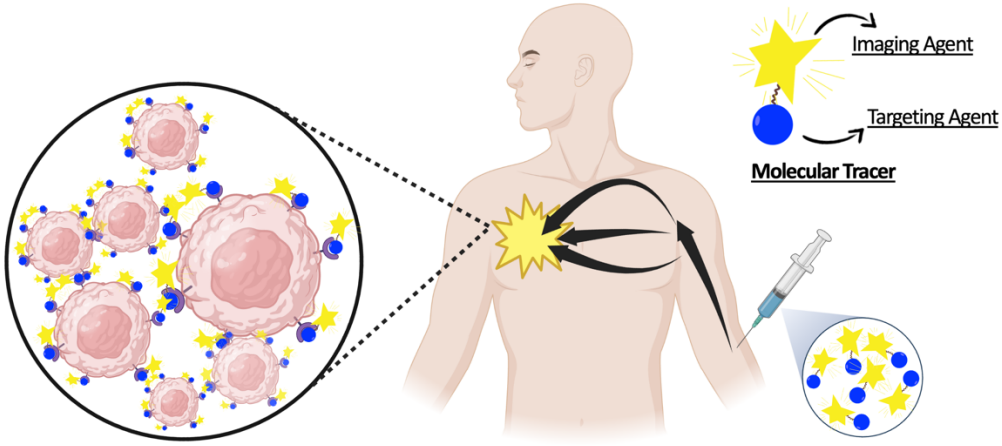

Figure 1-1. Illustration of molecular imaging. Molecular tracer is composed of a targeting agent and an imaging agent. Molecular tracer will bind to the biomarker of selection and will accumulate subsequently. Signal will be detected under specific imaging modality.

Various imaging modalities have been developed for molecular imaging, including positron emission tomography (PET),[3,4] single photon emission computed tomography (SPECT),[5–7] magnetic resonance imaging (MRI),[8–10] and ultrasound (US).[11,12] The selection of an appropriate imaging modality depends on the specific biochemical process to be visualized and the type of imaging data to be obtained. Factors including spatial resolution, temporal resolution, sensitivity, depth of penetration.

PET is a functional imaging technique which utilized radiotracers to visualized and to measure the changes in metabolic processes and other physiological activities. PET is widely used in the imaging of tumor and search for cancer metastases.[13] [^{18}F]Fluorodeoxyglucose (^{18}F-FDG) is a commonly used tracer in clinical oncology for cancer detection (**Fig. 1-1**). ^{18}F-FDG is a modified glucose ring fluorinated at position 2, and it is taken up by cells that consume glucose and is phosphorylated by hexokinase. Because cancer cells have increased metabolism, ^{18}F-FDG tends to accumulate in tumors. Imaging of ^{18}F-FDG through PET scan would therefore reveal the tissue metabolic activity and therefore detect the cancer metastasis. Apart from the detection of cancer metastasis, PET imaging is also used in neurology through measurement of blood flow to the brain with ^{15}O, such as $H_2{}^{15}O$, $C^{15}O$, and $^{15}O_2$.[14] PET has been considered the most sensitive imaging technique for non-invasive study.[15] However, PET involves the exposure to ionizing radiation, which raises the safety concerns. In addition, PET has the limitation of low spatial resolution (~4-5 mm).

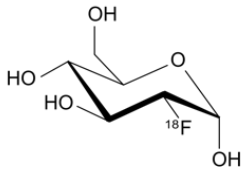

Figure 1-2. Structure of ^{18}F-FDG.

SPECT is a nuclear medicine tomographic imaging technique using gamma rays. To conduct SPECT, a radioligand composed of a marker radioisotope and a specific ligand will be taken by the patient. This radioligand will bind to specific tissues based on the targeting ligand. The emission of the gamma ray will be observed by a gamma camera for imaging. SPECT imaging has a favorable high sensitivity with detection limits as low as picomolar-levels.[5] In additional, SPECT allows for 3D imaging which permits accurate localization of tissues expressing the molecular target in 3D space. This enables SPECT to provide

information about localized function in internal organs, such as functional cardiac[16] or functional brain imaging.[17] However, SPECT imaging is limited by low spatial resolution, compared with other modalities such as MRI and computerized tomography (CT). Also, similar to PET, SPECT relies on ionizing radiation which raises safety concerns.

Ultrasonic imaging is a common diagnostic technique which utilizes sound waves with frequencies greater than 20,000 Hz and does not require ionizing radiation. Ultrasonic images, known as sonograms, are created through sending ultrasonic pulses into tissue through a probe. The ultrasound pulses would echo off tissues with different reflection properties and be returned to the probe. Signal would be recorded and displayed as an image. Ultrasonic imaging has been widely used for imaging of internal body structures including tendons,[18] muscles,[19] joints,[20] and internal organs.[21] Ultrasonic imaging has the advantages of being low cost, non-invasive, and avoids radiation. Ultrasonic imaging also allows for real time imaging study.[22] However, with the inability of sound waves to travel through air or bone efficiently, ultrasonic imaging is not as effective at imaging body parts that have gas in them or are hidden by bone, including the lung or head.

1.2 Magnetic Resonance Imaging

Magnetic resonance imaging (MRI) is a medical imaging technique that is widely used in clinical settings for medical diagnosis, staging and follow-up of disease. MRI uses a strong magnetic field, magnetic field gradients, and radio waves to create detailed images of anatomic structures, physiological functions, and molecular composition of tissues.[23]

MRI is based on the principles of nuclear magnetic resonance (NMR). In general, a spin, which is a rotating object possessing angular momentum, is first aligned with the applied strong magnetic field B_0. A radiofrequency field B_1 is next applied perpendicular to the B_0 for a very short time, and this applied radiofrequency pulse results in the alignment of the spin being tipped off. (**Fig. 1-3**) The precessing nuclear spin subsequently relaxes to the original alignment through either T_1 spin-lattice relaxation or T_2 spin-spin relaxation. Precession of the nuclear spins in the plane perpendicular to the magnetic field induces the voltage change in the detection coil and signals are recorded over time. For image analysis, typically more than 4

million voxels are obtained where each voxel contains an individual NMR signal, a magnetic field gradient will be used to introduce a very slight difference in frequency and/or phase in the signal. This minute discrepancy will be used to locate the voxel for the whole image. (**Fig. 1-4**)

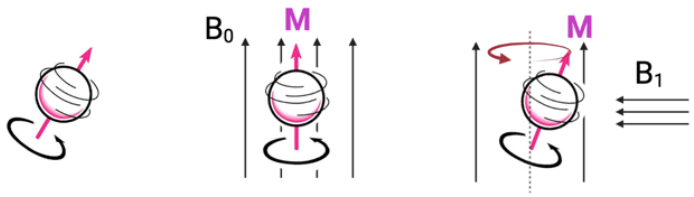

Figure 1-3. Illustration of precession. Spin aligned with/against the applied static magnetic field B_0. A perpendicular radiofrequency field B_1 was applied within short time and magnetization (M) can be tipped out of the initial alignment with B_0 and start to precess.

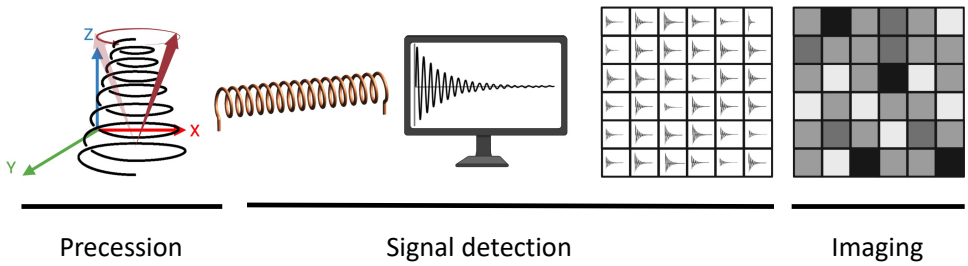

Figure 1-4. Illustration of detection of the MR signal. The precession of the magnetization would generate a current in the receiver coil, The signal is a sine wave oscillating and each signal differs sightly in phase and frequency which encodes the location of the individual pixel. Signal would then be transformed into the image.

MRI is a non-invasive imaging technique which enables the observation of anatomic structures, molecular composition of tissues and physiological functions. MRI has the advantage of using non-ionizing radiation, has good soft tissue contrast resolution, high-resolution imaging, and multiplanar imaging capabilities.[24] However, a major weakness of MRI is its inherent low sensitivity. While other modalities such

as PET and SPECT have the picomolar sensitivity, MRI limit of detection is typically within the micromolar to millimolar range.[25,26]

^{1}H MRI is a highly developed technology and is commonly found in clinical settings. ^{1}H in water molecules and in fat are the main source of ^{1}H MRI signal due to their abundance in the human body. Signal from the fat tissue is usually suppressed with fat tissue showing high signal in MRI. Such undesired signal would not only cover the signal of other tissues, but also result in chemical shift artifact.[27] ^{1}Hs is highly abundant in human body. Concentration and magnetic properties of ^{1}H vary with anatomy. These variations result in a background intensity that is inherently nonhomogeneous. To enhance the contrast between a target tissue and the background, using contrast agent is the most commonly used strategy to enhance the signal to noise. These contrast agents can be classified into two categories: paramagnetic ion complexes and superparamagnetic magnetite particles. Paramagnetic ion complexes (**Fig. 1-5**), usually containing gadolinium Gd^{3+}, shorten the T_1 relaxation time of the nearby water molecules. A short T_1 enables the faster recovery of signal and would therefore increase signal intensity on T_1-weighted images. Superparamagnetic magnetite particles, usually containing manganese Mn^{2+}, reduce the T_2 relaxation time and would therefore decrease the signal intensity on T_2-weighted images. Under current clinical administration, a high dose of contrast agent is needed for around 0.1 mmol/kg of body weight (e.g. 6.8 mmol contrast agent for an adult of 150 lbs),[28] which raises certain safety concerns of toxic effects such as nephrogenic systemic fibrosis and gadolinium deposition disease.[29]

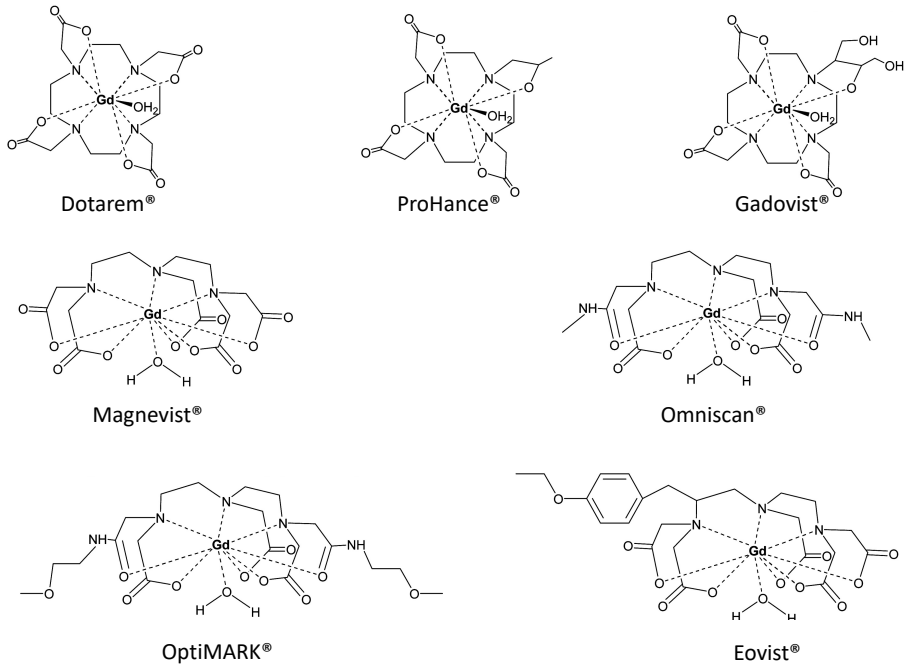

Figure 1-5. Structures of selected commercially available Gd^{3+} chelate MR agents.

1.3 ^{19}F MRI

As an alternative strategy of contrast to overcome the inherent low sensitivity of ^{1}H MRI, introducing a 'second color' or 'hot spot' has been gaining increasing attention through using other heteronuclear MRI atoms, such as ^{13}C,[30] ^{23}Na,[31] ^{31}P,[32] or ^{19}F.[33] ^{19}F holds great potential with it 100% natural abundance, a high gyromagnetic ratio close to ^{1}H (40.08 MHz·T^{-1} VS 42.58 MHz·T^{-1}), a ½ nuclear spin, and a sensitivity 83% of that of ^{1}H. In additional, there are only trace amounts of mobile ^{19}F (~ 10^{-6} M) present in the human body, indicating a very limited background signal in ^{19}F MRI. Such limited background noise would allow ^{19}F MRI to provide quantitative information.

With limited endogenous ^{19}F present being detectable, ^{19}F MRI signal would be only from the exogenous ^{19}F atoms contained in the fluorinated tracers. However, the lack of endogenous fluorine highlights a major weakness of ^{19}F MRI – the low sensitivity. Significant efforts have been made for improving MRI performance including more tailored pulse sequence and utilizing the paramagnetic contrast agent to shorten the T_1 relaxation.[34] Alternatively, a well-designed ^{19}F MRI tracer can improve the ^{19}F MRI sensitivity significantly. Specifically, an 'ideal' ^{19}F MRI tracer has the properties of high fluorine content, a

single resonance in ^{19}F NMR, a short T_1 and a long T_2, facile preparation, chemical and biological stability, and low toxicity. The mainstream ^{19}F MRI tracer can be categorized into three groups: perfluorocarbon liquids, fluorinated small molecules, and fluorinated polymers.

1.4 Perfluorocarbon liquids for ^{19}F MRI

Perfluorocarbon liquids (PFCs) are compounds in which all hydrogen atoms are replaced with fluorine atoms. PFCs remains one of the main categories of ^{19}F MRI tracers. With the high electronegativity of fluorine, the carbon-fluorine bond has a significant dipole and an unusual bond strength of up to 130 kcal/mol bond dissociation energy.[35] Consequently, PFCs exhibit fairly distinct properties to their C-H containing analogues. PFCs tend to have highly thermal, chemical, and oxidative stability, high vapor pressure, weak surface tension, limited intermolecular interactions, and excellent biosafety. Moreover, PFCs are highly hydrophobic and lipophobic with a strong tendency to aggregate under physiological conditions. As a result, for most application of PFCs for ^{19}F MRI, formulation of PFCs into nanoemulsions is necessary to ensure the concentration be sufficient to be detected by ^{19}F MRI.[36] Yet nanoemulsions tend to suffer droplet heterogeneity, instability, limited biocompatibility, and environmental concerns.[33,37,38] Nanoparticle encapsulation is one approach to address this stability challenge.[39,40] Matsushita et.al reported the fluorine accumulated silica nanoparticle for MRI contrast enhancement (FLAME) to contain high concentration of PFCE in the core of nanoparticle for ^{19}F MRI application. PFCE-containing FLAME demonstrated a chemically modifiable surface, dispersibility in water, biocompatibility, and high stability.[41,42] Lee at.al utilized ultraporous mesostructured silica nanoparticles (UMNs) to load multiple liquid PFCs including perfluoro-15-crown-5-ether, perfluorodecalin, and perfluoro(tert-butylcyclohexane).[43] Oximetry with PFCE-loaded UMNs were demonstrated followingly. A common challenge for PFCs is the difficulties in their structural engineering. Spectral performance in most cases will have significant changes and therefore vigilance is demanded into the design of structural modification to avoid the undesired multiple resonance which would result in chemical shift artifact.

The frequently used PFCs include hexafluorobenzene (HFB), perfluorooctyl bromide (PFOB), perfluoro-15-crown-5-ether (PFCE) (**Fig. 1-6**). HFB is commonly used for ^{19}F MRI oximetry due to its high

in vivo sensitivity.[44] HFB has good O_2 solubility and the dissolving of O_2 would change the longitudinal relaxation T_1 of HFB due to the paramagnetic property of O_2. PFC has a liner relationship between the longitudinal relaxation rate ($1/T_1$) and the oxygen partial pressure; therefore, pO_2 of the tissue could be determined through the acquisition of a T_1 map through ^{19}F MRI.[45] PFOB has a linear structure with 17 ^{19}F atoms in total and is commercially available. This FDA-approved PFC has been used for both oximetry[46] and imaging.[47] Compared with other PFCs, one advantage of PFOB is its enhanced clearance rate.[48] However, one major weakness of PFOB is its 8 resonances in the ^{19}F NMR spectrum which is detrimental to signal-to-noise ratio and the subsequent sensitivity as well. In addition, PFOB is susceptible to chemical shift artifacts in ^{19}F MRI with some resonances located within 12 ppm distance, which has been reported as the minimum difference in frequency to avoid chemical shift artifacts.[49] A common strategy to minimize the chemical shift artifact is through using pre-saturation radiofrequency pulses to suppress the undesired resonances[50]. PFCE has a high fluorine content of 20 ^{19}F atoms and has a favorable one single resonance due to its symmetric macrocyclic structure. It has been widely studies in ^{19}F MRI for cell tracking and targeted drug delivery.[51]

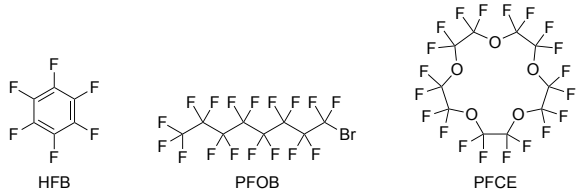

Figure 1-6. Structures of selected perfluorocarbons commonly used in ^{19}F MRI.

1.5 Fluorinated Polymers for ^{19}F MRI

Fluorinated polymer is a second major category for ^{19}F MRI tracers. Fluorinated polymer allows for higher fluorine content to overcome the low sensitivity of ^{19}F MRI and enjoys the versatility with tailorable properties based on monomer selection. Highly fluorinated polymer building blocks are hydrophobic and tend to self-aggregate in aqueous solution. Apart from the commonly used nanoemulsion strategy as for PFCs, copolymerization is an alternative strategy to be nanoemulsion-free, where the hydrophilic building blocks is to be judiciously chosen.

The first report of ^{19}F MRI using fluorinated copolymer was published by Peng et al.[52] Diblock copolymer of acrylic acid with partially fluorinated acrylate and methacrylate monomers were synthesized. Spontaneous self-assembly of the linear copolymers form them into a stable micelle with a fluorine-rich core (**Fig. 1-7**). The micelle exhibited a strong signal in ^{19}F MRI, a short T_1 of around 600 ms and a long T_2 of around 300 ms, all of which are suitable for imaging. In addition to linear structures, copolymers of other structures have also been studies. Thurecht et al. synthesized a hyperbranched copolymer composed of two blocks dimethylaminoethylacrylate and trifluoroethyl acrylate (**Fig. 1-8**).[53] The polymeric particles showed good aqueous solubility and cytocompatibility. Despite a short T_2, *in vivo* images were successfully obtained under 10 min due to the high fluorine content. Herneisey et.al prepared a thermoresponsive perfluorocarbon emulsion hydrogel which can be detected by ^{19}F MRI.[54] Unlike most fluorinated copolymers where building blocks were connected covalently, this hydrogel is composed of perfluoro(polyethylene glycol dimethyl ether) (PFPE) emulsion droplets and polyethylenimine (PEI) through ionic cross-linking. (**Fig. 1-9**) The latest study reported by Reis et.al combined automated flow synthesis and machine learning for fluorinated copolymer development. This development led to over 10 copolymer compositions that outperformed the state-of-the-art materials.[55]

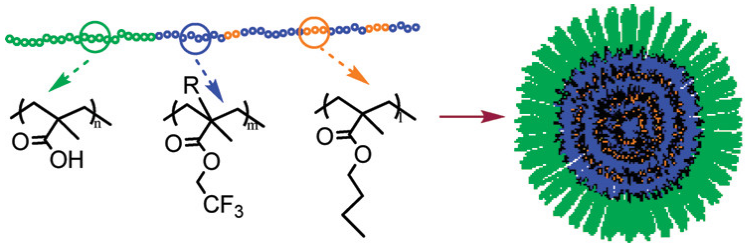

Figure 1-7. Illustration of the amphiphilic copolymers of PAA-*b*-P(*n*BA-*co*-TFE(M)A). Adapted with permission.[52] Copyright (2009) American Chemical Society.

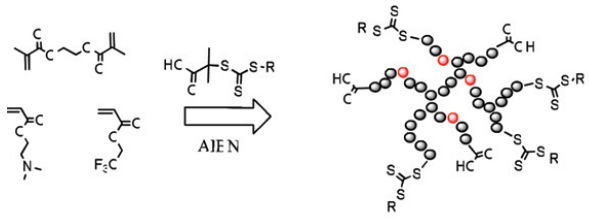

Figure 1-8. Illustration of the copolymers composed of dimethylaminoethylacrylate and trifluoroethyl acrylate. Adapted with permission.[56] Copyright (2010) American Chemical Society.

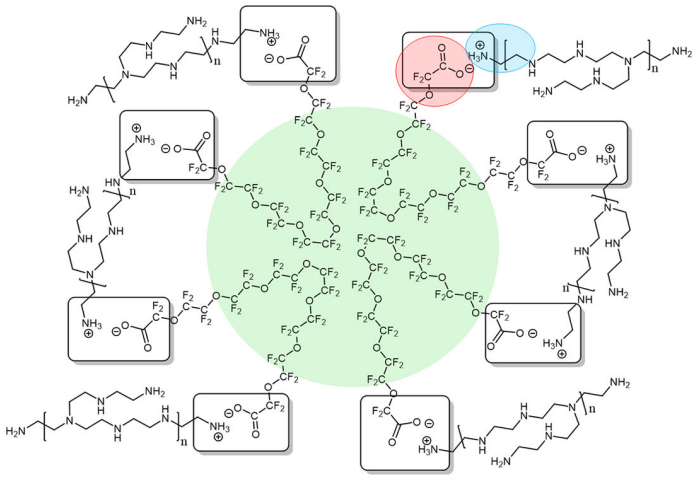

Figure 1-9. Structure of polyamine cross-linked perfluoropolyether hydrogels. Adapted with permission.[57] Copyright (2020) American Chemical Society.

In short, the challenge in fluorinated polymer for ^{19}F MRI is a balance between high fluorine content and favorable relaxation time. Higher fluorine content can be achieved through increase the degree of polymerization. However, this will result in an increase in the particle size. T_1 relaxation would therefore increase and T_2 would decrease. A long T_1 would result in unfavored long acquisition time and short T_2 would be detrimental to the SNR. Hence, a good balance between fluorine content and relaxation time is of paramount importance.

1.6 Fluorinated Small Molecules for ^{19}F MRI

Fluorinated small molecules are a third major category for ^{19}F MRI tracers. Fluorinated small molecules feature the higher flexibility in structural modification compared with PFCs. However, fluorinated small molecules suffer lower fluorine content compared with the PFCs of similar sizes. Moreover, unlike fluorinated polymers which can be emulsion-free with copolymerization of hydrophilic building blocks, for most fluorinated small molecules, encapsulation is still needed for adequate concentration to meet the detection limits.

Multiple fluorinated small molecules have been reported with premium ^{19}F MRI performance. Tirotta et.al reported a highly fluorinated ^{19}F MRI probe PERFECTA which has a symmetric structure.[58] (**Fig. 1-10**) Prepared in one step synthesis, PERFECTA features 36 equivalent ^{19}F atoms with a desired single resonance in ^{19}F NMR. PERFECTA has an acceptable T_1 relaxation time of ~600 ms and T_2 of ~190 ms. In addition, PERFECTA possessed excellent cellular compatibility and was successfully imaged in vivo. Jiang et.al developed a bispherical fluorocarbon molecule ^{19}FIT.[59] ^{19}FIT is composed of 2 hydrophilic building blocks and a highly fluorinated building block. (**Fig. 1-10**) Despite a lower fluorine content than PERFECTA and a multi-step synthesis, ^{19}FIT showed a single resonance in ^{19}F NMR, a successful in in vivo ^{19}F MRI, and, more importantly, is soluble in phosphate-buffered saline (PBS) buffer with a short T_1 relaxation of 160 ms. In addition, ^{19}FIT is structurally ready for further functionalization on the hydrophilic phase. Kadakia et.al reported a highly fluorinated Cu-based imaging agent CuL_1 for detection of cellular hypoxia[60] (**Fig. 1-10**). The CuL_1 construct has 18 equivalent ^{19}F atoms with a single resonance in ^{19}F NMR. ^{19}F MR signal was initially quenched with Cu^{2+} being paramagnetic; once reduced, the construct displayed a significant increase in signal intensity. Hypoxia was successfully detected in cellular studies with CuL_1 nanoemulsion. Lee et.al reported a new organofluorine temperature sensors through a combined experimental and computational approach.[61] These temperature sensors were designed for thermometry or calibration for oximetry through ^{19}F MRI. The lead sensor compound 6 (**Fig. 1-10**) showed a nearly two-fold increase in temperature sensitivity compared with the gold standard perfluorotributylamine (PFTBA).

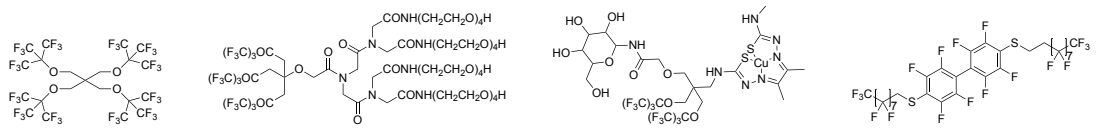

PERFECTA ^{19}FIT CuL_1 Compound 6

Figure 1-10. Structures of selected fluorinated small molecules: PERFECTA, ^{19}FIT, CuL_1 and compound 6.

1.7 ^{19}F MRI Oximetry and Thermometry

Oxygenation is essential for tissue health; rapid cellular dysfunction could be caused with the reduction in oxygen supply. Meanwhile, oxygen is a very important variable in the medical intervention such as tumors, peripheral vascular diseases, and stroke treatment. It has been found prognostically valuable through measuring the oxygen tension (pO_2) in the tumor.[62] Therefore, tissue oxygen tension measurement have a significant impact in disease prognosis.

Several techniques have been used for oximetry. Polarographic needle electrode has been considered the gold standard for oximetry and has been widely used in clinics.[63] The major weakness of polarographic needle electrode is its susceptibility to changes in pH, salinity, and ionic strength. In addition, polarographic needed electrode is regarded as invasive, despite multiple efforts have been made to minimize the invasiveness.

As a non-invasive technique, ^{19}F MRI has been widely studied for oximetry and has been successfully applied *in vivo* in the preclinical setting.[64] ^{19}F MRI, with limited endogenous ^{19}F atoms to be detected, allows the quantitative analysis with the exogenous ^{19}F atoms. In MRI oximetry, exogenous reporter molecules, usually perfluorocarbon liquids are administrated. Oxygen is paramagnetic as such dissolved oxygen leads to both a shortened spin-lattice relaxation T_1 and spin-spin relaxation T_2. Given the linear response of the relaxation time to oxygen concentration, a calibration curve can be developed to quantitate oxygen levels.[65] PFCs are highly oxygen soluble, allowing a broad range of oxygen for detection. Moreover, PFCs' hydrophobicity minimizes the exchange of aqueous ions with the surrounding tissue which would perturb R_1 ($=1/T_1$). In general, ^{19}F MRI oximetry is determined based on the linear dependence of the ^{19}F spin lattice

relaxation rate R_1 (=$1/T_1$) on pO_2. Hexafluorobenzene (HFB) and perfluoro-15-crown-5-ether (PFCE) are the most common reporters for oximetry, with both having a single resonance with high fluorine content and high pO_2 sensitivity.

However, ^{19}F MRI oximetry is susceptible to the changes in temperature. R_1 is temperature dependent and varies between the PFCs. For example, PFCE, despite a high pO_2 sensitivity, is also temperature sensitive. The relative error introduced into pO_2 determination by 1 ºC error in temperature is 3 torr/ ºC.[66] Therefore, the temperature calibration would be necessary for an accurate oximetry.

MRI has also been applied for thermometry. Several MR parameters were shown to be sensitive to changes in temperature: the proton density, T_1 and T_2 relaxation times, the diffusion coefficient, magnetization transfer, and the proton resonance frequency (PRF).[67] While most of the works are ^1H MRI-based, ^{19}F MRI thermometry have also been gaining attentions. PFCs used for *in vitro* and *in vivo* thermometry was first reported by Berkowitz et al. where perfluorotributylamine (PFTBA) was selected for thermometry.[68] A linear relationship of changes in resonance frequency and the temperature was found with a sensitivity ~ 9×10^{-3} ppm/°C. PFTBA has been the gold standard for ^{19}F MRI thermometry, however, it has several weakness. For example, PFTBA has multiple resonances with close frequencies, resulting in the potential chemical shift artifact. Also, PFTBA is a potent greenhouse gas.[69] The environmental persistence of PFTBA has been a heightened concern. Hence, it's necessary to design new temperature sensors which can address the limitation of PFTBA. An ideal temperature sensor should have the following properties: liquid, high sensitivity, limited resonances of non-close frequencies, degradability. The liquid state of the temperature sensor allows for facile encapsulation, which enables the higher concentration of PFCs to overcome the general low sensitivity issue of ^{19}F MRI. Limited resonances would help improve the SNR, which is beneficial to the sensitivity; meanwhile, with resonances not having similar frequencies, undesired chemical shift artifacts can be minimized. These limitations will be addressed in chapter 2 through a systematic study of a second generation temperature sensors based on the our progress in the development of first generation temperature sensors.[61]

1.8 Fluorinated Biopolymers for ^{19}F MRI

While PFCs and fluorinated polymers are the two most developed categories of ^{19}F MRI tracers, fluorinated peptides and proteins complement strategies for synthetic polymers and offer a mechanism for modulating stability *in vivo* through protease degradation or subsequent amide hydrolysis. Mizukami et al. in 2008 reported a peptide-based ^{19}F MRI probes for the detection of the protease activity (**Fig. 1-11**).[70] Paramagnetic Gd^{3+} complex was attached at the N-terminus of caspase-3 substrate peptide sequence and trifluoromethoxybenzyl group was attached to the C-terminus. When Gd^{3+} and CF_3 groups are of close proximity, the strong paramagnetic relaxation enhancement of Gd^{3+}+ shorted the T_2 of CF_3 significantly and resulted in an attenuation of ^{19}F MRI signal. After the peptide was cleaved by protease, the T_2 of CF_3 was recovered, and the ^{19}F MRI signal was able to be recovered. A phantom ^{19}F MRI was obtained of 1 mM peptide probe after incubating with a specific protease. Under the similar idea, Yue et al. in 2017 reported a peptide probe for detection of matrix metalloproteases (MMP-2).[71] A nonafluoro-tert-butyl containing group was attached at the N-terminus of an MMP-2 peptide substrate and Gd^{3+} complex was attached to the C-terminus. Incubating with MMP-2 cleaved the peptide and resulted in the recovery of ^{19}F MRI signal. A single resonance was observed in ^{19}F NMR after proteolysis and a phantom MRI image was obtained at 2.5 mM of the fluorinated sensor. Apart from protease detection, a fluorinated peptide-based construct was also reported for cation detection through ^{19}F MRI.[72] Preslar et al. in 2017 reported detection of Ca^{2+} through ^{19}F MRI with peptide amphiphiles. Tridecafluoroheptanoyl group was attached to different amphiphiles which tend to self-assemble into nanofibers. It was found that with the increase of Ca^{2+}, the morphology of nanofibers would change in the width, and consequently decrease the ^{19}F MRI intensity.

Those studies all indicated a great potential of fluorinated peptide being a new category besides PFCs, fluorinated small molecules, and fluorinated polymers. The design of highly fluorinated peptides as the imaging agents for ^{19}F MRI will be discussed in chapter 3.

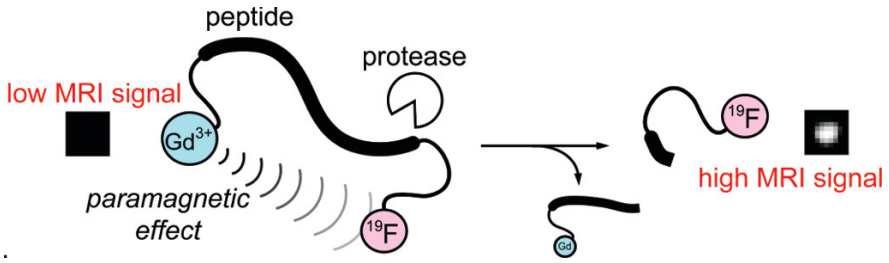

Figure 1-11. Illustration of peptide-based ^{19}F MRI probes for the detection of the protease activity. Adapted with permission.[70] Copyright (2008) American Chemical Society.

1.9 Intrinsically disordered scaffold for fluorinated peptide

While fluorinated peptides for ^{19}F MRI have been gaining increasing attention, in most of the designs previously discussed, peptides act as either functional linkers or hydrophilic moiety for nanoparticles. The importance of the peptide backbone for containing fluorine atoms was not fully studied and retains great potentials for ^{19}F MRI applications. Frieden et al. in 1993 reported a study of ^{19}F NMR responses with the protein folding.[73] 6-fluoro-tryptophan was incorporated into position 6 and 82 of intestinal fatty acid binding protein (IFABP). ^{19}F NMR was conducted on both the native IFABP and the unfolded IFAPB through treatment of urea. It was noticed that the chemical shift of the resonances of W82 and W6 were becoming similar when IFABP got unfolded. Li and Frieden in 2005 reported another study of the protein IFABP.[56] 4-fluorophenylalanine was selected as fluorinated amino acid and was incorporated in all eight phenylalanine sites (Phe^{2}, Phe^{17}, Phe^{47}, Phe^{55}, Phe^{62}, Phe^{68}, Phe^{93}, Phe^{128}). (**Fig. 1-12**) ^{19}F NMR spectra were obtained on fully labeled IFABP with unfolded states to different extent as a function of urea. It was reported that with the increase of unfolding, the sparse ^{19}F NMR resonances became degenerate leading to significant resonance overlap.

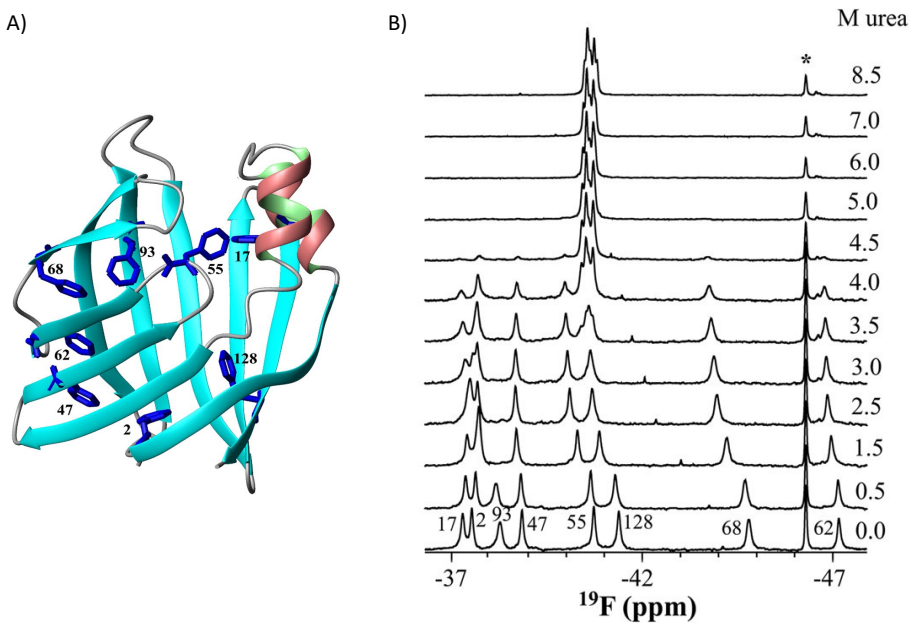

Figure 1-12. ^{19}F NMR resonance degeneracy under different unfolding extent. A) The crystal structure (PDB: 1IFB) of apo-IFABP. Eight phenylalanine residues were colored blue. B) ^{19}F-NMR spectra of apo-IFABP as a function of urea. Adapted with permission.[56] Copyright (2005) The American Society for Biochemistry and Molecular Biology.

Those two finding inspired our laboratories prior work, based on the observation that the signal degeneracy as a result of unfolding would not only help reduce the chemical shift artifacts but would help improve the signal intensity. Based on the notion of unfolded structure, Kirberger et al. in 2017 reported a series of a highly fluorinated, sequence-defined disordered peptide as a competent ^{19}F MRI imaging agent.[74] Peptide oligomers were composed of N-ε-trifluoroacetylated lysine (TFA-lysine) and lysine in an alternating pattern (**Fig. 1-13**). Lysine was selected to favor the aqueous solubility and meanwhile disfavor both aggregation and formation of secondary structure with the electrostatic repulsion from the polycations on the side chain. A single narrow degenerate signal was observed of the individual peptides and fluorine content can be achieved up to 30 ^{19}F atoms per peptide. In addition, those peptides had good aqueous solubility and a $T_1 < 2$ s. These results all indicated the potential of peptide-based ^{19}F MRI imaging agent. Structurally

similar fluorinated peptides, composed of an asparagine analogue carrying a perfluoro-tert-butyl group, have now also been reported showing high biostability when used in zebrafish embryos by the Ulrich lab.[75]

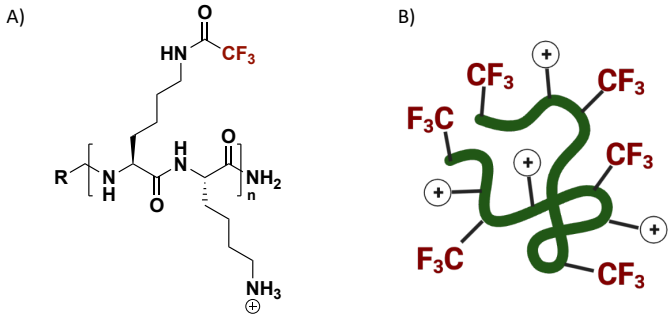

Figure 1-13. Disordered ^{19}F peptide design. A) Generic structure of disordered ^{19}F peptides. B) Disordered peptide design showing ^{19}F sources alternating with positive charge.

Despite the promising results of a ^{19}F MRI peptide construct, a significant weakness mentioned in both studies was the relatively low detection limit for phantom ^{19}F MRI. This indicated the necessity to further engineer the peptide construct including increasing the fluorine content and shorten the T_1 relaxation which will be discuses in chapter 3.

1.10 Solid Phase Peptide Synthesis

Solid phase peptide synthesis (SPPS) is a well-established method for peptide synthesis. Pioneered by Merrifield, SPPS enables the rapid preparation of peptide through successive reaction of amino acid derivatives on polymeric resins.[76] The solid support is functionalized with reactive groups (e.g. amine or hydroxyl groups) that link to the nascent peptide chain. With the synthesized peptides covalently attached to the solid support, excessive reagents and side project can be removed through washing and filtering steps. The facile purification is one major advantages over solution phase peptide synthesis.

Peptide synthesis through SPPS is usually coupled in a C terminus to N terminus direction. (**Fig. 1-14**) Individual amino acid to be coupled to the N-terminus of peptide on solid phase must be protected on its both N-terminus and side chain using appropriate protecting groups such as fluorenylmethoxycarbonyl (Fmoc) or

tert-Butyloxycarbonyl (Boc) groups, depending on the side chain and the protection strategy used. For example, in the commonly used Fmoc-SPPS, the N-terminus of the amino acids are Fmoc-protected which are liable to deprotection under basic condition. The side chains of the amino acids are orthogonally protected by groups which are stable under basic condition but would be deprotected under acid condition, such as Boc, allyloxycarbonyl (Alloc), and trityl (Trt) groups. Synthesis in general is through an alternating N-terminus deprotection and coupling reaction cycles. Amino acid is first coupled to the resin. The amine at the N-terminus of peptide on solid phase is then deprotected and allows for the coupling of next activated amino acid. Washing and filtering steps are following with individual coupling or deprotection step to wash away the excessive reagents and reactants. The cycle is repeated till the synthesis of full-length peptide. The crude peptide is then cleaved from the resin and the protecting groups on the side chains are deprotected at the same time with cleavage cocktail.

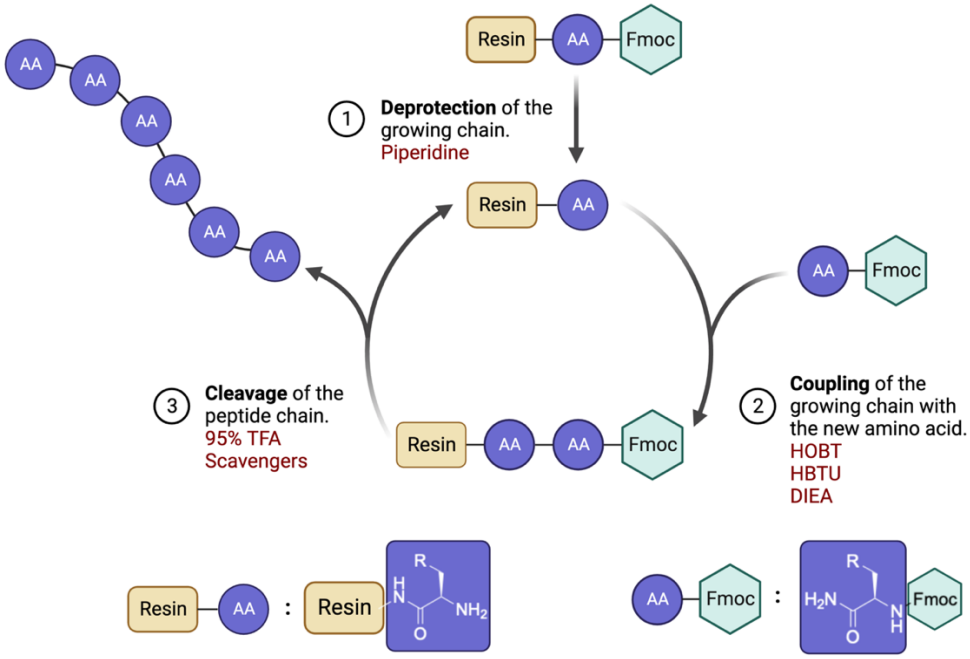

Figure 1-14. Scheme of Fmoc-solid phase peptide synthesis.

Crude peptide can be precipitated using a non-polar solvent such as diethyl ether to remove organic byproducts. The crude peptide is next purified with reverse phase HPLC and characterized by MALDI.

SPPS is a very useful method for peptide synthesis. The main limitation is that SPPS is not suitable for preparation of very long peptide if over 70 amino acids. The exponential accumulation of byproducts would result in a big challenge in purification for long peptide.[77] Alternatively, peptide ligation would be preferred for longer peptide preparation or recombinant protein expression.

1.11 Epidermal Growth Factor Receptor in Breast Cancer

Despite significant efforts in breast cancer diagnosis and treatment, breast cancer remains the most life-threatening disease in women.[78] Most commonly, breast cancer is associated with the dysregulation of hormone receptor for estrogen and progesterone.[79] Tyrosine kinase receptors of EGFR/ErbB family are quite often found upregulated in many common human cancers, such as non-small cell lung cancers and breast cancers. EGFR/ErbB family includes ErbB1/EGFR1, ErbB1/EGFR1, ErbB2/Her2, ErbB3/Her3 and ErbB4/Her4. The amount of EGFRs expression has been utilized as an indication of the extent of dysregulation.

Triple negative breast cancer has a poor prognosis, and it has a shorter overall survival than other breast cancer subtypes. EGFR1 is commonly over-expressed in triple negative breast cancer cases. Hence, EGFR1 is a good target to be detected for triple negative breast cancer prognosis and diagnosis. The extracellular region of EGFR1 is composed of four domains, of which domains I and III are related in sequence and so as domains II and IV (**Fig. 1-15**). The intracellular region of EGFR1 is composed of tyrosine kinase domain. Both regions are connected with transmembrane and juxtamembrane domains.

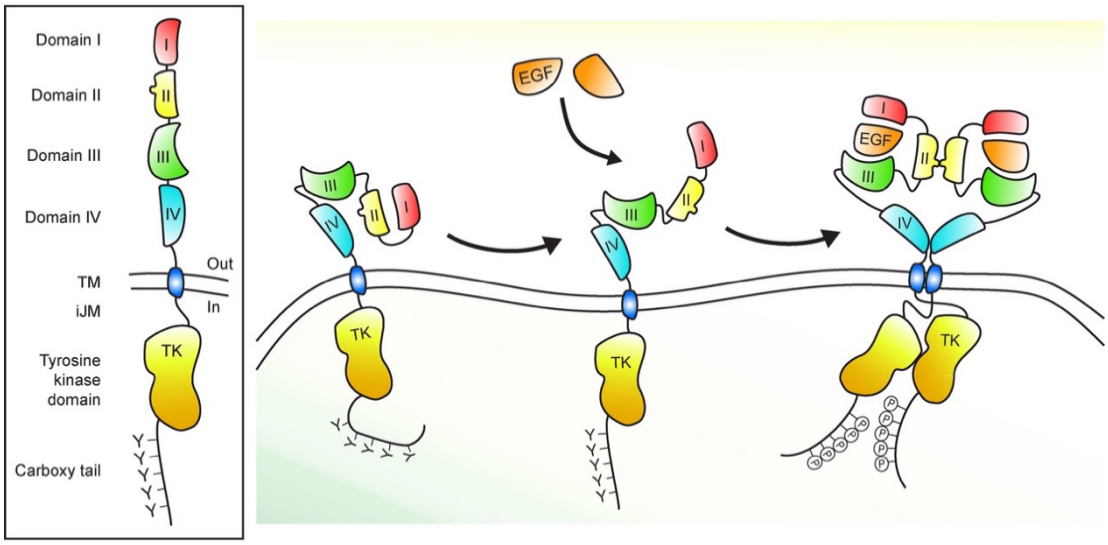

Figure 1-15. Schematic representation of the EGFR and EGF-induced receptor activation. Adapted with permission.[80]

EGFR1 is regulated by peptide ligands including epidermal growth factor (EGF). Upon activation of EGFR1 with ligand, EGFR1 would dimerize, and transphosphorylation would happen at tyrosine residue at the C-terminus of EGFR1 (**Fig. 1-15**). Several intracellular signal proteins would then be recruited and subsequently activating intracellular signaling pathways. Pathways include the RAS-RAF-MEK-ERK pathway, the JAK–STAT pathway, the PLCγ–PKC-CAMK cascade, and the PIL3-AKT-mTOR signaling cascade.

As EGFR1 is involved in cellular transformation, certain inhibitors have been developed. Those inhibitors demonstrated the anti-proliferation against EGFR1. The first class of inhibitors are monoclonal antibodies (mAbs), such as Cetuximab and Panitumumab. (**Fig. 1-16**) Those mAbs would bind specifically to the extracellular domain of EGFR1, blocking the ligand binding, blocking the receptor dimerization, and the subsequent signaling. The second class of inhibitors are small molecules tyrosine kinase inhibitors, such as Gefitinib and Erlotinib. (**Fig. 1-16**) They both bind to the intracellular tyrosine kinase domain to inhibit the phosphorylation and the subsequent signaling. The third class of inhibitors are chimeric antigen receptor T cells or NK cells. Those cells are engineered to bear an antibody fragment and would bind to cancer cells to induce an immune response.

EGFR1 was selected as the biomarker for ^{19}F MRI molecular imaging in both chapter 3 and chapter 4.

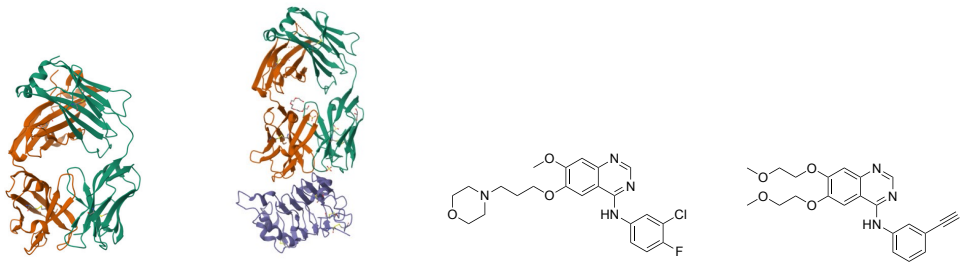

Figure 1-16. Structures of inhibitors of EGFR1. Monoclonal antibodies: Cetuximab (PDB: 1YY8) and Panitumumab (PDB: 5SX4). Small molecules: Gefitinib and Erlotinib.

1.12 DHFR and Chemically Self-Assembled Nanorings

Multivalency is commonly sought after in therapeutics and diagnostic probe designs. In therapeutics, multivalence could be realized through covalent modification on mAbs or mAb fragments, while the uniform high valency (>4) is very challenging to obtain. In diagnostic probe design such as ^{19}F MRI imaging agent, a dendrimer is a common strategy to improve the fluorine content. However, dendrimers require very long and elaborate syntheses, and they have complex cytocompatibility and cellular update.[33]

A protein-based multivalent construct named chemically self-assembled nanoring (CSAN) was reported in the Wagner's group.[81] CSAN is assembled through the binding of DHFR-DHFR fusion proteins and dimerizer bivalent methotrexate (bis-MTX). Fusion proteins were genetically engineered where two E. Coli DHFR proteins were joined together through a short peptide linker. With a proper length of DHFR-connecting peptide linker, it was discovered that a primary CSAN, with an average oligomer size of eight copies, would be formed within minute when DHFR-DHFR was incubated with bis-MTX (**Fig. 1-17**).[81]

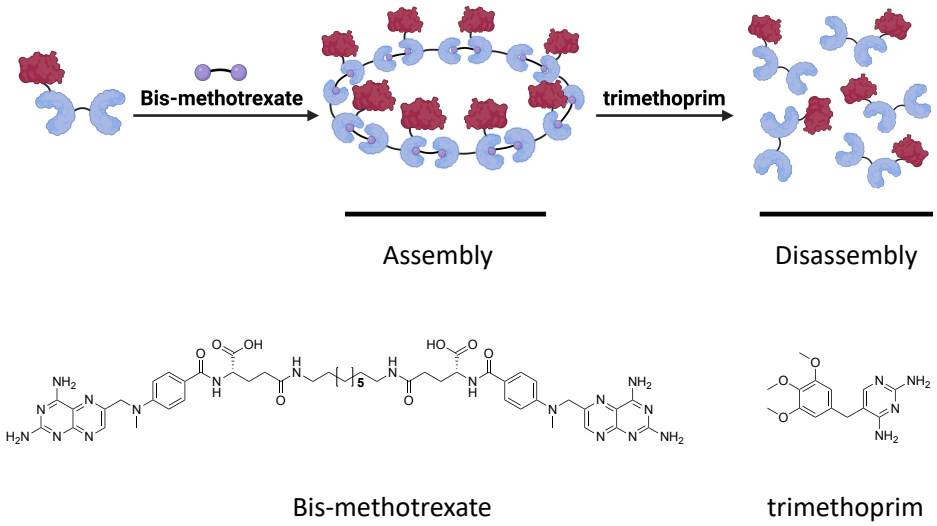

Figure 1-17. Schematic representation of CSAN assembly and disassembly and structures of bis-methotrexate (bis-MTX) and trimethoprim. CSAN is formed through incubating monomeric E_1-DD with dimerizer bis-MTX. CSAN is dissembled when incubated with trimethoprim.

Diverse functionalization on CSANs have been reported over the years in applications such as immunotherapy and imaging. Shah et al. in 2016 reported the *in vivo* microPET/CT imaging on mice bearing U-87 MG xenografts.[82] An EGFR-targeting peptide was engineered to the DHFR-DHFR fusion protein to target U-87 MG cells; DOTA[^{64}Cu] was synthesized to the dimerizer bis-MTX. A significant tumor accumulation of ^{64}Cu labeled CSAN was observed by microPET/CT imaging. Shen et al in 2015 reported the immunotherapeutic application of CSAN.[83] Anti-CD3 scFv and CD-22 targeting scFv were engineered to DHFR-DHFR fusion protein individually. The consequent bispecific CSAN bound to both CD3 subunit of the PAR T-cells and the CD22 antigen on malignant B cells for immunotherapeutic purpose. A similar strategy was also used for a bispecific CSAN which bound to both CD3 subunit of the PAR T-cells and EpCAM of MCF-7 cells with cytotoxicity being observed.[84]

With octameric CSANs having a large size of over 400 KDa, the excretion would be challenge. However, one favorable feature of CSANs over other macromolecules is that CSANs can be dissembled with the

treatment of FDA-approved trimethoprim to monomeric DHFR-DHFR protein,[85] which would help against the retention.[86]

The usage of CSANs as a multivalent construct for design of ^{19}F MRI tracers will be discussed in chapter 4.

1.13 Preface to Dissertation

The following chapters focus on the development of ^{19}F MRI temperature sensors (chapter 2) and the ^{19}F MRI molecular tracers (chapter 3 and 4). Chapter 2 describes the design, synthesis, and characterization of second generation temperature sensors in addition to environmental degradation studies. Chapter 3 introduces the design of highly fluorinated peptides as ^{19}F MRI imaging agents and the removal of non-specific cellular interactions. Cell-based NMR experiments is covered with the preparation of EGFR-targeting molecular tracers with lead peptides. Chapter 4 covers the multivalent engineering of the molecular tracer construct in chapter 3 through using CSANs as a means for signal amplification in ^{19}F MR-based experiment. The appendix discusses two projects based on stapled peptides: one is about the stapled peptides on their cellular interaction with albumin under the collaboration with Ratmir Derda group, the other one is about the macrocyclization on MLL fragments.

Chapter 2

Fluorous Liquids for Magnetic Resonance-based Thermometry with Enhanced Responsiveness and Environmental Degradation

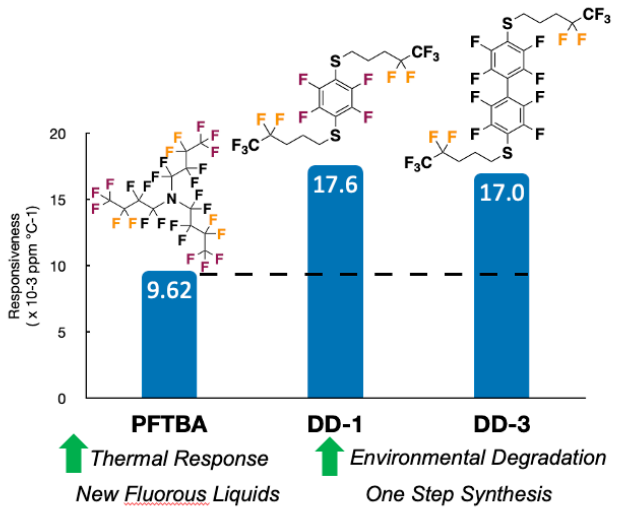

'Fluorous Liquids for Magnetic Resonance-Based Thermometry with Enhanced Responsiveness and Environmental Degradation'

Jiaqian Li, Thomas F. Mundhenke, Thomas G. Smith, William A. Arnold, and William C. K. Pomerantz

Analytical Chemistry **2023** *95* (14), 6071-6079

Motivation for Research

The motivation of this work was based on our previous studies of the development of molecular sensors for MR-based thermometry. This work aimed to develop new sensors with improved sensitivity, and at the same time overcome the major weakness of the previously reported sensors: difficulties in encapsulation and environmental persistence concerns.

2.1 Introduction

Non-invasive measurement of temperature is vital for determining local tissue temperatures. These measurements are used for evaluating disease pathology and medical interventions such as high intensity focused ultrasound,[1] low temperature hyperthermia,[2] hypothermia,[3] radiofrequency ablation,[4] and thermal ablation.[5] Additionally, *in vivo* oximetry measurements are also sensitive to temperature fluctuations, requiring accurate temperature determination.[6] Magnetic resonance imaging (MRI) is one such approach that is used in the clinic. The gold standard thermometry measurement is based on changes in the proton-resonance frequency of water (PRF) with the highest responsiveness in most tissues of ~10×10^{-3} ppm/°C.[7] However, for absolute temperature measurements, reference frequencies are required. PRF temperature measurements are also susceptible to error from magnetic field drift and have low sensitivity in fatty tissue.[1] Such limitations have led to the development of heteronuclear approaches including using ^{23}Na,[8] ^{129}Xe,[9] and ^{19}F.

Fluorine-based magnetic resonance applications have been mainly limited to preclinical studies due to current limitations in the availability of ^{19}F MRI systems for clinical use. There are several advantages of ^{19}F-magnetic resonance that make this an attractive strategy for further development. Given its similar gyromagnetic ratio to ^{1}H, ^{19}F is the second most sensitive stable NMR active nucleus, with 83% signal sensitivity relative to ^{1}H. In addition, the absence of naturally occurring mobile fluorine provides a background-free spectrum that can be used in combination with ^{1}H MRI for anatomical imaging.[10] Organofluorine temperature sensors have previously been developed based on changes in nuclear relaxation or chemical shift changes.[11,12] Perfluorocarbon liquids are particularly attractive for formulating into

nanoemulsions or encapsulating into nanoparticles. These fluorous liquid formulations help overcome the inherently low sensitivity of magnetic resonance measurements for *in vivo* cell tracking studies, oximetry, and thermometry.[10,13–15]

The perfluorocarbon liquid, perfluorotributylamine (PFTBA, **Figure 2-1**), was the first organofluorine compound to be used for *in vivo* thermometry with a temperature responsiveness of ~9 × 10^{-3} ppm/°C approaching the PRF responsiveness and remains one of the most responsive ^{19}F sensors.[16] Given the temperature dependence of fluorocarbon-based oximetry agents, based on T_1 relaxation,[17] PFTBA can be used in combination for temperature calibration. However, several potential difficulties are encountered when using PFTBA including multiple resonances with similar frequencies. These resonances may lead to chemical shift artifacts and a responsiveness below the PRF.[18] Additionally, PFTBA is a potent greenhouse gas.[19] There is also heightened concern about use and environmental persistence of compounds with perfluorinated alkyl groups.[19–21]

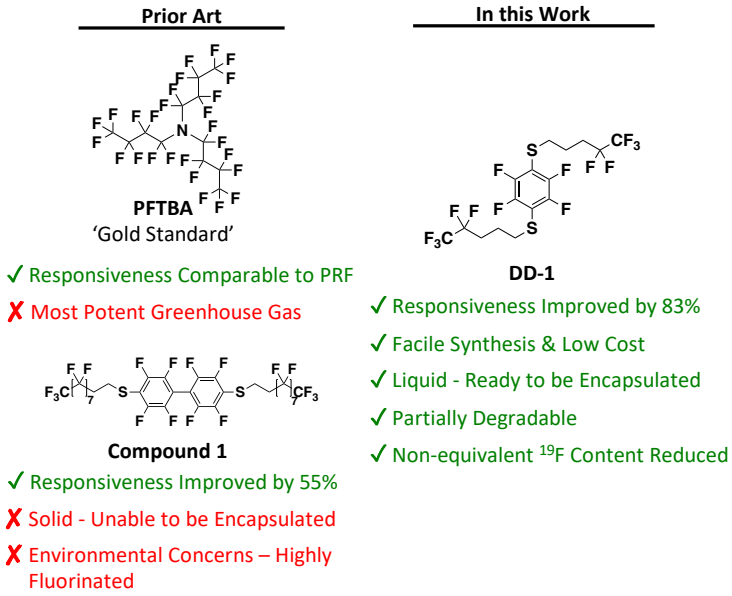

Figure 2-1. Molecular structures and attributes of current and previously reported fluorinated magnetic resonance-based thermometry agents PFTBA, 1 and DD-1.

Previously we reported new organofluorine temperature sensors including **1** (**Figure 2-1**) through a combined experimental and computational approach that improved upon the PFTBA temperature responsiveness and PRF by almost two-fold,[22] where I contributed to the synthesis of **1**. However, **1** possessed several key limitations. The first was a concern over too many fluorine resonances of similar chemical shift which could lead to chemical shift artifacts for ^{19}F MRI. The second concern was that similar to PFTBA, **1** still possessed a long polyfluorinated tail, raising concerns over environmental persistence. Finally, while PFTBA is a room temperature liquid and is readily formulated in our mesoporous silica nanoparticles, **1** is a solid making this process significantly more challenging.[22,23] To address these challenges, we sought to redesign our original temperature sensors, using shorter fluorinated tails based on prior computational predictions,[22] while evaluating heteroatom effects, and the aromatic core on phase behavior and temperature responsiveness. We further evaluated the potential for degradation under simulated environmental and wastewater treatment conditions for three of our lead candidates. We conclude from these studies, that short fluorine chains attached to a perfluoroaromatic core provide simplified and more responsive temperature sensors than PFTBA and our previous sensors, and a liquid phase for future loading studies into nanoparticles. Degradation analyses further show that incorporation of arylfluorine groups lead to more readily degraded parent compounds than perfluoroalkyl substances [24] and should be beneficial for designing future organofluorine materials beyond temperature sensors.

2.2 Results and Discussion

2.2.1 Design and Synthesis of Second-Generation Fluorinated Temperature Sensors.

To improve upon the phase behavior and thermal responsiveness of **1**, we designed several second-generation fluorinated small molecules through variation in the aromatic core, fluorinated tail length, and heteroatom oxidation state (**DD-1**–**DD-7**, **Figure 2-2**). All temperature sensors maintained the structural symmetry for increasing the number of magnetically equivalent fluorine atoms for high signal sensitivity. With the exception of **DD-7**, these sensors also reduce the overall number of fluorine resonances which could lead to potential artifacts in ^{19}F magnetic resonance applications. The selection of aromatic cores in our temperature sensor design was also expanded. While **1** had a perfluorobiphenyl core, a similarly responsive

analog **2** had a more simplified perfluorophenyl core. Inclusion of these aryl fluorine groups were important as the respective ^{19}F resonances were essential for maintaining a high temperature responsiveness. In addition, a structurally similar perfluorophenyl sulfide and a perfluorophenyl sulfone core were introduced to evaluate if these functional groups would lead to additional thermal responsiveness or alter the phase behavior of the final compound through introduction of two additional rotatable bonds. Secondly, based on our previous computational predictions, a shorter alkyl chain containing a perfluoroethyl group was predicted to slightly improve the thermal responsiveness while reducing the number of fluorine atoms from the highly fluorinated -$(CF_2)_7$-CF_3 alkyl chains of **1** and **2**.[22] Such an alkyl chain was anticipated to reduce potential chemical shift artifacts and reduce environmental persistence. The -S-$(CH_2)_3$-CF_2-CF_3 group found in **DD-1–DD-6** maintains the CF_2 group adjacent to a CH_2 which was the second most responsive fluorine group in **1** and **2**. Such a tail has been produced on large scale providing a readily available functional group as it is a key building block for the synthesis of the FDA-approved drug, Fulvestrant.[31] Finally, sulfide oxidation states were modified in **DD-2**, **DD-4**, and **DD-6** to evaluate the heteroatom effects on thermal responsiveness.

All seven new temperature sensors were synthesized under the optimized reaction conditions, enabling facile synthesis (**Figure 2**). Specifically, temperature sensors were prepared through an S_NAr reaction. Compounds **DD-2** and **DD-4** required one extra oxidation of **DD-1** and **DD-3** to provide the respective sulfones. Yields of the S_NAr reactions using thiol HS-$(CF_2)_7$-CF_3 were low, 21% to 24%, while the yields with HS-$(CH_2)_3$-CF_2-CF_3 fell in the range of 53% to 78%. In the case of **DD-2** and **DD-4–DD-7** the sulfur oxidation state or incorporation within the aromatic core did not lead to altered phase behavior at room temperature resulting in white solids. However, in the case of **DD-1** and **DD-3** which possess the shorter fluorinated alkyl chains and either a perfluorophenyl or perfluorobiphenyl group respectively, a room temperature liquid was obtained. These two molecules were of particular interest for facilitating future nanoparticle encapsulation studies using our established loading approach.[23]

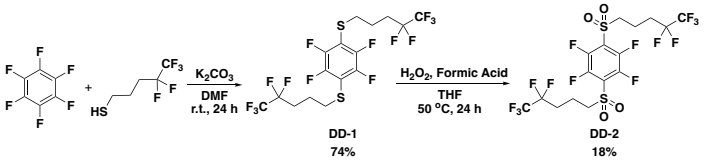

Name	Aromatic Core	Aliphatic Chain R=	State	Yield %
DD-1		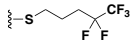	Liquid	74
DD-2	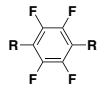	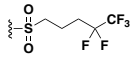	Solid	18
2		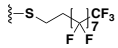	Solid	18
DD-3		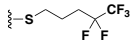	Liquid	62
DD-4	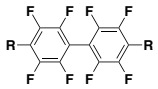	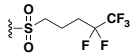	Solid	35
1		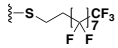	Solid	33
DD-5	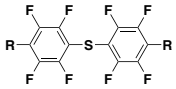	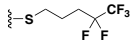	Solid	78
DD-6	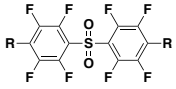	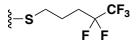	Solid	53
DD-7		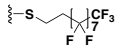	Solid	20

Figure 2-2. Synthesis, structures of fluorinated temperature sensors, and corresponding room temperature phase behavior. Top) Representative synthetic scheme of **DD-1** and **DD-2**. Bottom) Structure of **DD-1**–**DD-7** and compound **1** and **2** with corresponding phase characteristics.

2.2.2 Structure-Property Relationship Studies of Fluorinated Temperature Sensors.

We next sought to investigate the temperature responsiveness of our newly synthesized compounds for comparison to both PFTBA and previously characterized compounds **1** and **2**. While our prior analyses were conducted in chloroform, here we first conducted our analyses in THF to ensure solubility of all compounds.[22] Figure 2-3 depicts the responsiveness for **DD-1–DD-7**, **1**, **2** and PFTBA under these new conditions. In this case, the thermal responsiveness is only reported for the two most responsive pairs of fluorine resonances, which in most cases remain the CF_2 group adjacent to a CH_2 group, and an aryl fluorine group. Under these conditions, all compounds led to a significant increase in responsiveness of 19% (**DD-2**) to up to 75% (**DD-3**) relative to PFTBA with a responsiveness of 9.45×10^{-3} ppm/°C under these conditions.

Within the data set of new fluorinated temperature sensors, the effect on responsiveness revealed a significant structure-property relationship. First, the effect of short alkyl chains with fewer ^{19}F atoms was analyzed. A comparison of matched sensor pairs with the same aromatic core and heteroatom oxidation state showed side chains of shorter length and fewer ^{19}F atoms to be 13% and 14% more responsive for **DD-1** versus **2**, and **DD-3** versus **1** respectively. Matched pair **DD-6** and **DD-7** containing a sulfone group was an exception where both showed a low responsiveness. The origin of this effect is explained below. Nevertheless, we conclude the short alkyl chain with fewer ^{19}F atoms remains the most beneficial when sulfones are excluded.

The effect of different aromatic cores on responsiveness was next evaluated. **DD-1**, **DD-3**, **DD-5** and **DD-6** all have the same -$(CH_2)_3$-CF_2-CF_3 fluorinated alkyl chain. In this case, **DD-1**, **DD-3** and **DD-5** have comparable responsiveness at ~16×10^{-3} ppm/°C, while **DD-6** containing the perfluorobiphenylsulfone core was significantly less responsive (11.5×10^{-3} ppm/°C) than the other three sensors. These results indicated that of the four proposed aromatic cores, no additional advantage could be determined, while sulfur oxidation of the central sulfide proved detrimental.

Surprisingly, a further look at the sulfonyl group-containing sensors revealed that the sulfonyl group whether within the core or substituted on the outer para positions of the aromatic core were also detrimental to the temperature response. In this case, **DD-2** and **DD-4**, the oxidized analogs of the highly responsive **DD-1** and **DD-3**, each lost 21% and 22% responsiveness from oxidation. The reduced responsiveness occurs based on a change in the direction of the chemical shift of the aryl fluorine in response to temperature. This resonance in **DD-2** and **DD-4** now moves upfield (**Figure 2-4**), whereas in **DD-1** and **DD-3** it moves downfield (**Figure 2-3, and 2-5**) providing a larger chemical shift change relative to the CF_2 resonance.

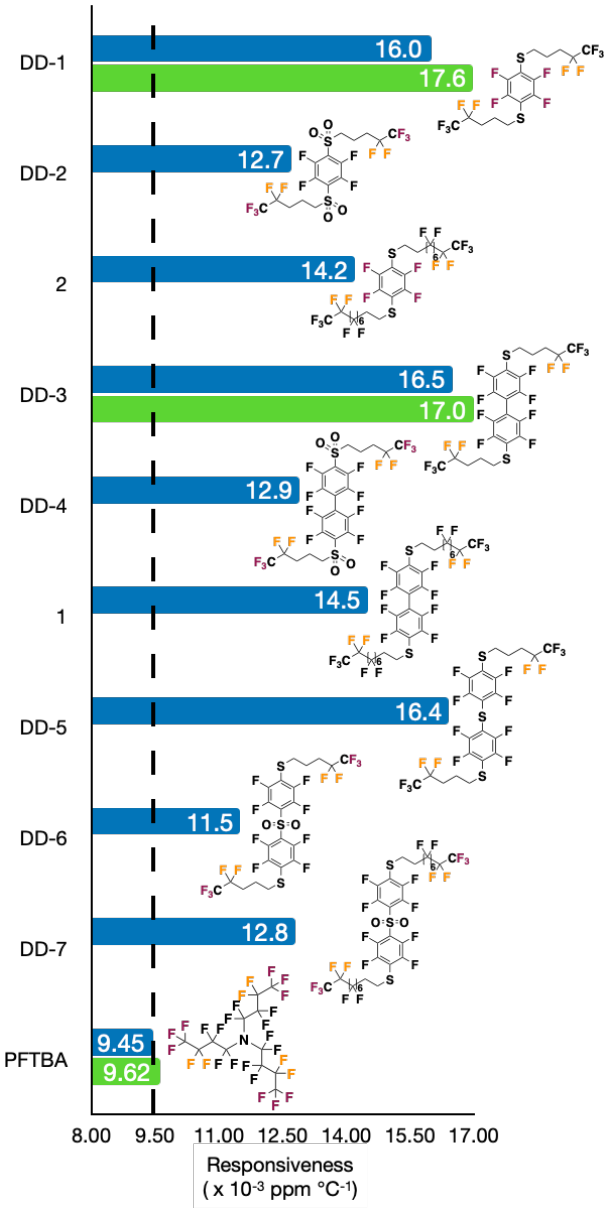

Figure 2-3. Responsiveness of **DD-1**–**DD-7**, compounds **1** and **2**, and PFTBA. Bars in blue are responsiveness in THF-d8; bars in green are responsiveness in phosphate buffer. Dash line indicates thermos responsiveness of PFTBA. Fluorine groups used for temperature determination are showed in gold and maroon. Maroon coloring of the aryl fluorine group is not indicated if there is ambiguity in resonance assignment.

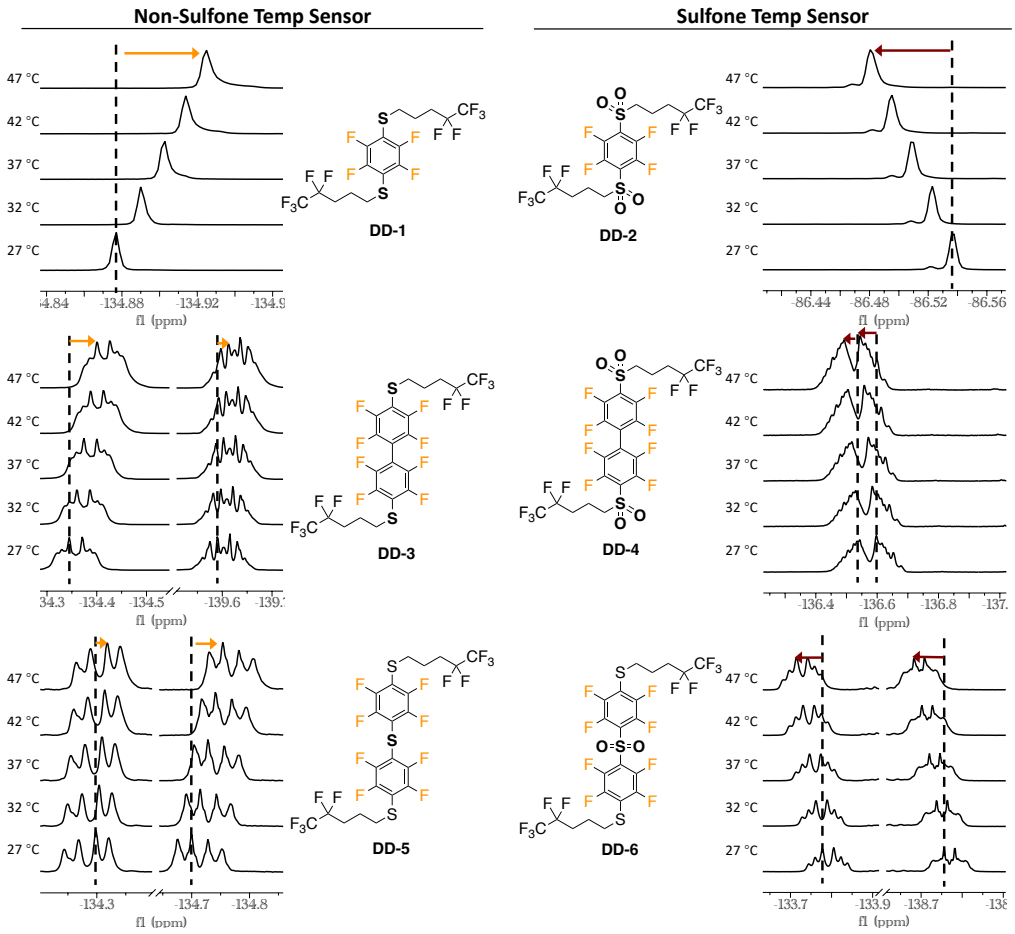

Figure 2-4. Temperature response of aryl ^{19}F resonances on temperature sensors. On the left are the spectra (aromatic region) of non-sulfone containing temperature sensors, where aromatic resonance(s) move upfield with the increase of temperature. On the right are the spectra (aromatic region) of sulfone containing temperature sensors, where aromatic resonance(s) move downfield with the increase of temperature.

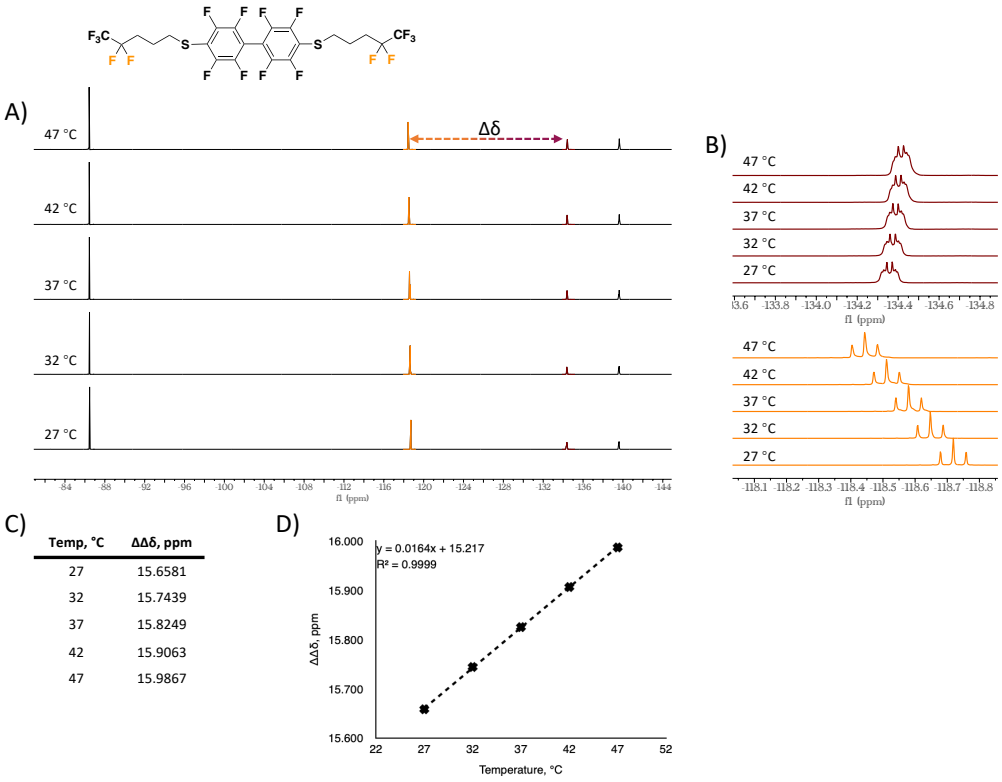

Figure 2-5. Temperature measurement and responsiveness determination of **DD-3** in THF-d_8. (A) ^{19}F NMR spectra of **DD-3** at different temperatures. Highlighted are the resonances repair determining the temperature responsiveness. (B) Expanded regions of the highlighted resonances. (C) Table of the $\Delta\Delta\delta$ at different temperatures. (D) Temperature responsiveness plot of **DD-3** with $\Delta\Delta\delta(T) = 16.5 \times 10^{-3} \pm 0.08 \times 10^{-3}$ ppm °C^{-1} (n = 3, mean ± SD).

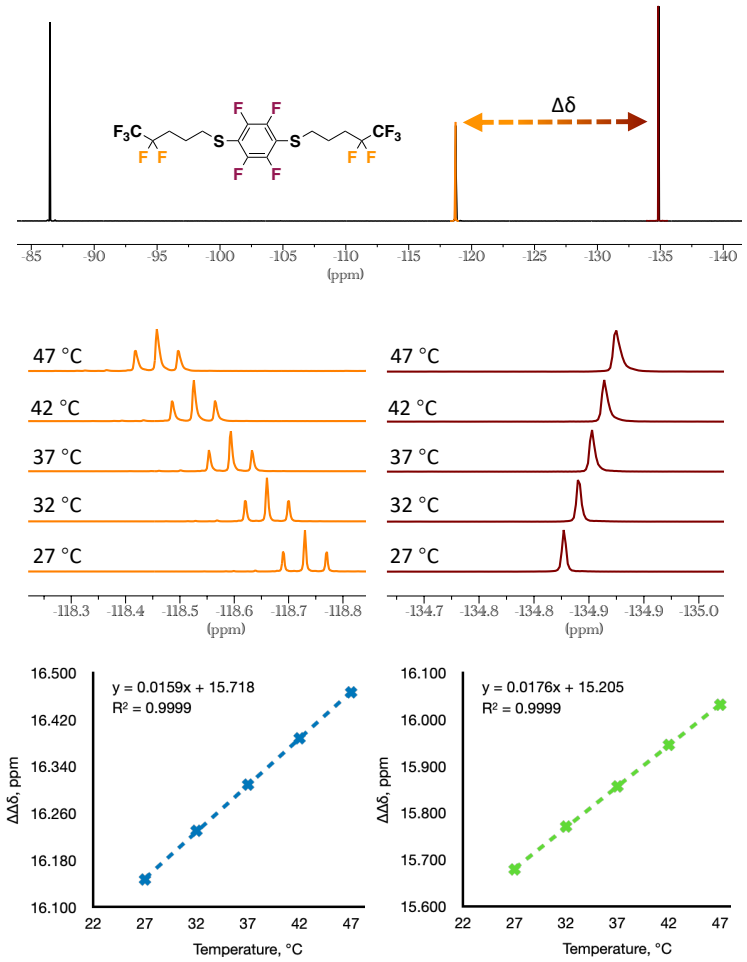

Figure 2-6. Spectra and temperature response of **DD-1** resonances by ^{19}F NMR. (A) Structure and spectrum of **DD-1** in THF-d_8 at 27 ºC. Fluorine groups are colored to match the two resonances used to determine the temperature responsiveness. (B) Selected regions of the ^{19}F NMR spectra used for analysis with the CF_2 resonance (left) and the Ar-F (right). (C) Temperature response of **DD-1** in THF-d_8 with 16.0 ± 0.05 × 10^{-3} ppm °C^{-1} (n=3, mean ± SD) in blue and temperature response of **DD-1** in phosphate buffer with 17.6 ± 0.05 × 10^{-3} ppm °C^{-1} (n=3, mean ± SD) in green.

In addition to **DD-1** and **DD-3** having the desired liquid phase characteristics and being the most responsive sensors, these two small molecules were also shown to have sufficient aqueous solubility up to 200 µM (**Figure 2-7**) for analysis of their responsiveness in water, which we were unable to do with **1** and **2**. In this case, PFTBA showed an aqueous responsiveness of 9.62 x 10^{-3} ppm/°C, similar to the literature

value. **DD-1** and **DD-3** showed an 83% and 77% improvement in responsiveness with 17.6 ± 0.05 × 10^{-3} ppm/°C and 17.0 ± 0.82 × 10^{-3} ppm/°C respectively.

A)

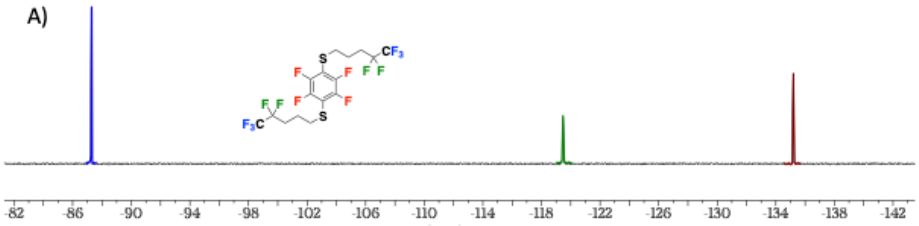

B)

Concentration, μM	Normalized Intensity (δ, -87 ppm)	Normalized Intensity (δ, -120 ppm)	Normalized Intensity (δ, -135 ppm)
250	3.033	2.883	2.787
200	2.105	2.103	2.016
150	1.403	1.403	1.497
100	1.000	1.000	1.000
50	0.478	0.494	0.405
10	0.097	0.225	0.081

C)

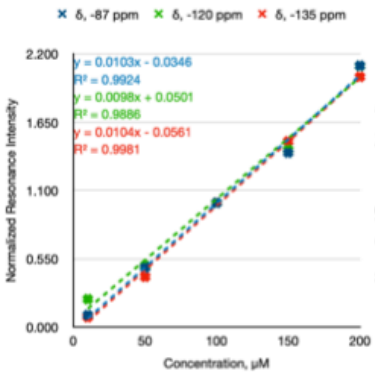

D)

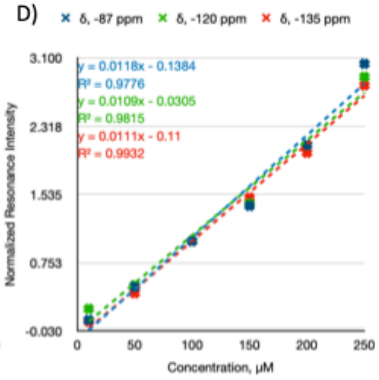

Figure 2-7. Solubility limit determination of **DD-1** in phosphate buffer. (A) ^{19}F NMR spectra of **DD-1** in phosphate buffer (B) Table of normalized signal intensity of individual resonance at different concentration. All signal intensities of resonances of 100 μM **DD-1** were set to 1. C) Normalized intensity chart of 3 individual resonances at different concentration, excluding 250 μM. D) Normalized intensity chart of 3 individual resonances at different concentration, including 250 μM. The R^2 of the CF_3 (-87 ppm) resonance line is only 0.9776.

Summarizing our initial results, of the seven new sensors, **DD-1**, **DD-3**, and **DD-5** were all more responsive than PFTBA and previously characterized **1** and **2** (**Figure 2-3**). In addition, **DD-1** and **DD-3** with short fluorinated alkyl tails, both form a favorable liquid phase at room temperature for future encapsulation studies with nanoparticles for ^{19}F MRI experiments (**Figure 2-2**), while a central sulfide in the

aromatic core prevents room temperature liquid phase formation. Given their aqueous solubility, improved responsiveness could be measured for **DD-1** and **DD-3** in water, and bodes well for future biological applications with these compounds.

2.2.3 Degradation studies of temperature sensors, DD-1, DD-3, and DD-5 by Direct Photolysis.

Our previous analysis of the environmental degradation profile of various fluorinated pharmaceuticals and model compounds revealed a significant difference in degradation propensity between fluorinated functional groups when exposed to simulated environmental photolysis or oxidative water treatment conditions.[32,33] Given concerns over the environmental persistence of highly fluorinated molecules, we evaluated the degradation profile of **DD-1**, **DD-3**, and **DD-5** under photolysis and oxidative conditions. As a first experiment, we obtained UV-Vis absorption spectra of **DD-1**, **DD-3**, and **DD-5** to evaluate the propensity to absorb sufficient light with wavelengths > 290 nm (solar light) under ambient conditions. UV-Vis spectra (**Figure 2-8**), show substantial overlap with the lamp output, indicating the potential for direct photolysis by sunlight or UV-lamps.

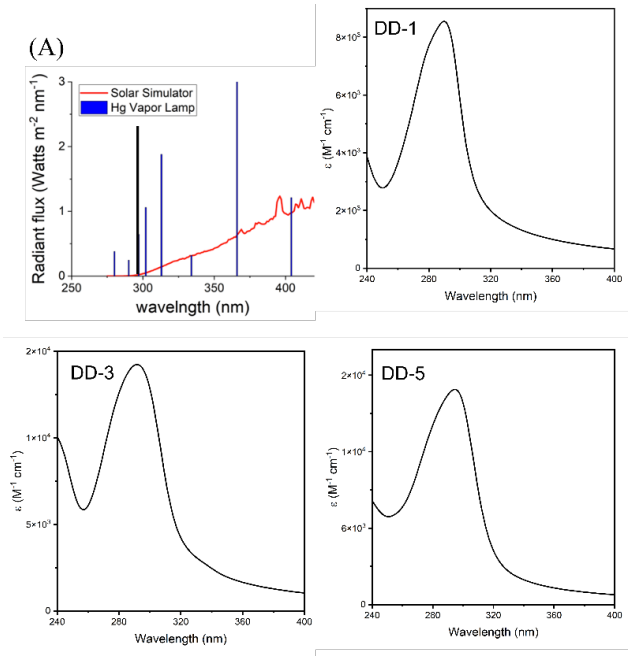

Figure 2-8. Spectra of degradation irradiation and compounds' UV absorption. (A) Solar simulator and mercury vapor lamp irradiation spectra (per nm) with 290 nm filter (black line). UV Absorption spectra of 50 µm **DD-1**, **DD-3**, and **DD-5** in the pH = 7 buffer.

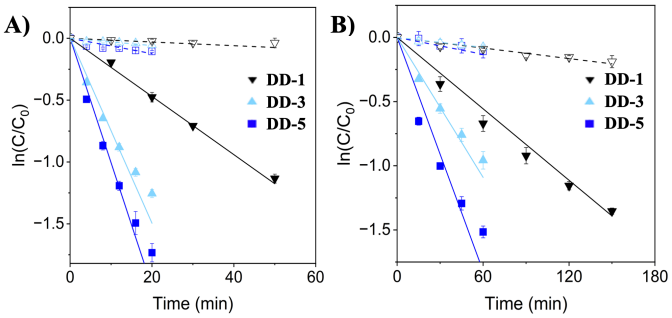

Figure 2-9. Photochemical degradation kinetic plots of **DD-1** (▾), **DD-3** (▲), and **DD-5** (■) at 10 µM with photolysis (filled) and dark controls (open) in (A) the mercury vapor lamp and (B) the solar simulator. (A) Under mercury vapor lamp, the kinetic rate constant of degradation of **DD-1** is $2.29 \pm 0.10 \times 10^{-2}$ min^{-1}, **DD-3** is $6.78 \pm 0.71 \times 10^{-2}$ min^{-1}, and **DD-5** is $9.29 \pm 0.90 \times 10^{-2}$ min^{-1}. (B) Under solar simulator, the kinetic rate constant of degradation of **DD-1** is $0.96 \pm 0.08 \times 10^{-2}$ min^{-1}, **DD-3** is $1.68 \pm 0.17 \times 10^{-2}$ min^{-1}, and **DD-5** is $2.80 \pm 0.56 \times 10^{-2}$ min^{-1}. Reported errors are 95% confidence intervals. Experiments were in 10 mM pH = 7 phosphate buffer and contained residual DMSO from the stock solution. Error bars indicate the standard deviation of measured concentrations of triplicate experiments.

Reverse-phase HPLC was used for quantifying degradation kinetics by direct photolysis. Under both the mercury vapor lamp and solar simulator light sources **DD-5** had the fastest rate constants followed by **DD-3** then **DD-1**, (**Figure 2-9**). The quantum yields, determined using the solar simulator, were 0.0272 mol Ei^{-1} for **DD-1**, 0.0267 mol Ei^{-1} for **DD-3**, and 0.0520 mol Ei^{-1} for **DD-5**, with the higher quantum yields being consistent with the fastest rate of degradation. the UV light gave higher intensity energy with more focused wavelength while solar simulator having lower intensity with more similar spectral energy distribution as of the sun.'. This is due to the high intensity UV light produced compared to the solar simulator which has a spectral energy distribution more similar to the sun. All compounds had half lives in the range of 7 to 30 minutes with the mercury vapor lamp and 25 to 72 minutes in the solar simulator.

2.2.4 Fluorine Mass Balance.

To determine if any of the fluorinated functional groups were susceptible to degradation, we turned to quantitative ^{19}F NMR. The environmental persistence and potential impact of these fluorinated temperature sensors will be a function of not only the persistence of the parent compound, but also that of any fluorinated reaction products. Photolysis and ozonation represent natural and engineered processes, respectively, that could degrade these compounds after their use and introduction into the water system. ^{19}F NMR spectra were taken to quantify and partition degradation products from the parent compound signals for photolysis and ozonation (**Figure 2-10 and 2-11**).

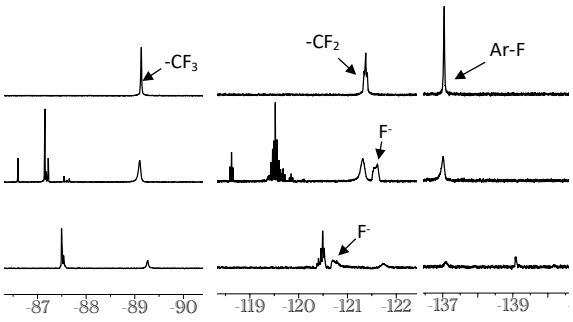

Figure 2-10. ^{19}F-NMR spectra of **DD-1** showing chemical shifts of fluorinated groups in the parent compound and reaction products. Top: Selected spectral regions of untreated **DD-1**. Middle: Selected spectral regions of **DD-1** following partial degradation by the solar simulator. Bottom: Selected spectral regions of **DD-1** following partial degradation by ozone. Fluoride (F^-) produced from degradation reactions is indicated for clarity. Spectra in the left, middle, and right regions are scaled differently for visibility.

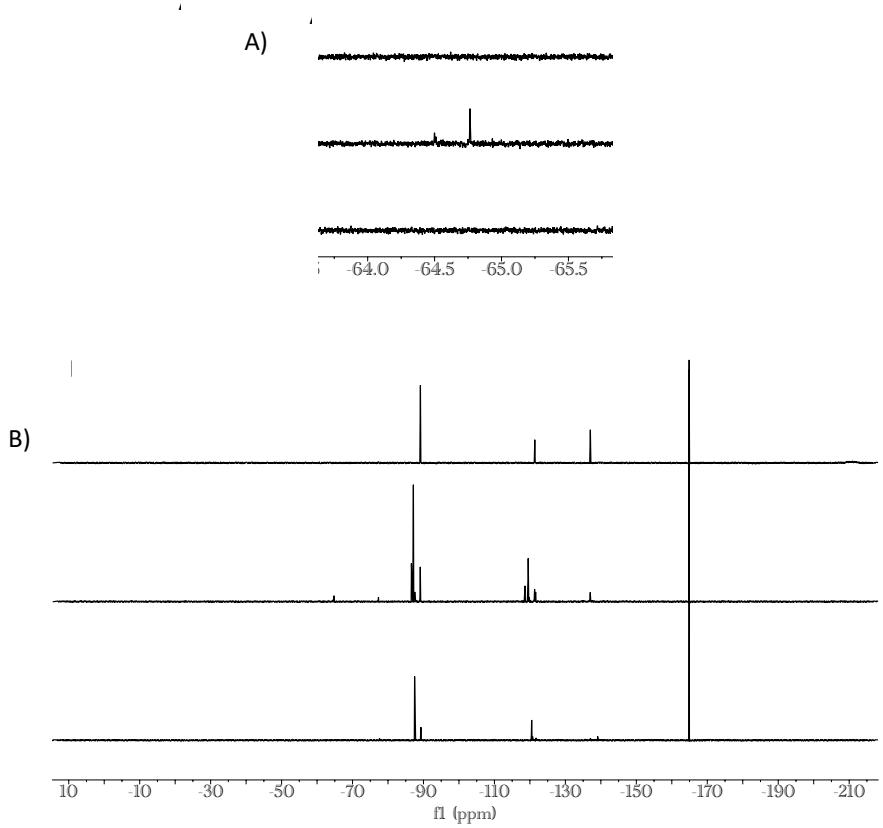

Figure 2-11. ^{19}F-NMR degradation spectra of **DD-1** showing chemical shifts of fluorinated groups in the parent compound and reaction products. A) Selected spectra region of **DD-1** under untreated, solar simulator-treated, ozone-treated conditions. Top: Selected spectral region of untreated **DD-1**. Middle: Selected spectral region of **DD-1** following partial degradation by the solar simulator. Bottom: Selected spectral region of **DD-1** following partial degradation by ozone. B) Full spectra of **DD-1** under untreated, solar simulator-treated, ozone-treated conditions. Top: Full spectrum of untreated **DD-1**. Middle: Full spectrum of **DD-1** following partial degradation by the solar simulator. Bottom: Full spectrum of **DD-1** following partial degradation by ozone.

Table 2-1 shows the mass balance for **DD-1** determined using ^{19}F NMR under photolysis and ozonation conditions. The solutions analyzed contained 50 μM of **DD-1** with 14 fluorine atoms, thus a total fluorine concentration of 700 μM, with 200 μM attributed to the aromatic fluorines (Ar-F; -137.0 ppm), 200 μM attributed to the CF_2 (-121.3 ppm), and 300 μM attributed to the CF_3 (-89.1 ppm) as shown in Figure 6. For

photolysis and ozonation, 61% and 87% of the parent Ar-F signal was lost respectively. A peak at -139.1 ppm appeared following ozonation and is hypothesized to be a hydroxylated aromatic ring product, which is a known reaction process for aromatics during ozonation.[34] For the parent CF_2, the signal decreased by 45% and 79%, but new CF_2 products appeared upfield. Under both degradative conditions, new peaks appear in the near regions of the CF_2, likely due to ring opening processes. These triplets and multiplets were allocated as CF_2 because the splitting patterns and chemical shifts resemble that of CF_2 groups, and our assumption is that the CF_2 motif does not degrade. For the parent CF_3, the signal decreased by 38% and 69%, again with new CF_3 products appearing upfield. An excess of 39 μM and 48 μM for the solar simulator and ozonation, respectively, was found within the CF_3 region. These groups are hypothesized to be products produced by opening of the aromatic ring, which could be vinyl fluorines with oxygen and/or sulfur substituents, which could result in an upfield shift. It has previously been shown that during the photolysis or ozonation of halogenated phenols, vinyl ring opening products are possible via oxidative free radical attack.[35]

Fluoride (F^-) production via photolysis was 79 μM and 117 μM for ozonation. The F^- peak for ozonation is shifted slightly upfield compared to that of photolysis, but it was deemed the F^- peak because of the broad signal and sensitivity to solvent composition commonly seen experimentally in our previous work.[32,33] While F^- production is believed to be from the aromatic fluorines as previously demonstrated, not all the Ar-F can be accounted for via F^-.[32,33] This is supported by the sum of the concentrations of fluorine for the Ar-F, F^-, and ring opening products/vinyl fluorine being 198 μM and 200 μM for photolysis and O_3, respectively. Given ~10% error in quantification, these concentrations are equal to the initial Ar-F present. To confirm this hypothesis further mass spectrometry studies would need to be conducted. Similar trends were observed for **DD-3** and **DD-5** in the CF_2 and CF_3 region (**Figure 2-12**, and **2-13**), with new peaks appearing near the parent CF_2 and CF_3 peaks. A difference between **DD-1** and **DD-3**/**DD-5** is that for the latter, the F^- peak is overlapping with the parent CF_2 peaks, thus F^- was calculated assuming that the CF_2 motif does not degrade.

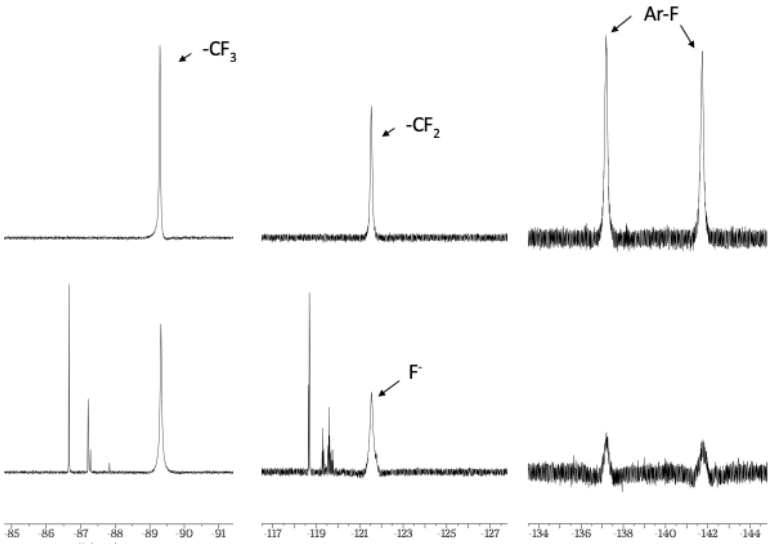

Figure 2-12. ^{19}F-NMR degradation spectra of **DD-3** showing chemical shifts of fluorinated groups in the parent compound and reaction products. Top: Selected spectral regions of untreated **DD-3**. Bottom: Selected spectral regions of **DD-3** following partial degradation by solar simulator. Fluoride (F^-) produced from degradation reactions is indicated for clarity. Spectra in the left, middle, and right regions are scaled differently for visibility.

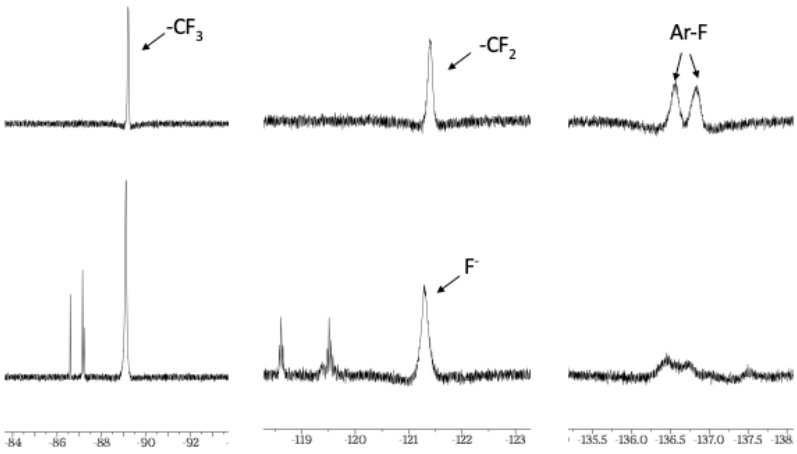

Figure 2-13. ^{19}F-NMR degradation spectra of **DD-5** showing chemical shifts of fluorinated groups in the parent compound and reaction products. Top: Selected spectral regions of untreated **DD-5**. Bottom: Selected

spectral regions of **DD-5** following partial degradation by solar simulator. Fluoride (F^-) produced from degradation reactions is indicated for clarity. Spectra in the left, middle, and right regions are scaled differently for visibility.

We conclude from these degradation studies that our new temperature sensors have a sufficient UV-visible absorption cross-section to enable aromatic photolysis degradation pathways which produce F^- and ring opening products. While the aromatic cores were found to undergo chemical transformations, these studies show that the CF_2 and CF_3 motifs remain unchanged under these degradative conditions, resulting in the formation of new fluorinated degradation products. Previous studies have shown that both photolysis and H_2O_2 treatment have limited capacity to degrade CF_2 and CF_3 alkyl motifs.[36–39] Other processes using hydrated electrons,[40] photocatalysts, [39] and hydrothermal alkaline treatment [41] to degrade these moieties. Use of these treatments would require capture of excreted temperature sensors before they were introduced to the sewer system or environment.

Table 2-1. DD-1 mass balance under solar simulator and ozone degradation by quantitative ^{19}F-NMR. Parental resonances marked as Italics.

Parental Motif	δ (ppm)	Concentration (μM)	Solar Degradation Motif	δ (ppm)	Concentration (μM)	O_3 Degradation Motif	δ (ppm)	Concentration (μM)
Ar-F	*-137.0*	206	Ar-F	*-137.0*	80	Ar-F	-139.1 *-137.0*	55
$-CF_2$	*-121.3*	200	$-CF_2$	*-121.3* -118.6 to -120.6	110 98	$-CF_2$	*-121.3* -118.6 to -120.6	42 138
$-CF_3$	*-89.1*	299	$-CF_3$	*-89.1*	299[a]	$-CF_3$	*-89.1*	299[a]
			F^-	-121.5	79	F^-	-120.7	117
			Ring opening product/ Vinyl F	-86.6 to -87.5 -64.8[b]	36 3	Ring opening product/ Vinyl F	-86.6 to -87.5	48
Total fluorine: 705			Total fluorine: 705			Total fluorine: 699		

[a] $-CF_3$ is assumed to be non-degraded

Table 2-2. **DD-3** Mass balance under solar simulator by quantitative ^{19}F-NMR. Parental resonances marked as *Italics*

Parental Motif	δ (ppm)	Concentration (μM)	Solar Degradation Motif	δ (ppm)	Concentration (μM)
Ar-F	*-141.8*	210	Ar-F	*-137.0*	~0
Ar-F	*-137.0*	193	Ar-F	*-137.0*	~0
$-CF_2$	*-121.6*	203	$-CF_2$	*-121.6* -118.7 to -119.7	135 68
$-CF_3$	*-89.3*	318	$-CF_3$	*-89.3*	318[a]
			F^-	-121.6	161[b]
			Ring opening product/ Vinyl F	-86.7 to -87.8	221[a]
Total fluorine: 924			Total fluorine: 903		

[a]The additional fluorine in this region of the spectrum is assumed to arise from ring opening products and the quantity of this product was calculated by assuming that the CF_3 is not degraded. The growth of the peak at -89.3 ppm indicates that the ring opening products/vinyl F also at appear this shift.

[b]The additional fluorine quantified in this region is assumed to be F^- within the peak at -121.6 ppm. The amount of F^- was determined assuming the CF_2 is not degraded.

2.3 Conclusion

In these studies, we have demonstrated a rational design of highly temperature responsive fluorinated small molecules for magnetic resonance-based thermometry. Two of these molecules form room temperature liquids for future encapsulation studies, and can be synthesized in a single step from readily available starting materials. These results build on our earlier results of a first-generation temperature sensor, which while more sensitive than the commonly used PFTBA, suffered from limited water solubility and was a solid at room temperature limiting facile use in aqueous systems such as through the loading into nanoparticles. Additionally, the highly fluorinated alkyl tail raised concerns over environmental persistence. In our newest

designs our lead compound **DD-1** provides further improvement in temperature responsiveness, while greatly reducing the non-magnetically equivalent fluorine atoms to maintain high signal sensitivity while minimizing chemical shift artifacts. Finally, using a combined analytical approach of quantitative ^{19}F NMR and HPLC analysis, we demonstrate the advantage of using arylfluorine groups in organofluorine designs, which provide a mechanism for sufficient absorption of UV light to enhance environmental photolytic degradation and degradation under water processing conditions over more persistent aliphatic fluorine groups. Still, either further refinement of the fluorinated moieties, evaluation of additional treatment, or capture of excreted material would be needed to ensure persistent fluorinated products are not released. While not studied here, these sensors, may also find use in combination with magnetic resonance-based oximetry measurements which are temperature sensitive. One possible scenario would be the PFCE-**DD-1** dual sensor. PFCE is one of the most common reporters for oximetry, which features a high pO_2 sensitivity and a single resonance with high fluorine content. However, it is also very temperature sensitive, with a 3 torr/ ^oC error in pO_2 determination. With **DD-1**'s strength in absolute temperature determination with high sensitivity, temperature can be precisely calibrated and would result in a subsequent precise pO_2 determination. Alternatively, **DD-1** might be one reporter for oximetry with the perk of self-temperature calibration. pO_2 sensitivity of **DD-1** is worth study in the future. Considering the low aqueous solubility of **DD-1** and the inherent low sensitivity in ^{19}F MRI, for either oximetry or thermometry applications, encapsulation is deemed necessary to prepare the reporter for achieving high PFC concentration. While nanoemulsions have been the mainstream construct through using surfactants, nanoparticles are exhibiting their versatility, including further functionalization. **DD-1** encapsulated in nanoparticles would be an interesting construct for more advanced studies in either oximetry or thermometry.

2.4 Supplementary Information

2.4.1 Synthesis of compounds

Materials

Hexafluorobenzene was purchased from Oakwood Chemical (Estill, SC). Decafluorobiphenyl was purchased from Sigma-Aldrich (St. Louis, MO). Pentafluorophenyl sulfide was purchased from Matrix

Scientific (Columbia, SC). 4,4,5,5,5-Pentafluoro-1-pentanethiol was purchased from Ambeed (Arlington Heights, IL). 3,3,4,4,5,5,6,6,7,7,8,8,9,9,10,10,10-heptadecafluorodecane-1-thiol was purchased from Santa Cruz Biotechnology (Dallas, TX). Other chemicals and reagents were purchased from Sigma-Aldrich (St. Louis, MO) without further purification.

pentafluorophenyl sulfone

Pentafluorophenyl sulfide (915 mg, 2.50 mmol) and m-CPBA (1726 mg, 10.00 mmol) were suspended in 10 mL of DCM in a sealed tube. The reaction mixture was heated in a 110 °C oil bath for 24 h. The reaction mixture was then cooled to room temperature diluted with DCM to dissolve all of the precipitates. The reaction mixture was washed with 1M K_2CO_3 (50 mL x 3). Organic layer was then washed with brine, dried with anhydrous $MgSO_4$, and concentrated under reduced pressure. The crude product was purified by Combi-flash chromatography (5% ethyl acetate and hexane) to obtain the product as white solid (717 mg ,72%)

^{13}C NMR (126 MHz, Chloroform-*d*) δ 146.00, 145.47, 138.22, 116.70.

^{19}F NMR (471 MHz, Chloroform-*d*) δ -135.25 (m, *J* = 19.1, 9.9, 9.1, 5.9 Hz, 4F), -140.54 (m, *J* = 21.3, 8.1 Hz, 2F), -157.02 (m, *J* = 20.9, 7.0 Hz, 4F). Spectral data match those of the reported reference. [1,2]

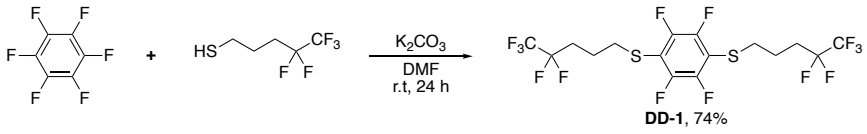

(perfluoro-1,4-phenylene)bis((4,4,5,5,5-pentafluoropentyl)sulfane (DD-1)

Hexafluorobenzene (23 µL, 0.20 mmol) was dissolved in 3 mL of DMF followed by addition of 4,4,5,5,5-Pentafluoro-1-pentanethiol (60 µL, 0.40 mmol) and then K_2CO_3 (80 mg, 0.60 mmol) to the solution. The resulting reaction mixture was stirred at room temperature for 24 h. The reaction was quenched with brine (10 mL) and extracted with ethyl acetate (5 mL x 3). The organic layers were combined, dried with

anhydrous $MgSO_4$, and concentrated under reduced pressure. The crude product was purified by Combi-flash chromatography (0-100% ethyl acetate in hexane) to obtain the product as clear oil. (78 mg, 74%)

^{1}H NMR (500 MHz, Chloroform-*d*) δ 3.02 (t, *J* = 7.0 Hz, 1H), 2.23 (tt, *J* = 17.8, 7.9 Hz, 2H), 1.86 (dt, *J* = 14.7, 7.1 Hz, 1H).

^{13}C NMR (126 MHz, THF) δ 147.38, 119.41, 116.07, 114.23, 33.56, 28.75, 20.94.

^{19}F NMR (471 MHz, Chloroform-*d*) δ -85.49 (s, 6F), -118.01 (t, *J* = 18.1 Hz, 4F), -133.09 (s, 4F).

HRMS is not available due to insufficient compound ionization for detection.

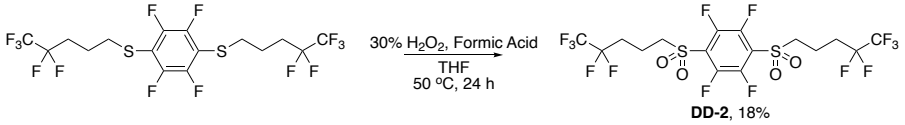

DD-2, 18%

1,2,4,5-tetrafluoro-3,6-bis((4,4,5,5,5-pentafluoropentyl)sulfonyl)benzene (DD-2)

DD-1 (50 mg, 0.094 mmol) was dissolved in 2 mL of THF. Formic acid (600 µL, 15.90 mmol) and 30% hydrogen peroxide (0.75 g, 6.62 mmol) were added to the solution. The resulting reaction mixture was stirred at 50 °C for 24 h. The reaction was quenched with brine (10 mL) and extracted with ethyl acetate (5 mL x 3). The organic layers were combined, dried with anhydrous $MgSO_4$, and concentrated under reduced pressure. The crude product was purified by Combi-flash chromatography (0-100% ethyl acetate in hexane) to obtain the product as white solid. (10 mg, 18%)

^{1}H NMR (500 MHz, THF-d_8) δ 3.68 – 3.61 (m, 1H), 2.40 (tt, *J* = 18.2, 8.2 Hz, 2H), 2.13 (p, *J* = 7.8 Hz, 1H).

^{13}C NMR (126 MHz, THF) δ 145.31, 123.45, 119.31, 115.78, 55.87, 28.56, 14.15.

^{19}F NMR (471 MHz, THF-d_8) δ -86.54 (s, 6F), -119.34 (t, *J* = 18.6 Hz, 4F), -135.49 (s, 4F).

HRMS is not available due to insufficient compound ionization for detection.

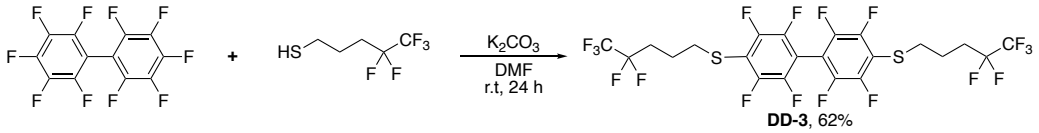

DD-3, 62%

perfluoro-[1,1'-biphenyl]-4,4'-diyl)bis((4,4,5,5,5-pentafluoropentyl)sulfane (DD-3)

Decafluorobiphenyl (68 mg, 0.20 mmol) was dissolved in 3 mL of DMF. 4,4,5,5,5-Pentafluoro-1-pentanethiol (60 µL, 0.40 mmol) was added to the solution followed by addition of K_2CO_3 (80 mg, 0.60 mmol). The resulting reaction mixture was stirred at room temperature for 24 h. The reaction was quenched with brine (10 mL) and extracted with ethyl acetate (5 mL x 3). The organic layers were combined, dried with anhydrous $MgSO_4$, and concentrated under reduced pressure. The crude product was purified by Combi-flash chromatography (0-100% ethyl acetate in hexane) to obtain the product as clear oil. (84 mg, 62%)

^{1}H NMR (500 MHz, Chloroform-*d*) δ 3.11 (t, *J* = 7.0 Hz, 1H), 2.26 (tt, *J* = 17.8, 7.8 Hz, 2H), 1.94 (p, *J* = 7.2 Hz, 1H).

^{13}C NMR (126 MHz, THF) δ 147.44, 144.22, 119.42, 117.05, 116.08, 106.78, 33.55, 28.82, 21.15.

^{19}F NMR (471 MHz, Chloroform-*d*) δ -85.46 (s, 6F), -117.95 (t, *J* = 17.8 Hz, 4F), -132.79 – -132.93 (m, 4F), -137.29 (m, 4F).

HRMS is not available due to insufficient compound ionization for detection.

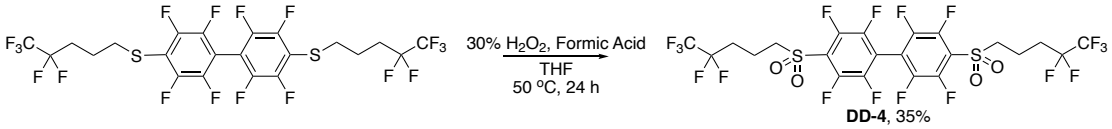

2,2',3,3',5,5',6,6'-octafluoro-4,4'-bis((4,4,5,5,5-pentafluoropentyl)sulfonyl)-1,1'-biphenyl (DD-4)

DD-3 (50 mg, 0.073 mmol) was dissolved in 2 mL of THF. Formic acid (600 µL, 15.90 mmol) and 30% hydrogen peroxide (0.75 g, 6.62 mmol) were subsequently added to the solution. The resulting reaction mixture was stirred at 50 °C for 24 h. The reaction was quenched with brine (10 mL) and extracted with ethyl acetate (5 mL x 3). The organic layers were combined, dried with anhydrous $MgSO_4$, and concentrated under reduced pressure. The crude product was purified by Combi-flash chromatography (0-100% ethyl acetate in hexane) to obtain the product as white solid. (19 mg, 35%)

^{1}H NMR (500 MHz, THF-d_8) δ 3.74 – 3.67 (m, 4H), 2.45 (td, *J* = 18.5, 9.9 Hz, 4H), 2.21 (p, *J* = 7.8 Hz, 4H).

^{13}C NMR (126 MHz, THF) δ 145.19, 144.57, 121.68, 119.33, 115.83, 111.20, 55.95, 28.61, 14.16.

^{19}F NMR (471 MHz, THF-d_8) δ -86.51 (s, 6F), -119.30 (t, *J* = 18.6 Hz, 4F), -136.43 – -136.72 (m, 8F).

HRMS is not available due to insufficient compound ionization for detection.

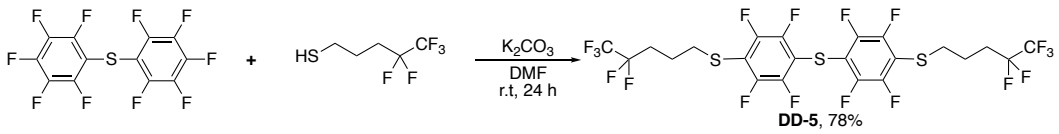

DD-5, 78%

bis(2,3,5,6-tetrafluoro-4-((4,4,5,5,5-pentafluoropentyl)thio)phenyl)sulfane (DD-5)

Pentafluorophenyl sulfide (72 mg, 0.20 mmol) was dissolved in 3 mL of DMF. 4,4,5,5,5-Pentafluoro-1-pentanethiol (60 μL, 0.40 mmol) was subsequently added to the solution followed by K_2CO_3 (80 mg, 0.60 mmol). The resulting reaction mixture was stirred at room temperature for 24 h. The reaction was quenched with brine (10 mL) and extracted with ethyl acetate (5 mL x 3). The organic layers were combined, dried with anhydrous $MgSO_4$, and concentrated under reduced pressure. The crude product was purified by Combi-flash chromatography (0-100% ethyl acetate in hexane) to obtain the product as white solid. (112 mg, 78%)

^{1}H NMR (500 MHz, THF-d_8) δ 3.10 (t, J = 7.1 Hz, 4H), 2.31 (tt, J = 18.4, 8.0 Hz, 4H), 1.85 (p, J = 7.3 Hz, 4H).

^{13}C NMR (126 MHz, THF) δ 147.25, 146.97, 119.39, 116.41, 116.04, 111.25, 33.45, 28.77, 21.03.

^{19}F NMR (471 MHz, THF-d_8) δ -86.50 (s, 6F), -118.76 (t, J = 18.7 Hz, 4F), -134.28 (dd, J = 25.1, 11.0 Hz, 4F), -134.71 (dd, J = 24.8, 11.4 Hz, 4F).

HRMS is not available due to insufficient compound ionization for detection.

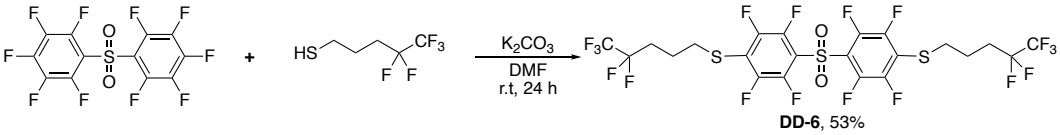

DD-6, 53%

sulfonylbis(2,3,5,6-tetrafluoro-4,1-phenylene))bis((4,4,5,5,5-pentafluoropentyl)sulfane (DD-6)

Pentafluorophenyl sulfone (80 mg, 0.20 mmol) was dissolved in 3 mL of DMF. 4,4,5,5,5-Pentafluoro-1-pentanethiol (60 μL, 0.40 mmol) was subsequently added to the solution followed by K_2CO_3 (80 mg, 0.60 mmol). The resulting reaction mixture was stirred at room temperature for 24 h. The reaction was quenched with brine (10 mL) and extracted with ethyl acetate (5 mL x 3). The organic layers were combined, dried with anhydrous $MgSO_4$, and concentrated under reduced pressure. The crude product was purified by Combi-flash chromatography (0-100% ethyl acetate in hexane) to obtain the product as white solid. (79 mg, 53%)

^{1}H NMR (500 MHz, Chloroform-*d*) δ 3.18 (t, *J* = 7.2 Hz, 4H), 2.21 (tt, *J* = 17.6, 7.7 Hz, 4H), 1.94 (p, *J* = 7.3 Hz, 4H).

^{13}C NMR (126 MHz, THF-d_8) δ 146.92, 144.54, 123.45, 119.38, 119.32, 116.01, 33.02, 28.83, 21.27.

^{19}F NMR (471 MHz, Chloroform-*d*) δ -85.47 (s, 6F), -117.98 (t, *J* = 18.0 Hz, 4F), -131.49 (m, 4F), -136.45 – -136.57 (m, 4F).

HRMS is not available due to insufficient compound ionization for detection.

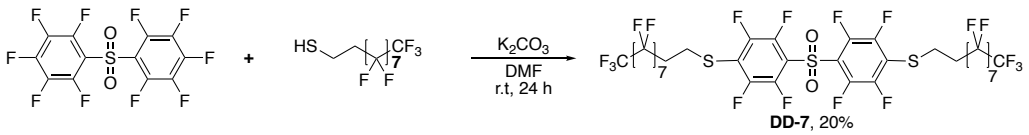

DD-7, 20%

sulfonylbis(2,3,5,6-tetrafluoro-4,1-phenylene))bis((3,3,4,4,5,5,6,6,7,7,8,8,9,9,10,10,10-heptadecafluorodecyl)sulfane (DD-7)

Pentafluorophenyl sulfone (80 mg, 0.20 mmol) was dissolved in 3 mL of DMF. 3,3,4,4,5,5,6,6,7,7,8,8,9,9,10,10,10-heptadecafluorodecane-1-thiol (114 µL, 0.40 mmol) was subsequently added to the solution followed by K_2CO_3 (80 mg, 0.60 mmol). The resulting reaction mixture was stirred at room temperature for 24 h. The reaction was quenched with brine (10 mL) and extracted with ethyl acetate (5 mL x 3). The organic layers were combined, dried with anhydrous $MgSO_4$, and concentrated under reduced pressure. The crude product was purified by Combi-flash chromatography (0-100% ethyl acetate in hexane) to obtain the product as a white solid. (54 mg, 20%)

^{1}H NMR (500 MHz, THF-d_8) δ 3.50 – 3.39 (m, 1H), 2.68 (tt, *J* = 18.0, 8.0 Hz, 1H).

^{13}C NMR (126 MHz, THF) δ 146.83, 144.57, 122.98, 119.51, 117.95, 117.30, 111.34, 111.10, 111.02, 110.97, 110.45, 108.62, 31.77, 24.99.

^{19}F NMR (471 MHz, THF-d_8) δ -81.83 (s, 6F), -114.59 (m, 4F), -122.19 – -122.64 (m, 12F), -123.20 – -123.42 (m, 4F), -123.85 (m, 4F), -126.75 – -126.92 (m, 4F), -133.67 – -134.08 (m, 4F), -138.61 (m, 4F).

HRMS is not available due to insufficient compound ionization for detection.

2.4.2 Experimental

^{19}F NMR Variable Temperature Measurements.

For temperature measurements in organic solvent, compounds were dissolved in THF-d_8 and measured with Bruker AVANCE III 500 equipped with a 5 mm BBFO SmartProbe. For measure of compounds dissolved in THF-d_8, ^{19}F spectra were obtained at 471 MHz with dummy scans = 4, acquisition time = 0.57 s, delay time = 1 s, pre-scan delay = 6.5 μs, and the number of scans = 16. The temperature was increased by passing heated N_2 gas over the spinning sample which was monitored by an internal instrument temperature probe. The temperature was allowed to stabilize for 3 min before scanning. For temperature measurements in aqueous solution, compounds were dissolved in DMSO first and then added to 10 mM pH = 6.9 phosphate buffer/D_2O (9:1 v/v) to make 5% DMSO stock in 500 μL phosphate buffer/D_2O. Samples were measured with Bruker AVANCE III 500 equipped with a 5 mm BBFO SmartProbe. ^{19}F spectra were obtained at 471 MHz with dummy scans = 4, acquisition time = 0.57 s, delay time = 1 s, pre-scan delay = 6.5 μs, and the number of scans = 2048. The temperature was increased by passing heated N_2 gas over the spinning sample which was monitored by an internal instrument temperature probe. The temperature was allowed to stabilize for 10 min before scanning.

^{19}F NMR Aqueous Solubility Limit Measurements.

Compound was dissolved in DMSO and then added to 10 mM pH = 6.9 phosphate buffer/D_2O (9:1 v/v) to make 5% DMSO stock in 500 μL phosphate buffer/D_2O at concentration of 10/50/100/150/200/250 μM. Samples were measured with Bruker AVANCE III 500 equipped with a 5 mm BBFO SmartProbe. ^{19}F spectra were obtained at 471 MHz with dummy scans = 4, acquisition time = 0.57 s, delay time = 1 s, pre-scan delay = 6.5 μs, and the number of scans = 800.

UV-Visible Spectra.

Stock solutions of **DD-1**, **DD-3**, and **DD-5** were prepared at 10 mM in DMSO and stored in the dark. A 10 mM phosphate buffer at pH 7 was prepared and stock solutions were diluted to 50 μM. UV-visible absorption spectra were obtained using a Horiba Aqualog.

Photolysis Experiments.

Stock solutions were diluted to 10 μM in the phosphate buffer for kinetic experiments and 50 μM for ^{19}F NMR experiments. Solutions were placed in 10 mL quartz tubes sealed with cork stoppers with no contact to the solution. The solutions were photolyzed in (i) an Atlas Suntest CPS+ solar simulator with a 1500 W xenon lamp at an intensity of 765 W m^{-2} using a wavelength range of 290-800 nm at a 30° angle, and (ii) a 450 W medium pressure polychromatic mercury vapor lamp with a quartz immersion well with cooling water circulation, a Pyrex 280 nm cutoff filter (Ace Glass), and a merry-go-round sample holder. Samples were photolyzed until ~60 to 80% degradation of the parent compound was achieved. For each compound an equivalent tube was prepared and wrapped in aluminum foil as a dark control. Experiments were performed in triplicate.

Photolysis Kinetics and Quantum Yields.

A minimum of five spaced time points ranging from 60-180 min for the solar simulator and 20-60 min for the mercury vapor lamp were taken to determine the loss of the parent compound concentration using high-pressure liquid chromatography (HPLC) combined with a variable wavelength UV detector (Agilent 1100 series). First order rate constants were found by regression of $\ln(C/C_0)$ versus time where C_0 is the initial concentration and C is the concentration in μM. The direct photolysis quantum yields in the solar simulator were found using a p-nitroanisole-pyridine (PNA-PYR) actinometer and relationships from Dulin and Mill,[25] Leifer[26] and updated calculations by Laszakovits et al. [27]

Ozone-mediated degradation.

The 10 mM DMSO stock solution of **DD-1** was used to make 100 mL of a 50 μM solution in the 10 mM pH = 7 phosphate buffer. The solution was placed in an Erlenmeyer flask in an ice bath. Ozone (O_3) was produced using ultra-high pure oxygen gas (99.99%) with a Pacific Ozone O_3 generator and bubbled directly into the sample solution. O_3 concentration was previously measured using UV-Vis spectroscopy (Beckman Coulter DU 530). The concentration of O_3 (with an ε =3000 M^{-1} cm^{-1}) was determined by direct absorbance at 258 nm. By using a 3:1 dilution, the absorbance obtained is equivalent to the O_3 concentration in mM.[28] After 30 minutes the O_3 concentration in ultrapure water was 0.61 mM or 29.16 mg/L. Samples were taken

over time for 300 minutes and parent compound degradation was monitored via HPLC. O_3 was chosen to simulate oxidation processes used in water and wastewater treatment plants.[29,30] O_3 is a selective oxidant that rapidly degrades in aqueous environments to an array of reactive oxygen species, including hydroxyl radical (•OH) which a non-selective oxidant.[29]

Responsiveness Determination

Temperature responsiveness was determined based linear plotting of the chemical shift difference ($\Delta\Delta\delta$) of the resonance pair at difference temperature (T). Resonances moving to the most upfield resonance and moving downfield with the largest change as a function of temperature were chosen as resonance pairs. The slope of the linear plot was used to determine the temperature responsiveness.

HPLC Methods for Degradation Monitoring

HPLC was developed to monitor the degradation level through photolysis or ozone-treatment. 20 µL of samples were injected to Agilent 1100 series HPLC with an Eclipse XDBC18 4.6 x 150 mm column with 3.5 µm particle diameter. Samples were eluted under AcCN/phosphate buffer pH 3 (9:1 v/v) mobile phase at 1 mL/min flow rate and detected at 288 nm wavelength.

UV Spectra and Quantum Yields.

The chemical actinometer p-nitroanisole-pyridine (PNA-PYR) was used. The stock solution of pyridine was made in ultrapure water at 0.5 M. PNA was recrystallized twice in petroleum ether and stock solutions were made in ACN at a concentration of 1 mM. The concentrations of PNA/PYR (30 µM /7 µM) were irradiated and used to obtain the ratio of rate constants of the fluorinated temperature sensor and the actinometer (k_{dc}/k_{da}). The molar absorptivities of the actinometers (ε_{PNA}) were estimated using linear regression using three different concentrations (10, 25, and 50 µM) in ultrapure water.

$$\phi_{dc} = \frac{k_{dc}\sum_{\lambda}(I_{\lambda}\varepsilon_{\lambda a})}{k_{da}\sum_{\lambda}(I_{\lambda}\varepsilon_{\lambda c})}\phi_{da}$$

$$\phi_{PNA} = \phi_{da} = 0.29[PYR] + 0.0029$$

Where I_λ is the irradiance of incident light in einsteins m^{-2} s^{-1} at a fixed λ (lamp spectra in Figure SX1) and ε_λ is the molar adsorption coefficient of (a) actinometer i.e., PNA and (c) compound as a function of wavelength. The wavelength range was 280 to 400 nm. The molar absorptivities of the compounds were determined by measuring the average absorption spectra of 50 μM solutions in the pH = 7 buffer.

^{19}F NMR for Mass Balance

Wilmad 18 cm (7 in.) length class A glass 500 MHz NMR tubes with 5 mm outer diameter were used for analysis. D_2O was added to each sample for a final concentration of 10% (v/v). Hexafluorobenzene (HFB) was used as an internal standard with a reference chemical shift (-164.9 ppm). HFB (50 μM) in isopropyl alcohol (IPA) was sealed in a melting-point capillary tube and placed inside the NMR tube with the solution of interest. A 600 MHz Avance Neo NMR equipped with a 5 mm three-channel TCI inverse cryoprobe for ^{19}F NMR spectral acquisition without ^{1}H decoupling was used to analyze and quantify the parent compound, and final photolysis samples. The experimentally determined parameters for sufficient signal-to-noise and complete longitudinal relaxation for accurate measurements were 4096 scans, 10 s delay time (D1), and 0.9 s acquisition time (AQ). An explanation of the ^{19}F-NMR quantification method is below. To account for the comparison of HFB in the smaller diameter melting point tube, a ratio between the concentration of fluorine in the melting-point tube to the concentration of fluorine in the NMR tube was calculated. For this, 500 μL of a 50 μM difluorophenol standard (DFP) in ultrapure water (spiked from a 3 mM stock solution of DFP in DMSO for complete dissolution) with 10% deuterium oxide was added into the NMR tube and the melting-point tube containing the 50 μM HFB standard was placed in the NMR tube. The relationship follows the equation below,

$$\frac{Area_{DFP}}{[DFP] * DFP_{\#F}} = \frac{Area_{HFB} * IS_{ratio}}{[HFB] * HFB_{\#F}}$$

with DFP and HFB having the same concentration of 50 μM. The ratio between single fluorine atoms can be calculated by solving for the IS_{ratio} in the equation. The DFP sample with the HFB standard was run three times, taking an average for the final ratio for each melting temp tube standard. [3,4]

$$IS_{ratio} = \frac{2 * Area_{DFP}}{Area_{HFB}}$$

Each standard was individually labeled. The NMR tube-melting point tube pair was kept the same and tubes were not exchanged amongst each other to maintain reproducibility. After each use, both melting-point and NMR tubes were rinsed with methanol. One tube containing a known concentration standard DFP in water (spiked from the DMSO stock) was used to check for any loss or change in areas of the HFB peaks due to potential sample loss from evaporation. IS_{ratio} values were recalculated using standard DFP in water spiked from a DMSO stock before each run to take into account any changes in areas for all the tubes in the experiments as compared to the previous calculated HFB areas. The new IS_{ratios} recalculated with each new experiment were used to calculate the concentrations of unknown fluorine in the samples. Bruker Topspin 4.0.7 was used to analyze the NMR spectra. Following peak integration, areas were converted into moles of fluorine following the equations below.

$$\left(\frac{Area_{peak}}{[F_{unknown}]}\right) = \frac{Area_{HFB} * IS_{Ratio}}{[HFB] * HFB_{\#F}}$$

$$[F_{unknown}] = Area_{peak} * \left(\frac{[HFB]}{\frac{Area_{HFB} * IS_{ratio}}{HFB_{\#F}}}\right)$$

Following this an additional calculation was mad for the dilution factor of the addition of D_2O,

$M_1V_1=M_2V_2$

where M_1 is the concentration found from the total volume, V_1 being the total volume of 535 µL, V_2 being 485 µL of sample and M_2 being the final fluorine concentration.

2.4.3 Supplement Figures

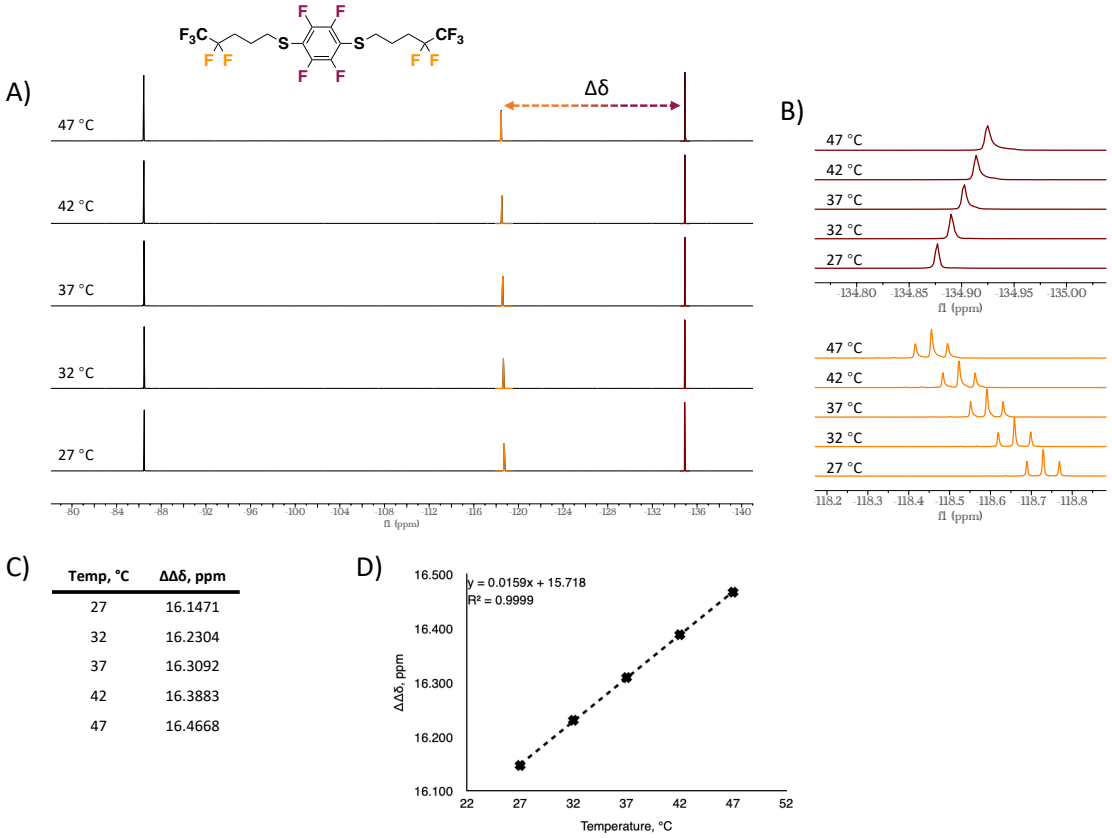

Temp, °C	ΔΔδ, ppm
27	16.1471
32	16.2304
37	16.3092
42	16.3883
47	16.4668

Figure 2-14. Temperature measurement and responsiveness determination of **DD-1** in THF-d8. (A) ^{19}F NMR spectra of **DD-1** at different temperatures. Highlighted are the resonances pair for determining the temperature responsiveness. (B) Expended regions of the highlighted resonances. (C) Table of the $\Delta\Delta\delta$ at different temperatures. (D) Temperature responsiveness plot of **DD-1** with $\Delta\Delta\delta(T) = 16.0 \times 10^{-3} \pm 0.05 \times 10^{-3}$ ppm °C^{-1} (n = 3, mean ± SD).

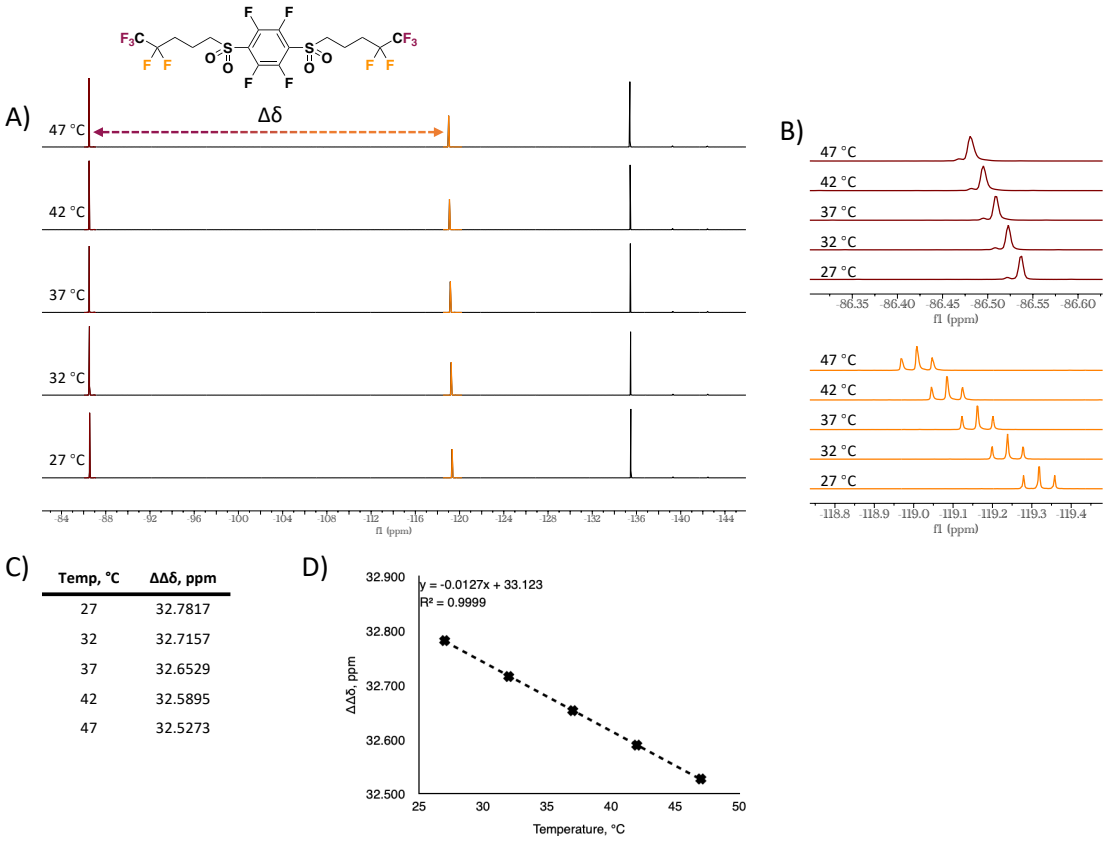

Figure 2-15. Temperature measurement and responsiveness determination of **DD-2** in THF-d8. (A) ^{19}F NMR spectra of **DD-2** at different temperatures. Highlighted are the resonances repair determining the temperature responsiveness. (B) Expanded regions of the highlighted resonances. (C) Table of the $\Delta\Delta\delta$ at different temperatures. (D) Temperature responsiveness plot of **DD-2** with $\Delta\Delta\delta(T) = 12.7 \times 10^{-3}$ ppm °C^{-1}.

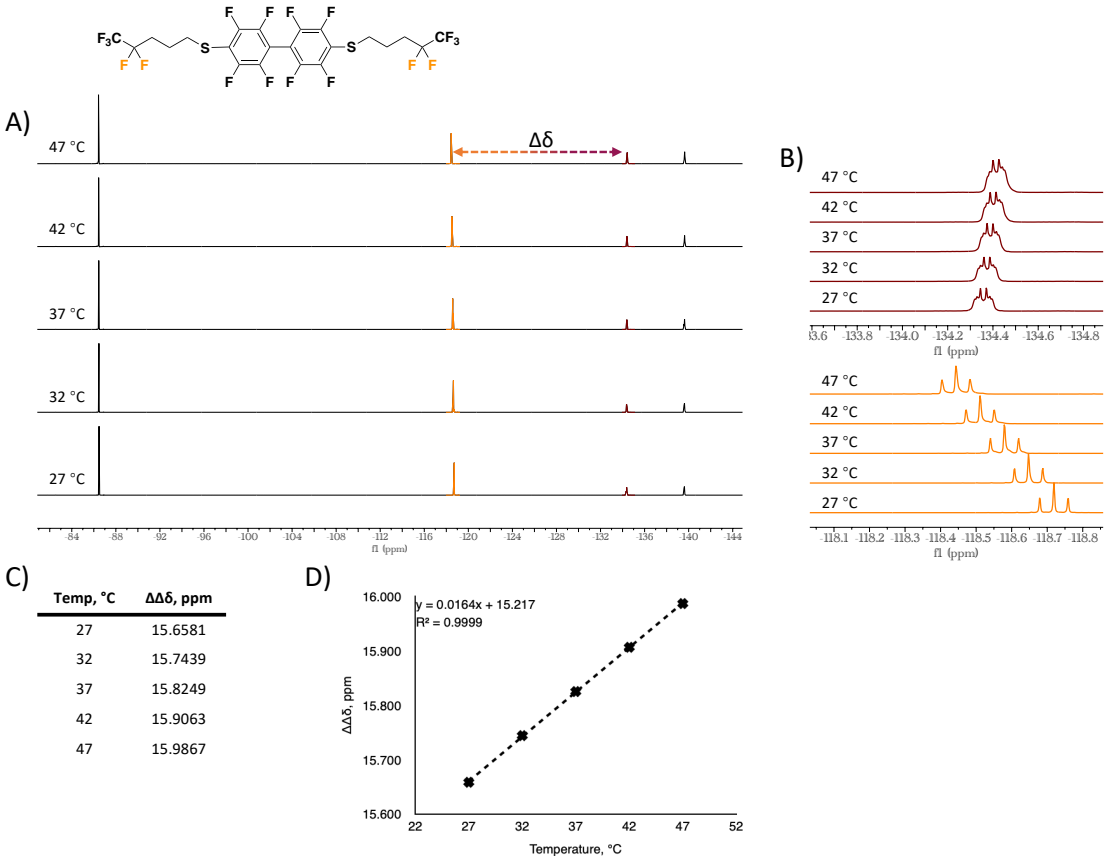

Temp, °C	ΔΔδ, ppm
27	15.6581
32	15.7439
37	15.8249
42	15.9063
47	15.9867

Figure 2-16. Temperature measurement and responsiveness determination of **DD-3** in THF-d8. (A) ^{19}F NMR spectra of **DD-3** at different temperatures. Highlighted are the resonances repair determining the temperature responsiveness. (B) Expanded regions of the highlighted resonances. (C) Table of the $\Delta\Delta\delta$ at different temperatures. (D) Temperature responsiveness plot of **DD-3** with $\Delta\Delta\delta(T) = 16.5 \times 10^{-3} \pm 0.08 \times 10^{-3}$ ppm °C^{-1} (n = 3, mean ± SD).

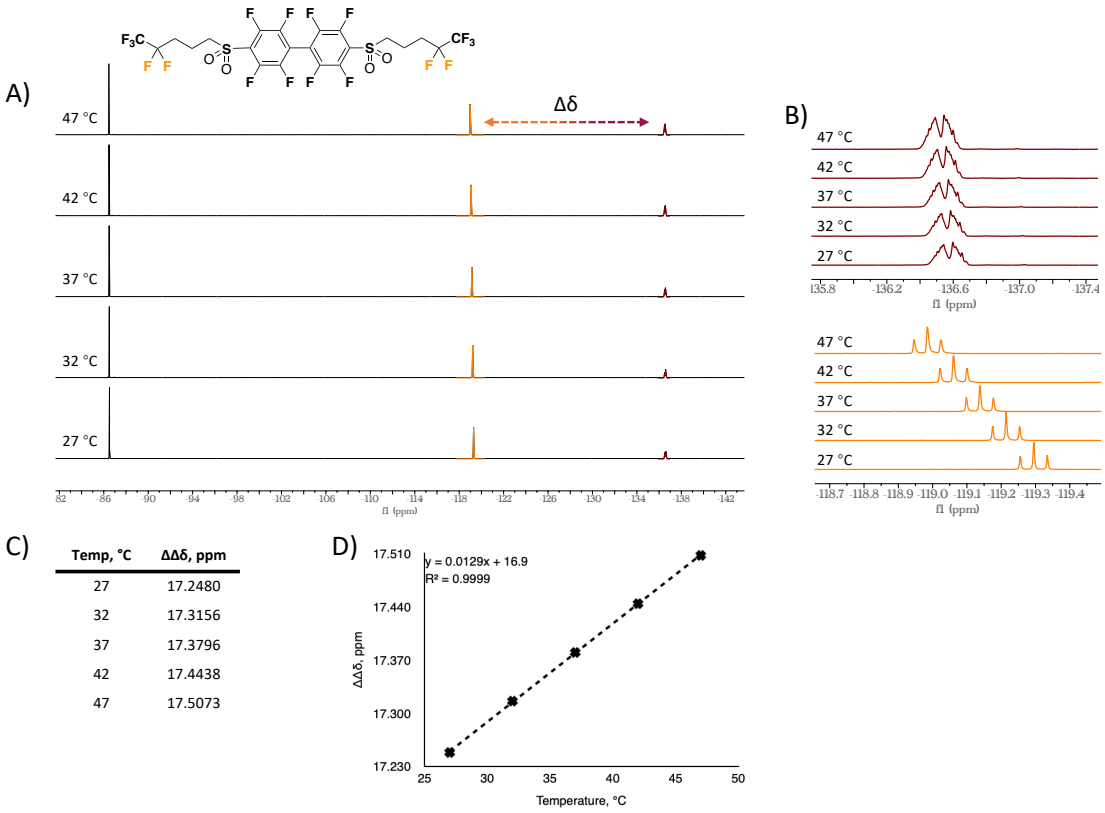

Figure 2-17. Temperature measurement and responsiveness determination of **DD-4** in THF-d8. (A) ^{19}F NMR spectra of **DD-4** at different temperatures. Highlighted are the resonances repair determining the temperature responsiveness. (B) Expanded regions of the highlighted resonances. (C) Table of the $\Delta\Delta\delta$ at different temperatures. (D) Temperature responsiveness plot of **DD-4** with $\Delta\Delta\delta(T) = 12.9 \times 10^{-3}$ ppm °C^{-1}.

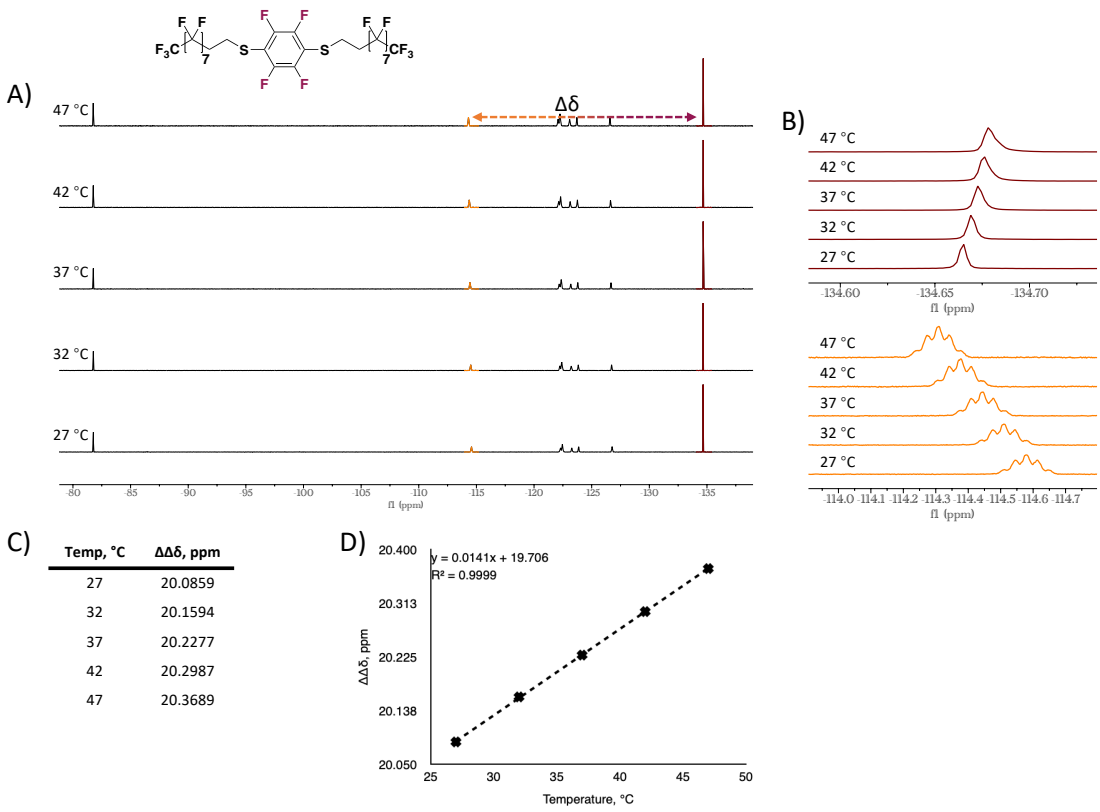

Temp, °C	ΔΔδ, ppm
27	20.0859
32	20.1594
37	20.2277
42	20.2987
47	20.3689

Figure 2-18. Temperature measurement and responsiveness determination of **2** in THF-d8. (A) ^{19}F NMR spectra of **2** at different temperatures. Highlighted are the resonances repair determining the temperature responsiveness. (B) Expanded regions of the highlighted resonances. (C) Table of the $\Delta\Delta\delta$ at different temperatures. (D) Temperature responsiveness plot of **2** with $\Delta\Delta\delta(T) = 14.2 \times 10^{-3}$ ppm °C^{-1}.

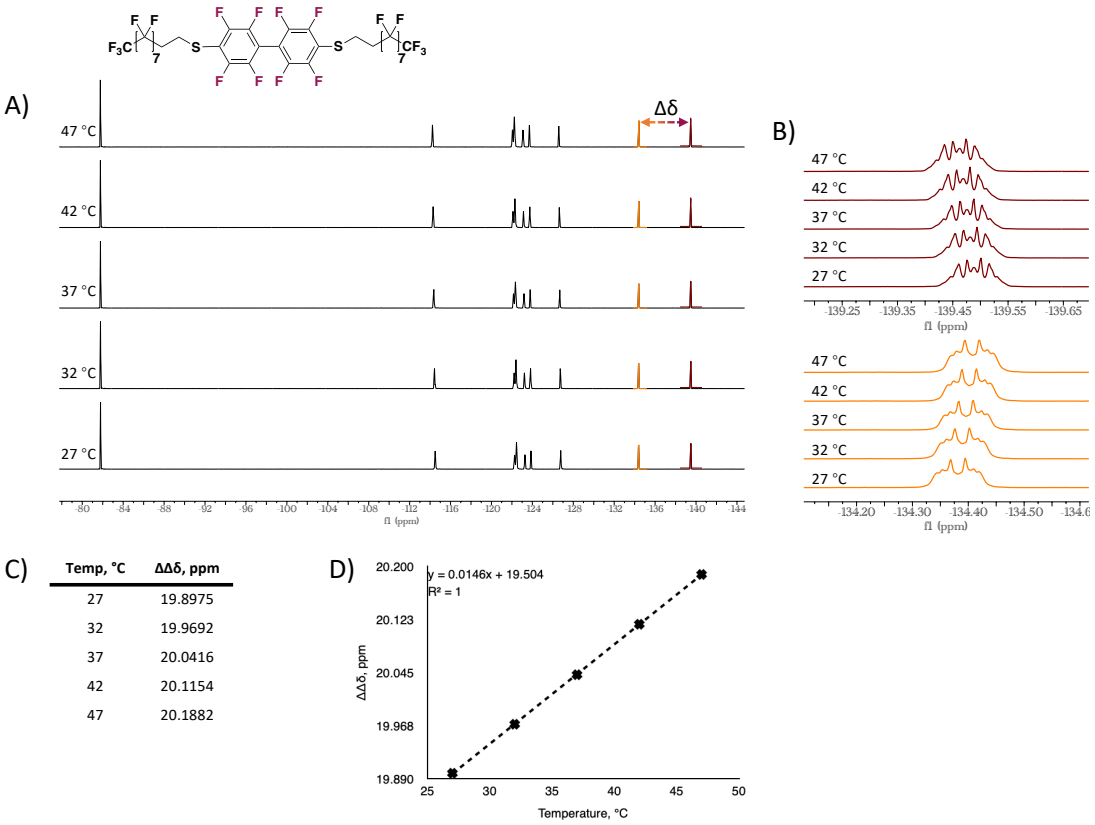

Temp, °C	ΔΔδ, ppm
27	19.8975
32	19.9692
37	20.0416
42	20.1154
47	20.1882

Figure 2-19. Temperature measurement and responsiveness determination of **1** in THF-d8. (A) ^{19}F NMR spectra of **1** at different temperatures. Highlighted are the resonances repair determining the temperature responsiveness. (B) Expanded regions of the highlighted resonances. (C) Table of the $\Delta\Delta\delta$ at different temperatures. (D) Temperature responsiveness plot of **1** with $\Delta\Delta\delta(T) = 14.5 \times 10^{-3}$ ppm °C^{-1}.

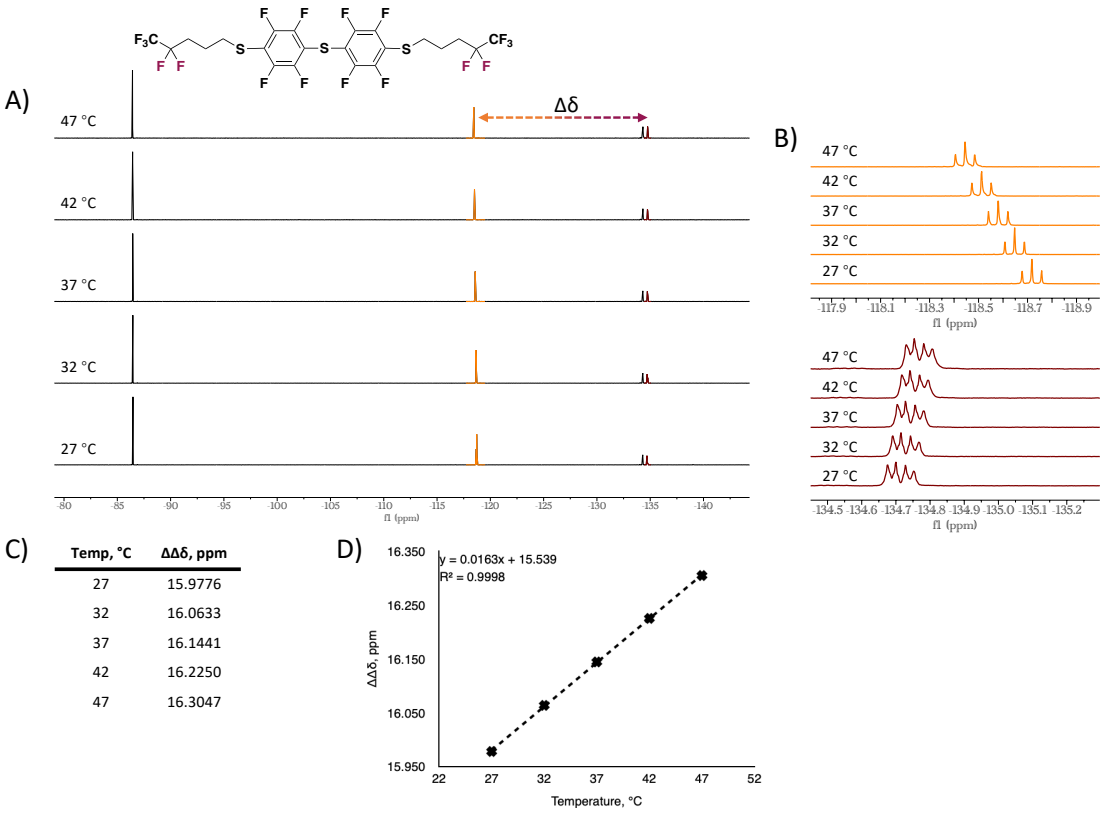

Temp, °C	ΔΔδ, ppm
27	15.9776
32	16.0633
37	16.1441
42	16.2250
47	16.3047

Figure 2-20. Temperature measurement and responsiveness determination of **DD-5** in THF-d8. (A) ^{19}F NMR spectra of DD-5 at different temperatures. Highlighted are the resonances repair determining the temperature responsiveness. (B) Expanded regions of the highlighted resonances. (C) Table of the $\Delta\Delta\delta$ at different temperatures. (D) Temperature responsiveness plot of DD-5 with $\Delta\Delta\delta(T) = 16.4 \times 10^{-3} \pm 0.09 \times 10^{-3}$ ppm °C^{-1} (n = 3, mean ± SD).

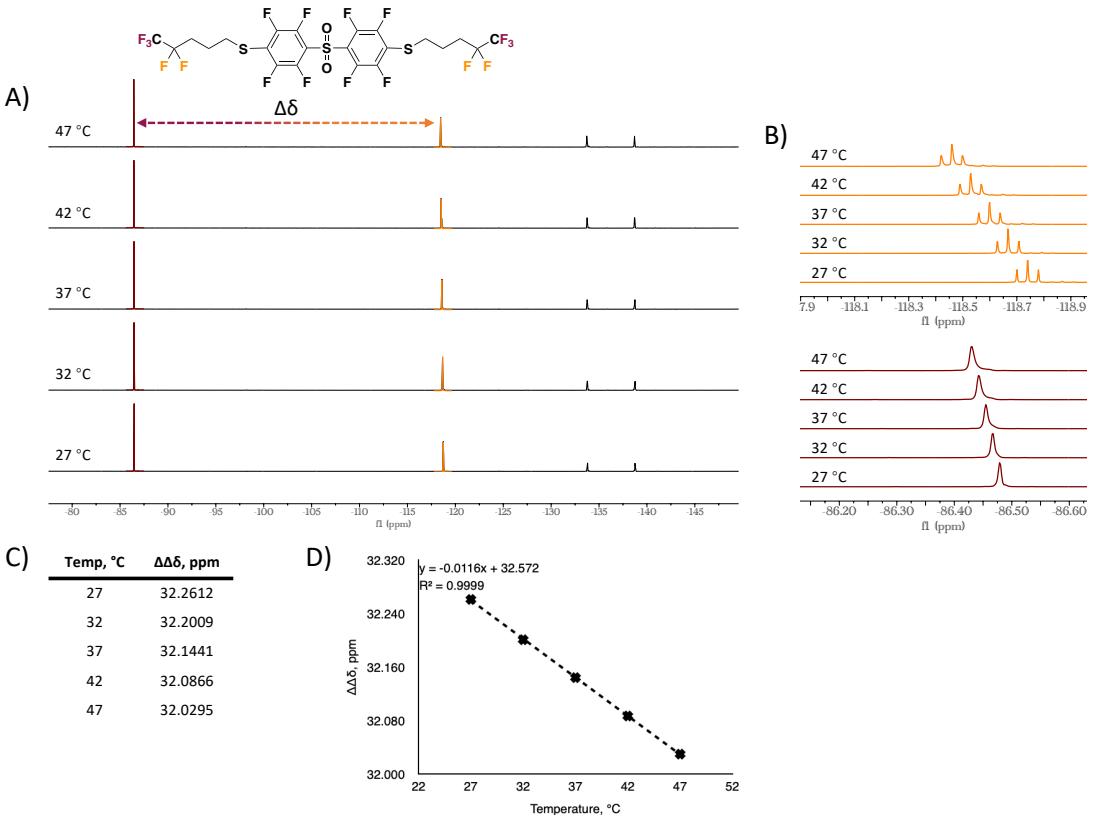

Temp, °C	ΔΔδ, ppm
27	32.2612
32	32.2009
37	32.1441
42	32.0866
47	32.0295

Figure 2-21. Temperature measurement and responsiveness determination of **DD-6** in THF-d8. (A) ^{19}F NMR spectra of **DD-6** at different temperatures. Highlighted are the resonances repair determining the temperature responsiveness. (B) Expanded regions of the highlighted resonances. (C) Table of the $\Delta\Delta\delta$ at different temperatures. (D) Temperature responsiveness plot of **DD-6** with $\Delta\Delta\delta(T) = 11.5 \times 10^{-3}$ ppm °C^{-1}.

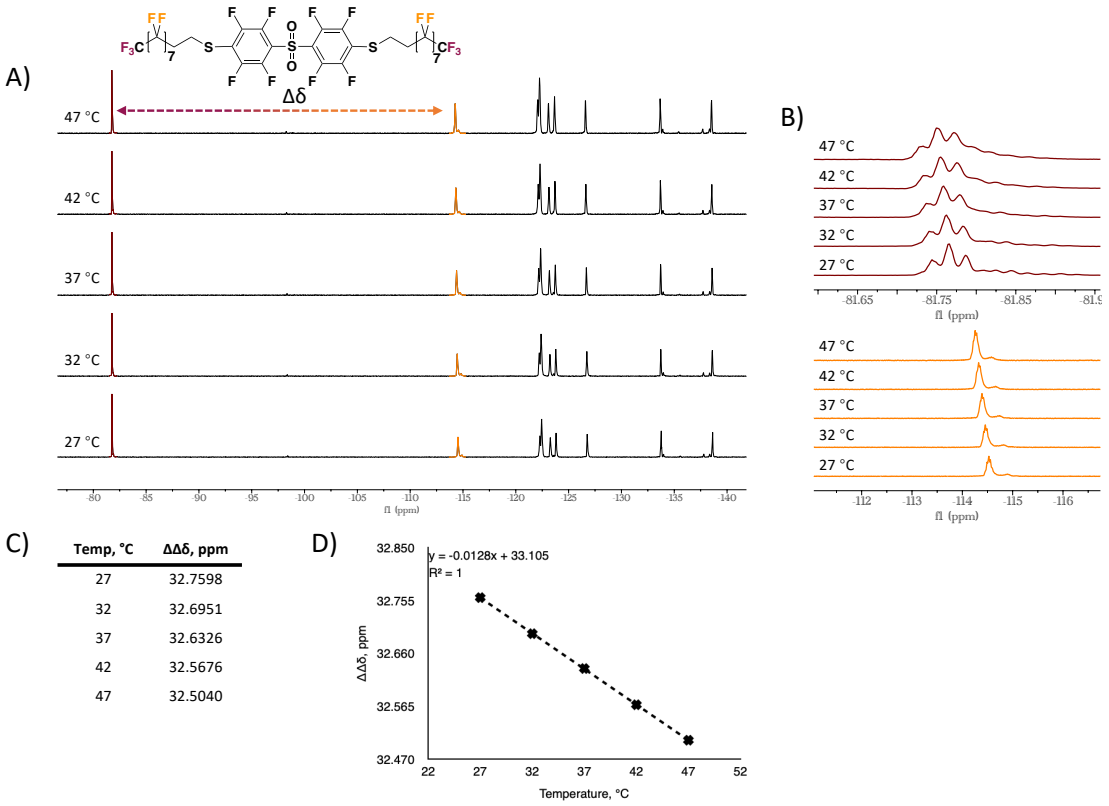

Temp, °C	ΔΔδ, ppm
27	32.7598
32	32.6951
37	32.6326
42	32.5676
47	32.5040

Figure 2-22. Temperature measurement and responsiveness determination of **DD-7** in THF-d8. (A) ^{19}F NMR spectra of **DD-7** at different temperatures. Highlighted are the resonances repair determining the temperature responsiveness. (B) Expanded regions of the highlighted resonances. (C) Table of the $\Delta\Delta\delta$ at different temperatures. (D) Temperature responsiveness plot of **DD-7** with $\Delta\Delta\delta(T) = 12.8 \times 10^{-3}$ ppm °C^{-1}.

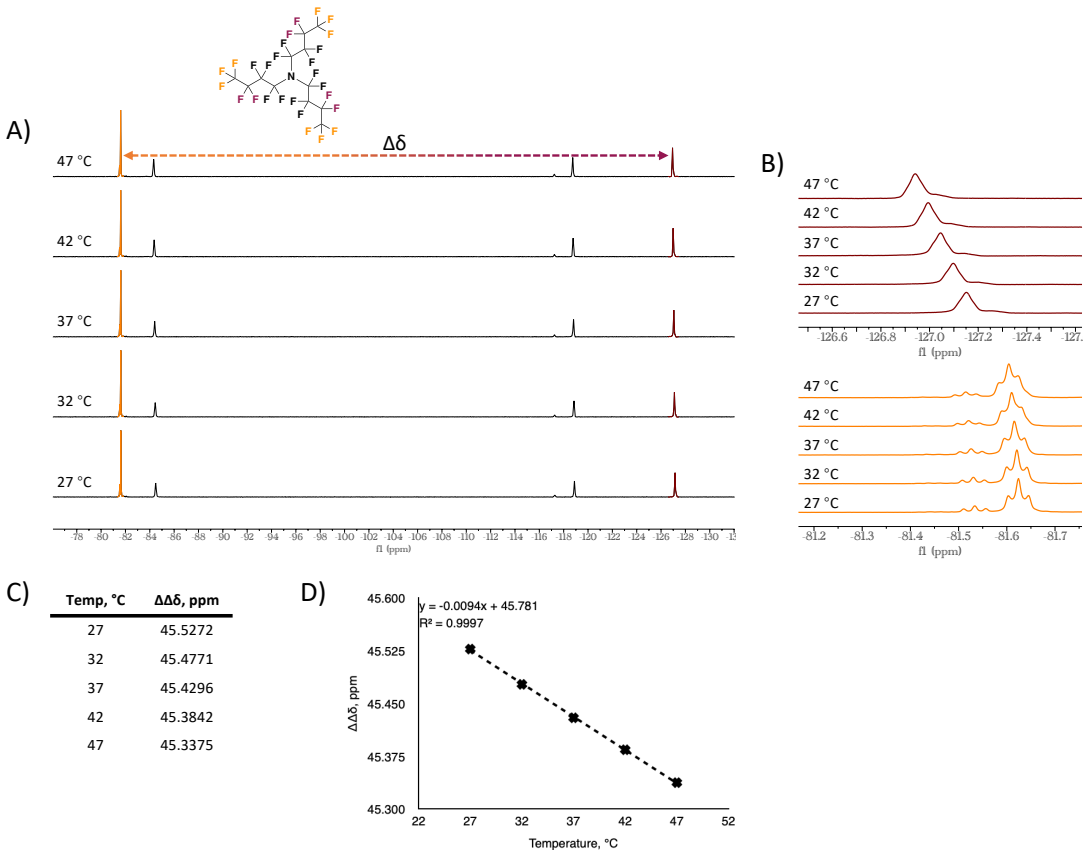

Temp, °C	ΔΔδ, ppm
27	45.5272
32	45.4771
37	45.4296
42	45.3842
47	45.3375

Figure 2-23. Temperature measurement and responsiveness determination of PFTBA in THF-d8. (A) ^{19}F NMR spectra of PFTBA at different temperatures. Highlighted are the resonances repair determining the temperature responsiveness. (B) Expanded regions of the highlighted resonances. (C) Table of the $\Delta\Delta\delta$ at different temperatures. (D) Temperature responsiveness plot of PFTBA with $\Delta\Delta\delta(T) = 9.45 \times 10^{-3}$ ppm °C^{-1}.

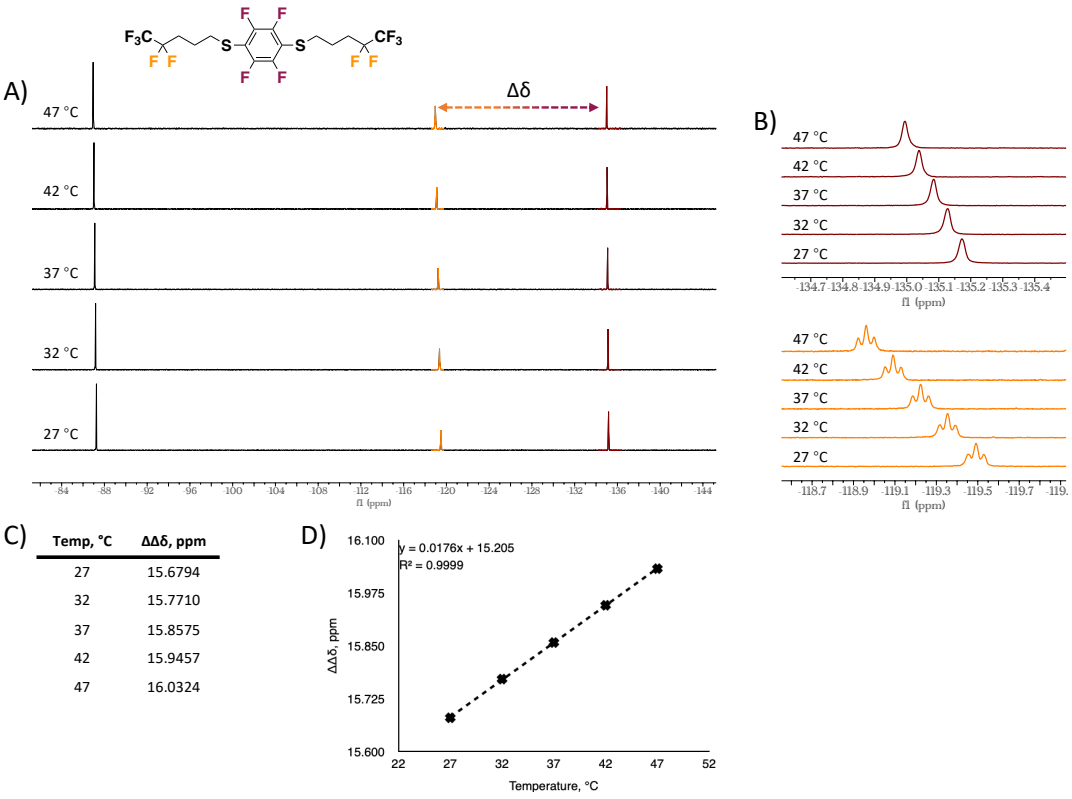

Temp, °C	ΔΔδ, ppm
27	15.6794
32	15.7710
37	15.8575
42	15.9457
47	16.0324

Figure 2-24. Temperature measurement and responsiveness determination of **DD-1** in phosphate buffer. (A) ^{19}F NMR spectra of DD-1 at different temperatures. Highlighted are the resonances repair determining the temperature responsiveness. (B) Expanded regions of the highlighted resonances. (C) Table of the $\Delta\Delta\delta$ at different temperatures. (D) Temperature responsiveness plot of DD-1 with $\Delta\Delta\delta(T) = 17.6 \times 10^{-3} \pm 0.05 \times 10^{-3}$ ppm °C^{-1} (n = 3, mean ± SD).

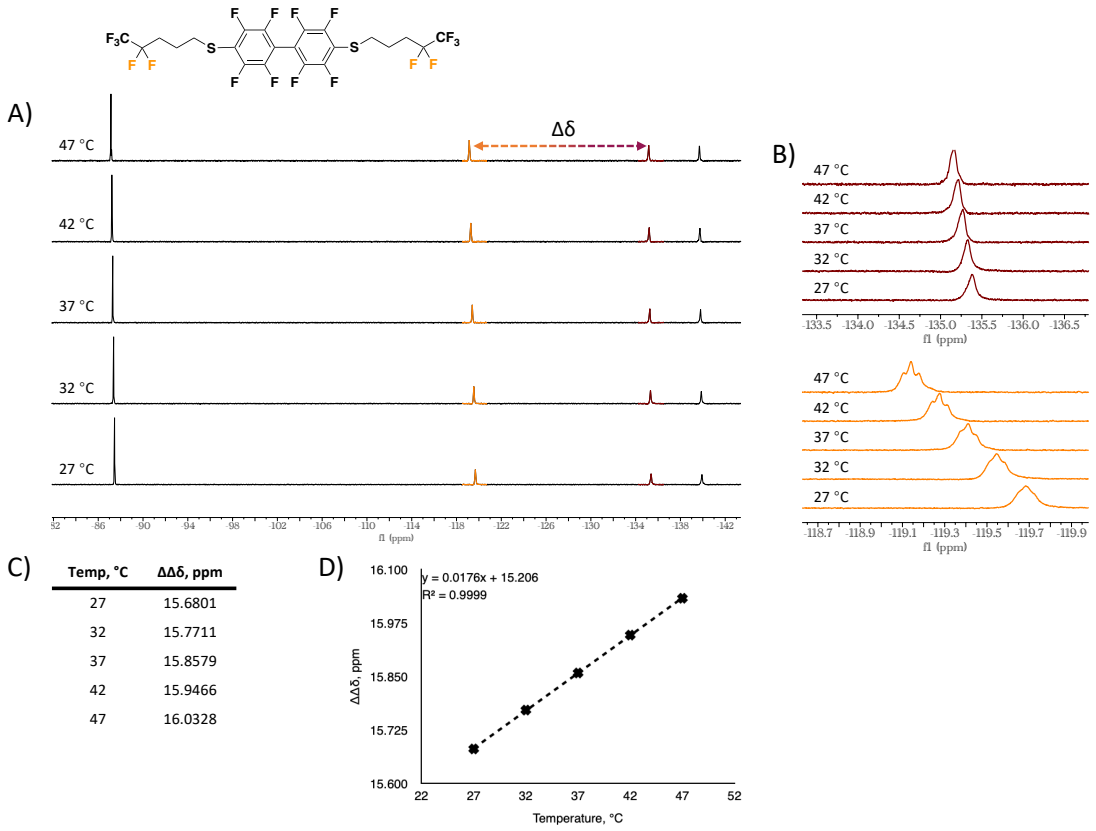

Temp, °C	ΔΔδ, ppm
27	15.6801
32	15.7711
37	15.8579
42	15.9466
47	16.0328

Figure 2-25. Temperature measurement and responsiveness determination of **DD-3** in phosphate buffer. (A) ^{19}F NMR spectra of **DD-3** at different temperatures. Highlighted are the resonances repair determining the temperature responsiveness. (B) Expanded regions of the highlighted resonances. (C) Table of the $\Delta\Delta\delta$ at different temperatures. (D) Temperature responsiveness plot of **DD-3** with $\Delta\Delta\delta(T) = 17.0 \times 10^{-3} \pm 0.82 \times 10^{-3}$ ppm °C^{-1} (n = 3, mean ± SD).

Chapter 3

Design of Highly Fluorinated Peptides for Cell-based ^{19}F NMR

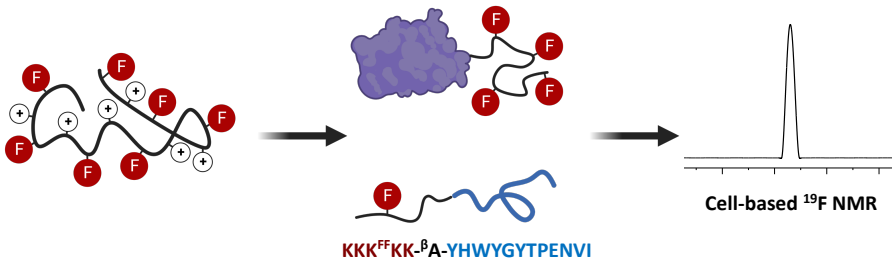

'Design of Highly Fluorinated Peptides for Cell-based ^{19}F NMR'

Jiaqian Li, Steven F. Kirberger, Yiao Wang, Huarui Cui, Carston R. Wagner, and William C. K. Pomerantz

Bioconjugate Chemistry **2023** *34* (8), 1477-1485

Motivation for Research

The motivation of this work was based on a new class of peptide-based ^{19}F MRI imaging agents reported by our group. The peptide-based construct showed great potential with its tunability for spectral performance, biocompatibility, physical and physiochemical properties, and further functionalization. In this work, we utilized the design idea of those peptides and at the same time aimed to overcome the weakness of low sensitivity and non-specific binding. We focused on incorporating various amino acids with improved fluorine content into peptides to improve the sensitivity and structural/sequence modifications to remove the non-specific binding. We were also interested in conducting preliminary molecular imaging with molecular tracers composed of the lead peptide.

3.1 Introduction

While conventional medical imaging focuses on visualization of organs and tissues for diagnosis and medical intervention, molecular imaging enables the visualization, characterization, and quantification of specific molecular targets at the cellular level.[1] Among the molecular imaging modalities, magnetic resonance imaging (MRI) has the advantages of high spatial and temporal resolution,[2] excellent soft tissue contrast,[3] non-invasiveness, and lack of ionizing radiation. While the low sensitivity of MRI remains a weakness, significant effort has been dedicated to improve data processing[4] and developing new contrast agents.[5,6] One strategy is through the use of (super)paramagnetic contrast agents affecting the T_1 and T_2 relaxation.[7–9] However, using standard clinical MRI techniques, administration of high concentration of lanthanide contrast agents is required, which raises the concerns of toxicity.[10]

As a complimentary method, ^{19}F MRI is gaining increasing attention for imaging applications, including molecular imaging. Molecular imaging agents are composed of a specific recognition group for a molecular target and an imaging domain (e.g. **Fig. 3-1**). ^{19}F holds great potential with its 100% natural abundance, a similar signal sensitivity to ^{1}H MRI, and limited tissue background signal due to only trace amounts of mobile ^{19}F in the human body. The lack of background signal in ^{19}F MRI leads to high contrast imaging and allows for quantitative analysis. ^{19}F MRI can also serve as a ‘second color’ or ‘hot spot’ with other imaging

modalities including ^{1}H MRI,[11] optical fluorescence imaging,[12] ultrasonic imaging,[13] computed tomography (CT),[14] and photoacoustic imaging.[15]

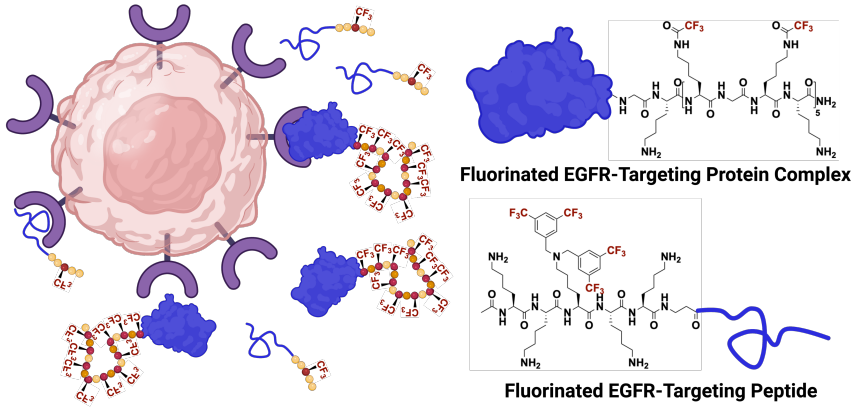

Figure 3-1. A proposed molecular imaging approach using either a fluorinated EGFR-targeting protein or a fluorinated EGFR-targeting peptide. Targeting moiety is colored blue.

Low sensitivity is a critical issue for ^{19}F MRI-based molecular imaging agents. Apart from increasing the magnetic field strength and pulse sequence optimization,[16] imaging agent design also plays a vital role for boosting the sensitivity for optimal ^{19}F MRI performance. Ideally, ^{19}F MRI imaging agents should have high fluorine content and produce a well resolved signal in the ^{19}F NMR spectrum. To date, ^{19}F MRI imaging agents can be classified into several categories: perfluorocarbon (PFC) or highly fluorinated liquids, fluorinated small molecules, and fluorinated polymers. PFCs have a high fluorine content; yet their significant hydrophobicity requires formulation into nanoemulsions.[17] Nanoemulsions can suffer droplet heterogeneity, instability, limited biocompatibility, and environmental concerns.[6,18,19] Nanoparticle encapsulation is one approach to address this stability challenge.[20,21] Fluorinated polymers, provide flexibility in the choice of building blocks, have a significant improvement in both biocompatibility and aqueous solubility, and do not require emulsification.[22,23] However, building blocks must be judiciously chosen for maintaining a high fluorine content, optimal magnetic resonance properties, biological stability, and avoiding persistence in the environment.[24–26]

Fluorinated peptides and proteins complement strategies for synthetic polymers and offer a mechanism for modulating stability in vivo through protease degradation or subsequent amide hydrolysis. Previously, a fluorinated poly-lysine-CF_3 peptide was reported for cell tracking through ^{19}F MRI[27]; a nanoscale micelle composed of fluorinated proteins in a block copolymer was also effective for in vivo ^{19}F magnetic resonance spectroscopy (MRS).[28] Our group reported a new class of highly fluorinated peptides as ^{19}F MRI imaging agents.[29] These sequence-defined peptides, composed of N-ε-trifluoroacetyllysine (K^{TFA}) and lysine in an alternating pattern, had good aqueous solubility and showed degenerate ^{19}F NMR signals through avoiding secondary structure. Structurally similar fluorinated peptides, composed of an asparagine analogue carrying a perfluoro-tert-butyl group, have now also been reported showing high biostability when used in zebrafish embryos.[30] Despite the success in phantom MR imaging, both reports showed a relatively low detection limit indicating the need for amino acids with higher fluorine content as biopolymer building blocks or longer peptides. Moreover, in unpublished work, we observed non-specific binding to multiple cell lines when we bioconjugated K^{TFA}-containing peptides to the targeting agent. We have now reexamined our previous designs to develop more biocompatible fluorinated imaging agents.

Here we synthesized four amino acids of high fluorine content and incorporated them into diverse peptide sequences through solid phase peptide synthesis. While possessing good ^{19}F NMR behavior, our initial peptides exhibited a significant degree of non-specific binding towards A549 cells which was related to a balance of increased positive charge and overall peptide hydrophobicity. Non-specific binding was ultimately removed through peptide redesign. Finally, as an initial experiment towards developing a molecular imaging agent, both a fluorinated EGFR-targeting peptide and an EGFR-targeting protein complex E_1-DD bioconjugated to our lead peptides were synthesized (**Fig. 3-1**). Initial cell-based ^{19}F NMR demonstrated the potential suitability of fluorinated peptides for ^{19}F imaging.

3.2 Results and Discussion

3.2.1 Design and Synthesis of Amino Acids with High Fluorine Content

Our previous studies focused on using amino acids functionalized with a trifluoroacetamide, K^{TFA}. With only three magnetically equivalent fluorine atoms per amino acid, the lower fluorine content required long

peptide sequences (21 residues) to be synthesized for overcoming the low detection limit of ^{19}F MRI, maintaining sufficient charge for promoting the unfolded state of the peptide, and promoting aqueous solubility. To address this challenge, we synthesized several highly fluorinated amino acids based on modified syntheses through new designs or from the literature. These four amino acids are referred to here as K^F, K^{FF}, C^F, and E^F (**Fig. 3-2**). The bis(trifluoromethyl)benzyl group incorporated onto a lysine side-chain (K^F) previously reported by Papeo et al,[32] has a two-fold increase in fluorine content relative to K^{TFA}. As an additional advantage, the positive charge on the side chain is maintained which would facilitate peptide solubility and promote electrostatic repulsion of the peptide in the folded state. The amino acid K^{FF} has an additional bis(trifluoromethyl)benzyl group. This amino acid is particularly attractive as K^{FF} has the highest fluorine content among all amino acids studied here. Moreover, K^{FF} only requires a two-step synthesis starting from Fmoc-Lys-OtBu (**Fig. 3-3**) with an overall yield of 76% using a modified alkylation strategy from prior reports.[32]

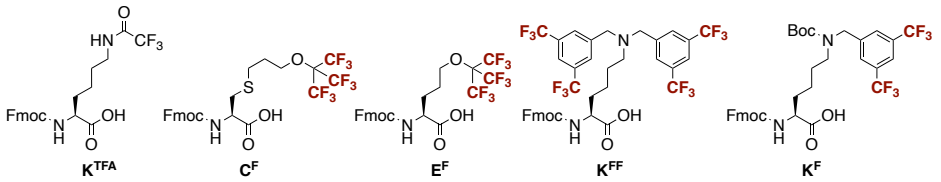

Figure 3-2. Structures of K^{TFA}, C^F, E^F, K^F, and K^{FF}. The CF_3 group in new fluorinated amino acids are bold and colored.

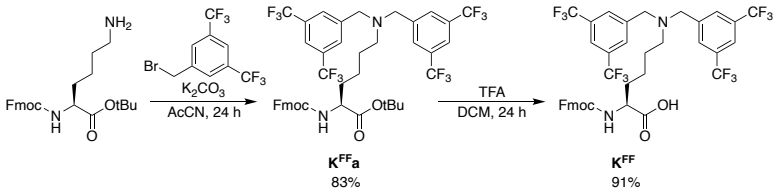

Figure 3-3. Synthetic route of K^{FF}

A second fluorinated motif of interest is the perfluorotertbutyl group, which has previously been used as a reporter for ^{19}F NMR[33] and ^{19}F MRI[30,34,35] due to its nine magnetically equivalent fluorine atoms. The

amino acid E^F is based on a modified synthesis of perfluorotertbutylhomoserine from Buer et al.[36] Synthesis of E^F started from Fmoc-glutamic acid-OtBu instead of homoserine (**Fig. 3-4**). This amino acid was chosen due to a longer side chain to facilitate narrow fluorine resonances from the higher flexibility.

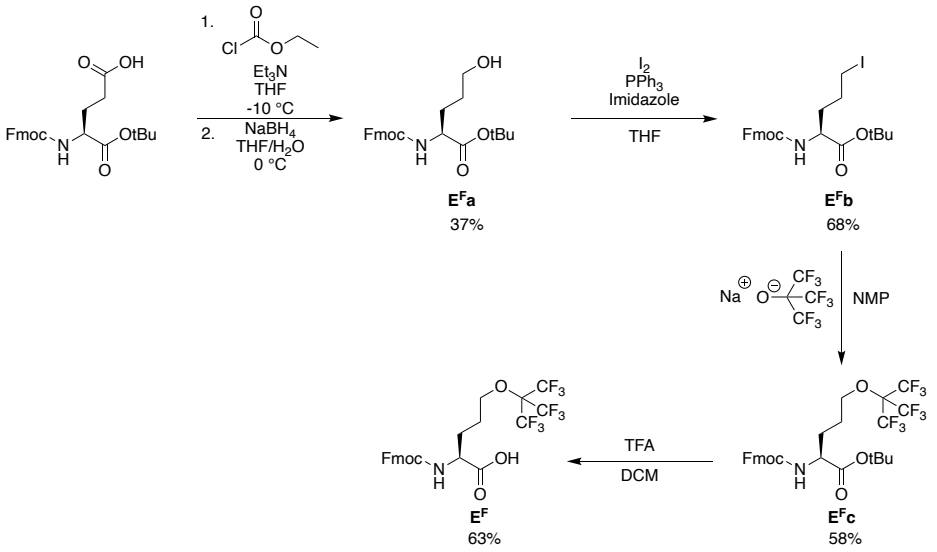

Figure 3-4. Synthetic route of E^F.

Finally, as a new amino acid, we synthesized a modified cysteine derivative containing the perfluorotertbutyl group, C^F (**Fig. 3-5**). Given the longer carbon-sulfur bond length, this amino acid was anticipated to further increase the side-chain flexibility resulting in narrower NMR linewidths. In addition, the sulfide group of C^F enables the additional modulation of physicochemical properties through oxidation to either a sulfoxide or sulfone to improve aqueous solubility.

Following their synthesis, ^{19}F NMR was used and confirmed all four amino acids exhibited one single resonance. With the increased high fluorine content and a single ^{19}F resonance, these four amino acids were evaluated as building blocks for imaging agents based on the ^{19}F NMR performance following their incorporation into peptides via solid phase synthesis.

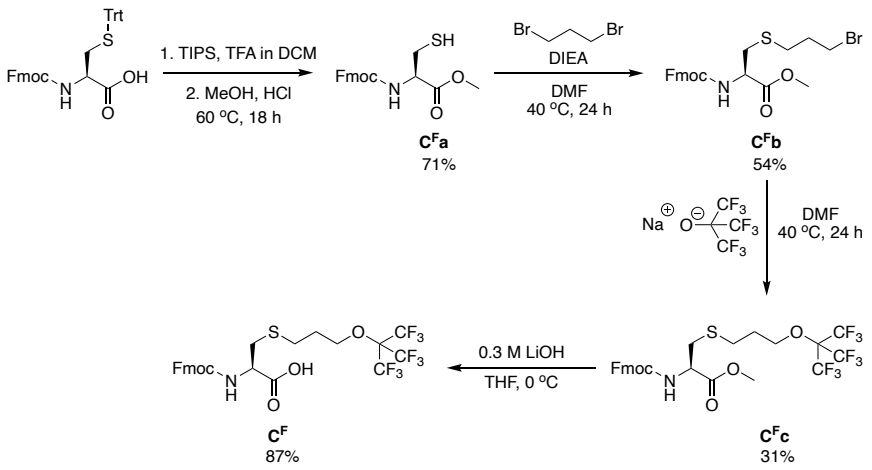

Figure 3-5. Synthetic route of C^F.

3.2.2 ^{19}F NMR Performance of Peptides Composed of New Fluorinated Amino Acids

With four highly fluorinated amino acids in hand, we next incorporated these amino acids into highly cationic peptide sequences and evaluated their ^{19}F NMR performance as well as the aqueous solubility (**Fig. 3-6A**). In these sequences, an alternating pattern of positively charged groups and fluorinated amino acids was maintained similar to **1**, which previously led to a favorable overlap of ^{19}F NMR resonances when the peptide adopted the unfolded state in aqueous solution (**Fig. 3-6A**).[29] Peptide length was also determined based on the number of total fluorine atoms. First, the K^{FF}-based peptide **TB-1**, with two K^{FF} incorporated (24 fluorine atoms), has a fluorine wt% of 28%, an 87% improvement over **1** (**Fig. 3-6A**). **TB-1** showed a sharp single ^{19}F NMR resonance with a narrow full width at half maximum (FWHM) of 5.49 Hz (**Fig. 3-6B**). As an attempt to further increase the fluorine content of the peptide, we incorporated one more K^{FF} in **TB-2**. However, this modification resulted in reduced aqueous solubility in part due to the two large benzyl sidechains. The ^{19}F NMR spectrum from the remaining peptide in solution led to multiple resonances with a FWHM of 79.3 Hz (**Fig. 3-7**). A structurally similar **TB-3** was next synthesized with arginine substituting for lysine. However, neither the solubility nor the ^{19}F NMR performance could be significantly improved (**Fig. 3-7**). From these studies, we determined that peptides composed of two K^{FF} would have a good balance between fluorine content, aqueous solubility, and ^{19}F NMR performance. The peptide **TB-4** containing the less hydrophobic amino acid, K^F, showed both good solubility and a single ^{19}F NMR resonance with FWHM

of 12.5 Hz (**Fig. 3-6B**). It also featured the second highest fluorine content (30 fluorine atoms) and a 26% fluorine wt% (73% improvement of 1) (**Fig. 3-6A**). In this case, instead of relying on a cationic lysine side chain to promote the unfolded state of the peptide, a protonatable side chain can now be accessed directly with K^F.

A)

Peptide	Sequence	^{19}F Content	^{19}F wt%	FWHM (Hz)	Total Charges
1	Ac-K(K^{TFA}K)$_{10}$-NH_2	30	15	6.48	+11
TB-1	Ac-K(K^{FF}K)$_2$-NH_2	24	28	5.49	+3
TB-2	Ac-K(K^{FF}K)$_3$-NH_2	36	30	79.3	+4
TB-3	Ac-R(K^{FF}R)$_3$-NH_2	36	28	51.9	+4
TB-4	Ac-G(K^{F}G)$_5$-NH_2	30	26	12.5	+5
TB-5	Ac-K(E^{F}K)$_4$-NH_2	36	34	30.9	+5
TB-6	Ac-Y^{β}AK(C^{F}K)$_4$-NH_2	36	28	46.6	+5
TB-7	Ac-Y^{β}AK($C_{(IV)}{}^{F}$K)$_4$-NH_2	36	27	538	+5
TB-8	Ac-Y^{β}AK($C_{(VI)}{}^{F}$K)$_4$-NH_2	36	27	152	+5
TB-9	Ac-K(K^{TFA}GK^{TFA}K)$_5$-NH_2	30	19	17.0	+6

B)

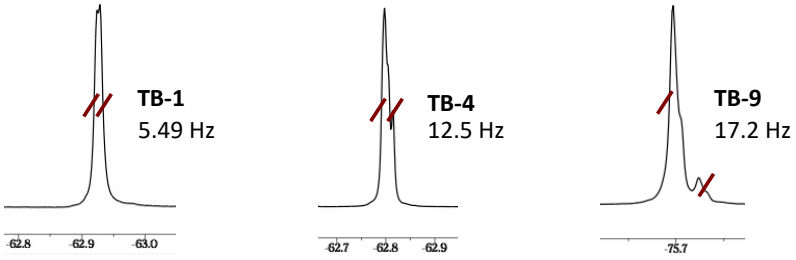

Figure 3-6. Structures and spectra of fluorinated peptides. A) Primary structures of peptides composed of new fluorinated amino acids with fluorine content, fluorine weight percentage (wt%), FWHM, and total charges. Fluorinated amino acids were colored red. B) ^{19}F NMR spectra of selected best-performing fluorinated peptides **TB-1**, **TB-4**, and **TB-9**.

The final two amino acids E^F and C^F suffered from poor NMR performance. While **TB-5**, composed of four E^F, possessed the highest fluorine content and good solubility, the peptide demonstrated inadequate ^{19}F NMR performance with three observable resonances and an overall FWHM of 30.9 Hz (**Fig. 3-7**). Having the same issues as **TB-2**, C^F-based **TB-6**, with the highest fluorine content, had both low aqueous solubility and a poor ^{19}F NMR performance (**Fig. 3-7**). To improve solubility, oxidation was conducted on **TB-6** to

lead to sulfoxide-containing **TB-7** as a mixture of diastereomeric peptides and sulfone-containing **TB-8**. Unfortunately, the more polar sulfoxide groups on **TB-7** and sulfone groups on **TB-8** were unable to improve the solubility substantially and the oxidation did not lead to an improvement of the ^{19}F NMR performance and increased resonance dispersion. (**Fig. 3-7**)

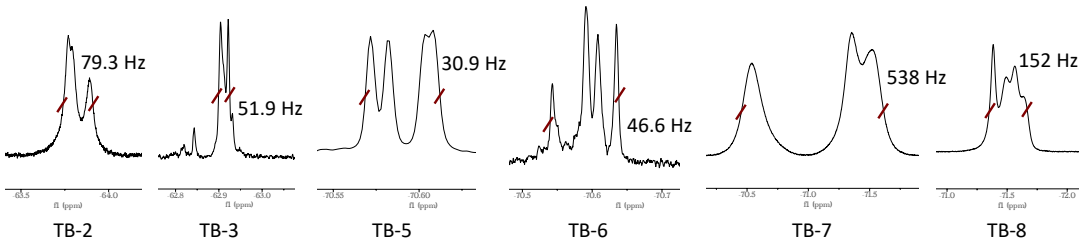

Figure 3-7. ^{19}F NMR spectra of the under-performing fluorinated peptides **TB-2**, **TB-3**, **TB-5**, **TB-6**, **TB-7**, and **TB-8**.

Summarizing our initial results, of the eight peptides, **TB-1** and **TB-4** feature a high fluorine content, a desired single narrow set of resonances, and acceptable aqueous solubility. With incorporation of a more highly fluorinated building block, peptide length can be decreased, resulting in an increase in the overall fluorine wt%. Together with **1**, these three peptides were selected for further evaluation as imaging tags for future molecular imaging applications.

3.2.3 Cellular interaction Studies of Fluorinated Peptides

In unpublished work, we bioconjugated **1** to a short EGFR-targeting peptide based on the sequence (YRWYGYTPQNVLGGGC).[37] However, in preliminary flow cytometry experiments non-specific binding towards both high EGFR-expressing cells and non-EGFR-expressing cells was observed raising concerns for future molecular imaging applications (data not shown, see the thesis of Steven Kirbreger). Therefore, we turned our attention to reducing this non-specific cell binding, as future molecular imaging applications would need a tag with limited or no binding characteristics towards cells not expressing the desired receptor.

Towards this goal, we evaluated our leading peptides **1**, **TB-1** and **TB-4** to quantify the level of non-specific binding with cells. Fluorescein was attached to the N-terminus of each peptide to facilitate

fluorescent cell analysis by flow cytometry. These peptides are called **FAM-1**, **FAM-TB-1**, and **FAM-TB-4** (**Fig. 3-8**). We chose a high EGFR-expressing A549 non-small cell lung cancer line for analysis. As anticipated from our unpublished data, the flow cytometry results showed significant non-specific binding of **FAM-1** towards A549 cells when the peptide concentration was increased from 50 to 500 nM (**Fig. 3-9A**, and **3-9B**). Confocal fluorescence microscopy further confirmed cellular interactions. Intense fluorescence signal was observed with a punctate pattern (**Fig. 3-9C**), indicating a substantial internalization of **FAM-1** into A549 which may also contribute to the high signal. We attribute the cell interactions and uptake to the high positive charge on the peptide (+11, based on ionizable amino acid side chains). Encouragingly, flow cytometry results of **FAM-TB-1** with a reduced positive charge (+3) showed limited non-specific cellular interactions (**Fig. 3-10**). However, **FAM-TB-4** (+5) maintained a significant non-specific binding towards A549, with flow cytometry results showing the binding starting at as low as 5 nM with a dramatic increase at 500 nM (**Fig. 3-11**). These results supported the reduction of cationic charge for removing the cellular interactions, although other factors may play a role.

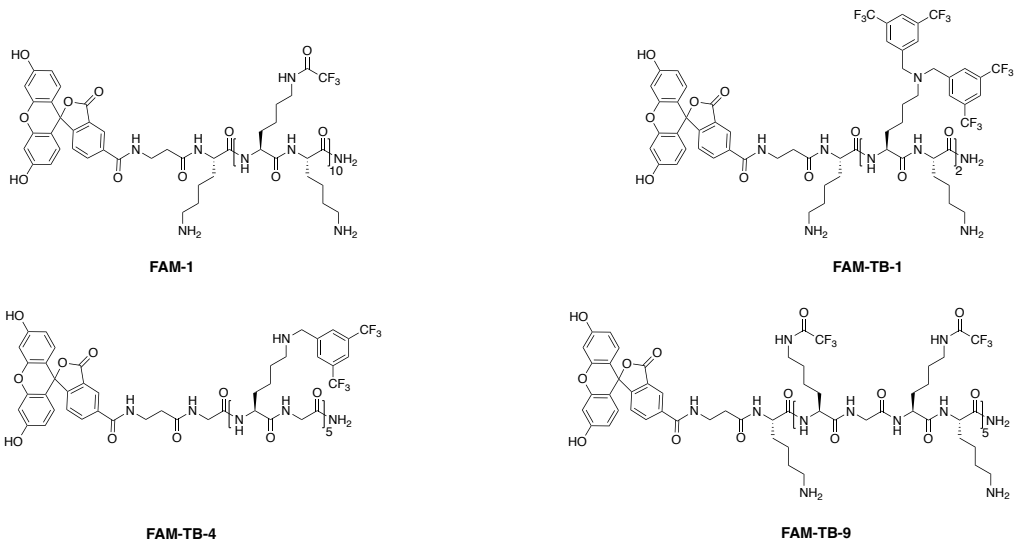

Figure 3-8. Structures of peptides for confocal fluorescence microscopy experiments.

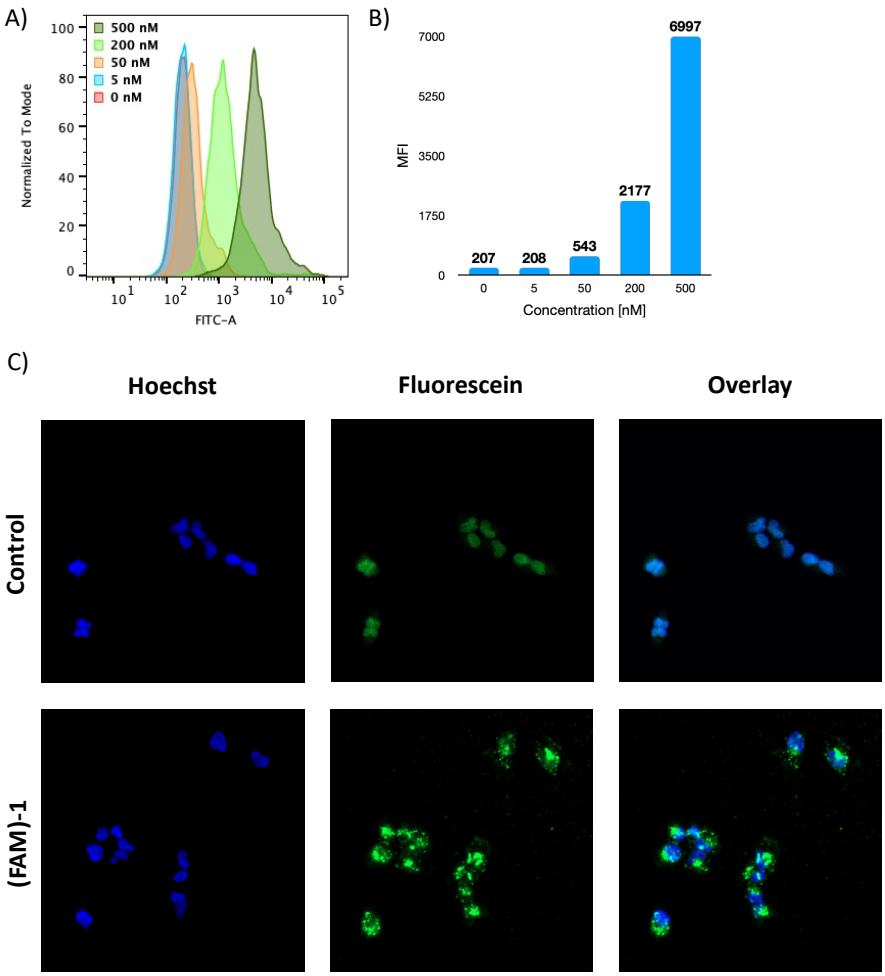

Figure 3-9. (FAM)-1 interactions and internalization into A549 non-small cell lung cancer (NSCLC) cells. A) Flow cytometry results show the increase in fluorescence intensity with the increase in **(FAM)-1** concentration from 0-500 nM, indicating non-specific binding toward A549. B) Chart of the mean fluorescence intensity (MFI) of **(FAM)-1** bound to A549 at concentration from 0-500 nM. Non-specific binding was significant starting at 50 nM. C) Fluorescent microscopy of **(FAM)-1** with A549 at 500 nM. Punctate pattern indicates the internalization of **(FAM)-1** into A549, while co-staining shows a limited amount of **(FAM)-1** entered the nuclei. In the DMSO control, background fluorescence was localized in the nucleus.

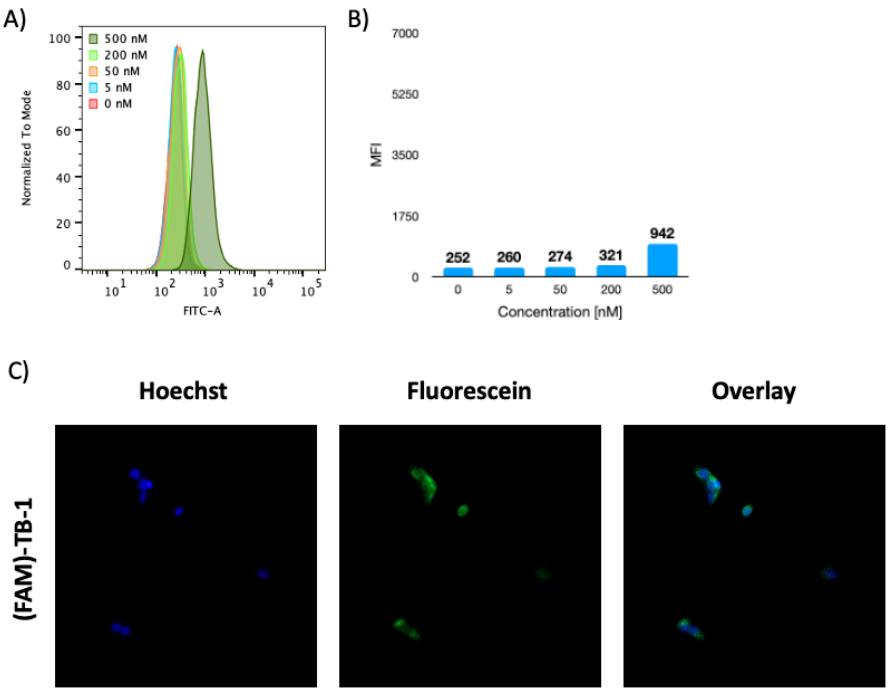

Figure 3-10. **(FAM)-TB-1** cellular interaction studies to A549. A) Flow cytometry results shows the limited increase in fluorescence intensity with the increase in **(FAM)-TB-1** concentration from 0 nM to 500 nM, indicating limited non-specific bining toward A549. B) Chart of the MFI of **(FAM)-TB-1** bound to A549. No significant increase in MFI was observed with a slight increase in MFI at 500 nM. C) Fluorescence microscopy of **(FAM)-TB-1** with A549 at 500 nM. Limited fluorescence was observed of **(FAM)-TB-1** to A549.

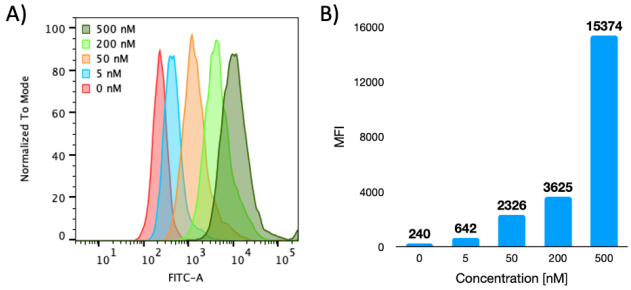

Figure 3-11. **(FAM)-TB-4** cellular interaction studies to A549. A) Flow cytometry results shows the increase in fluorescence intensity with the increase in **(FAM)-TB-4** concentration from 0 nM to 500 nM, indicating

non-specific binding toward A549. B) Chart of the MFI of **(FAM)-TB-4** bound to A549 at concentration from 0 nM to 500 nM. Non-specific binding was significant starting at 50 nM.

3.2.4 Structural Modification to Reduce Non-specific Binding

With **1** and **TB-4** maintaining a high degree of non-specific cell interactions and internalization, a peptide sequence modification was attempted to mitigate these effects. Given the highly polycationic side chain of **1** as a potential source of non-specific binding, we replaced half of the lysine residues with glycine leading to **TB-9** which reduced the total charge from +11 to +6, while maintaining the alternating pattern of fluorinated amino acid, K^{TFA} (**Fig. 3-6A**). **TB-9** maintained a good aqueous solubility and a FWHM of 17.2 Hz in ^{19}F NMR (**Fig. 3-6B**). Flow cytometry results (**Fig. 3-12A**, and **3-12B**) also indicated a significant reduction in non-specific binding. Confocal fluorescence microscopy confirmed minimal cell surface binding and internalization (**Fig. 3-12C**) relative to the background fluorescence seen with DMSO treated cells. However, for **TB-4**, we were unable to further reduce the charges on the side chain due to the fact that all charges on **TB-4** are from K^F. Alternative modification on **TB-4** to reduce non-specific binding will be explored in future designs.

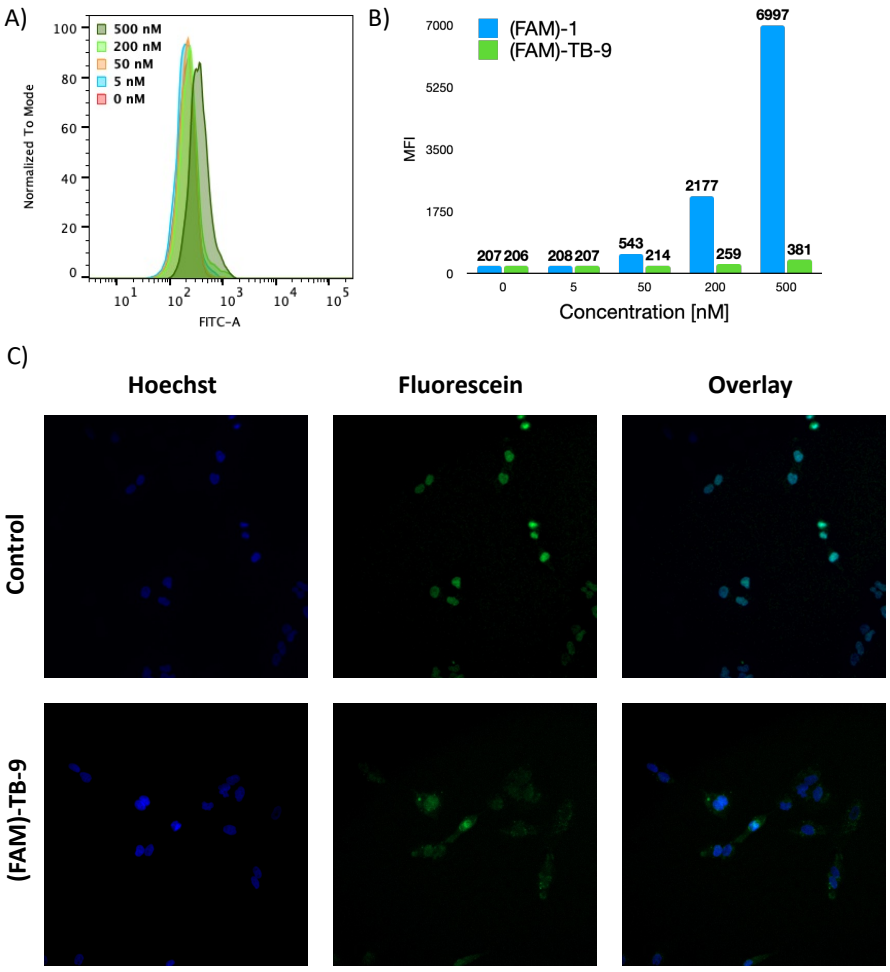

Figure 3-12. Structure modification of **(FAM)-1** to **(FAM)-TB-9** significantly reduced the non-specific binding to A549 NSCLC cells. A) Flow cytometry results show the limited increase in fluorescence intensity with the increase in **(FAM)-TB-9** concentration from 0-500 nM, indicating no obvious non-specific binding towards A549 cells. B) Chart of the MFI of **(FAM)-1** and **(FAM)-TB-9** bound to A549 cells individually at concentration from 0-500 nM. C) Fluorescent microscopy of **(FAM)-TB-9** with A549 cells at 500 nM. In the DMSO control, background fluorescence was localized in the nucleus.

3.2.5 Bioconjugation of fluorinated peptides to EGFR-targeting peptides and proteins for ^{19}F NMR analysis.

After successful removal of non-specific cell binding and maintenance of a high signal fluorinated peptide, we revisited designing targeting agents for molecular imaging. To this end, we selected two targeting

agents. First, a short 12 residue peptide (YHWYGYTPENVI) designed to bind EGFR with high affinity[38] was selected. A short peptide sequence (**KKK^{FF}KK**) was included containing a single K^{FF} amino acid through Fmoc solid phase synthesis. Secondly, a fibronectin-based protein construct, E$_1$-DD was selected. Kilic et al. used a modified version of this protein construct as a therapeutic approach for T cell-mediated killing of EGFR-overexpressing cancer cells.[39] Due to an accessible single cysteine near the C-terminus, we performed a conjugate addition reaction with a maleimide-terminated **TB-9** (**Fig. 3-13A**).

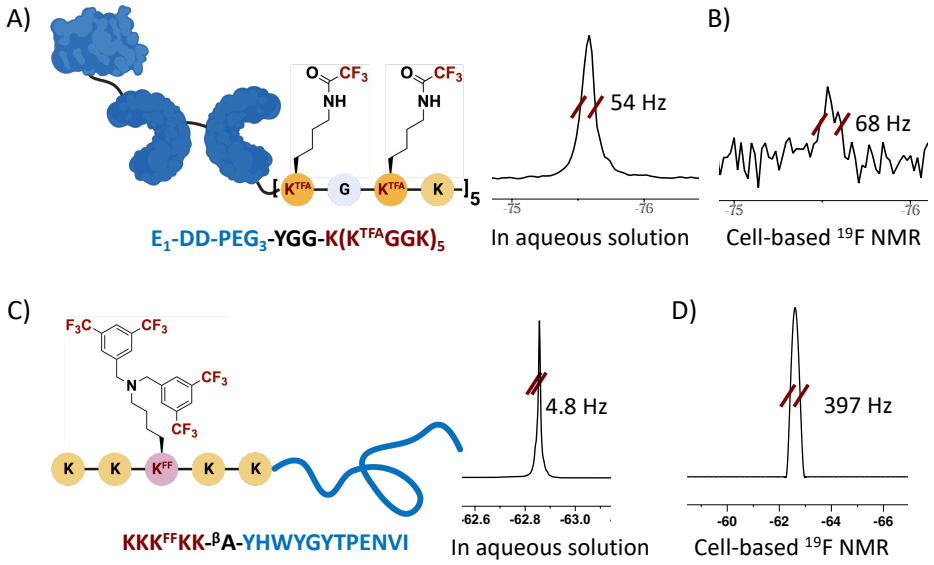

Figure 3-13. Fluorinated constructs for molecular imaging and the spectra. A) Illustration of **TB-9** (maroon) bioconjugated to targeting agent E$_1$-DD (blue). The corresponding ^{19}F NMR resonance is shown on the right. B) The corresponding cell-based ^{19}F NMR spectrum using **TB-9**-bioconjugated E$_1$-DD targeting A431 cells. C) Illustration of a fluorinated peptide for molecular imaging and the ^{19}F NMR spectra in aqueous solution. The targeting peptide (blue) was attached to K^{FF}-containing imaging sequence (maroon). The corresponding ^{19}F NMR spectrum is shown on the right in aqueous solution. D) The corresponding cell-based ^{19}F NMR spectrum using peptide (**KKK^{FF}KK-^{β}A-YHWYGYTPENVI**) targeting A431 cells. The Spectrum was obtained with 50 scans.

For both the fluorinated-peptide and protein construct, good ^{19}F NMR performance was observed in aqueous solution. For E$_1$-DD, resonance degeneracy was maintained with the FWHM of 54 Hz (**Fig. 3-13A**) despite the high molecular weight of this protein construct. A broadening in resonance was expected, and we

attributed it to a decreased tumbling rate with the 3 kDa peptide, **TB-9**, now attached to a 55 kDa E_1-DD protein. In contrast, a narrower resonance with a FWHM of 4.8 Hz was observed for the smaller EGFR-targeting peptide (**Fig. 3-13C**).

Given the ^{19}F NMR performance in vitro, we attempted a preliminary in-cell ^{19}F NMR experiment using A431 breast cancer cells, containing a high copy number of EGFR (~ 2 x 10^6 copies per cell in A431 versus ~ 0.1 x 10^6 per cell in A549) and a fast rate of internalization for intracellular accumulation of our fluorinated probes. Unfortunately, limited signal was observed for E_1-DD (**Fig. 3-13B**). This low signal may be due to its high molecular weight affecting the NMR performance in cells or a perturbed interaction with EGFR from peptide bioconjugation. A detailed characterization of the protein-EGFR interaction will be further assessed in future studies. Alternatively, an intense but broadened (FWHM 397 Hz) fluorine signal was observed (**Fig. 3-13D**) for the small EGFR-targeting peptide with only 50 scans, supporting the use of lower molecular weight designs, and the fast internalization rate of EGFR for concentrating the peptide signal. No signal was observed in the supernatant, when the cells were pelleted as a control (**Fig. 3-14**). While further optimization is needed, an additional advantage for using E_1-DD, is the ability of this protein to oligomerize into stable nanorings.[40] This self-assembly could further increase the number of fluorinated peptides that can be delivered to a single receptor for imaging, and will be investigated in the future alongside EGFR-targeting peptides for ^{19}F MRI-based molecular imaging applications.

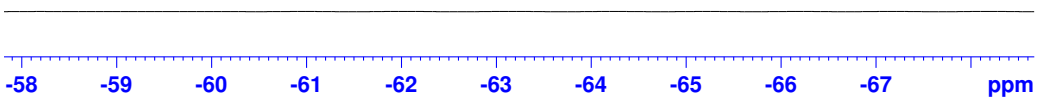

Figure 3-14. Full spectrum of cell-based ^{19}F NMR experiment leakage check (number of scans of 50). No signal was observed, indicating the signal is from the fluorinated peptide in the cells but not in the medium.

3.3 Conclusion

In these studies, we have demonstrated the syntheses of highly fluorinated amino acids and the design and evaluation of high fluorine-content peptides as future ^{19}F MRI molecular imaging tags. These studies build on our earlier results of peptide-based ^{19}F MRI agents, which despite the advantages of high degenerate ^{19}F signal and favorable physiochemical properties, suffered from low sensitivity and undesired non-specific binding. In our latest design, K^{FF}-based **TB-1** exhibited a sharp and degenerate ^{19}F signal, an acceptable aqueous solubility, and an 87% increase in ^{19}F wt%. Together with the previously reported peptide **1**, we examined their non-specific binding to A549 cells. Through structural modification on **1**, reducing overall positive charge to give **TB-9** also limited the non-specific binding while maintaining the overall NMR performance. As a first step towards imaging EGFR-overexpressing cancer cells, we synthesized a fluorinated EGFR targeting peptide and bioconjugated **TB-9** to EGFR-targeting agent E_1-DD. In both cases, a narrow ^{19}F signal was maintained in aqueous solution indicating a good flexibility of the peptides, while the EGFR-targeting peptide maintained a high-signal via cell-based ^{19}F NMR. These fluorinated biopolymers are promising candidates for ^{19}F MRI molecular imaging. For E_1-DD, future work will further improve the fluorine content through oligomerization of the bioconjugated monomeric protein into nanorings for imaging studies.

3.4 Supplementary Information

3.4.1 Synthesis of compounds

Materials

Fmoc-Lys(Boc)-OH, Fmoc-Lys(Tfa)-OH, Fmoc-Cys(Trt)-OH, Fmoc-Glu(OtBu)-OH, and 1-Hydroxy benzotriazole (HOBT) were purchased from Chem-Impex (Wood Dale, IL). Fmoc-Tyr(tBu)-OH, Fmoc-β-Ala-OH, 3,5-Bis(trifluoromethyl)benzaldehyde, 3,5-Bis(trifluoromethyl)benzyl bromide, and N,N-Diisopropylethylamine (DIEA) were purchased from Sigma-Aldrich (St. Louis, MO). Fmoc-Arg(Pbf)-OH was purchased from Spectrum (New Brunswick, NJ). Fmoc-Gly-OH and 2-(1H-benzotriazol-1-yl)-1,1,3,3-tetramethyluronium hexafluorophosphate (HBTU) were purchased from NovaBiochem (San Diego, CA).

Fmoc-L-Lys-OtBu*HCl was purchased from Iris Biotech (Marktredwitz, DE). Perfluoro-tert-butanol was purchased from Oakwood Chemical (Hampton County, SC).

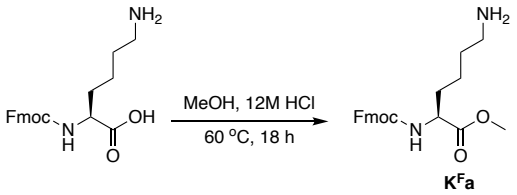

methyl (((9*H*-fluoren-9-yl)methoxy)carbonyl)-*L*-lysinate (K^Fa)

Fmoc-L-Lys-OH (1125 mg, 3.05 mmol) was suspended in 10 mL of MeOH. 20 drops of 12 M HCl were added to the suspension. The reaction mixture was refluxed at 60 °C for 24 h. The solvent was removed, and the mixture was precipitated in ethyl ether. The precipitate was collected through vacuum filtration and washed with excess ethyl ether to obtain the product as a white solid (935 mg, 80%).

^{1}H NMR (500 MHz, MeOD) δ 7.82 (d, *J* = 7.5 Hz, 2H), 7.69 (dd, *J* = 9.4, 7.5 Hz, 2H), 7.41 (t, *J* = 7.3 Hz, 2H), 7.33 (td, *J* = 7.4, 1.1 Hz, 2H), 4.44 (dd, *J* = 10.6, 6.8 Hz, 1H), 4.36 (dd, *J* = 10.6, 6.9 Hz, 1H), 4.28 – 4.15 (m, 2H), 3.74 (s, 3H), 2.99 – 2.86 (m, 2H), 1.94 – 1.83 (m, 1H), 1.81 – 1.61 (m, 3H), 1.48 (dtd, *J* = 16.0, 9.0, 6.4 Hz, 2H).

^{13}C NMR (126 MHz, MeOD) δ 172.95, 157.31, 143.88, 143.75, 141.24, 127.41, 126.77, 126.75, 124.82, 124.75, 119.56, 66.51, 53.66, 51.37, 39.12, 30.61, 26.58, 22.44.

HRMS (ESI-TOF) m/z: calcd. for $C_{22}H_{27}N_2O_4^+$ 383.1971 $[M+H]^+$; found 383.1974.

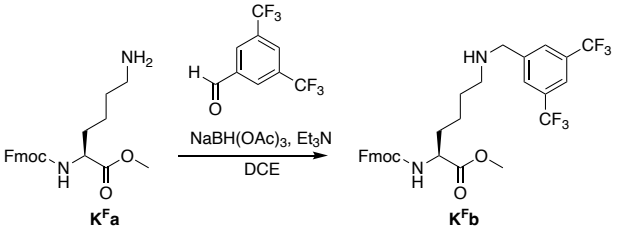

methyl N^2-(((9*H*-fluoren-9-yl)methoxy)carbonyl)-N^6-(3,5-bis(trifluoromethyl)benzyl)-*L*-lysinate (K^Fb)

K^Fa (1.30 g, 3.11 mmol) was suspended in 25 mL of 1,2-dichloroethane. Triethylamine (433 μL, 3.11 mmol) were added to the suspension. 3,5-bistrifluoromethylbenzaldehyde (752.1 mg, 3.11 mmol) was added

and the reaction mixture was stirred at room temperature for 10 min. Sodium triacetoyxborohydride (1.01 g, 4.75 mmol) was then added and reaction mixture was stirred at room temperature for 24 h. The reaction mixture was quenched with 25 mL of saturated $NaHCO_3$ aqueous solution and extracted with DCM (10 mL X 3). The organic layers were combined, dried with $MgSO_4$, and concentrated under reduced pressure. The crude compound was purified by Combi-flash chromatography (0-10% DCM in methanol) to obtain the product as a white solid (695 mg, 37%).

^{1}H NMR (500 MHz, Chloroform-*d*) δ 7.80 (s, 2H), 7.78 – 7.73 (m, 3H), 7.59 (dd, *J* = 7.8, 4.1 Hz, 2H), 7.40 (t, *J* = 7.5 Hz, 2H), 7.31 (t, *J* = 7.4 Hz, 2H), 5.32 (d, *J* = 8.3 Hz, 1H), 4.40 (m, 3H), 4.22 (t, *J* = 7.0 Hz, 1H), 3.89 (s, 2H), 3.76 (s, 3H), 2.63 (t, *J* = 7.0 Hz, 2H), 1.86 (m, 1H), 1.69 (m, 1H), 1.54 (m, 2H), 1.42 (m, 2H).

^{13}C NMR (126 MHz, Chloroform-*d*) δ 172.95, 155.93, 143.90, 143.75, 141.34, 131.75, 131.49, 131.22, 128.26, 127.73, 127.09, 127.06, 125.08, 124.48, 122.31, 121.10, 120.01, 119.75, 66.99, 53.74, 52.80, 52.45, 48.96, 47.18, 39.13, 32.53, 29.28, 28.90, 22.90, 22.40.

^{19}F NMR (471 MHz, Chloroform-*d*) δ -62.77(s, 6F).

HRMS (ESI-TOF) m/z: calcd. for $C_{31}H_{31}F_6N_2O_4^+$ 609.2188 $[M+H]^+$; found 609.2199.

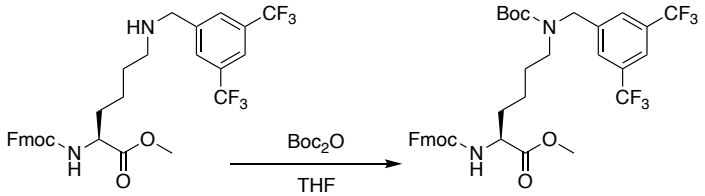

K^Fb **K^Fc**

methyl N^2-(((9*H*-fluoren-9-yl)methoxy)carbonyl)-N^6-(3,5-bis(trifluoromethyl)benzyl)-N^6-(*tert*-butoxycarbonyl)-*L*-lysinate (K^Fc)

K^Fb (608 mg, 1.00 mmol) was dissolved in 4 mL of THF. Separately, Boc anhydride (334 mg, 1.53 mmol) was dissolved in 1 mL of THF. The anhydride solution in THF was added to the **K^Fb** solution in THF. The reaction mixture was stirred at room temperature for 3 h. Solvent was removed, and the crude product was dissolved in 15 mL of DCM, and washed with H_2O (10 mL x 3). The organic layer was dried with $MgSO_4$

and concentrated under reduced pressure. The crude compound was purified by Combi-flash chromatography (0-100% ethyl acetate in hexane) to obtain the product as a clear oil (560 mg, 79%).

^{1}H NMR (500 MHz, DMSO-d_6) δ 8.01 (s, 1H), 7.88 (d, J = 4.7 Hz, 4H), 7.74 (d, J = 7.9 Hz, 1H), 7.69 (dd, J = 7.7, 4.1 Hz, 2H), 7.40 (t, J = 7.4 Hz, 2H), 7.31 (t, J = 7.4 Hz, 2H), 4.52 (s, 2H), 4.35 – 4.24 (m, 2H), 4.20 (m, 1H), 3.98 (m, 1H), 3.60 (s, 3H), 3.20 (t, J = 27.8 Hz, 2H), 1.62 (d, J = 29.1 Hz, 2H), 1.33 (m, 13H).

^{13}C NMR (126 MHz, DMSO-d_6) δ 172.38, 156.46, 143.08, 142.97, 140.40, 131.04, 130.78, 130.51, 126.57, 125.94, 124.03, 124.00, 121.55, 119.71, 118.71, 79.62, 65.71, 59.32, 53.05, 50.45, 29.98, 26.34, 21.88, 18.64, 12.25.

^{19}F NMR (471 MHz, DMSO-d_6) δ -65.19 (s, 6F).

HRMS (ESI-TOF) m/z: calcd. for $C_{36}H_{39}F_6N_2O_6^+$ 709.2712 $[M+H]^+$; found 709.2732.

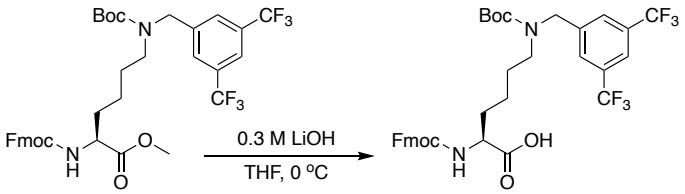

N^2-(((9*H*-fluoren-9-yl)methoxy)carbonyl)-N^6-(3,5-bis(trifluoromethyl)benzyl)-N^6-(*tert*-butoxycarbonyl)-*L*-lysine (K^F)

K^Fc (514 mg, 0.73 mmol) was dissolved in 5 mL of THF. 500 µL of 0.3 M LiOH aqueous solution were added dropwise on ice. The reaction was monitored through TLC (ethyl acetate:heaxane = 2:3) Upon completion, the reaction was quenched with 1 M HCl and extracted with ethyl acetate (10 mL x 3). Organic layers were combined, dried with $MgSO_4$, and concentrated under reduced pressure. The crude compound was purified by Combi-flash chromatography (0-10% DCM in methanol) to obtain the product as a white solid (135 mg, 27%).

^{1}H NMR (500 MHz, Chloroform-d) δ 7.83 – 7.70 (m, 3H), 7.66 (s, 2H), 7.63 – 7.47 (m, 2H), 7.39 (t, J = 7.3 Hz, 2H), 7.30 (t, J = 7.4 Hz, 2H), 4.63 – 4.26 (m, 5H), 4.21 (t, J = 7.0 Hz, 1H), 3.24 (d, J = 50.0 Hz, 2H), 1.99 – 1.32 (m, 15H).

^{13}C NMR (126 MHz, Chloroform-*d*) δ 175.76, 156.22, 143.81, 143.68, 141.32, 132.01, 131.74, 131.48, 127.75, 127.08, 126.51, 125.08, 124.35, 122.18, 121.25, 120.01, 107.98, 81.03, 67.20, 53.55, 50.16, 47.13, 46.88, 31.61, 29.12, 28.29, 27.81, 27.44, 23.93, 22.22.

^{19}F NMR (471 MHz, Chloroform-*d*) δ -62.89 (s, 6F).

HRMS (ESI-TOF) m/z: calcd. for $C_{35}H_{35}F_6N_2O_6^-$ 693.2402 [M-H]$^-$; found 693.2002.

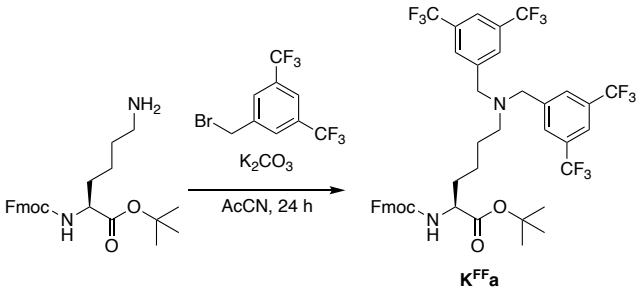

K^{FF}a

***tert*-butyl N^2-(((9*H*-fluoren-9-yl)methoxy)carbonyl)-N^6,N^6-bis(3,5-bis(trifluoromethyl)benzyl)-*L*-lysinate (K^{FF}a)**

Fmoc-Lysine-OtBu (115 mg, 0.25 mmol) was suspended in 2 mL AcCN. K_2CO_3 (207 mg, 1.50 mmol was added and the reaction mixture was stirred at room temperature for 10 min. 3,5-bis(trifluoromethyl)benzyl bromide (200 μL, 1.10 mmol) was added to the reaction mixture. The reaction mixture was stirred at room temperature for 24 h and subsequently diluted with 10 mL of brine followed by washing with DCM (5 mL X 3). The organic layers were combined, dried with $MgSO_4$, and concentrated under reduced pressure. The crude compound was purified by Combi-flash chromatography (0-100% ethyl acetate in hexane) to obtain the product as a clear oil (182 mg, 83%)**.**

^{1}H NMR (500 MHz, Chloroform-*d*) δ 7.82 (s, 4H), 7.78 – 7.72 (m, 4H), 7.58 (d, *J* = 7.5 Hz, 2H), 7.43 – 7.36 (m, 2H), 7.30 (m, 2H), 5.32 (d, *J* = 8.0 Hz, 1H), 4.43 – 4.29 (m, 2H), 4.22 (m, 2H), 3.78 (s, 4H), 2.60 (s, 2H), 1.45 (s, 15H).

^{13}C NMR (126 MHz, Chloroform-*d*) δ 171.48, 155.91, 143.91, 141.31, 132.20, 131.94, 131.67, 131.40, 128.52, 127.71, 127.04, 126.48, 125.09, 124.31, 122.14, 121.34, 119.98, 82.27, 66.98, 57.74, 54.49, 53.99, 47.16, 34.68, 32.75, 31.60, 27.96, 26.57, 25.29, 22.81, 14.13.

^{19}F NMR (471 MHz, Chloroform-*d*) δ -62.93 (s, 12H).

HRMS (ESI-TOF) m/z: calcd. for $C_{44}H_{40}F_{12}N_2O_4^+$ 877.2874 $[M+H]^+$; found 877.2892

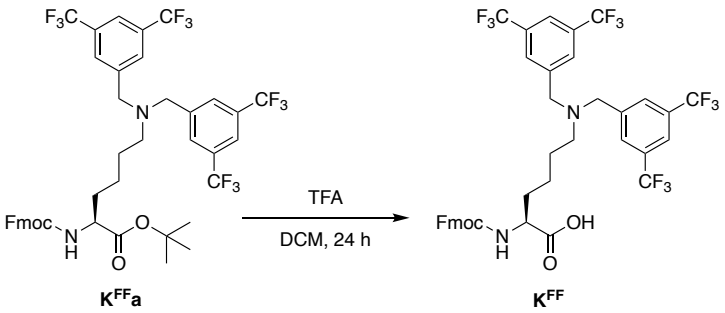

N^2-(((9*H*-fluoren-9-yl)methoxy)carbonyl)-N^6,N^6-bis(3,5-bis(trifluoromethyl)benzyl)-*L*-lysine (K^{FF})

K^{FF}a (134 mg, 0.15 mmol) was dissolved in 2 mL of DCM. 2 mL of TFA was added to the solution and the reaction mixture was stirred at room temperature for 24 h. TFA was removed under a stream of nitrogen. The crude compound was purified by Combi-flash chromatography (0-10% DCM in methanol) to obtain the product as white solid (112 mg, 91%).

^{1}H NMR (500 MHz, Chloroform-*d*) δ 10.74 (s, 4H), 7.89 (d, *J* = 8.7 Hz, 6H), 7.72 (d, *J* = 7.5 Hz, 2H), 7.54 (m, 2H), 7.37 (t, *J* = 7.4 Hz, 2H), 7.27 (t, *J* = 7.6 Hz, 2H), 5.75 (d, *J* = 7.7 Hz, 1H), 4.37 (m, 7H), 4.16 (t, *J* = 6.8 Hz, 1H), 3.29 – 3.06 (m, 2H), 2.04 – 1.44 (m, 6H).

^{13}C NMR (126 MHz, Chloroform-*d*) δ 175.06, 174.76, 161.54, 161.23, 160.91, 160.59, 156.76, 143.44, 143.31, 141.21, 133.39, 133.12, 132.85, 132.58, 131.03, 130.80, 127.86, 127.10, 125.74, 124.95, 124.61, 124.28, 123.57, 121.40, 120.03, 119.23, 118.73, 116.44, 114.15, 111.87, 67.98, 67.56, 56.58, 53.69, 53.10, 46.87, 31.33, 22.32, 22.04.

^{19}F NMR (471 MHz, Chloroform-*d*) δ -63.32 (s, 12F).

HRMS (ESI-TOF) m/z: calcd. for $C_{39}H_{33}F_{12}N_2O_4^+$ 821.2248 $[M+H]^+$; found 821.2265

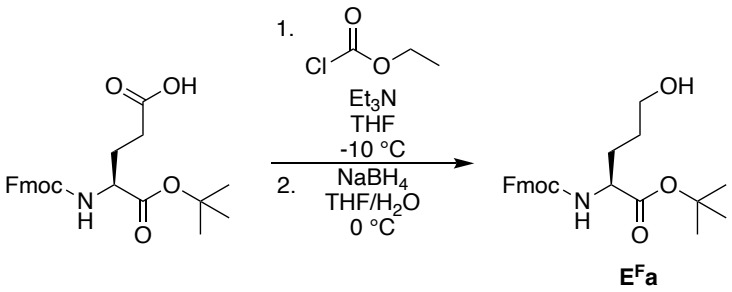

$\mathbf{E^Fa}$

***tert*-butyl (*S*)-2-((((9*H*-fluoren-9-yl)methoxy)carbonyl)amino)-5-hydroxypentanoate ($\mathbf{E^Fa}$)**

Fmoc-L-glutamic acid-α tert butyl ester (1.00 g, 2.36 mmol, 1 eq) was dissolved in 4 mL of anhydrous THF. The solution was cooled to -10 °C, followed by slow addition of Et_3N (363 µL, 2.61 mmol, 1.10 eq). Separately, ethyl chloroformate (250 µL, 2.62 mmol, 1.1 eq) was dissolved in 2 mL of anhydrous THF and added slowly to the solution containing Fmoc-L-glutamic acid-α tert butyl ester. The mixture turned white and heterogenous and was stirred at -10 °C for 90 min, followed by gravity filtration. Separately, sodium borohydride (194 mg, 5.12 mmol, 2.2 eq) was suspended in 2 mL of H_2O and cooled to 0 °C. Slowly, the filtrate was added to the borohydride solution and was stirred at 0 °C for 30 min. The mixture was quenched with 1 M HCl and diluted with ethyl acetate. The organic layer was washed 3X with $NaHCO_3$, followed by water and brine then dried over $MgSO_4$. Following filtration and removal of solvent, the crude compound was purified by Combi-flash chromatography (0-100% ethyl acetate in hexane) to obtain the product as a clear oil (357 mg, 37%).

^{1}H NMR (500 MHz, Chloroform-*d*) δ 7.76 (d, *J* = 7.6 Hz, 2H), 7.60 (d, *J* = 7.5 Hz, 2H), 7.40 (t, *J* = 7.5 Hz, 2H), 7.31 (t, *J* = 7.5 Hz, 2H), 5.52 (d, *J* = 8.2 Hz, 1H), 4.39 (d, *J* = 7.2 Hz, 2H), 4.30 (q, *J* = 6.8 Hz, 1H), 4.22 (t, *J* = 7.0 Hz, 1H), 3.68 (t, *J* = 6.2 Hz, 2H), 2.07 – 1.88 (m, 2H), 1.76 (tt, *J* = 14.0, 6.7 Hz, 1H), 1.62 (m, 2H), 1.48 (s, 9H).

^{13}C NMR (126 MHz, Chloroform-*d*) δ 171.58, 155.99, 143.89, 143.74, 141.27, 127.66, 127.02, 125.08, 119.94, 82.24, 66.88, 62.17, 53.94, 47.17, 31.17, 29.56, 28.08, 27.98.

HRMS (ESI-TOF) m/z: calcd. for $C_{24}H_{30}NO_5^+$ 434.1943 $[M+H]^+$; found 434.1908.

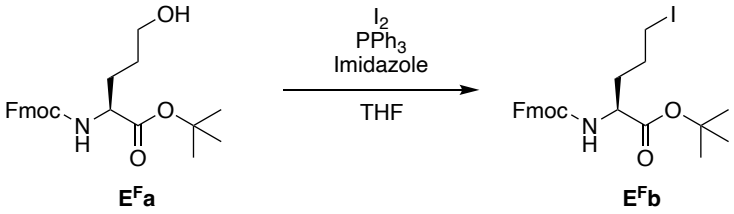

$\mathbf{E^Fa}$ $\mathbf{E^Fb}$

***tert*-butyl (*S*)-2-((((9*H*-fluoren-9-yl)methoxy)carbonyl)amino)-5-iodopentanoate ($\mathbf{E^F}$b)**

Iodine (267 mg, 1.05 mmol, 1.3 eq) was dissolved in 3 mL of THF, followed by addition of triphenylphosphine (277 mg, 1.06 mmol, 1.3 eq) and imidazole (72.4 mg, 1.06 mmol, 1.3 eq). The mixture was stirred for 15 min, followed by addition of $\mathbf{E^Fa}$ (333 mg, 0.810 mmol, 1.0 eq) dissolved in 2 mL of THF. The solution was stirred for 2 h, followed by dilution with ethyl acetate, and washing 3X with H_2O. The organic layer was washed with brine, dried with $MgSO_4$, and concentrated under reduced pressure. The crude compound was purified by Combi-flash chromatography (0-100% ethyl acetate in hexane) to obtain the product as a brown oil (288 mg, 68%).

^{1}H NMR (500 MHz, Chloroform-*d*) δ 7.77 (d, *J* = 7.5 Hz, 2H), 7.60 (d, *J* = 7.5 Hz, 2H), 7.41 (t, *J* = 7.5 Hz, 2H), 7.32 (td, *J* = 7.5, 2.8 Hz, 2H), 5.35 (d, *J* = 8.1 Hz, 1H), 4.41 (qd, *J* = 10.7, 7.0 Hz, 2H), 4.32 – 4.25 (m, 1H), 4.22 (t, *J* = 6.9 Hz, 1H), 3.26 – 3.20 (m, 1H), 3.17 (tt, *J* = 9.8, 4.9 Hz, 1H), 1.93 (m, 2H), 1.79 (m, 2H), 1.49 (s, 9H).

^{13}C NMR (126 MHz, Chloroform-*d*) δ 171.12, 155.77, 143.87, 143.71, 141.30, 127.69, 127.05, 125.09, 125.03, 119.98, 119.96, 82.54, 66.88, 53.38, 47.19, 33.69, 28.95, 28.01, 5.73.

HRMS (ESI-TOF) m/z: calcd. for $C_{24}H_{29}INO_4^+$ 544.0961 $[M+H]^+$; found 544.0893.

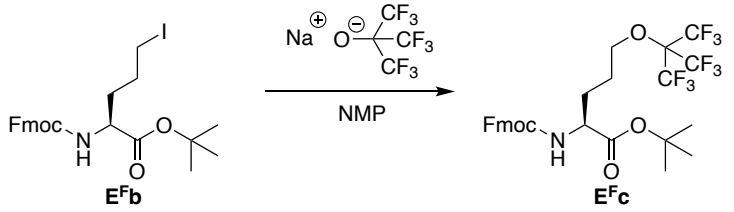

$\mathbf{E^Fb}$ $\mathbf{E^Fc}$

***tert*-butyl (*S*)-2-((((9*H*-fluoren-9-yl)methoxy)carbonyl)amino)-5-((1,1,1,3,3,3-hexafluoro-2-(trifluoromethyl)propan-2-yl)oxy)pentanoate ($\mathbf{E^F}$c)**

$\mathbf{E^Fb}$ (288 mg, 0.552 mmol, 1.0 eq) was dissolved in 2 mL of NMP, followed by addition of sodium perfluorotertbutoxide (157 mg, 0.608 mmol, 1.1 eq). The reaction mixture was stirred at rt for 18 h. Upon

completion, the mixture was diluted with ethyl acetate, and washed 3X with H_2O. The Organic layer was washed with brine, dried with $MgSO_4$, and concentrated under reduced pressure. The crude compound was purified by Combi-flash chromatography (0-100% ethyl acetate in hexane) to obtain the product as a white solid (203 mg, 58%).

^{1}H NMR (500 MHz, Chloroform-*d*) δ 7.77 (d, *J* = 7.3 Hz, 2H), 7.60 (dd, *J* = 7.6, 2.4 Hz, 2H), 7.40 (td, *J* = 7.5, 2.7 Hz, 2H), 7.32 (tt, *J* = 7.4, 1.6 Hz, 2H), 5.37 (d, *J* = 8.0 Hz, 1H), 4.44 – 4.38 (m, 2H), 4.30 (q, *J* = 6.8, 6.3 Hz, 1H), 4.22 (t, *J* = 6.9 Hz, 1H), 4.07 – 4.02 (m, 2H), 1.97 (tq, *J* = 15.0, 5.1 Hz, 1H), 1.81 – 1.64 (m, 2H), 1.48 (s, 9H).

^{13}C NMR (126 MHz, Chloroform-*d*) δ 171.19, 155.84, 143.88, 143.71, 141.32, 127.70, 127.03, 125.08, 125.03, 119.98, 119.95, 82.50, 68.95, 66.88, 53.62, 47.20, 37.01, 33.70, 28.86, 27.89, 25.39.

^{19}F NMR (471 MHz, Chloroform-*d*) δ -70.37 (s, 9F).

HRMS (ESI-TOF) m/z: calcd. for $C_{28}H_{28}F_9NO_5Na^+$ 652.1721 $[M+H]^+$; found 652.1695.

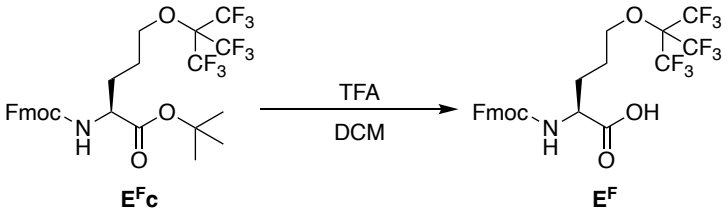

E^{F}c **E^F**

(*S*)-2-((((9*H*-fluoren-9-yl)methoxy)carbonyl)amino)-5-((1,1,1,3,3,3-hexafluoro-2-(trifluoromethyl) propan-2-yl)oxy)pentanoic acid (E^F)

E^{F}c (178 mg, 0.283 mmol, 1.0 eq) was dissolved in 2 mL of DCM, followed by addition of 2 mL of TFA and 25 µL of triisopropylsilane. The reaction mixture was stirred at rt for 3 h, followed by removal of solvent. The crude mixture was dissolved in 5 mL of ethyl acetate and washed 3X with 5mL of 1 M HCl. The organic layer was washed with brine, dried with $MgSO_4$, and concentrated under reduced pressure after filtration to obtain the product as white solid (102 mg, 63%).

^{1}H NMR (500 MHz, DMSO- *d6*) δ 12.66 (s, 1H), 7.90 (d, *J* = 7.6 Hz, 2H), 7.73 (dd, *J* = 7.5, 3.7 Hz, 2H), 7.70 (d, *J* = 8.2 Hz, 1H), 7.42 (t, *J* = 7.4 Hz, 2H), 7.33 (t, *J* = 7.4 Hz, 2H), 4.34 – 4.29 (m, 2H), 4.23 (t, *J* = 7.1 Hz, 1H), 4.09 (q, *J* = 5.8 Hz, 2H), 3.98 (td, *J* = 8.5, 4.9 Hz, 1H), 1.84 (dq, *J* = 10.0, 5.5 Hz, 1H), 1.77 – 1.61 (m, 3H).

^{13}C NMR (126 MHz, DMSO-*d*6) δ 173.46, 156.04, 143.70 (d, *J* = 10.1 Hz), 140.62, 127.52, 126.92, 125.15, 125.14, 121.08, 120.01, 119.99, 118.75, 69.77, 65.47, 53.13, 46.56, 26.54, 25.86.

^{19}F NMR (471 MHz, DMSO-*d*6) δ -69.96 (s, 9F).

HRMS (ESI-TOF) m/z: calcd. for $C_{24}H_{19}F_9NO_5^-$ 572.1122 [M-H]$^-$; found 572.1369.

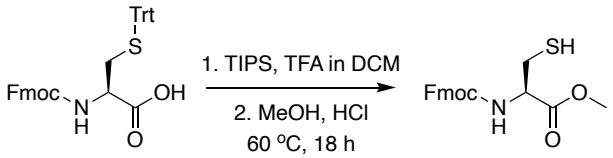

C^{F}a

methyl (((9*H*-fluoren-9-yl)methoxy)carbonyl)-*L*-cysteinate (C^{F}a)

Fmoc-L-Cys(Trt)-OH (1.00 g, 1.71 mmol) was suspended in 10 mL of DCM. Triisopropylsilane (200 μL, 2.00 mmol) was added to the suspension, followed with 5 mL of TFA. The reaction mixture was stirred at room temperature for 30 min. DCM and TFA were removed through a stream of nitrogen. The reaction mixture was then dissolved in 20 mL of MeOH. 20 drops of 37% HCl were added to the solution and reacted at 60 °C for 18 h. The solvent was removed, and the crude product was purified by Combi-flash chromatography (0-100% ethyl acetate in hexane) to obtain the product as a white solid. (507 mg, 71%)

^{1}H NMR (500 MHz, Chloroform-*d*) δ 7.78 (d, *J* = 7.6 Hz, 2H), 7.61 (d, *J* = 7.1 Hz, 2H), 7.41 (m, 2H), 7.33 (m, 2H), 5.73 (d, *J* = 7.8 Hz, 1H), 4.68 (m, 1H), 4.44 (m, 2H), 4.24 (t, *J* = 6.9 Hz, 2H), 3.80 (s, 3H), 3.01 (m, 2H), 1.37 (t, *J* = 9.0 Hz, 1H).

^{13}C NMR (126 MHz, Chloroform-*d*) δ 170.49, 155.67, 143.82, 143.65, 141.38, 141.35, 127.81, 127.14, 127.12, 125.12, 125.06, 120.07, 120.05, 67.15, 55.25, 52.88, 47.19, 27.16.

HRMS (ESI-TOF) m/z: calcd. for $C_{19}H_{20}NO_4S^+$ 357.1113 [M+H]$^+$; found 358.1115.

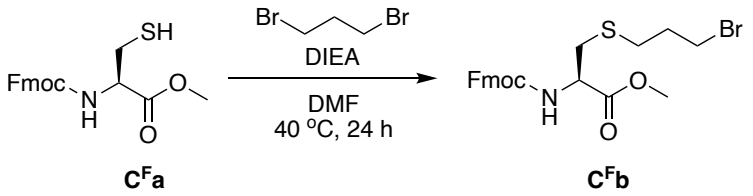

C^{F}a **C^{F}b**

methyl *N*-(((9*H*-fluoren-9-yl)methoxy)carbonyl)-*S*-(3-bromopropyl)-*L*-cysteinate (C^{F}b)

C^{F}a (200 mg, 0.56 mmol) was dissolved in 3 mL of anhydrous DMF with molecular sieves. 1,3-dibromopropane (68 µL, 0.67 mmol) was added dropwise to the reaction mixture. DIEA (97 µL, 0.56 mmol) was then added and reaction mixture was stirred at 40 °C for 24 h. The reaction was quenched with brine (10 mL) and extracted with DCM (5 mL x 3). Organic layers were combined, dried with $MgSO_4$, and concentrated under reduced pressure. The crude compound was purified by Combi-flash chromatography (0-100% ethyl acetate in hexane) to obtain the product as a white solid (144 mg, 54%).

^{1}H NMR (500 MHz, Chloroform-*d*) δ 7.77 (d, *J* = 7.4 Hz, 2H), 7.62 (d, *J* = 7.8 Hz, 2H), 7.41 (m, 2H), 7.33 (m, 2H), 5.70 (d, *J* = 8.1 Hz, 1H), 4.64 (dt, *J* = 8.0, 5.1 Hz, 1H), 4.42 (d, *J* = 7.2 Hz, 2H), 4.25 (t, *J* = 7.0 Hz, 1H), 3.80 (s, 3H), 3.48 (t, *J* = 6.4 Hz, 2H), 3.02 (m, 2H), 2.69 (t, *J* = 6.9 Hz, 2H), 2.09 (tt, *J* = 6.7, 6.6 Hz, 2H).

^{13}C NMR (126 MHz, Chloroform-*d*) δ 171.17, 155.74, 145.68, 143.83, 143.74, 141.35, 141.09, 127.80, 127.69, 127.14, 125.13, 124.80, 124.76, 120.06, 67.25, 53.77, 52.82, 47.15, 46.94, 37.12, 35.54, 34.53, 32.11, 31.89, 30.95.

HRMS (ESI-TOF) m/z: calcd. for $C_{22}H_{25}BrNO_4S^+$ 478.0687 $[M+H]^+$; found 478.0696.

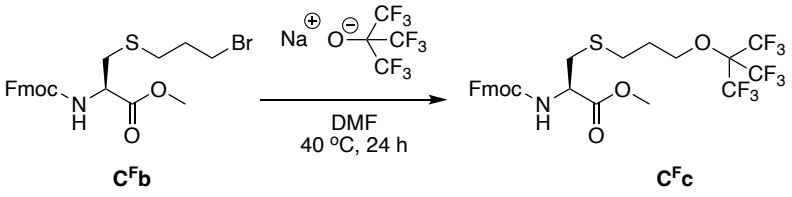

C^{F}b **C^{F}c**

***N*-(((9*H*-fluoren-9-yl)methoxy)carbonyl)-*S*-(3-((1,1,1,3,3,3-hexafluoro-2-(trifluoromethyl)propan-2-yl)oxy)propyl)-*L*-cysteinate (C^{F}c)**

C^{F}b (200 mg, 0.42 mmol) was dissolved in 2 mL of DMF with molecular sieves. Sodium perfluoro-tert-butanoxide (108 mg, 0.42 mmol) was then added to the reaction mixture. The reaction mixture was stirred

at 40 °C for 24 h. The reaction was quenched with brine (10 mL) and extracted with DCM (5 mL x 3). The organic layers were combined, dried with $MgSO_4$, and concentrated under reduced pressure. The crude compound was purified by Combi-flash chromatography (0-100% ethyl acetate in hexane) to obtain the product as a white solid (81 mg, 31%).

^{1}H NMR (500 MHz, Chloroform-*d*) δ 7.77 (d, *J* = 7.6 Hz, 2H), 7.61 (d, *J* = 7.2 Hz, 2H), 7.41 (t, *J* = 7.5 Hz, 2H), 7.32 (t, *J* = 7.5 Hz, 2H), 5.64 (d, *J* = 7.8 Hz, 1H), 4.63 (dd, *J* = 7.9, 5.1 Hz, 1H), 4.42 (m, 2H), 4.24 (t, *J* = 7.0 Hz, 1H), 4.10 (t, *J* = 5.6 Hz, 2H), 3.79 (s, 3H), 3.01 (m, 2H), 2.63 (t, *J* = 7.1 Hz, 2H), 1.94 (tt, *J* = 6.5, 6.4 Hz, 2H).

^{13}C NMR (126 MHz, Chloroform-*d*) δ 171.16, 155.72, 143.81, 143.71, 141.34, 127.77, 127.10, 125.09, 123.85, 121.52, 120.03, 119.19, 116.85, 67.86, 67.25, 54.17, 53.65, 53.13, 52.70, 50.54, 48.54, 47.12, 34.57, 29.64, 28.50, 23.17.

^{19}F NMR (471 MHz, Chloroform-*d*) δ -70.34 (s, 9F).

HRMS (ESI-TOF) m/z: calcd. for $C_{26}H_{25}F_9NO_5S^+$ 634.1309 $[M+H]^+$; found 634.1320.

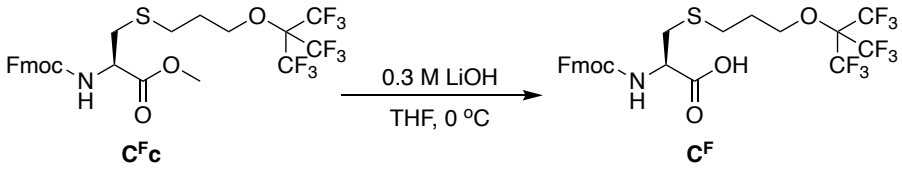

C^Fc **C^F**

***N*-(((9*H*-fluoren-9-yl)methoxy)carbonyl)-*S*-(3-((1,1,1,3,3,3-hexafluoro-2-(trifluoromethyl) propan-2-yl)oxy)propyl)-*L*-cysteine (C^F)**

C^Fc (100 mg, 0.16 mmol) was dissolved in 5 mL of THF. 500 μL of 0.3 M LiOH aqueous solution were added dropwise on ice. The reaction was monitored through TLC (ethyl acetate:heaxane = 2:3) Upon completion, the reaction was quenched with 1 M HCl and extracted with ethyl acetate (10 mL x 3). The organic layers were combined, dried with $MgSO_4$, and concentrated under reduced pressure. The crude compound was purified by Combi-flash chromatography (0-10% DCM in methanol) to obtain the product as white solid (86 mg, 87%).

^{1}H NMR (500 MHz, Chloroform-*d*) δ 7.76 (d, *J* = 7.5 Hz, 2H), 7.59 (d, *J* = 6.1 Hz, 2H), 7.40 (t, *J* = 7.3 Hz, 2H), 7.31 (t, *J* = 7.3 Hz, 2H), 5.63 (s, 1H), 4.64 (m, 1H), 4.41 (m, 2H), 4.23 (t, *J* = 6.9 Hz, 1H), 4.09 (t, *J* = 6.0 Hz, 2H), 3.04 (m, 2H), 2.66 (t, *J* = 6.3 Hz, 2H), 1.94 (tt, *J* = 6.5, 6.4 Hz, 2H).

^{13}C NMR (126 MHz, Chloroform-*d*) δ 174.59, 155.95, 143.71, 143.60, 143.55, 141.33, 129.70, 127.81, 127.11, 125.06, 121.51, 120.23, 120.04, 119.17, 67.78, 67.42, 53.48, 47.08, 34.11, 29.72, 29.58, 28.53, 23.39.

^{19}F NMR (471 MHz, Chloroform-*d*) δ -70.34 (s, 9F).

HRMS (ESI-TOF) m/z: calcd. for $C_{25}H_{23}F_9NO_5S^+$ 620.1153 $[M+H]^+$; found 620.1163.

3.4.2 Experimental

General Method for Peptide Preparation

Solid Phase Peptide Synthesis

All peptides except **TB-7** and **TB-8** were synthesized on NovaSyn TGR ® resin using a CEM MARS Xtraction Microwave Reactor on a 25 μmol scale. Prior to acylation reaction, N^{α} -Fmoc protected amino acid (100 μmol, 4.0 eq) was dissolved in 1 mL of DMF, followed with activation with HOBT (200 μL of 0.5 M solution in DMF, 4.0 eq), HBTU (200 μL of 0.5 M solution in DMF, 4.0 eq) and DIEA (200 μL of 1.0 M solution in DMF, 8.0 eq). The reaction mixture was added to the resin and heated at 70 °C (400 W power, 2 min ramping and 4 min holding cycle). The reaction mixture was then drained, and resin was washed with DMF 3 times, DCM 3 times, and DMF 3 times. 9-fluorenylmethyoxycarbonyl (Fmoc) group was deprotected by addition of piperidine (2 mL, 20% v/v in DMF) to the resin and heating to 80 °C (400 W power, 2 min ramping and 2 min holding cycle). The reaction mixture was then drained, and resin was washed with DMF 3 times, DCM 3 times, and DMF 3 times. The coupling and deprotection steps were repeated unitl the full-length peptide was synthesized. Following the final deprotection step, the N-terminus was either acetylated or acylated with a fluorescein group (described below). The acetylation reaction was conducted at room temperature with 500 μL of acetic anhydride, 100 μL of triethylamine (TEA), and 1.4 mL DCM for 90 minutes. Prior to attaching the fluorescein group at the N-terminus, 5-carboxy fluorescein (100 μmol, 4.0 eq) was dissolved in 1 mL of DMF, followed with activation with HOBT (200 μL of 0.5 M solution in DMF, 4.0 eq), HBTU (200 μL of 0.5 M solution in DMF, 4.0 eq) and DIEA (200 μL of 1.0 M solution in DMF, 8.0 eq).

The reaction mixture was added to the resin and reacted at room temperature overnight. The reaction mixture was then drained, and resin was washed with DMF 3 times, DCM 3 times, and DMF 3 times.

Peptide Cleavage and Deprotection

Peptides were cleaved from the resin and the side chains were deprotected at the same time through treatment of 1.9 mL of trifluoroacetic acid (TFA), 100 µL of thioanisole, 60 µL of triisopropylsilane (TIPS), and 40 µL of anisole at room temperature for 2 h. The resulting solution was drained from the syringe and precipitated into cold diethyl ether. Peptides were then pelleted via centrifugation (2000 x g, 3 min at 4 °C). The supernatant was decanted.

RP-HPLC Purification of Peptides

Crude peptides were dissolved in a 50:50 mixture of 0.1% TFA in H_2O: acetonitrile. The crude solution was purified using a Dionex Ultimate 3000 RP-HPLC using a C-18 column. The identity of the purified peptides was determined using an Ab-Sciex 5800 MALDI-TOF/TOF Mass Spectrometer utilizing α-cyano-4-hydroxycinaminic acid matrix). The purity of fraction was confirmed by analytical RP-HPLC (Dionex Ultimate 3000 RP-HPLC using a C-18 column). HPLC fractions containing product were collected and lyophilized.

Oxidation Reaction of Peptides

Synthesis of **TB-7**

TB-6 was dissolved in 600 µL of MeOH and 100 µL of H_2O_2. Reaction mixture was stirred at room temperature for 20 h. Reaction MeOH was removed through a stream of nitrogen. Crude mixture was then dissolved in 50% AcCN in H_2O (0.1% TFA) and purified via Dionex Ultimate 3000 RP-HPLC using a C-18 column.

Synthesis of **TB-8**

TB-6 was dissolved in 20 µL of MeOH and 80 µL of formic acid under water bath. 5 µL of performic acid was added to peptide solution. Reaction mixture was stirred for 2.5 h under water bath. Crude mixture was then diluted in 50% AcCN in H_2O (0.1% TFA) and purified via Dionex Ultimate 3000 RP-HPLC using a C-18 column.

1D ^{19}F NMR

All ^{19}F NMR spectra of peptides were obtained using a 470 MHz Bruker 500 Spectrometer with a 5 mm Prodigy TCI cryoprobe. Peptides were dissolved in 10% D_2O in H_2O. Spectra were acquired at acquisition time of 0.57 s, relaxation delay of 1 s, receiver gain of 183.

Cell Lines and Cell Culture

The human cancer cell lines, A549 and A431 cells were previously purchased from the the American Type Culture Collection (ATCC) and were validated via the STR fingerprinting service at the Cytogenetics and Cell Authentication Core (CCAC) in the Department of Genetics at MD Anderson Cancer Center. The cell lines were tested and certified as mycoplasma-free using PCR Mycoplasma Detection Kit (Applied Biological Materials Inc., Cat: G238). Raji cells were provided through the courtesy of the Wagner group (University of Minnesota). A549 and A431 cells were cultured in Dulbecco's Modified Eagle's Medium (DMEM) with 4.5 g/L glucose, L-glutamine, and supplemented with 10% fetal bovine serum (FBS), 100 U/mL penicillin, and 100 µg/mL streptomycin at 37 °C with 5.0% CO_2. Raji cells were cultured in Roswell Park Memorial Institute (RPMI) medium with L-glutamine and supplemented with 10% FBS, 100 U/mL penicillin, and 100 µg/mL streptomycin at 37 °C with 5.0% CO2.

Confocal Fluorescence Microscopy

100,000 A549 cells were plated into 35 mm µ-Dish in a total volume of 2 mL. Cells were incubated overnight at 37 °C till they reached 70% confluency. Media was aspirated and cells were rinse 2 times with DMEM media and were dosed with 500 nM fluorescent peptide samples in DMEM (0.5% DMSO). Cells were incubated for 60 minutes at 37°C and 5% CO_2 and followed with aspiration and rinsing 3 times with DPBS. Cells were fixed with 1 mL of 4% paraformaldehyde with light shaking for 10 min. Paraformaldehyde

was removed and cells were rinsed 3 times with PBS. 1 mL of 1 μg/mL Hoechst 34580 was added to the cells for nucleus stain with light shaking for 10 min. Hoechst was removed and cells were rinsed 3 times with DPBS. Cells were then imaged using Zeiss - Widefield & TIRF Microscopy.

Flow Cytometry

A549 cells were first trypsinized and 500,000 cells were added to each well of 12 wells plates. Appropriate amounts of peptides dissolved in DMEM (0.5% DMSO) were added to the cells to final concentration of 0 nM, 5 nM, 50 nM, 200 nM, 500 nM. Cells were incubated for 60 minutes at 37°C and 5% CO_2. After incubation, cells were recovered by pipetting and then were transferred to Eppendorf tubes and spun at 300 rpm for 5 min. Pellets were washed 3 times with DPBS and then resuspended in DPBS without filtration. FACS analysis was conducted on BD LSRFortessa™ X-20 Cell Analyzer at the University Flow Cytometry Resource (UFCR).

Protein Expression and Purification

E_1-DD-CVIA fusion proteins were produces in T7 Express competent E. *coli* cells. E. *coli* cell glycerol stock is provided through the courtesy of the Wagner group (University of Minnesota). The E. coli cells were cultured at 37 °C (250 rpm) to the point when the OD_{600} reached 0.6-0.8, and then the protein was expressed at 37 °C for 6 hours by the addition of IPTG (0.5 mM). Cells were centrifuged down. 40 mL of lysis buffer (50 mM phosphate, 300 mM NaCl, pH 7.4) and 40 mg phenylmethanesulfonyl fluoride (PMSF) were added to the cell pallet and stirred for 30 min at room temperature. Cells were then put on ice and sonicated in 30 second intervals followed by 60 seconds of cooling for a total of 12 minutes sonication time. The lysed cells were centrifuged at 100,000 x g for 30 minutes. The supernatant was filtered. Ni affinity purification was performed using a Ni HisTrap FF 5 mL column (GE Healthcare) on an AKTA Fast Protein Liquid Chromatography (FPLC) system by monitoring the absorbance at 280 nm. Proteins were eluted with a 0-100% gradient of wash buffer (50 mM phosphate, 100 mM NaCl, 40 mM imidazole, pH 7.4) and elution buffer (50 mM phosphate, 100 mM NaCl, 400 mM imidazole, pH 7.4) across 20 column volumes. The protein solution was buffer exchanged into PBS buffer (50 mM PBS, pH 7.4) using a HiPrep desalting column (GE Healthcare)

equilibrated with 1 column volume of buffer. Purified protein was analyzed by SDS-page electrophoresis and LC-MS using an Orbitrap Elite Hybrid Mass Spectrometer. The LC-MS data was analyzed by Thermo Scientific Protein Deconvolution.

Bioconjugation

1.4 μL of 32mM TCEP in pH 7.3 PBS buffer was added to 280 μL of 32 μM E_1-DD protein in pH 7.3 PBS buffer at 4°C. After 1 h, 1.9 μL of 23 mM of **Mal-TB-9** in DMSO was first added to 280 μL of pH 7.3 PBS buffer and then added to the E_1-DD protein solution. Bioconjugation was reacted at 4°C for 24 h. The reaction mixture was then purified through PD-10 desalting column (Sephadex G-25 resin). The protein was collected and concentrated. The bioconjugated proteins were characterized by SDS-page electrophoresis and LC-MS using an Orbitrap Elite Hybrid Mass Spectrometer. The LC-MS data was analyzed by Thermo Scientific Protein Deconvolution.

Cell-based ^{19}F NMR

A431 cells were first trypsinized and were then washed with DMEM for 3 times to inhibit trypsin completely. 10,000,000 cells were added to a 75 mL culture flask. Appropriate amount of fluorinated peptide was dissolved in DMEM (1% DMSO) and added to cells to final concentration of 2 μM. The A431 cells were incubated for 30 minutes at 37°C and 5% CO_2. After incubation, cells were recovered by pipetting and then were transferred to Eppendorf tubes and spun at 300 rpm for 5 min. Pellets were washed 2 times with DPBS and 1 time with L-15 medium (10% D_2O). Cells were resuspended with 150 μL of L-15 medium (10% D_2O) and transferred to 3 mm shigemi NMR tube. A ^{19}F NMR spectrum was obtained using a Bruker 600-MHz Avance NEO with CryoProbe 5-mm TCI cryoprobe. Spectra were acquired at 37°C with acquisition time of 0.005 s, relaxation delay of 3 s, and a receiver gain of 57.

A cell leakage check was followed with the sample being centrifuged down and supernatant was transferred to another 3 mm shigemi NMR tube. A ^{19}F NMR spectrum was obtained using a Bruker 600-MHz Avance NEO with CryoProbe 5-mm TCI cryoprobe. Spectra were acquired at 37°C with acquisition time of 0.005 s, relaxation delay of 3 s, receiver gain of 57.

3.4.3 Supplement Figures

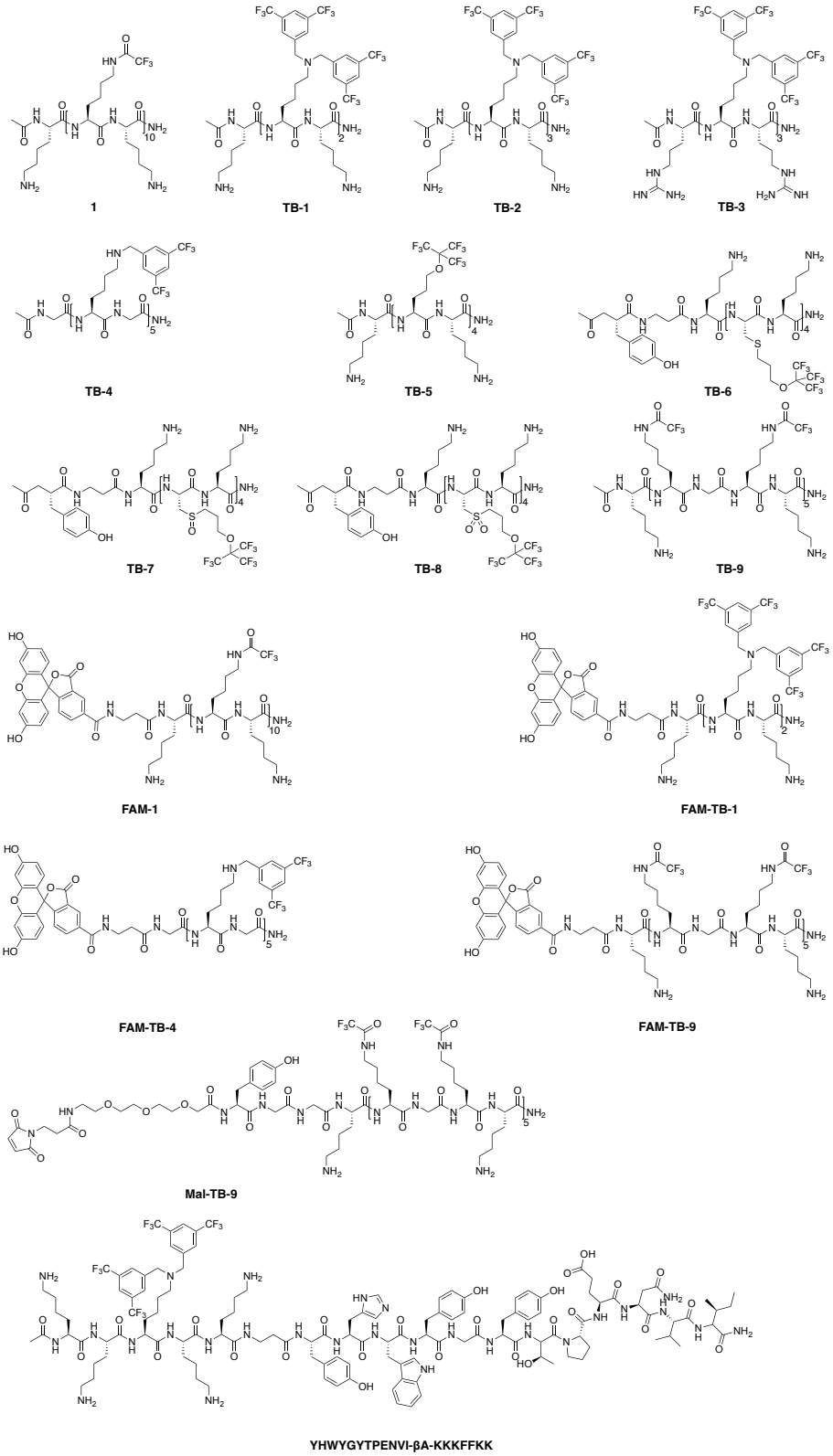

Figure 3-15. Structures of all peptides concerned in this work.

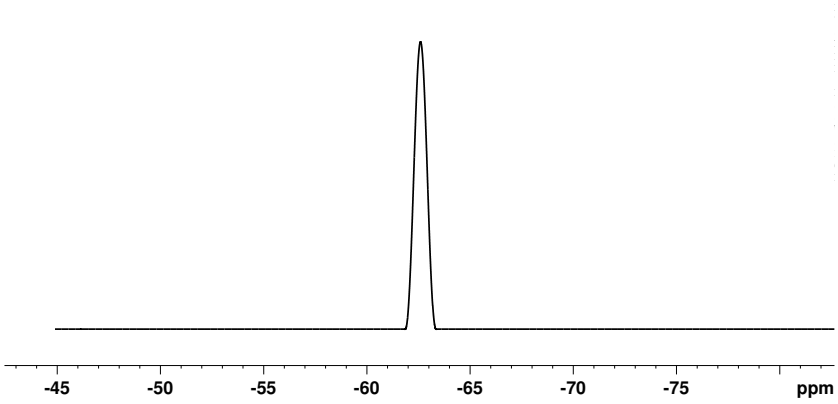

Figure 3-16. Full spectrum of cell-based ^{19}F NMR experiment (number of scans of 1000).

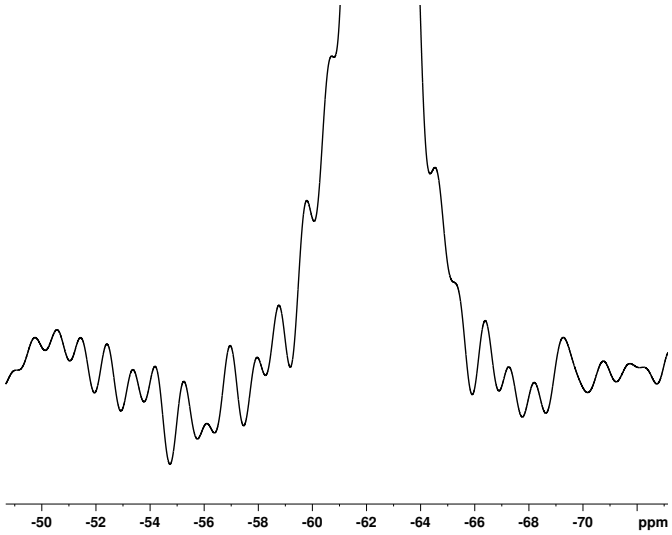

Figure 3-17. Expanded spectrum of cell-based ^{19}F NMR experiment (number of scans of 1000). Baseline noise is shown here demonstrating the high signal to noise.

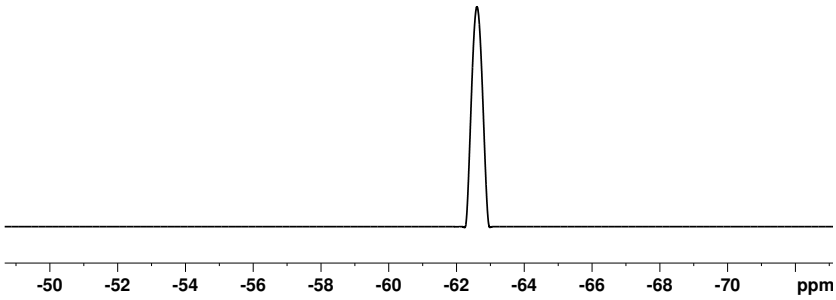

Figure 3-18. Full spectrum of cell-based ^{19}F NMR experiment (number of scans of 50).

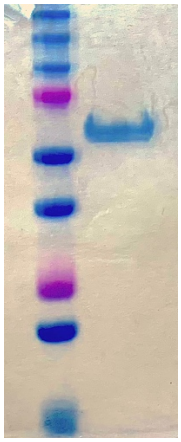

Figure 3-19. SDS-PAGE gel of fluorinated protein complex with **Mal-TB-9** bioconjugated to E_1-DD.

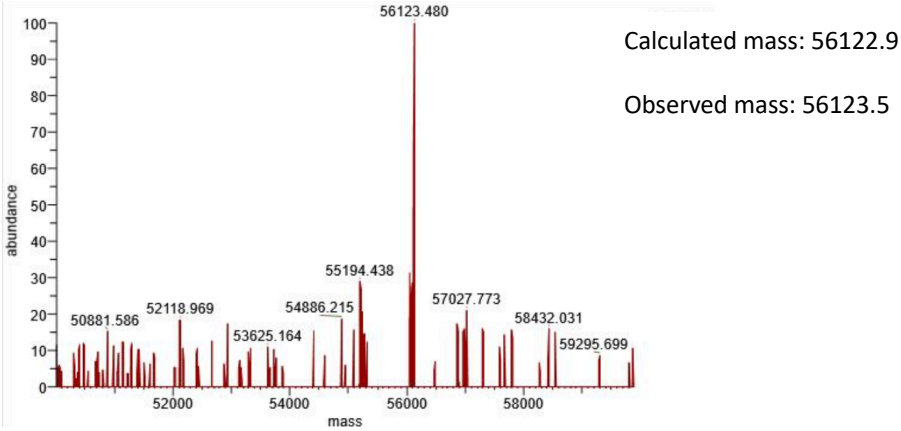

Figure 3-20. LC-MS spectrum of fluorinated protein complex with **Mal-TB-9** bioconjugated to E_1-DD.

E_1-DD protein was bioconjugated with **Mal-TB-9** and characterized by LC-MS.

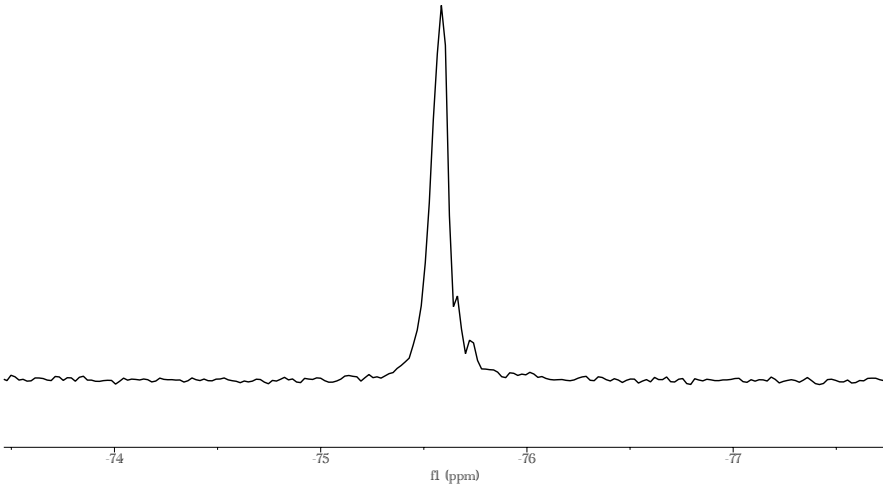

Figure 3-21. ^{19}F NMR spectrum of fluorinated protein complex with **Mal-TB-9** bioconjugated to E_1-DD. Bioconjugated E_1-DD protein showed a single resonance with a half-width of 44.5 Hz.

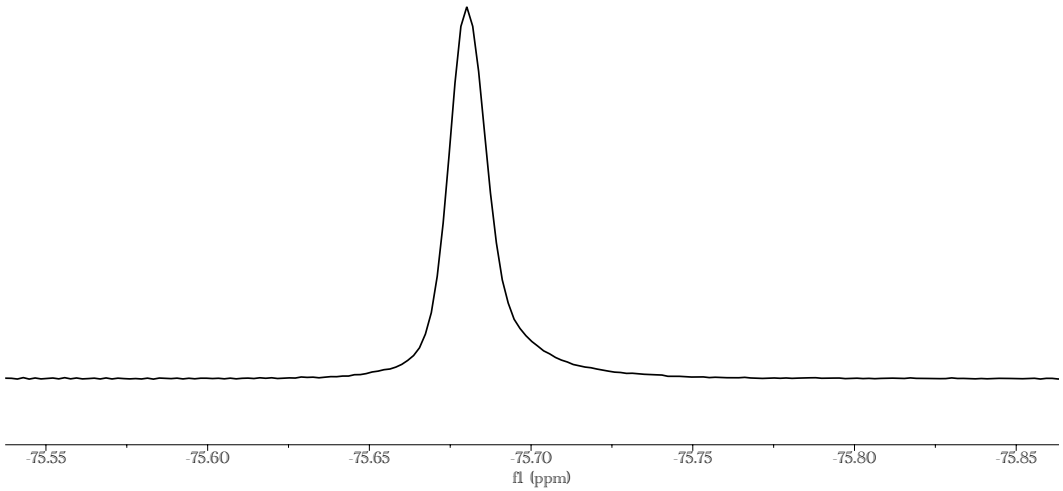

Figure 3-22. ^{19}F NMR of **1** (470 MHz, 10% D_2O, 90% H_2O).

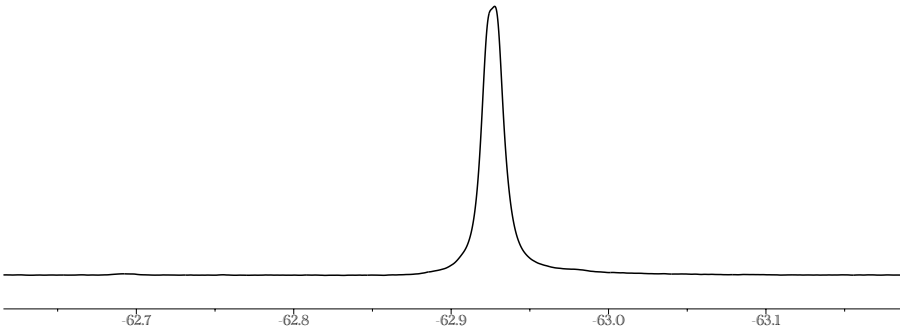

Figure 3-23. ^{19}F NMR of **TB-1** (470 MHz, 10% D_2O, 90% H_2O).

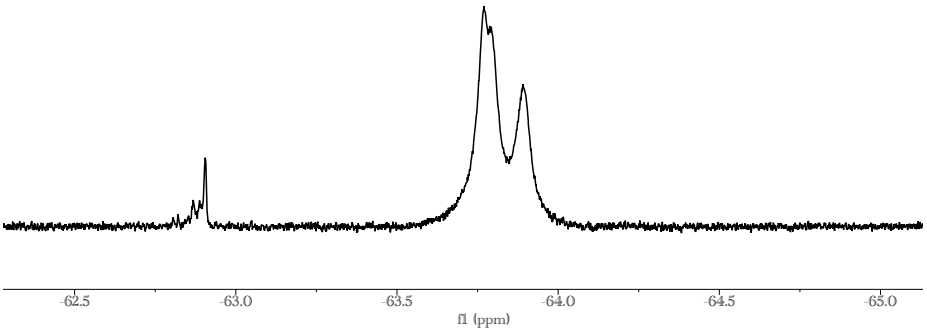

Figure 3-24. ^{19}F NMR of **TB-2** (470 MHz, 10% D_2O, 90% H_2O).

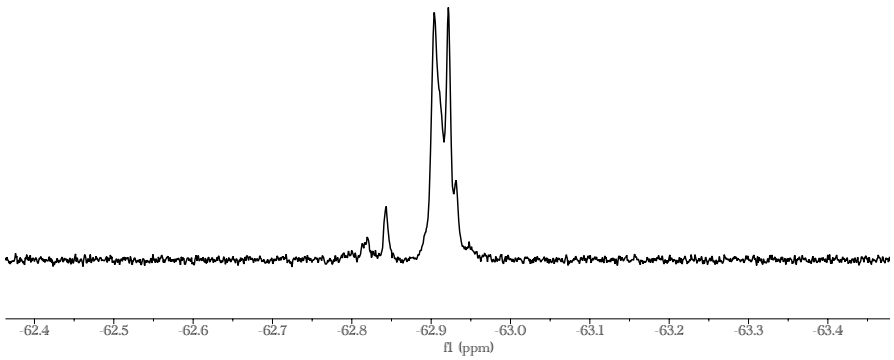

Figure 3-25. ^{19}F NMR of **TB-3** (470 MHz, 10% D_2O, 90% H_2O).

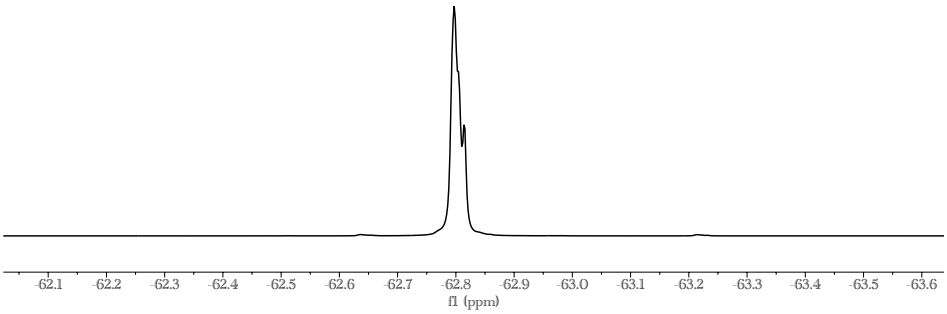

Figure 3-26. ^{19}F NMR of **TB-4** (470 MHz, 10% D2O, 90% H2O).

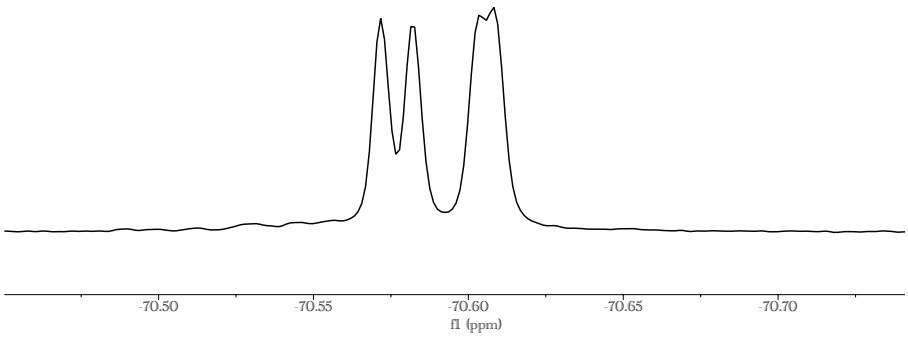

Figure 3-27. ^{19}F NMR of **TB-5** (470 MHz, 10% D_2O, 90% H_2O).

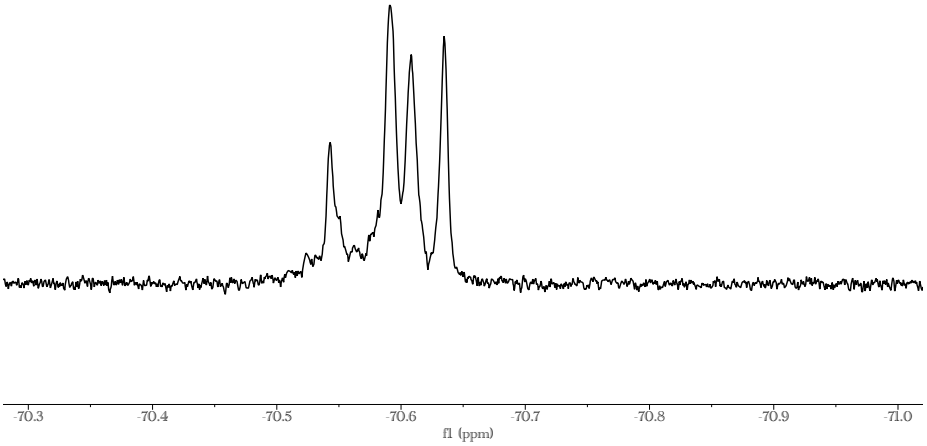

Figure 3-28. ^{19}F NMR of **TB-6** (470 MHz, 10% D_2O, 90% H_2O).

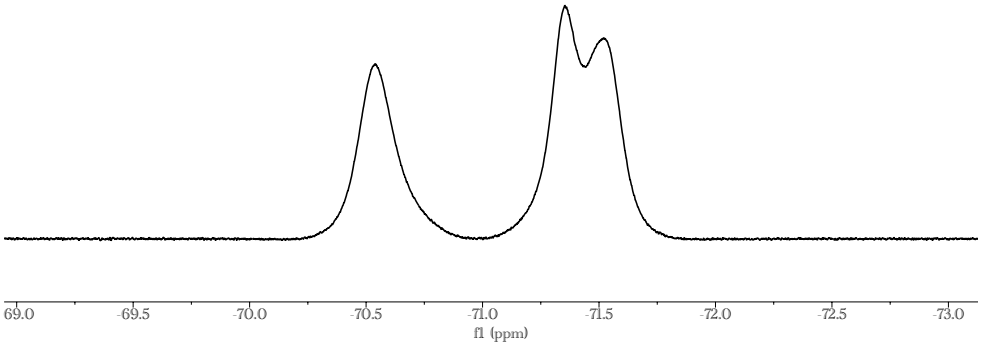

Figure 3-29. ^{19}F NMR of **TB-7** (470 MHz, 10% D_2O, 90% H_2O).

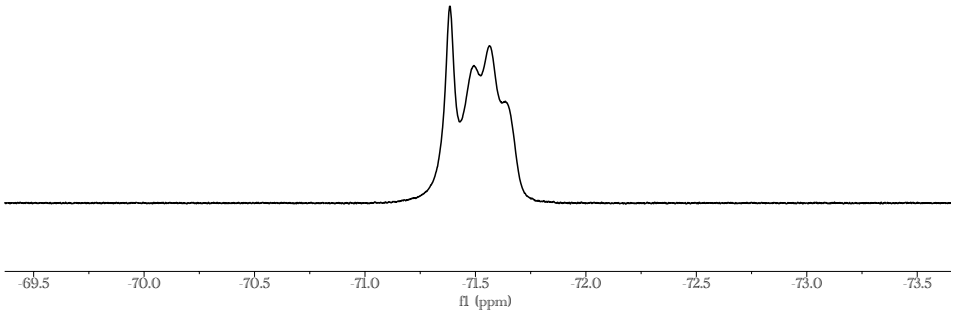

Figure 3-30. ^{19}F NMR of **TB-8** (470 MHz, 10% D_2O, 90% H_2O).

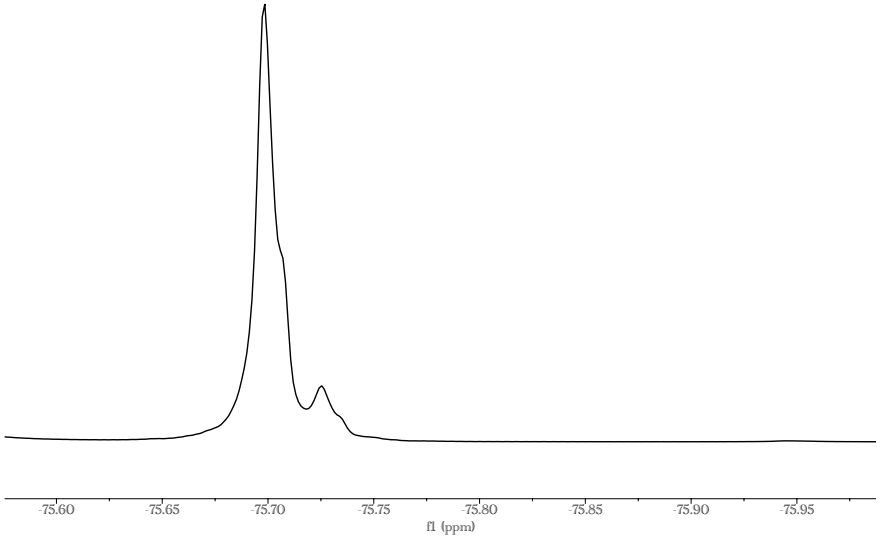

Figure 3-31. ^{19}F NMR of **TB-9** (470 MHz, 10% D_2O, 90% H_2O).

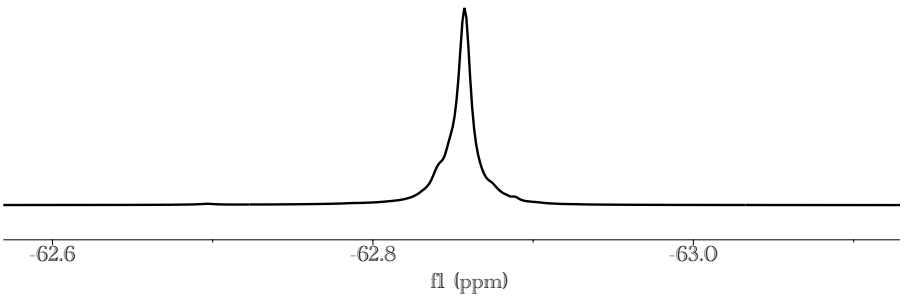

Figure 3-32. ^{19}F NMR of fluorinated peptide KKK^{FF}KK$^{\beta}$AYHWYGYTPENVI (470 MHz, 10% D_2O, 90% H_2O). Peptide showed a single resonance with a half-width of 4.8 Hz

Chapter 4

Multivalent Highly-Fluorinated-Peptide-Bioconjugated Nanorings for On-Cell ^{19}F NMR

'Multivalent Highly-Fluorinated-Peptide-Bioconjugated Nanorings for On-Cell ^{19}F NMR'

Jiaqian Li, Yiao Wang, Mark. D. Distefano, Carston R. Wagner, and William C. K. Pomerantz

In preparation

Motivation for Research

The motivation of this work was based on the progress made in chapter 3. While the fluorinated peptide-bioconjugated E_1-DD constructed showing a desired single resonance in ^{19}F NMR in aqueous solution, very limited signal was able to be observed in cell-based ^{19}F NMR experiments. In this work, I investigated the factors resulting in the limited signal and attempted to recover the signal through structural engineering on the construct. In addition, to further improve the fluorine content, the bioconjugated E_1-DD was assembled into multivalent nanoring for signal amplification. I was also interested in whether the construct can be imaged in phantom ^{19}F MRI.

4.1 Introduction

Molecular imaging enables the visualization, characterization, and quantification of biological events at the cellular and molecular level.[1] While conventional medical imaging focuses on diagnosis, surgical guidance, and treatment monitoring, molecular imaging shows great potential for early and specific disease detection, as well as efficient and rational therapeutic drug development.[2] Among the molecular imaging modalities, magnetic resonance imaging (MRI) possesses high spatial and temporal resolution,[3] excellent soft tissue contrast,[4] non-invasiveness, and avoids ionizing radiation.[5] However, the inherent low sensitivity is the primary weakness of MRI. Considerable efforts have been made including creating hyperpolarized states,[6] optimizing radiofrequency detectors,[7,8] improving data processing approaches,[9,10] and developing new imaging agents.[11] Development of paramagnetic contrast agents is one strategy used to improve sensitivity by affecting the relaxation leading to improved contrast and reduced scan times. However, under standard clinical MRI techniques, administration of a high concentration of lanthanide contrast agents is required (e.g., 469 mg/mL for MAGNEVIST®). In addition, environmental concerns of gadolinium contrast agents have been raised as an emerging microcontaminant.[12] Incomplete clearance and cumulative deposits in brain and other tissues in healthy subjects have also been reported, [13–15] which raises concerns over toxicity.

One complimentary strategy to overcome the low sensitivity is the development of the ‘hot spot’ or ‘second color’ imaging using heteronuclear MRI atoms. Highly fluorinated molecules have been gaining

increasing interest for imaging applications.[16] ^{19}F has favorable properties including a 100% natural abundance, a sensitivity close to ^{1}H, and trace amount of mobilized ^{19}F present in the human body.[16] The limited detectable endogenous ^{19}F gives rise to minimal background signal, leading to high contrast and enabling quantitative analysis.

^{19}F MRI-based molecular imaging suffers an inherent low sensitivity, where a millimolar range for tissue concentration of a ^{19}F MRI molecular tracer is required for in vivo detection, thus requiring highly fluorinated imaging agents.[17] A ^{19}F MRI molecular tracer for molecular imaging is composed of a fluorinated imaging agent and a targeting agent. Significant efforts have been made to improve the sensitivity of ^{19}F MRI. Besides enhancing the magnetic field, data processing,[9,10] and optimizing pulse sequences,[18] developing more tailored ^{19}F MRI imaging agents also plays an important part in boosting sensitivity. An ideal ^{19}F MRI imaging agent has the properties of a high fluorine content, a single dominant resonance in the ^{19}F NMR spectrum, and favorable relaxation parameters.[19] ^{19}F MRI imaging agents can be grouped into several categories: perfluorocarbon liquids (PFCs), fluorinated polymers, and small molecules. PFCs have high fluorine content with high fluorine weight percentage (wt%). However, for imaging applications, the significant hydrophobicity of PFCs requires the use of nanoemulsions, which are susceptible to droplet heterogeneity, limited biocompatibility, and environmental concerns.[16,20,21] Fluorinated polymers, offer more flexibility in choices of building blocks, have tunable biocompatibility, versatile functionality, and aqueous solubility which make nanoemulsion-free options possible.[22] However, fluorinated polymers tend to have multiple resonances in the ^{19}F NMR spectra, although not always the case, and therefore are susceptible to undesired chemical shift artifacts in ^{19}F MRI. Moreover, it is often difficult to possess high fluorine content to reach the detection limit and at the same time maintain favorable relaxation parameters and aqueous solubility.[22,23]

Fluorinated peptides are complementary strategies to fluorinated polymers. Fluorinated peptides with their versatility in choice of amino acids, feature precise sequence-defined structures and highly tunable biocompatible properties. Previously, our group reported a new class of highly fluorinated peptides as ^{19}F MRI imaging agents. Composed of N-ε-trifluoroacetyllysine (K^{TFA}) and lysine in an alternating pattern, these peptides possessed high aqueous solubility and a single degenerate signal. One weakness of our fluorinated peptides was the low detection limit in a phantom MRI experiment. To overcome the low sensitivity, in later work, we prepared several amino acids with increased fluorine content and incorporated them into shorter

peptides of increased ^{19}F wt%. Subsequently, we observed non-specific binding of our lead peptides to cancerous cells which was removed through sequence modification. However preliminary cell-based experiments using protein-based molecular imaging constructs showed limited signal, indicating the need to further improve the sensitivity.

Multivalency is one strategy to improve the fluorine content of ^{19}F MRI imaging agent to improve the sensitivity. Commonly seen in dendrimers, the multivalent construct, with well-defined, repeating branched polymeric chains emanating from a central core, allows the incorporation of more fluorine atoms.[24] The highly symmetric structure also leads to a single resonance.[25] However, dendrimers require long syntheses and their large size can lead to concerns over clearance.[16] Chemical self-assembly nanorings (CSANs) are alternative multivalent constructs suitable for ^{19}F MRI molecular tracer design. CSANs formed through oligomerization of dimeric dihydrofolate reductase (DD) with a bis-methotrexate (bisMTX) ligand possess an average size distribution of an octameric ring .[26] CSANs can be further functionalized through fusing various binding moieties to the DD subunits (e.g. **Fig. 1**). In addition, CSANs can be disassembled by treatment with the FDA-approved antibiotic, trimethoprim, facilitating clearance.[27]

Here we studied the cellular interaction of our previously reported ^{19}F MRI molecular tracer, composed of E_1-DD and a lead fluorinated peptide. Structural modification and the subsequent cellular studies on the molecular tracer revealed a balance of fluorine content and binding affinity toward EGFR-expressing cells for optimal tracer design. The lead monomeric molecular tracer was then assembled into the octameric CSAN. Optimal spectral performance and EGFR-specific binding affinity were successfully maintained. In a final cell-based ^{19}F NMR experiment. Through manipulating the cellular internalization, our optimized fluorine-labeled CSAN exhibited an amplified signal with highly favorable spectral parameters compared with its monomeric moiety.

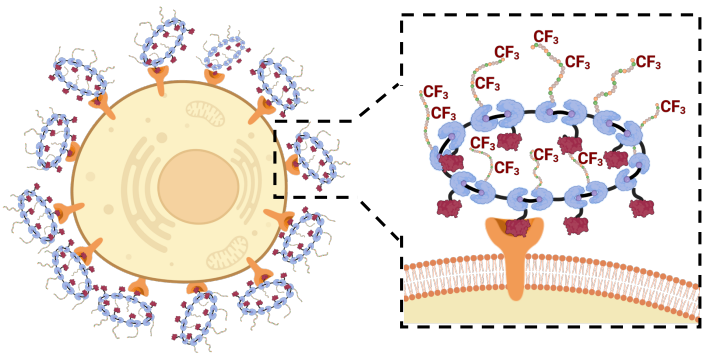

Figure 4-1. Illustration of fictionalized CSANs for ^{19}F MRI molecular imaging. Functionalized CSANs are composed of a protein-specific targeting agent and fluorinated peptide imaging agent. Binding of the targeting agent to biomarkers allows for molecular imaging with high specificity.

4.2 Results and Discussion

In our previous studies, a prototype protein complex **RTC-1** was prepared as a ^{19}F MRI molecular tracer (**Fig. 2A**). **RTC-1** was composed of an EGFR-targeting E_1-DD fusion protein containing a 4-residue C-terminal cysteine containing sequence, CVIA. While previous research has used this recognition motif for enzyme-mediated farnesylation reactions,[27] due to the single cysteine in the entire protein, we elected to conduct a bioconjugation reaction with a maleimide terminated highly fluorinated, peptide 1 (**Fig. 4-2**). **RTC-1** led to a favorable ^{19}F NMR spectrum, for which a single degenerate signal was observed with a narrow resonance with a full width half maximum (FWHM) of 54 Hz was obtained (**Fig. 4-3B**). However, in preliminary cell-based ^{19}F NMR experiment, very limited signal was observed where **RTC-1** was incubated with high-EGFR expressing A431 epidermoid carcinoma cells. Our working hypothesis at the time was that the fluorine content of the cellular sample was not high enough to be detected by ^{19}F NMR requiring higher fluorine labeling, or the dynamics associated with being attached to the cell surface or internalization was leading to unfavorable resonance broadening. A third hypothesis was that the peptide bioconjugation was perturbing the affinity of the protein construct for EGFR. To help address these questions, a systematic cellular interaction study would be needed to help improve our designs.

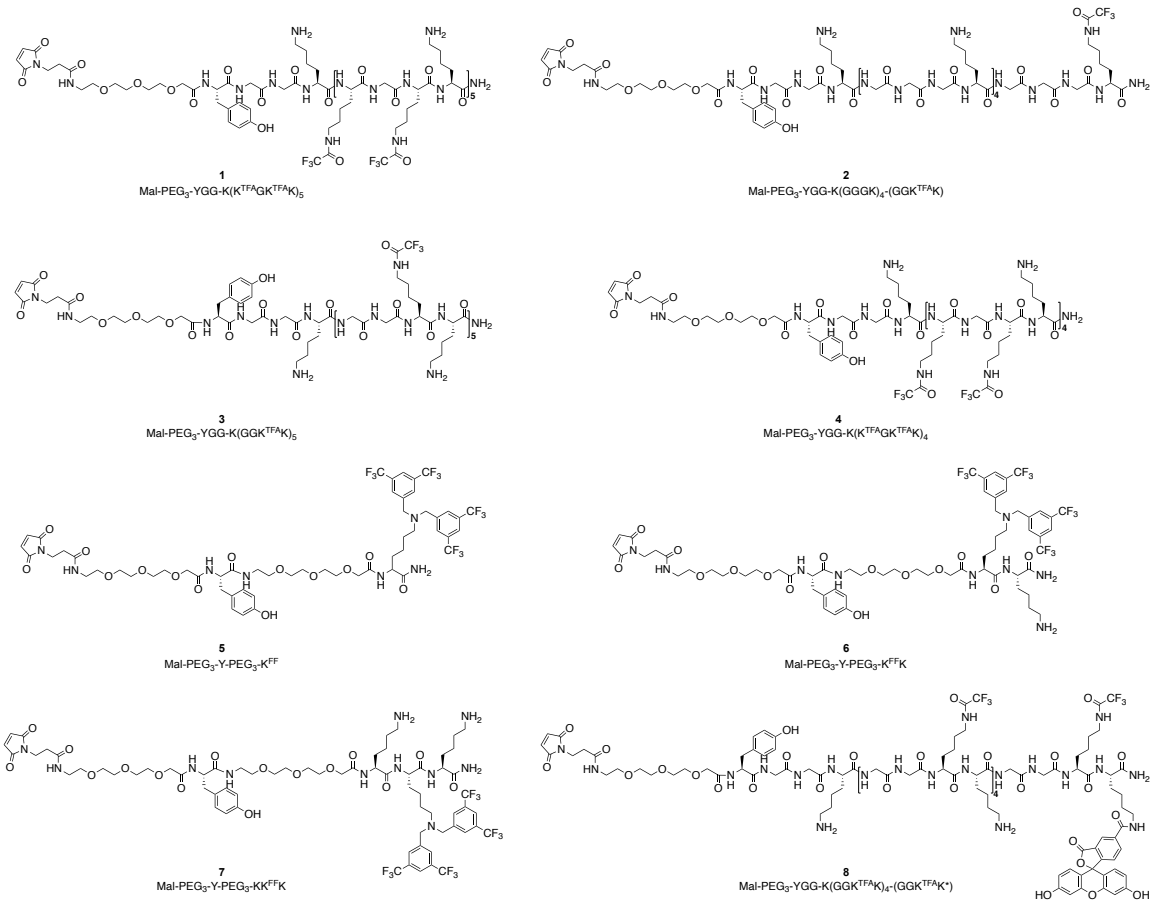

Figure 4-2. Structures of peptides used in bioconjugation to E_1-DD.

A)

Name	Sequence	^{19}F Content	K_d (nM)
RTC-1	E_1-DD-PEG_3-YGG-K($K^{TFA}GK^{TFA}K)_5$	30	2028
RTC-2	E_1-DD-PEG_3-YGG-K$(GGGK)_4$-$(GGK^{TFA}K)$	3	140
RTC-3	E_1-DD-PEG_3-YGG-K$(GGK^{TFA}K)_5$	15	188 ± 50.6
RTC-4	E_1-DD-PEG_3-YGG-K($K^{TFA}GK^{TFA}K)_4$	24	3158
RTC-5	E_1-DD-PEG_3-Y-PEG_3-K^{FF}	12	145
RTC-6	E_1-DD-PEG_3-Y-PEG_3-$K^{FF}K$	12	352
RTC-7	E_1-DD-PEG_3-Y-PEG_3-$KK^{FF}K$	12	306

B)

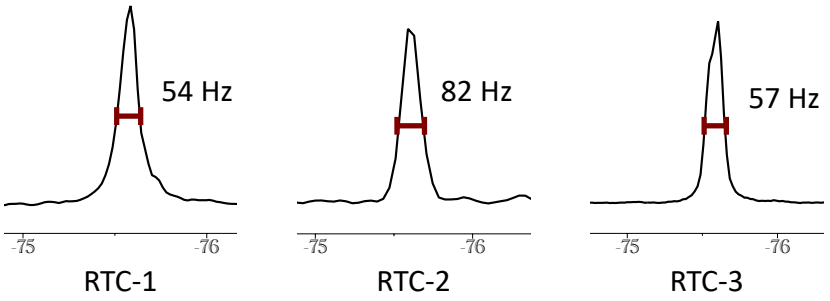

Figure 4-3. Structures and spectra of bioconjugated E_1-DD complex. A) Structures of E_1-DD complex composed of highly fluorinated peptides with fluorine contents, and binding affinities to A549 cells. B) ^{19}F NMR spectra of selected best-performing bioconjugated E_1-DD complex **RTC-1**, **RTC-2**, and **RTC-3.**

Using previously prepared **RTC-1,** binding affinity studies were first performed using flow cytometry to evaluate the functional effects from fluorinated peptide bioconjugation on interacting with high EGFR-expressing A549 cells. Compared with the parental E_1-DD with a measured K_d of 103 nM (**Fig. 4-4**), The affinity of **RTC-1** was determined to be 15-fold weaker ($K_d = 2.03 \times 10^3$ nM), (**Fig 4-5**). With a significantly reduced binding affinity, the initial concentration of **RTC-1** (500 nM) in the cell-based ^{19}F NMR experiment could be one reason for the limited observed signal.

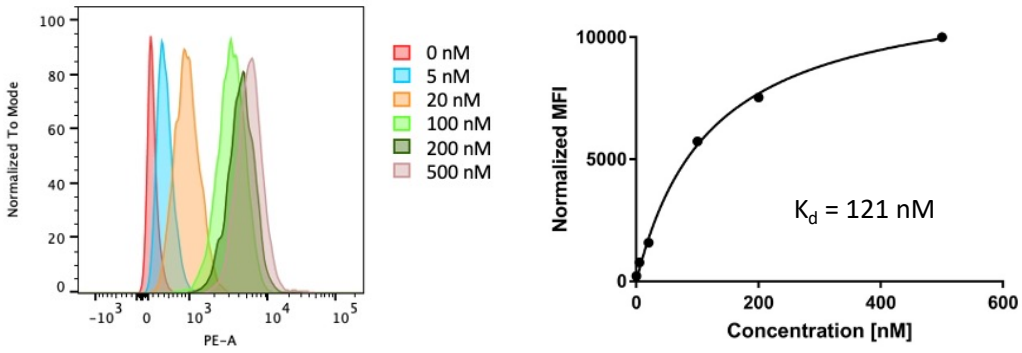

Figure 4-4. Affinity determination of E_1-DD to A549 cells through flow cytometry. Left: binding histogram. Right: binding curve.

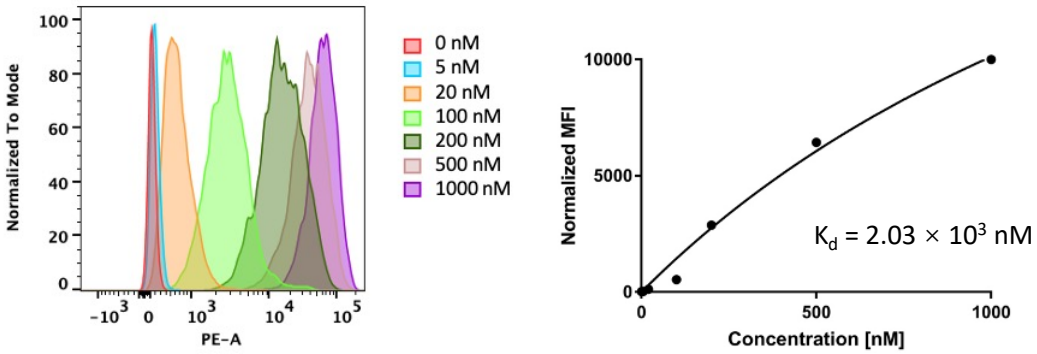

Figure 4-5. Affinity determination of **RTC-1** to A549 cells through flow cytometry. K_d measured as 2.03 × 10^3 nM. Left: binding histogram. Right: binding curve.

In an attempt to recover the binding affinity, structural modification on **RTC-1** was performed. High fluorination has a tendency to alter the biophysical and physiochemical properties of modified molecules.[28] As such, the bioconjugation with highly fluorinated peptide **1** may, as a result, interfere with the binding characteristics of E_1-DD to A549 cells. Hence, we modified the structures of peptide **1** where the number of K^{TFA} residues were reduced and replaced with glycine. Three maleimide terminated peptides **2**,**3**, and **4** were synthesized with the total fluorine content being reduced to 3, 15, and 24, respectively (**Fig. 4-2**). The charges on the peptides' side chain remained unchanged to favor aqueous solubility and to promote the unfold state,

and to minimize the non-specific binding as previously described in Chapter 3. The alternating pattern of K^{TFA} peptide **1** was also maintained to favor the signal degeneracy in the ^{19}F NMR spectrum. These three peptides were bioconjugated to E_1-DD individually to form **RTC-2**, **RTC-3**, and **RTC-4** (**Fig. 4-3A**) through thiol-maleimide reactions. Size exclusive chromatography (SEC) was used to remove unreacted peptide and the success in bioconjugation was confirmed by both LC-MS and SDS-PAGE gel analysis.

^{19}F NMR was performed on those structurally modified proteins to ensure an optimal spectral performance prior to the nanoring assembly. **RTC-2**, **RTC-3**, and **RTC-4** each showed a single degenerate resonance with FWHM of 82 Hz, 57 Hz, and 47 Hz, respectively (**Fig. 4-3B**). The highly overlapping resonances is favored, which avoids the undesired chemical shift artifact and gives rise to a high signal for future ^{19}F MRI applications. The spectral performance also reflects the high flexibility of the peptide construct, where a degenerate resonance with acceptable FWHM was maintained after being bioconjugated to a bulky E_1-DD of 52 KDa. These results support the use of sequence-defined peptides for other molecular imaging application.

Binding affinity studies were conducted on the three modified proteins using flow cytometry. Encouragingly, both **RTC-2** and **RTC-3** had their binding affinities maintained close to the parental E_1-DD, with the K_d being measured of 140.2 nM and 188.9 ± 50.6 nM respectively (**Fig. 4-6 and 4-7A**). However, **RTC-4**, despite a lower fluorine content (24 ^{19}F) than **RTC-1** (30 ^{19}F), showed a similar K_d to **RTC-1** of 3160 nM (**Fig**. **4-8**). The affinity studies indicated that, for the E_1-DD protein complex to retain a good affinity to EGFR-expressing cells, a fluorine content of 15 fluorine atoms is optimal for this particular peptide sequence. Intermediate fluorine content with 1 to 2 additional K^{TFA} may also prove beneficial but were not evaluated in this case.

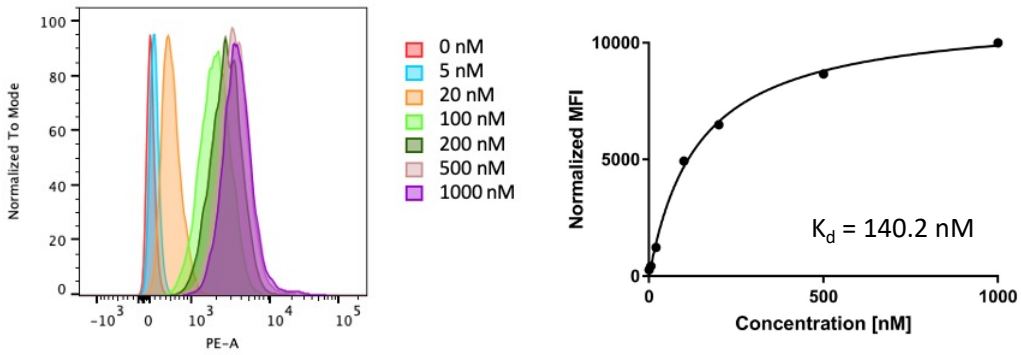

Figure 4-6. Affinity determination of **RTC-2** to A549 cells through flow cytometry. K_d measured as 140.2 nM. Left: binding histogram. Right: binding curve.

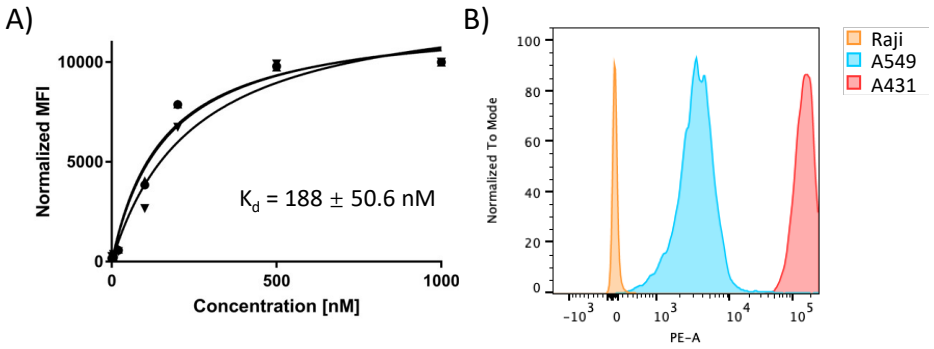

Figure 4-7. Binding characteristics of **RTC-3**. A) Binding affinity determination of **RTC-3** to A549 cells using flow cytometry. K_d measured as 188 ± 50.6 nM (n=3). B) Binding specificity experiment of **RTC-3**. Flow cytometry result showed that **RTC-3** bound selectively to A431 cells over A549 cells with limited binding to Raji cells.

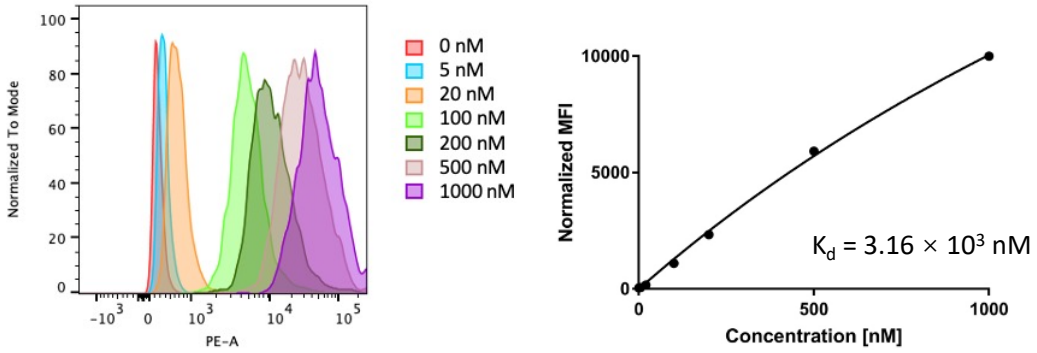

Figure 4-8. Affinity determination of **RTC-4** to A549 cells through flow cytometry. K_d measured as 3.16 × 10^3 nM. Left: binding histogram. Right: binding curve.

Binding specificity of the best performing **RTC-3** to EGFR-expressing cells was then assessed with flow cytometry. Three cell lines with different EGFR-expressing levels were chosen, A431 cells (~ 2 x 10^6 copies per cell), A549 cells (~ 0.1 x 10^6 copies per cell), and non-EGFR-expressing Raji cells. **RTC-3** bound selectively to A431 cells over A549 cells with limited binding to Raji cells (**Fig. 4-7B**).

To gain further insight into the cellular interaction between bioconjugated proteins and EGFR-expressing cells, confocal fluorescence microscopy was carried out. **RTC-3** was selected for fluorescent imaging due to its good binding affinity, desired spectral performance, and the highest fluorine content. To enable confocal imaging, peptide **8**, an analog of peptide **3**, was synthesized where the lysine of peptide 3 at the C-terminus was replaced with (5-FAM)lysine (**Fig. 4-2**). Fluorescein-tagged **RTC-3*** was prepared through bioconjugation of peptide **8** to E_1-DD. After incubation with A549 cells, **RTC-3*** was shown to bind to A549 cells and internalize. Punctate patterns were observed, indicating active uptake of **RTC-3*** into A549 cells (**Fig. 4-9**). The fast rate of internalization of **RTC-3*** is anticipated to help accumulate the fluorinated protein construct for MRI imaging instead of being limited to the number of receptors on the cell surface if the protein complex can only bind to the cell membrane receptor.

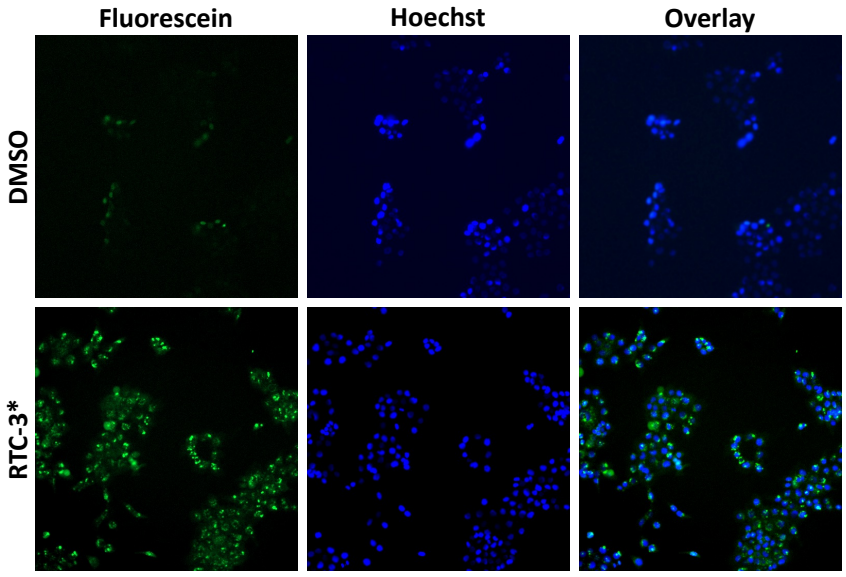

Figure 4-9. RTC-3* internalization into A549 cells and binding specificity toward different cells. Fluorescent microscopy of **RTC-3*** with A549 cells. Punctate pattern indicates the internalization of **RTC-3*** into A549 cells. In the DMSO control, background fluorescence was limited and localized in the nucleus.

Extrapolating from the studies on **RTC-1** and the subsequent modification, we next attempted to discover more bioconjugated E_1-DD proteins containing other fluorinated amino acids. Previously, we reported a molecular tracer, which was composed of an EGFR-targeting peptide moiety and a short K^{FF}-containing peptide as the imaging agent. A single degenerate signal was observed, and high SNR was obtained with 50 scans in the cell-based ^{19}F NMR experiment. However, this molecular tracer suffers a broad resonance (397 Hz), which hampers the sensitivity in future ^{19}F MRI application. Three K^{FF}-based peptides, **5**,**6**, and **7**, were synthesized which differed in the number of lysine residues. Only one K^{FF} was incorporated into each peptide to keep the fluorine content under 15 ^{19}F (**Fig. 4-2**). A PEG_3 linker was also incorporated into those peptides, as the spacer for additional flexibility to favor signal degeneracy and to improve the aqueous solubility. Three peptides were bioconjugated to E_1-DD individually to form **RTC-5**, **RTC-6**, and **RTC-7**. (**Fig. 4-3A**)

Binding studies were performed to assess any potential functional perturbation of the proteins. Compared with parental E_1-DD, **RTC-5** had a similar affinity of 144 nM (**Fig. 4-10A**) while both **RTC-6** and **RTC-7** showed slightly higher affinities of 352 nM and 306 nM (**Fig. 4-10B and 4-10C**) respectively.

In the context of the ^{19}F NMR spectral performance, none of the proteins maintained the signal degeneracy and resonances were spread from 192 Hz to 1290 Hz. While a lack of a signal resonance was surprising, the poor spectral performance may be due to the interaction between the bis(trifluoromethyl)benzyl groups on the K^{FF} side chain and protein surface of E_1-DD where rotation of the bis(trifluoromethyl)benzyl groups may be hindered and leading to multiple observable conformational states on the NMR timescale.

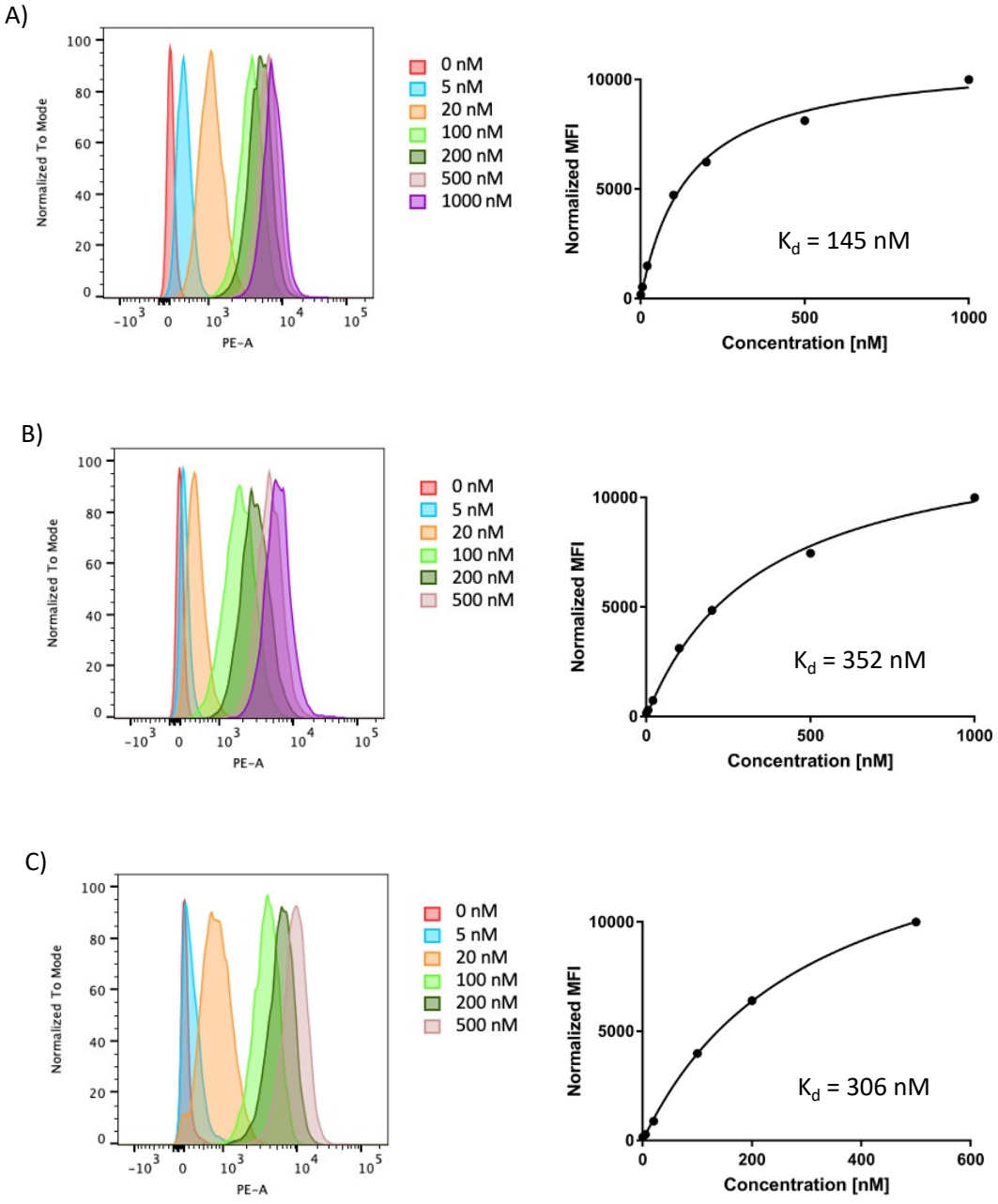

Figure 4-10. Affinity determination A549 cells through flow cytometry. Left: binding histogram. Right: binding curve. A) binding if **RTC-5** to A549 cells. K_d was measured 352 nM. B) binding if **RTC-6** to A549 cells. K_d was measured 145 nM. C) binding if **RTC-7** to A549 cells. K_d was measured 306 nM.

To further increase the fluorine content for higher sensitivity, the best performing protein, **RTC-3**, was selected to be engineered into a multivalent nanoring. **RTC-3** was incubated with a chemical dimerizer, bis-methotrexate (bis-MTX) for 30 min to form the nanoring **η-RTC-3** (**Fig. 4-11A**) as similarly reported by Wang et al.[27] Formation of the nanoring was characterized by SEC where a complex of larger size was eluted at 16 min (**Fig. 4-11B**). Compared with the parental octameric nanoring, **η-RTC-3** had a similar retention time in SEC (16.0 min vs 16.5 min), indicating the formation of the nanoring of comparable size. The protein assembly was further confirmed by dynamic light scattering (DLS) with a hydrodynamic radius of 20 ± 1.7 nm (**Fig. 4-11C**) close to 18.1 nm of the parental nanoring and thus consistent with the average octameric oligomeric size as previously reported. However, we attribute the slightly earlier retention and larger hydrodynamic radius, to the extra size from the bioconjugated peptides. With the assembly into an average octameric CSAN, the fluorine content of **η-RTC-3** was boosted to 120 ^{19}F, 8-fold over the fluorine content of **RTC-3**.

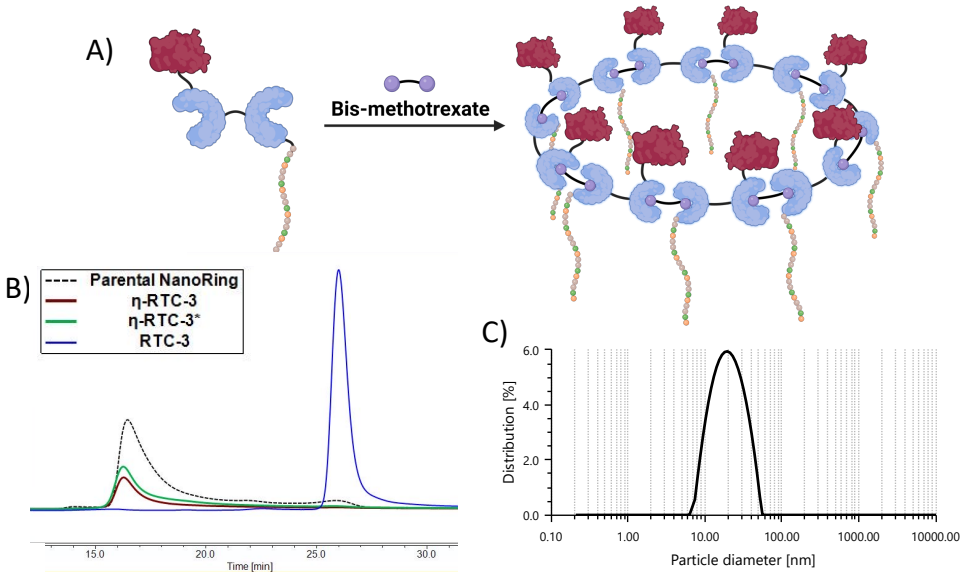

Figure 4-11. Formation of CSANs and characterizations. A) CSANs were assembled from the fluorinated peptide-bioconjugated E_1-DD in the presence of bis-MTX. B) SEC spectrum of the CSANs with the blue curve representing **RTC-3** monomer, maroon curve representing **η-RTC-3**, green curve representing **η-RTC-3***, and the dotted curve representing the unbioconjugated parental CSAN. Both **η-RTC-3** and **η-RTC-**

3* showed similar retention time to parental CSAN with no monomer peaks. C) The hydrodynamic diameter determination of **η-RTC-3** using DLS with a D_H of 20 ± 1.7 nm.

After confirming the CSAN assembly, both cellular binding and NMR performance were assessed prior to ensure **η-RTC-3** was suitable for cell-based imaging studies. Spectral analysis was carried out with ^{19}F NMR where two partially overlapped resonances were observed with a FWHM of 178 Hz (**Fig. 4-12A**). We attribute the increase in FWHM of **η-RTC-3** relative to the monomer due to a decreased tumbling rate of the larger nanoring assembly. The partial loss in signal degeneracy may be due to different spatial orientations of the fluorinated peptides within the nanoring.

Cellular binding studies towards A549 cells were examined through flow cytometry and confocal fluorescence microscopy. The affinity of **η-RTC-3** was determined to be 168 ± 42.2 nM (Fig. **4-12B**), close to the affinity of the monomeric **RTC-3**, 188.9 ± 50.6 nM, indicating a well maintain of the high affinity towards A549 cell after nanoring assembly. To note, the affinity determined (**Fig. 4-12B**) was based on the monomeric dissociation constants $K_{d,1}$, and the affinity of the nanoring **η-RTC-3**, $K_{d,N}$ was determined to be 2.6 ± 0.66 nM, based on the equation as previously reported[29] where valency of the octameric nanoring here was set to eight.

$$\text{Apparent } K_{d,\text{N}} = \frac{K_{d,1}}{Valency^2}$$

With **η-RTC-3** showing a very similar binding profile as **RTC-3** to A549 cells, binding specificity between the high EGFR-expressing A431 cells and non-EGFR-expressing cells were examined. As expected, **η-RTC-3** showed a selective binding to A431 cells, while very limited binding to Raji cells was observed (**Fig. 4-12C**). Binding affinity and selectivity towards high EGFR-expressing cells was maintained, similar to the monomeric construct. These results demonstrated the competence of **η-RTC-3** as a molecular tracer for cell-based imaging studies.

The binding characteristics of **η-RTC-3** towards EGFR over-expressing cells was also investigated by confocal fluorescence microscopy. Nanoring **η-RTC-3*** was assembled from **RTC-3*** under the same conditions for **η-RTC-3** assembly. Octameric ring formation was confirmed by SEC where a similar

retention time to **η-RTC-3** was observed (**Fig. 4-13**). **η-RTC-3*** was next incubated with A431 cells. The binding of **η-RTC-3*** to A431 cells with the punctate pattern was again observed indicating **η-RTC-3*** shared a similar internalization characteristic as the monomeric **RTC-3*(Fig. 4-12D)**.

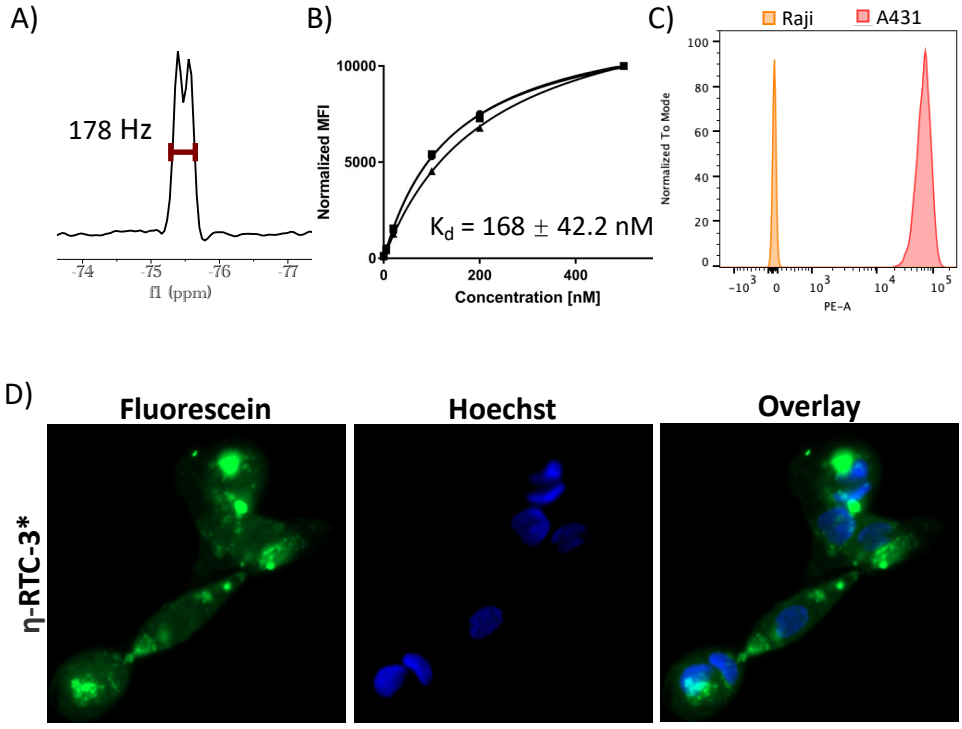

Figure 4-12. Spectrum and binding characterization of **η-RTC-3**. A) ^{19}F NMR spectrum of **η-RTC-3**. with FWHM of 178 Hz was observed. B) Binding affinity determination of **η-RTC-3** to A549 cells using flow cytometry. K_d measured as 168 ± 42.2 nM (n=3). C) Binding specificity experiment of **η-RTC-3**. Flow cytometry results showed that **η-RTC-3** bound selectively to A431 cells limited binding to Raji cells. D) Fluorescent microscopy of **η-RTC-3*** with A431 cells. Punctate pattern indicates the internalization of **η-RTC-3*** into A431 cells, while co-staining shows a limited amount of **η-RTC-3*** entered the nuclei.

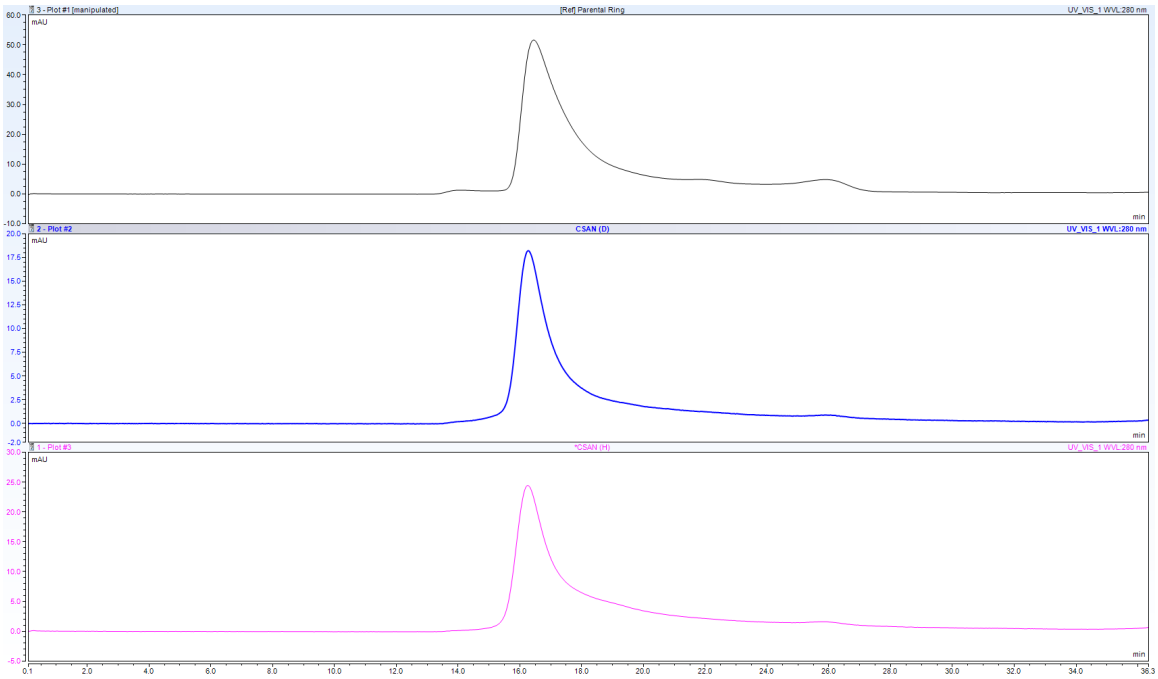

Figure 4-13. Stacked size exclusion chromatography of nanoring **η-E$_1$** (Top), **η-RTC-3** (Middle), **η-RTC-3*** (Bottom).

With nanoring **η-RTC-3** possessing high cellular affinity and selectivity, a cellular internalization characteristic, and an acceptable spectral performance, a cell-based ^{19}F NMR experiment was followed to examine whether the structural modified **RTC-3** and the multivalent nanoring **η-RTC-3** could generate signal. A431 cells were incubated with 500 nM **RTC-3** and 62.5 nM **η-RTC-3** (corresponding to 500 nM monomeric **RTC-3**) individually. However, no NMR signal was able to be observed in either cell samples similar to our previous results with **RTC-1**. **η-RTC-3**, with a fully recovered affinity and a 4-fold increase in fluorine content compared to **RTC-1**, showed no noticeable improvement in the NMR signal from **RTC-1**. This indicated that the structure of the molecular tracer or EGFR affinity are probably not the factors attributing to the loss of signal.

Prior studies have shown the increased viscosity and non-specific binding within the cell can significantly affect NMR performance and thus can be a significant factor affecting **RTC-3** and **η-RTC-3.** Increased chemical exchange from non-specific interactions and decreased diffusion are anticipated to both dramatically broaden the ^{19}F NMR signal leading to loss of signal. Based on such a hypothesis, we tested if

the signal could be recovered if the protein complex could be blocked from internalization (**Fig. 4-14A**). To block the internalization, we adjusted the incubation temperature from 37 ºC to 4 ºC. This time, for both **RTC-3** and **η-RTC-3** cell samples, ^{19}F NMR signal was successfully observed. In the **RTC-3** cell sample, signal with an acceptable SNR was observed after 3000 scans (**Fig. 4-14B**). However, signal degeneracy was lost, showing multiple resonances with a FWHM of 187 Hz. In contrast, in the **η-RTC-3** cell sample, a high SNR signal was observed in an ~3-fold reduced number of scans (1100 scans, **Fig. 4-14C**). In addition, signal degeneracy was successfully maintained with a reduced FWHM of 141 Hz. Due to the long relaxation times of fluorine nuclei, we also sought to determine the T_1 relaxation to verify our experimental conditions. Therefore the, T_1 of both **RTC-3** and **η-RTC-3** cell samples were measured by inversion-recovery experiments. The **RTC-3** cell sample had a T_1 of 2.46 s, while the **η-RTC-3** cell sample had a more favorable T_1 of 1.73 s as a shorter T_1 allows for shorter scan times for improving ^{19}F MRI sensitivity. We conclude from these experiments that the overall spectral performance of **η-RTC-3** was the most promising for further imaging applications.

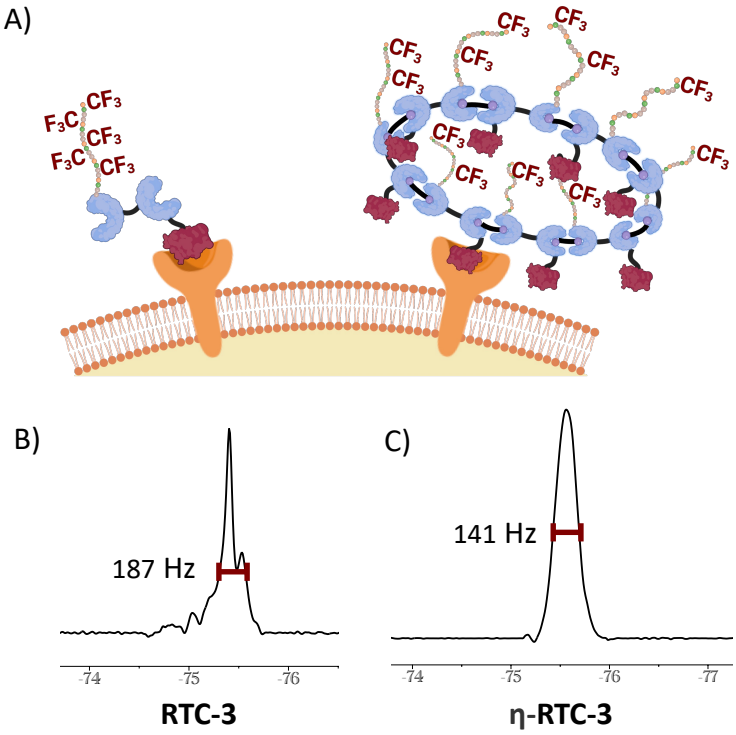

Figure 4-14. On-cell ^{19}F NMR. A) Illustration of **RTC-3** and **η-RTC-3** bound to the EGFR on the cells. B) On Cell ^{19}F NMR Spectra of **RTC-3** and η-RTC-3 with 187 Hz and 141 Hz, respectively. **RTC-3** showed multiple resonances while **η-RTC-3** showed degenerated signal.

With the success of cell-based ^{19}F NMR experiments (600 MHz) on **η-RTC-3**, an initial in vitro phantom MRI experiment was also attempted with a 9.4T (400 MHz) magnet at concentration of 62.5 nM. Unfortunately, in this preliminary experiment insufficient signal prevented further imaging. To reach the detection limit under a weaker magnet and a less sensitive probe, future work would focus on further engineer the nanoring **η-RTC-3** through increasing the fluorine content through new multivalent display approaches or adjusting the spectral properties such as T_1 and T_2 such as through contrast agents.

4.3 Conclusion

In these studies, we have demonstrated the rational design of a multivalent molecular tracer for guiding the design of future ^{19}F MRI molecular imaging agents. These studies build on our earlier results of a monomeric bioconjugated E_1-DD, which despite the advantages of high fluorine content and favorable spectral performance, had limited signal in cell-based ^{19}F NMR experiment. Cellular interaction studies revealed a balance of fluorine content and binding affinity to the targeted biomarker, EGFR. In our latest design, structure-optimized **RTC-3** exhibited a degenerate resonance in ^{19}F NMR as well as high affinity and specificity in targeting EGFR-expressing cells. To further increase the fluorine content, we assembled **RTC-3** into a multivalent CSAN, **η-RTC-3**. Binding characteristics of **η-RTC-3** were well maintained with good ^{19}F NMR behavior. In an attempt to image EGFR-expressing cancer cells, through manipulating the **η-RTC-3** from internalization which would result in signal attenuation, an amplified degenerate signal was observed via cell-based ^{19}F NMR in a short scan time. While current ^{19}F MRI studies have yet to prove successful, these studies highlight new design rules using fluorinated CSANs, and opportunities to improve their spectral behavior for ^{19}F MRI molecular imaging in the future.

4.4 Supplementary Information

4.4.1 Experimental

General Method for Peptide Preparation

Solid Phase Peptide Synthesis

All peptides were synthesized on NovaSyn TGR ® resin using CEM MARS Xtraction Microwave Reactor on a 25 μmol scale. Prior to acylation reaction, N^{α} -Fmoc protected amino acid (100 μmol, 4.0 eq) was dissolved in 1 mL of DMF, followed with activation with HOBT (200 μL of 0.5 M solution in DMF, 4.0 eq), HBTU (200 μL of 0.5 M solution in DMF, 4.0 eq) and DIEA (200 μL of 1.0 M solution in DMF, 8.0 eq). The reaction mixture was added to the resin and heated at 70 °C (400 W power, 2 min ramping and 4 min holding cycle). The reaction mixture was then drained, and resin was washed with DMF 3 times, DCM 3 times, and DMF 3 times. 9-fluorenylmethyoxycarbonyl (Fmoc) group was deprotected by addition of piperidine (2 mL, 20% v/v in DMF) to the resin and heating to 80 °C (400 W power, 2 min ramping and 2 min holding cycle). The reaction mixture was then drained, and resin was washed with DMF 3 times, DCM 3 times, and DMF 3 times. The coupling and deprotection steps were repeated till the full-length peptide was synthesized. Following the final deprotection step, the N-terminus was reacted with maleimide-NHS. Prior to attaching the maleimide-NHS at the N-terminus, maleimide-NHS (100 μmol, 4.0 eq) was dissolved in 1.4 mL of DMF, followed with DIEA (200 μL of 1.0 M solution in DMF, 8.0 eq). The reaction mixture was added to the resin and reacted at room temperature overnight. The reaction mixture was then drained, and resin was washed with DMF 3 times, DCM 3 times, and DMF 3 times.

Peptide Cleavage and Deprotection

Peptides were cleaved from the resin and the side chains were deprotected at the same time through treatment of 1.9 mL of trifluoroacetic acid (TFA), 100 μL of thioanisole, 60 μL of triisopropylsilane (TIPS), and 40 μL of anisole at room temperature for 2 h. The resulting solution was drained from the syringe and precipitated into cold diethyl ether. Peptides were then pelleted via centrifugation (2000 x g, 3 min at 4 °C). Supernatant was decanted.

RP-HPLC Purification of Peptides

Crude peptides were dissolved in a 50:50 mixture of 0.1% TFA in H_2O: acetonitrile. Crude solution was purified via Dionex Ultimate 3000 RP-HPLC using a C-18 column. The identity of the purified peptides was determined using an Ab-Sciex 5800 MALDI-TOF/TOF Mass Spectrometer utilizing α-cyano-4-hydroxycinaminic acid matrix). The purity of fraction was confirmed by analytical RP-HPLC (Dionex Ultimate 3000 RP-HPLC using a C-18 column). HPLC fractions containing product were collected and lyophilized.

Cell Lines and Cell Culture

The human cancer cell lines, A549 and A431 cells were previously purchased from the American Type Culture Collection (ATCC) and were validated via the STR fingerprinting service at the Cytogenetics and Cell Authentication Core (CCAC) in the Department of Genetics at MD Anderson Cancer Center. The cell lines were tested and certified as mycoplasma-free using PCR Mycoplasma Detection Kit (Applied Biological Materials Inc., Cat: G238). Raji cells were provided through the courtesy of the Wagner group (University of Minnesota). A549 and A431 cells were cultured in Dulbecco's Modified Eagle's Medium (DMEM) with 4.5 g/L glucose, L-glutamine, and supplemented with 10% fetal bovine serum (FBS), 100 U/mL penicillin, and 100 µg/mL streptomycin at 37 °C with 5.0% CO_2. Raji cells were cultured in Roswell Park Memorial Institute (RPMI) medium with L-glutamine and supplemented with 10% FBS, 100 U/mL penicillin, and 100 µg/mL streptomycin at 37 °C with 5.0% CO2.

Confocal Fluorescence Microscopy

100,000 A431 cells were plated into 35 mm µ-Dish in a total volume of 2 mL. Cells were incubated overnight at 37 °C till they reached 70% confluency. Media was aspirated and cells were rinse 2 times with DMEM media and were dosed with 500 nM **RTC-3*** or **η-RTC-3*** in DMEM (0.5% DMSO). Cells were incubated for 60 minutes at 37°C and 5% CO_2 and followed with aspiration and rinsing 3 times with DPBS. Cells were fixed with 1 mL of 4% paraformaldehyde with light shaking for 10 min. Paraformaldehyde was removed and cells were rinsed 3 times with DPBS. 1 mL of 1 µg/mL Hoechst 34580 was added to the cells

for nucleus stain with light shaking for 10 min. Hoechst was removed and cells were rinsed 3 times with DPBS. Cells were then imaged using Zeiss - Widefield & TIRF Microscopy.

Protein Expression and Purification

E_1-DD-CVIA fusion proteins were produces in T7 Express competent E. coli cells. E. coli cell glycerol stock is provided through the courtesy of the Wagner group (University of Minnesota). The E. coli cells were cultured at 37 °C (250 rpm) to the point when the OD_{600} reached 0.6-0.8, and then the protein was expressed at 37 °C for 6 hours by the addition of IPTG (0.5 mM). Cells were centrifuged down. 40 mL of lysis buffer (50 mM phosphate, 300 mM NaCl, pH 7.4) and 40 mg phenylmethanesulfonyl fluoride (PMSF) were added to the cell pallet and stirred for 30 min at room temperature. Cells were then put on ice and sonicated in 30 second intervals followed by 60 seconds of cooling for a total of 12 minutes sonication time. The lysed cells were centrifuged at 100,000 x g for 30 minutes. The supernatant was filtered. Ni affinity purification was done using a Ni HisTrap FF 5 mL column (GE Healthcare) on an AKTA Fast Protein Liquid Chromatography (FPLC) system by monitoring the absorbance at 280 nm. Proteins were eluted with a 0-100% gradient of wash buffer (50 mM phosphate, 100 mM NaCl, 40 mM imidazole, pH 7.4) and elution buffer (50 mM phosphate, 100 mM NaCl, 400 mM imidazole, pH 7.4) across 20 column volumes. Buffer exchange into PBS buffer (50 mM PBS, pH 7.4) was followed through a HiPrep desalting column (GE Healthcare) equilibrated with 1 column volume of buffer. Purified protein was analyzed by SDS-page electrophoresis and LC-MS using an Orbitrap Elite Hybrid Mass Spectrometer. The LC-MS data was analyzed by Thermo Scientific Protein Deconvolution.

Bioconjugation

1.4 µL of 32mM TCEP in pH 7.3 PBS buffer was added to 280 µL of 32 µM E_1-DD protein in pH 7.3 PBS buffer at 4°C. After 1 h, 1.9 µL of 23 mM of peptide in DMSO was first added to 280 µL of pH 7.3 PBS buffer and then added to the E_1-DD protein solution. Bioconjugation was reacted at 4°C for 24 h. Reaction mixture was then purified through PD-10 desalting column (Sephadex G-25 resin). Protein was collected and concentrated. The bioconjugated proteins were characterized by SDS-page electrophoresis and LC-MS using

an Orbitrap Elite Hybrid Mass Spectrometer. The LC-MS data was analyzed by Thermo Scientific Protein Deconvolution.

Nanoring formation and Characterization

1.8 μL of 2mM dimerizer, bis-MTX DMSO stock was added to 100 μL of pH 7.3 PBS buffer. Bis-MTX solution was added to 100 μL of 10 μM bioconjugated E_1-DD solution in an Eppendorf tube. Reaction mixture was reacted at room temperature for 40 min. Nanoring formation was characterized by SEC using a Superdex 200 Increase 10/300 gel filtration column (GE Healthcare Life Sciences, Cat: 2899094). The hydrodynamic diameters of nanoring **η-RTC-3** were measure with a Punk Dynamic Light Scattering unit (Unchained Laboratories).

Binding Affinity Assay

Binding affinity of bioconjugated E_1-DD complex and nanoring was studied by flow cytometry. A549 cells were harvested and washed with Dulbecco's phosphate-buffered saline (DPBS) for 3 times. Aliquots of 10 x 10^4 cells were then resuspended in DPBS solution containing bioconjugated E_1-DD complex or nanoring at concentration of 0 nM, 5 nM, 20 nM, 100 nM, 200 nM, 500 nM, 1000 nM respectively and incubated for 1 h at 4 ºC. Cells were then pelleted, washed with DPBS for 3 times, and resuspended in 50 μL of Alexa Fluor® 647 anti-His-tag antibody solution and incubated for 30 min at 4 ºC in the dark. Cells were then pelleted, washed with DPBS for 3 times, and resuspend with 1 mL of cold DPBS for analysis through BD LSR Fortessa™ X-20 Cell Analyzer at the University Flow Cytometry Resource (UFCR). Data analysis and K_d determination were processed through GraphPad Prism8. Data were fit with 'One site – Specific binding' under the equation $Y = B_{max} * X / (K_d + X)$.

Binding Selectivity Assay

Binding affinity of **RTC-3** and **η-RTC-3** was studied by flow cytometry. Raji was selected as non-EGFR-expressing cell line; A549 was selected as mid EGFR-expressing cell line; A431 was selected as high EGFR-expressing cell line. Cells were harvested and washed with Dulbecco's phosphate-buffered saline (DPBS) for 3 times. Aliquots of 10 x 10^4 cells were then resuspended in DPBS solution containing **RTC-3**

or **η-RTC-3** at concentration of 500 nM respectively and incubated for 1 h at 4 ºC. Cells were then pelleted, washed with DPBS for 3 times, and resuspended in 50 µL of Alexa Fluor® 647 anti-His-tag antibody solution and incubated for 30 min at 4 ºC in the dark. Cells were then pelleted, washed with DPBS for 3 times, and resuspend with 1 mL of cold DPBS for analysis through BD LSR Fortessa™ X-20 Cell Analyzer at the University Flow Cytometry Resource (UFCR).

In vitro ^{19}F NMR Experiment

For in cell ^{19}F NMR experiment, A431 cells were first trypsinized and were then washed with DMEM for 3 times to inhibit trypsin completely. 10,000,000 cells were added to a 75 mL culture flask. Appropriate amount of protein complex dissolved in 10 mL of warmed DMEM (0.5% DMSO) was added to cells to final concentration of 500 nM. Cells were incubated for 30 minutes at 37°C and 5% CO_2. After incubation, cells were recovered by pipetting and then were transferred to Eppendorf tubes and spun at 300 rpm for 5 min. Pellets were washed 2 times with DPBS and 1 time with L-15 medium (10% D_2O). Cells were resuspended with 150 µL of L-15 medium (10% D_2O) and transferred to 3 mm shigemi NMR tube. ^{19}F NMR spectrum was obtained using a Bruker 600-MHz Avance NEO with CryoProbe 5-mm TCI cryoprobe. Spectra were acquired at 37°C with acquisition time of 0.05 s, relaxation delay of 3 s, number of scans of 1000 for both **RTC-3** and **η-RTC-3** samples.

For on cell ^{19}F NMR experiment, A431 cells were first trypsinized and were then washed with DMEM for 3 times to inhibit trypsin completely. 10,000,000 cells were added to a 75 mL culture flask. Appropriate amount of protein complex dissolved in 10 mL of cold DMEM (0.5% DMSO) was added to cells to final concentration of 500 nM. Cells were incubated for 30 minutes at 4°C. After incubation, cells were recovered by pipetting and then were transferred to Eppendorf tubes and spun at 300 rpm for 5 min. Pellets were washed 2 times with cold DPBS and 1 time with cold L-15 medium (10% D_2O). Cells were resuspended with 150 µL of L-15 medium (10% D_2O) and transferred to 3 mm shigemi NMR tube. ^{19}F NMR spectrum was obtained using a Bruker 600-MHz Avance NEO with CryoProbe 5-mm TCI cryoprobe. Spectra were acquired at 4°C with acquisition time of 0.05 s, relaxation delay of 3 s, receiver gain of 64, and number of scans of 3000 for **RTC-3** sample and 1024 for **η-RTC-3** sample.

Leakage check was followed with the sample being centrifuged down and supernatant was transferred to another 3 mm shigemi NMR tube. ^{19}F NMR spectrum was obtained using a Bruker 600-MHz Avance NEO with CryoProbe 5-mm TCI cryoprobe. Spectra were acquired at 37°C with acquisition time of 0.05 s, relaxation delay of 3 s, receiver gain of 64, and number of scans of 3000 for RTC-3 sample and 1024 for **η-RTC-3** sample.

T_1 Determination

T_1 of **RTC-3** and **η-RTC-3** were determined through inversion recovery experiment with delay time of 0.25, 0.5, 0.8, 1, 2, 4, 8, 12 s. 8 spectra were obtained with a 90° pulse of 15 μs and D_1 of 8 s. Number of scans of 12 was set for the individual acquisition time of 0.3 s and relaxation time of 8 s was analyzed using the relaxation fitting functions within the software Topspin 4.1.4 (Bruker).

4.4.2 Supplement Figures

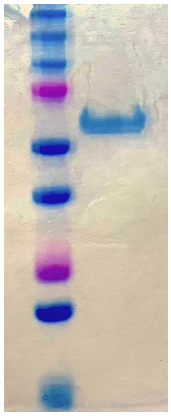

Figure 4-15. SDS-PAGE electrophoresis gel of **RTC-1.** Peptide 1 was bioconjugated to E_1-DD.

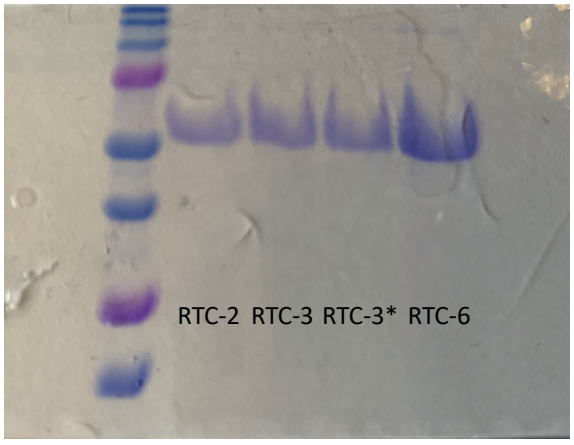

Figure 4-16. SDS-PAGE electrophoresis gel of **RTC-2, RTC-3, RTC-3*, and RTC-6.** Peptide 2 was bioconjugated to E_1-DD to give **RTC-2**; peptde 3 was bioconjugated to E_1-DD to give **RTC-3**; peptde 6 was bioconjugated to E_1-DD to give **RTC-6**; peptde 8 was bioconjugated to E_1-DD to give **RTC-3***.

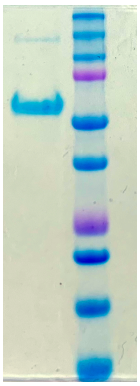

Figure 4-17. SDS-PAGE electrophoresis gel of **RTC-4.** Peptide 4 was bioconjugated to E_1-DD.

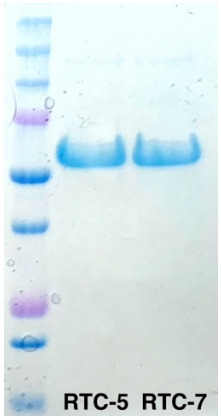

Figure 4-18. SDS-PAGE electrophoresis gel of **RTC-5 and RTC-7.** Peptide 5 was bioconjugated to E_1-DD to give **RTC-5**; peptde 7 was bioconjugated to E_1-DD to give **RTC-7**.

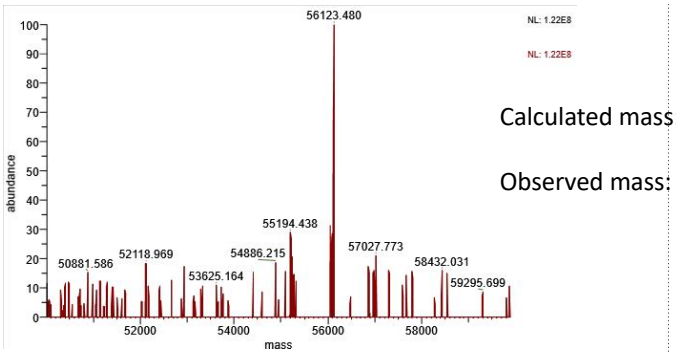

Figure 4-19. LC-MS spectrum of **RTC-1.** E_1-DD protein was bioconjugated with **1** and characterized by LC-MS.

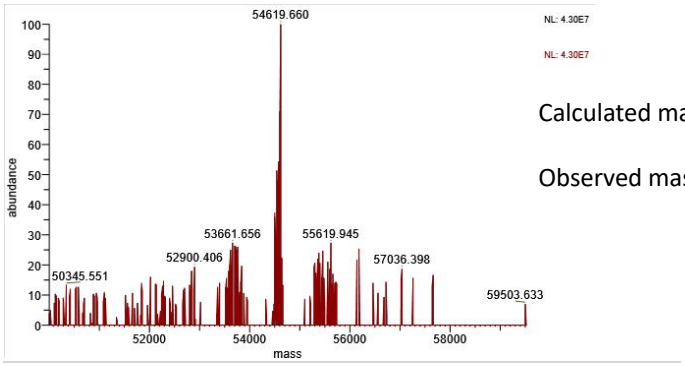

Figure 4-20. LC-MS spectrum of **RTC-2.** E_1-DD protein was bioconjugated with 2 and characterized by LC-MS.

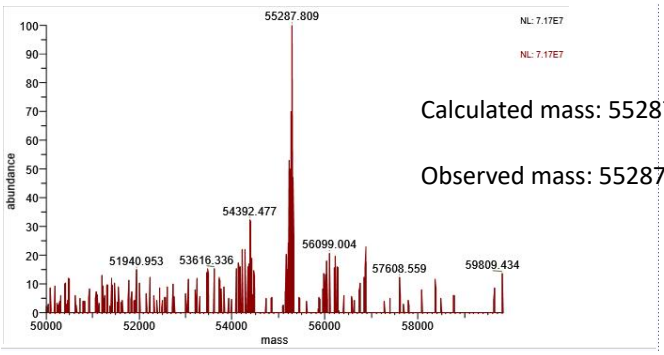

Figure 4-21. LC-MS spectrum of **RTC-3.** E_1-DD protein was bioconjugated with 3 and characterized by LC-MS.

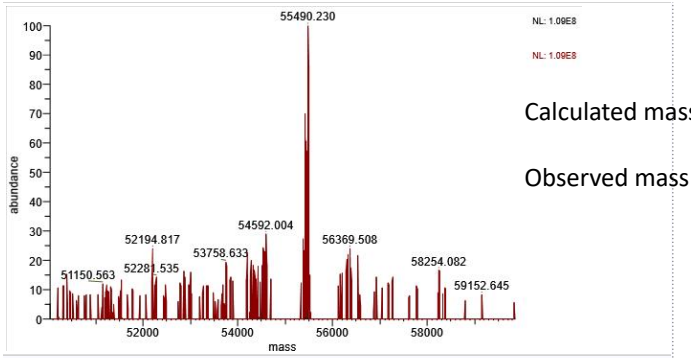

Figure 4-22. LC-MS spectrum of **RTC-4.** E_1-DD protein was bioconjugated with 4 and characterized by LC-MS.

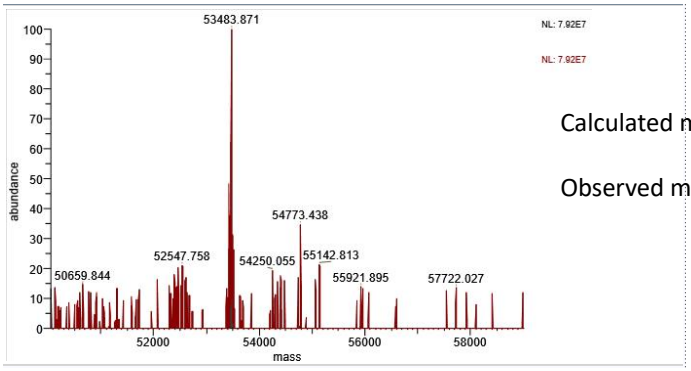

Figure 4-23. LC-MS spectrum of **RTC-5.** E_1-DD protein was bioconjugated with 5 and characterized by LC-MS.

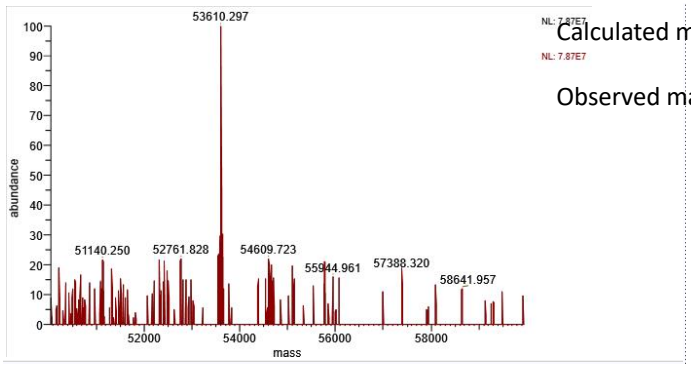

Figure 4-24. LC-MS spectrum of **RTC-6.** E_1-DD protein was bioconjugated with 6 and characterized by LC-MS.

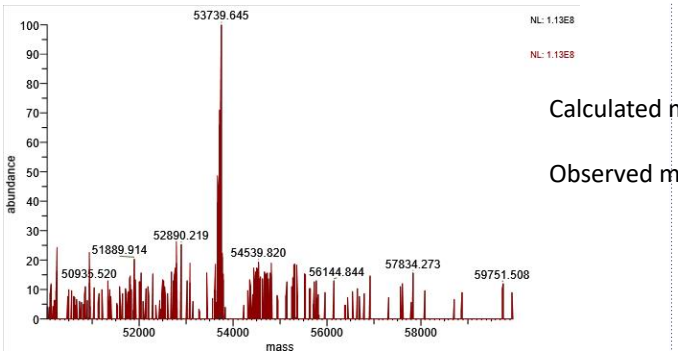

Figure 4-25. LC-MS spectrum of **RTC-7.** E_1-DD protein was bioconjugated with 7 and characterized by LC-MS.

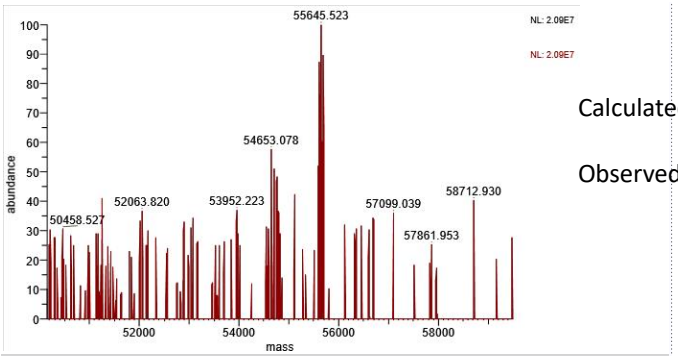

Figure 4-26. LC-MS spectrum of **RTC-3*.** E_1-DD protein was bioconjugated with 3* and characterized by LC-MS.

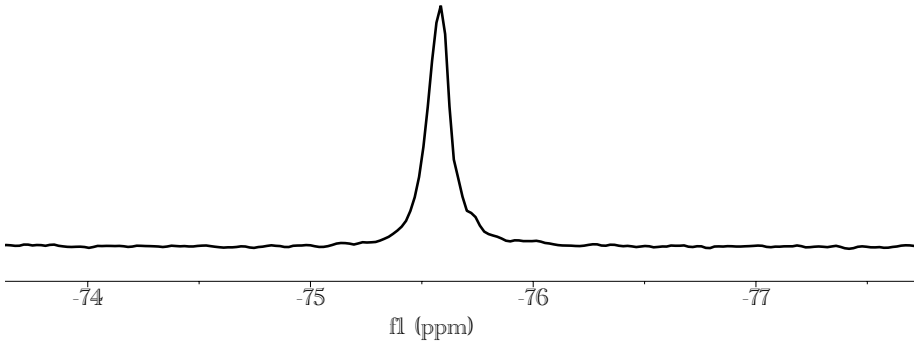

Figure 4-27. ^{19}F NMR of **RTC-1**.

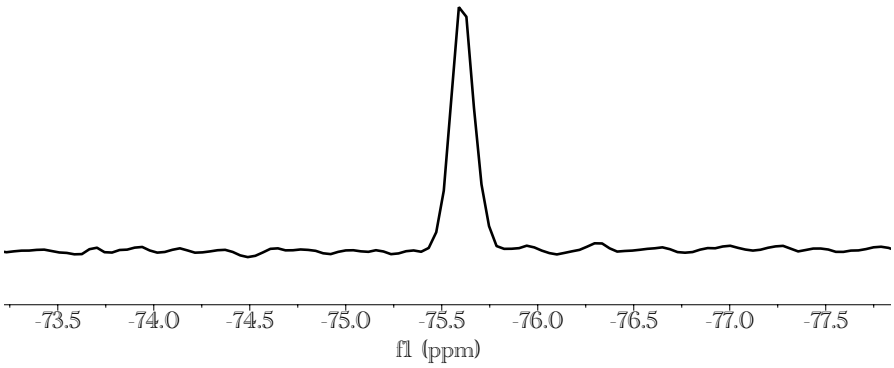

Figure 4-28. ^{19}F NMR of **RTC-2**.

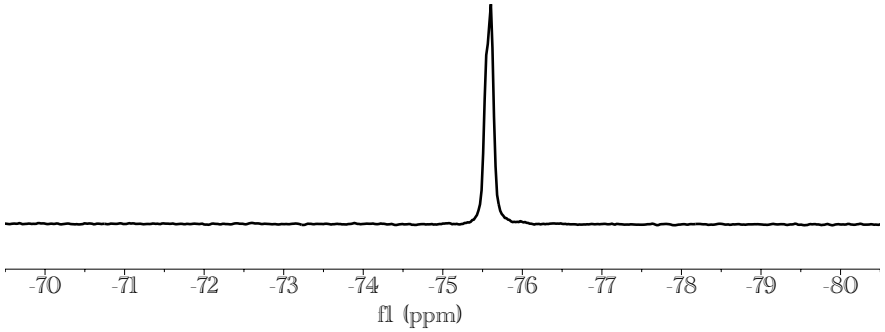

Figure 4-29. ^{19}F NMR of **RTC-3**.

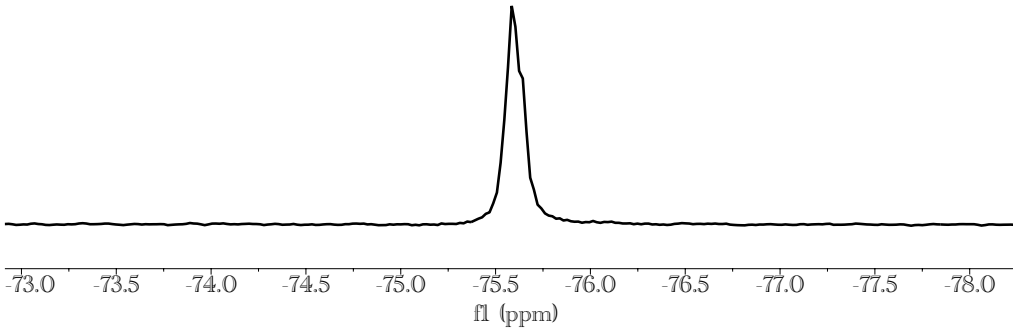

Figure 4-30. ^{19}F NMR of **RTC-4**.

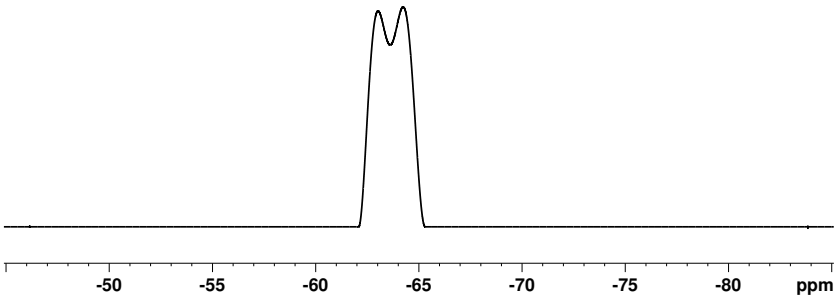

Figure 4-31. ^{19}F NMR of **RTC-5**.

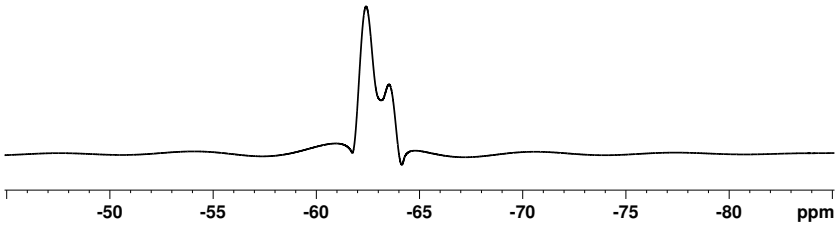

Figure 4-32. ^{19}F NMR of **RTC-6**.

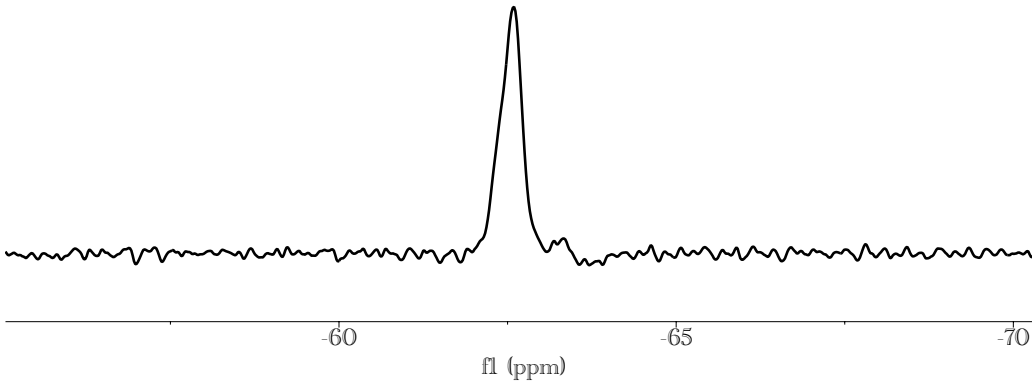

Figure 4-33. ^{19}F NMR of **RTC-7**.

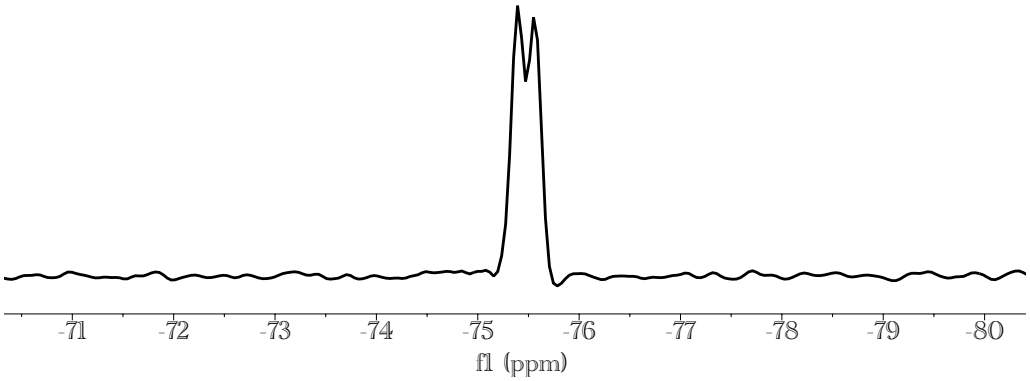

Figure 4-34. ^{19}F NMR of **RTC-8**.

Bibliography

(1) Gambhir, S. S. Molecular Imaging of Cancer with Positron Emission Tomography. *Nat. Rev. Cancer* **2002**, *2* (9), 683–693. https://doi.org/10.1038/nrc882.

(2) Gangadaran, P.; Ahn, B.-C. Molecular Imaging: A Useful Tool for the Development of Natural Killer Cell-Based Immunotherapies. *Front. Immunol.* **2017**, *8*, 1090. https://doi.org/10.3389/fimmu.2017.01090.

(3) Ametamey, S. M.; Honer, M.; Schubiger, P. A. Molecular Imaging with PET. *Chem. Rev.* **2008**, *108* (5), 1501–1516. https://doi.org/10.1021/cr0782426.

(4) Duclos, V.; Iep, A.; Gomez, L.; Goldfarb, L.; Besson, F. L. PET Molecular Imaging: A Holistic Review of Current Practice and Emerging Perspectives for Diagnosis, Therapeutic Evaluation and Prognosis in Clinical Oncology. *Int. J. Mol. Sci.* **2021**, *22* (8), 4159. https://doi.org/10.3390/ijms22084159.

(5) Khalil, M. M.; Tremoleda, J. L.; Bayomy, T. B.; Gsell, W. Molecular SPECT Imaging: An Overview. *Int. J. Mol. Imaging* **2011**, *2011*, 796025. https://doi.org/10.1155/2011/796025.

(6) Gomes, C. M.; Abrunhosa, A. J.; Ramos, P.; Pauwels, E. K. J. Molecular Imaging with SPECT as a Tool for Drug Development. *Adv. Drug Deliv. Rev.* **2011**, *63* (7), 547–554. https://doi.org/10.1016/j.addr.2010.09.015.

(7) Meikle, S. R.; Kench, P.; Kassiou, M.; Banati, R. B. Small Animal SPECT and Its Place in the Matrix of Molecular Imaging Technologies. *Phys. Med. Biol.* **2005**, *50* (22), R45. https://doi.org/10.1088/0031-9155/50/22/R01.

(8) Winter, P. M.; Caruthers, S. D.; Wickline, S. A.; Lanza, G. M. Molecular Imaging by MRI. *Curr. Cardiol. Rep.* **2006**, *8* (1), 65–69. https://doi.org/10.1007/s11886-006-0013-2.

(9) Gallagher, F. A. An Introduction to Functional and Molecular Imaging with MRI. *Clin. Radiol.* **2010**, *65* (7), 557–566. https://doi.org/10.1016/j.crad.2010.04.006.

(10) Jaffer, F. A.; Weissleder, R. Molecular Imaging in the Clinical Arena. *JAMA* **2005**, *293* (7), 855–862. https://doi.org/10.1001/jama.293.7.855.

(11) Kosareva, A.; Abou-Elkacem, L.; Chowdhury, S.; Lindner, J. R.; Kaufmann, B. A. Seeing the Invisible—Ultrasound Molecular Imaging. *Ultrasound Med. Biol.* **2020**, *46* (3), 479–497. https://doi.org/10.1016/j.ultrasmedbio.2019.11.007.

(12) Deshpande, N.; Needles, A.; Willmann, J. K. Molecular Ultrasound Imaging: Current Status and Future Directions. *Clin. Radiol.* **2010**, *65* (7), 567–581. https://doi.org/10.1016/j.crad.2010.02.013.

(13) Harry W. Schroeder III, M. D.; Lance T. Hall, M. D. Molecular Imaging of Brain Metastases with PET. *Exon Publ.* **2022**, 1–16. https://doi.org/10.36255/exon-publications.metastasis.brain-metastases.

(14) Miller-Thomas, M. M.; Benzinger, T. L. S. Neurological Applications of PET/MR. *Magn. Reson. Imaging Clin. N. Am.* **2017**, *25* (2), 297–313. https://doi.org/10.1016/j.mric.2016.12.003.

(15) Cherry, S. R.; Jones, T.; Karp, J. S.; Qi, J.; Moses, W. W.; Badawi, R. D. Total-Body PET: Maximizing Sensitivity to Create New Opportunities for Clinical Research and Patient Care. *J. Nucl. Med.* **2018**, *59* (1), 3–12. https://doi.org/10.2967/jnumed.116.184028.

(16) Flotats, A.; Carrió, I. Cardiac Neurotransmission SPECT Imaging. *J. Nucl. Cardiol.* **2004**, *11* (5), 587–602. https://doi.org/10.1016/j.nuclcard.2004.07.007.

(17) Warwick, J. M. Imaging of Brain Function Using SPECT. *Metab. Brain Dis.* **2004**, *19* (1), 113–123. https://doi.org/10.1023/B:MEBR.0000027422.48744.a3.

(18) Kim, N.-D.; Booth, L.; Amin, V.; Lim, J.; Udpa, S. Ultrasonic Image Processing for Tendon Injury Evaluation. In *Proceedings of the IEEE-SP International Symposium on Time-Frequency and Time-Scale Analysis (Cat. No.98TH8380)*; 1998; pp 241–244. https://doi.org/10.1109/TFSA.1998.721406.

(19) Turo, D.; Otto, P.; Shah, J. P.; Heimur, J.; Gebreab, T.; Zaazhoa, M.; Armstrong, K.; Gerber, L. H.; Sikdar, S. Ultrasonic Characterization of the Upper Trapezius Muscle in Patients with Chronic Neck Pain. *Ultrason. Imaging* **2013**, *35* (2), 173–187. https://doi.org/10.1177/0161734612472408.

(20) Kustroń, P.; Korzeniowski, M.; Lewandowski, M.; Witek, B.; Rozbicki, J. A High Frequency Ultrasonic Imaging of Welded Joints. In *2016 IEEE International Ultrasonics Symposium (IUS)*; 2016; pp 1–4. https://doi.org/10.1109/ULTSYM.2016.7728848.

(21) Insana, M. F. Ultrasonic Imaging of Microscopic Structures in Living Organs. *Int. Rev. Exp. Pathol.* **1996**, *36*, 73–92.

(22) Lento, P. H.; Primack, S. Advances and Utility of Diagnostic Ultrasound in Musculoskeletal Medicine. *Curr. Rev. Musculoskelet. Med.* **2007**, *1* (1), 24–31. https://doi.org/10.1007/s12178-007-9002-3.

(23) Chan, R. W.; Lau, J. Y. C.; Lam, W. W.; Lau, A. Z. Magnetic Resonance Imaging. In *Encyclopedia of Biomedical Engineering*; Narayan, R., Ed.; Elsevier: Oxford, 2019; pp 574–587. https://doi.org/10.1016/B978-0-12-801238-3.99945-8.

(24) Chou, E. T.; Carrino, J. A. Chapter 10 - Magnetic Resonance Imaging. In *Pain Management*; Waldman, S. D., Bloch, J. I., Eds.; W.B. Saunders: Philadelphia, 2007; pp 106–117. https://doi.org/10.1016/B978-0-7216-0334-6.50014-5.

(25) Lee, J. H.; Okuno, Y.; Cavagnero, S. Sensitivity Enhancement in Solution NMR: Emerging Ideas and New Frontiers. *J. Magn. Reson. San Diego Calif 1997* **2014**, *241*, 18–31. https://doi.org/10.1016/j.jmr.2014.01.005.

(26) Kircher, M. F.; Willmann, J. K. Molecular Body Imaging: MR Imaging, CT, and US. Part I. Principles. *Radiology* **2012**, *263* (3), 633–643. https://doi.org/10.1148/radiol.12102394.

(27) Delfaut, E. M.; Beltran, J.; Johnson, G.; Rousseau, J.; Marchandise, X.; Cotten, A. Fat Suppression in MR Imaging: Techniques and Pitfalls. *RadioGraphics* **1999**, *19* (2), 373–382. https://doi.org/10.1148/radiographics.19.2.g99mr03373.

(28) Ibrahim, M. A.; Hazhirkarzar, B.; Dublin, A. B. Gadolinium Magnetic Resonance Imaging. In *StatPearls*; StatPearls Publishing: Treasure Island (FL), 2023.

(29) Semelka, R. C.; Ramalho, J.; Vakharia, A.; AlObaidy, M.; Burke, L. M.; Jay, M.; Ramalho, M. Gadolinium Deposition Disease: Initial Description of a Disease That Has Been around for a While. *Magn. Reson. Imaging* **2016**, *34* (10), 1383–1390. https://doi.org/10.1016/j.mri.2016.07.016.

(30) Wang, Z. J.; Ohliger, M. A.; Larson, P. E. Z.; Gordon, J. W.; Bok, R. A.; Slater, J.; Villanueva-Meyer, J. E.; Hess, C. P.; Kurhanewicz, J.; Vigneron, D. B. Hyperpolarized 13C MRI: State of the Art and Future Directions. *Radiology* **2019**, *291* (2), 273–284. https://doi.org/10.1148/radiol.2019182391.

(31) Ouwerkerk, R.; Morgan, R. H. 23Na MRI: From Research to Clinical Use. *J. Am. Coll. Radiol. JACR* **2007**, *4* (10), 739–741. https://doi.org/10.1016/j.jacr.2007.07.001.

(32) Cade-Menun, B. J. Characterizing Phosphorus in Environmental and Agricultural Samples by 31P Nuclear Magnetic Resonance Spectroscopy. *Talanta* **2005**, *66* (2), 359–371. https://doi.org/10.1016/j.talanta.2004.12.024.

(33) Tirotta, I.; Dichiarante, V.; Pigliacelli, C.; Cavallo, G.; Terraneo, G.; Bombelli, F. B.; Metrangolo, P.; Resnati, G. ^{19} F Magnetic Resonance Imaging (MRI): From Design of Materials to Clinical Applications. *Chem. Rev.* **2015**, *115* (2), 1106–1129. https://doi.org/10.1021/cr500286d.

(34) Herynek, V.; Martinisková, M.; Bobrova, Y.; Gálisová, A.; Kotek, J.; Hermann, P.; Koucký, F.; Jirák, D.; Hájek, M. Low-Molecular-Weight Paramagnetic 19F Contrast Agents for Fluorine Magnetic Resonance Imaging. *Magma N. Y. N* **2019**, *32* (1), 115–122. https://doi.org/10.1007/s10334-018-0721-9.

(35) Lemal, D. M. Perspective on Fluorocarbon Chemistry. *J. Org. Chem.* **2004**, *69* (1), 1–11. https://doi.org/10.1021/jo0302556.

(36) Janjic, J. M.; Ahrens, E. T. Fluorine-Containing Nanoemulsions for MRI Cell Tracking. *WIREs Nanomedicine Nanobiotechnology* **2009**, *1* (5), 492–501. https://doi.org/10.1002/wnan.35.

(37) Meyer, K. L.; Carvlin, M. J.; Mukherji, B.; Sloviter, H. A.; Joseph, P. M. Fluorinated Blood Substitute Retention in the Rat Measured by Fluorine-19 Magnetic Resonance Imaging. *Invest. Radiol.* **1992**, *27* (8), 620.

(38) Lowe, K. C. Second-Generation Perfluorocarbon Emulsion Blood Substitutes. *Artif. Cells. Blood Substit. Immobil. Biotechnol.* **2000**, *28* (1), 25–38. https://doi.org/10.3109/10731190009119783.

(39) Anton, N.; Benoit, J.-P.; Saulnier, P. Design and Production of Nanoparticles Formulated from Nano-Emulsion Templates—A Review. *J. Controlled Release* **2008**, *128* (3), 185–199. https://doi.org/10.1016/j.jconrel.2008.02.007.

(40) Joseph, J. M.; Gigliobianco, M. R.; Firouzabadi, B. M.; Censi, R.; Di Martino, P. Nanotechnology as a Versatile Tool for 19F-MRI Agent's Formulation: A Glimpse into the Use of Perfluorinated and Fluorinated Compounds in Nanoparticles. *Pharmaceutics* **2022**, *14* (2), 382. https://doi.org/10.3390/pharmaceutics14020382.

(41) Matsushita, H.; Mizukami, S.; Sugihara, F.; Nakanishi, Y.; Yoshioka, Y.; Kikuchi, K. Multifunctional Core–Shell Silica Nanoparticles for Highly Sensitive 19F Magnetic Resonance Imaging. *Angew. Chem.* **2014**, *126* (4), 1026–1029. https://doi.org/10.1002/ange.201308500.

(42) Nakamura, T.; Matsushita, H.; Sugihara, F.; Yoshioka, Y.; Mizukami, S.; Kikuchi, K. Activatable 19F MRI Nanoparticle Probes for the Detection of Reducing Environments. *Angew. Chem. Int. Ed.* **2015**, *54* (3), 1007–1010. https://doi.org/10.1002/anie.201409365.

(43) Lee, A. L.; Gee, C. T.; Weegman, B. P.; Einstein, S. A.; Juelfs, A. R.; Ring, H. L.; Hurley, K. R.; Egger, S. M.; Swindlehurst, G.; Garwood, M.; Pomerantz, W. C. K.; Haynes, C. L. Oxygen Sensing with Perfluorocarbon-Loaded Ultraporous Mesostructured Silica Nanoparticles. *ACS Nano* **2017**, *11* (6), 5623–5632. https://doi.org/10.1021/acsnano.7b01006.

(44) Kodibagkar, V.; Wang, X.; Mason, R. Physical Principles of Quantitative Nuclear Magnetic Resonance Oximetry. *Front. Biosci. J. Virtual Libr.* **2008**, *13*, 1371–1384. https://doi.org/10.2741/2768.

(45) *Perfluorocarbons-Based 19F Magnetic Resonance Imaging in Biomedicine*. https://doi.org/10.2147/IJN.S255084.

(46) *High sensitivity 19F MRI of a perfluorooctyl bromide emulsion: application to a dynamic biodistribution study and oxygen tension mapping in the mouse liver and spleen - Giraudeau - 2012 - NMR in Biomedicine - Wiley Online Library*. https://analyticalsciencejournals.onlinelibrary.wiley.com/doi/full/10.1002/nbm.1781 (accessed 2023-06-17).

(47) Ratner, A. V.; Muller, H. H.; Bradley-Simpson, B.; Johnson, D. E.; Hurd, R. E.; Sotak, C.; Young, S. W. Detection of Tumors with 19F Magnetic Resonance Imaging. *Invest. Radiol.* **1988**, *23* (5), 361.

(48) Riess, J. G. Oxygen Carriers ("blood Substitutes")--Raison d'etre, Chemistry, and Some Physiology. *Chem. Rev.* **2001**, *101* (9), 2797–2920. https://doi.org/10.1021/cr970143c.

(49) Tanifum, E. A.; Patel, C.; Liaw, M. E.; Pautler, R. G.; Annapragada, A. V. Hydrophilic Fluorinated Molecules for Spectral 19F MRI. *Sci. Rep.* **2018**, *8* (1), 2889. https://doi.org/10.1038/s41598-018-21178-3.

(50) Bartusik, D.; Tomanek, B. Detection of (19)F-Labeled Biopharmaceuticals in Cell Cultures with Magnetic Resonance. *Adv. Drug Deliv. Rev.* **2013**, *65* (8), 1056–1064. https://doi.org/10.1016/j.addr.2013.04.010.

(51) Ahrens, E. T.; Flores, R.; Xu, H.; Morel, P. A. In Vivo Imaging Platform for Tracking Immunotherapeutic Cells. *Nat. Biotechnol.* **2005**, *23* (8), 983–987. https://doi.org/10.1038/nbt1121.

(52) Peng, H.; Blakey, I.; Dargaville, B.; Rasoul, F.; Rose, S.; Whittaker, A. K. Synthesis and Evaluation of Partly Fluorinated Block Copolymers as MRI Imaging Agents. *Biomacromolecules* **2009**, *10* (2), 374–381. https://doi.org/10.1021/bm801136m.

(53) Thurecht, K. J.; Blakey, I.; Peng, H.; Squires, O.; Hsu, S.; Alexander, C.; Whittaker, A. K. Functional Hyperbranched Polymers: Toward Targeted *in Vivo* ^{19} F Magnetic Resonance Imaging Using Designed Macromolecules. *J. Am. Chem. Soc.* **2010**, *132* (15), 5336–5337. https://doi.org/10.1021/ja100252y.

(54) Herneisey, M.; Salcedo, P. F.; Domenech, T.; Bagia, C.; George, S. S.; Tunney, R.; Velankar, S.; Hitchens, T. K.; Janjic, J. M. Design of Thermoresponsive Polyamine Cross-Linked Perfluoropolyether Hydrogels for Imaging and Delivery Applications. *ACS Med. Chem. Lett.* **2020**, *11* (10), 2032–2040. https://doi.org/10.1021/acsmedchemlett.0c00198.

(55) Reis, M.; Gusev, F.; Taylor, N. G.; Chung, S. H.; Verber, M. D.; Lee, Y. Z.; Isayev, O.; Leibfarth, F. A. Machine-Learning-Guided Discovery of ^{19} F MRI Agents Enabled by Automated Copolymer Synthesis. *J. Am. Chem. Soc.* **2021**, *143* (42), 17677–17689. https://doi.org/10.1021/jacs.1c08181.

(56) Li, H.; Frieden, C. Phenylalanine Side Chain Behavior of the Intestinal Fatty Acid-Binding Protein. *J. Biol. Chem.* **2005**, *280* (46), 38556–38561. https://doi.org/10.1074/jbc.M505435200.

(57) Herneisey, M.; Salcedo, P. F.; Domenech, T.; Bagia, C.; George, S. S.; Tunney, R.; Velankar, S.; Hitchens, T. K.; Janjic, J. M. Design of Thermoresponsive Polyamine Cross-Linked Perfluoropolyether Hydrogels for Imaging and Delivery Applications. *ACS Med. Chem. Lett.* **2020**, *11* (10), 2032–2040. https://doi.org/10.1021/acsmedchemlett.0c00198.

(58) Tirotta, I.; Mastropietro, A.; Cordiglieri, C.; Gazzera, L.; Baggi, F.; Baselli, G.; Bruzzone, M. G.; Zucca, I.; Cavallo, G.; Terraneo, G.; Baldelli Bombelli, F.; Metrangolo, P.; Resnati, G. A

Superfluorinated Molecular Probe for Highly Sensitive *in Vivo* ^{19} F-MRI. *J. Am. Chem. Soc.* **2014**, *136* (24), 8524–8527. https://doi.org/10.1021/ja503270n.

(59) Jiang, Z.-X.; Liu, X.; Jeong, E.-K.; Yu, Y. B. Symmetry-Guided Design and Fluorous Synthesis of a Stable and Rapidly Excreted Imaging Tracer for 19F MRI. *Angew. Chem. Int. Ed.* **2009**, *48* (26), 4755–4758. https://doi.org/10.1002/anie.200901005.

(60) Kadakia, R. T.; Xie, D.; Guo, H.; Bouley, B.; Yu, M.; Que, E. L. Responsive Fluorinated Nanoemulsions for ^{19} F Magnetic Resonance Detection of Cellular Hypoxia. *Dalton Trans.* **2020**, *49* (45), 16419–16424. https://doi.org/10.1039/D0DT01182G.

(61) Lee, A. L.; Pandey, A. K.; Chiniforoush, S.; Mandal, M.; Li, J.; Cramer, C. J.; Haynes, C. L.; Pomerantz, W. C. K. Development of a Highly Responsive Organofluorine Temperature Sensor for ^{19} F Magnetic Resonance Applications. *Anal. Chem.* **2022**, *94* (9), 3782–3790. https://doi.org/10.1021/acs.analchem.1c04248.

(62) Brizel, D. M.; Sibley, G. S.; Prosnitz, L. R.; Scher, R. L.; Dewhirst, M. W. Tumor Hypoxia Adversely Affects the Prognosis of Carcinoma of the Head and Neck. *Int. J. Radiat. Oncol. Biol. Phys.* **1997**, *38* (2), 285–289. https://doi.org/10.1016/s0360-3016(97)00101-6.

(63) Stone, H. B.; Brown, J. M.; Phillips, T. L.; Sutherland, R. M. Oxygen in Human Tumors: Correlations between Methods of Measurement and Response to Therapy. Summary of a Workshop Held November 19-20, 1992, at the National Cancer Institute, Bethesda, Maryland. *Radiat. Res.* **1993**, *136* (3), 422–434.

(64) Mason, R. P.; Zhao, D.; Pacheco-Torres, J.; Cui, W.; Kodibagkar, V. D.; Gulaka, P. K.; Hao, G.; Thorpe, P.; Hahn, E. W.; Peschke, P. Multimodality Imaging of Hypoxia in Preclinical Settings. *Q. J. Nucl. Med. Mol. Imaging Off. Publ. Ital. Assoc. Nucl. Med. AIMN Int. Assoc. Radiopharmacol. IAR Sect. Soc. Of* **2010**, *54* (3), 259–280.

(65) Hunjan, S.; Mason, R. P.; Constantinescu, A.; Peschke, P.; Hahn, E. W.; Antich, P. P. Regional Tumor Oximetry: 19F NMR Spectroscopy of Hexafluorobenzene 11Presented in Part at the International Society for Magnetic Resonance in Medicine Workshop on Cancer Physiology and Metabolism, Baltimore, MD, 7–9 August 1996. *Int. J. Radiat. Oncol.* **1998**, *41* (1), 161–171. https://doi.org/10.1016/S0360-3016(98)00020-0.

(66) Zhao, D.; Jiang, L.; P. Mason, R. Measuring Changes in Tumor Oxygenation. In *Methods in Enzymology*; Elsevier, 2004; Vol. 386, pp 378–418. https://doi.org/10.1016/S0076-6879(04)86018-X.

(67) Rieke, V.; Butts Pauly, K. MR Thermometry. *J. Magn. Reson. Imaging* **2008**, *27* (2), 376–390. https://doi.org/10.1002/jmri.21265.

(68) Berkowitz, B. A.; Handa, J. T.; Wilson, C. A. Perfluorocarbon Temperature Measurements Using 19F NMR. *NMR Biomed.* **1992**, *5* (2), 65–68. https://doi.org/10.1002/nbm.1940050204.

(69) Hong, A. C.; Young, C. J.; Hurley, M. D.; Wallington, T. J.; Mabury, S. A. Perfluorotributylamine: A Novel Long-Lived Greenhouse Gas. *Geophys. Res. Lett.* **2013**, *40* (22), 6010–6015. https://doi.org/10.1002/2013GL058010.

(70) Mizukami, S.; Takikawa, R.; Sugihara, F.; Hori, Y.; Tochio, H.; Wälchli, M.; Shirakawa, M.; Kikuchi, K. Paramagnetic Relaxation-Based ^{19} F MRI Probe To Detect Protease Activity. *J. Am. Chem. Soc.* **2008**, *130* (3), 794–795. https://doi.org/10.1021/ja077058z.

(71) Yue, X.; Wang, Z.; Zhu, L.; Wang, Y.; Qian, C.; Ma, Y.; Kiesewetter, D. O.; Niu, G.; Chen, X. Novel ^{19} F Activatable Probe for the Detection of Matrix Metalloprotease-2 Activity by MRI/MRS. *Mol. Pharm.* **2014**, *11* (11), 4208–4217. https://doi.org/10.1021/mp500443x.

(72) Preslar, A. T.; Lilley, L. M.; Sato, K.; Zhang, S.; Chia, Z. K.; Stupp, S. I.; Meade, T. J. Calcium-Induced Morphological Transitions in Peptide Amphiphiles Detected by 19F-Magnetic Resonance Imaging. *ACS Appl. Mater. Interfaces* **2017**, *9* (46), 39890–39894. https://doi.org/10.1021/acsami.7b07828.

(73) Frieden, C.; Hoeltzli, S. D.; Ropson, I. J. NMR and Protein Folding: Equilibrium and Stopped-Flow Studies. *Protein Sci.* **1993**, *2* (12), 2007–2014. https://doi.org/10.1002/pro.5560021202.

(74) Kirberger, S. E.; Maltseva, S. D.; Manulik, J. C.; Einstein, S. A.; Weegman, B. P.; Garwood, M.; Pomerantz, W. C. K. Synthesis of Intrinsically Disordered Fluorinated Peptides for Modular Design of High-Signal 19F MRI Agents. *Angew. Chem. Int. Ed.* **2017**, *56* (23), 6440–6444. https://doi.org/10.1002/anie.201700426.

(75) Meng, B.; Grage, S. L.; Babii, O.; Takamiya, M.; MacKinnon, N.; Schober, T.; Hutskalov, I.; Nassar, O.; Afonin, S.; Koniev, S.; Komarov, I. V.; Korvink, J. G.; Strähle, U.; Ulrich, A. S. Highly

Fluorinated Peptide Probes with Enhanced In Vivo Stability for 19F-MRI. *Small* **2022**, *18* (41), 2107308. https://doi.org/10.1002/smll.202107308.

(76) Merrifield, R. B. **Solid Phase Peptide Synthesis. I. The Synthesis of a Tetrapeptide**. *J. Am. Chem. Soc.* **1963**, *85* (14), 2149–2154. https://doi.org/10.1021/ja00897a025.

(77) Mueller, L. K.; Baumruck, A. C.; Zhdanova, H.; Tietze, A. A. Challenges and Perspectives in Chemical Synthesis of Highly Hydrophobic Peptides. *Front. Bioeng. Biotechnol.* **2020**, *8*, 162. https://doi.org/10.3389/fbioe.2020.00162.

(78) Bray, F.; Ferlay, J.; Soerjomataram, I.; Siegel, R. L.; Torre, L. A.; Jemal, A. Global Cancer Statistics 2018: GLOBOCAN Estimates of Incidence and Mortality Worldwide for 36 Cancers in 185 Countries. *CA. Cancer J. Clin.* **2018**, *68* (6), 394–424. https://doi.org/10.3322/caac.21492.

(79) Dai, X.; Xiang, L.; Li, T.; Bai, Z. Cancer Hallmarks, Biomarkers and Breast Cancer Molecular Subtypes. *J. Cancer* **2016**, *7* (10), 1281–1294. https://doi.org/10.7150/jca.13141.

(80) Sigismund, S.; Avanzato, D.; Lanzetti, L. Emerging Functions of the EGFR in Cancer. *Mol. Oncol.* **2018**, *12* (1), 3–20. https://doi.org/10.1002/1878-0261.12155.

(81) Carlson, J. C. T.; Jena, S. S.; Flenniken, M.; Chou, T.; Siegel, R. A.; Wagner, C. R. Chemically Controlled Self-Assembly of Protein Nanorings. *J. Am. Chem. Soc.* **2006**, *128* (23), 7630–7638. https://doi.org/10.1021/ja060631e.

(82) Shah, R.; Petersburg, J.; Gangar, A. C.; Fegan, A.; Wagner, C. R.; Kumarapperuma, S. C. *In Vivo* Evaluation of Site-Specifically PEGylated Chemically Self-Assembled Protein Nanostructures. *Mol. Pharm.* **2016**, *13* (7), 2193–2203. https://doi.org/10.1021/acs.molpharmaceut.6b00110.

(83) Shen, J.; Vallera, D. A.; Wagner, C. R. Prosthetic Antigen Receptors. *J. Am. Chem. Soc.* **2015**, *137* (32), 10108–10111. https://doi.org/10.1021/jacs.5b06166.

(84) Petersburg, J. R.; Shen, J.; Csizmar, C. M.; Murphy, K. A.; Spanier, J.; Gabrielse, K.; Griffith, T. S.; Fife, B.; Wagner, C. R. Eradication of Established Tumors by Chemically Self-Assembled Nanoring Labeled T Cells. *ACS Nano* **2018**, *12* (7), 6563–6576. https://doi.org/10.1021/acsnano.8b01308.

(85) Fegan, A.; Kumarapperuma, S. C.; Wagner, C. R. Chemically Self-Assembled Antibody Nanostructures as Potential Drug Carriers. *Mol. Pharm.* **2012**, *9* (11), 3218–3227. https://doi.org/10.1021/mp300303k.

(86) Li, Z.; Krippendorff, B.-F.; Shah, D. K. Influence of Molecular Size on the Clearance of Antibody Fragments. *Pharm. Res.* **2017**, *34* (10), 2131–2141. https://doi.org/10.1007/s11095-017-2219-y.

(87) Weissleder, R.; Mahmood, U. Molecular Imaging. *Radiology* **2001**, *219* (2), 316–333. https://doi.org/10.1148/radiology.219.2.r01ma19316.

(88) Villaraza, A. J. L.; Bumb, A.; Brechbiel, M. W. Macromolecules, Dendrimers and Nanomaterials in Magnetic Resonance Imaging: The Interplay Between Size, Function and Pharmacokinetics. *Chem. Rev.* **2010**, *110* (5), 2921–2959. https://doi.org/10.1021/cr900232t.

(89) Kilcoyne, R. F.; Richardson, M. L.; Porter, B. A.; Olson, D. O.; Greenlee, T. K.; Lanzer, W. Magnetic Resonance Imaging of Soft Tissue Masses. *Clin. Orthop.* **1988**, No. 228, 13–19.

(90) Webb, A. Increasing the Sensitivity of Magnetic Resonance Spectroscopy and Imaging. *Anal. Chem.* **2012**, *84* (1), 9–16. https://doi.org/10.1021/ac201500v.

(91) Terreno, E.; Castelli, D. D.; Viale, A.; Aime, S. Challenges for Molecular Magnetic Resonance Imaging. *Chem. Rev.* **2010**, *110* (5), 3019–3042. https://doi.org/10.1021/cr100025t.

(92) Caravan, P. Strategies for Increasing the Sensitivity of Gadolinium Based MRI Contrast Agents. *Chem. Soc. Rev.* **2006**, *35* (6), 512–523. https://doi.org/10.1039/B510982P.

(93) Caravan, P.; Ellison, J. J.; McMurry, T. J.; Lauffer, R. B. Gadolinium(III) Chelates as MRI Contrast Agents: Structure, Dynamics, and Applications. *Chem. Rev.* **1999**, *99* (9), 2293–2352. https://doi.org/10.1021/cr980440x.

(94) Wang, Y.-X. J. Superparamagnetic Iron Oxide Based MRI Contrast Agents: Current Status of Clinical Application. *Quant. Imaging Med. Surg.* **2011**, *1* (1), 35–40. https://doi.org/10.3978/j.issn.2223-4292.2011.08.03.

(95) Rogosnitzky, M.; Branch, S. Gadolinium-Based Contrast Agent Toxicity: A Review of Known and Proposed Mechanisms. *Biometals* **2016**, *29*, 365–376. https://doi.org/10.1007/s10534-016-9931-7.

(96) Placidi, M. P.; Botta, M.; Kálmán, F. K.; Hagberg, G. E.; Baranyai, Z.; Krenzer, A.; Rogerson, A. K.; Tóth, I.; Logothetis, N. K.; Angelovski, G. Aryl-Phosphonate Lanthanide Complexes and Their Fluorinated Derivatives: Investigation of Their Unusual Relaxometric Behavior and Potential Application as Dual Frequency 1H/19F MRI Probes. *Chem. – Eur. J.* **2013**, *19* (35), 11644–11660. https://doi.org/10.1002/chem.201300763.

(97) Rolfe, B. E.; Blakey, I.; Squires, O.; Peng, H.; Boase, N. R. B.; Alexander, C.; Parsons, P. G.; Boyle, G. M.; Whittaker, A. K.; Thurecht, K. J. Multimodal Polymer Nanoparticles with Combined ^{19} F Magnetic Resonance and Optical Detection for Tunable, Targeted, Multimodal Imaging *in Vivo*. *J. Am. Chem. Soc.* **2014**, *136* (6), 2413–2419. https://doi.org/10.1021/ja410351h.

(98) Koshkina, O.; Lajoinie, G.; Baldelli Bombelli, F.; Swider, E.; Cruz, L. J.; White, P. B.; Schweins, R.; Dolen, Y.; van Dinther, E. A. W.; van Riessen, N. K.; Rogers, S. E.; Fokkink, R.; Voets, I. K.; van Eck, E. R. H.; Heerschap, A.; Versluis, M.; de Korte, C. L.; Figdor, C. G.; de Vries, I. J. M.; Srinivas, M. Multicore Liquid Perfluorocarbon-Loaded Multimodal Nanoparticles for Stable Ultrasound and 19F MRI Applied to In Vivo Cell Tracking. *Adv. Funct. Mater.* **2019**, *29* (19), 1806485. https://doi.org/10.1002/adfm.201806485.

(99) Barnett, B. P.; Ruiz-Cabello, J.; Hota, P.; Ouwerkerk, R.; Shamblott, M. J.; Lauzon, C.; Walczak, P.; Gilson, W. D.; Chacko, V. P.; Kraitchman, D. L.; Arepally, A.; Bulte, J. W. M. Use of Perfluorocarbon Nanoparticles for Non-Invasive Multimodal Cell Tracking of Human Pancreatic Islets. *Contrast Media Mol. Imaging* **2011**, *6* (4), 251–259. https://doi.org/10.1002/cmmi.424.

(100) Swider, E.; Daoudi, K.; Staal, A. H. J.; Koshkina, O.; van Riessen, N. K.; van Dinther, E.; de Vries, I. J. M.; de Korte, C. L.; Srinivas, M. Clinically-Applicable Perfluorocarbon-Loaded Nanoparticles For In Vivo Photoacoustic, 19F Magnetic Resonance And Fluorescent Imaging. *Nanotheranostics* **2018**, *2* (3), 258–268. https://doi.org/10.7150/ntno.26208.

(101) Mastropietro, A.; De Bernardi, E.; Breschi, G. L.; Zucca, I.; Cametti, M.; Soffientini, C. D.; de Curtis, M.; Terraneo, G.; Metrangolo, P.; Spreafico, R.; Resnati, G.; Baselli, G. Optimization of Rapid Acquisition with Relaxation Enhancement (RARE) Pulse Sequence Parameters for 19F-MRI Studies. *J. Magn. Reson. Imaging* **2014**, *40* (1), 162–170. https://doi.org/10.1002/jmri.24347.

(102) Kaneda, M. M.; Caruthers, S.; Lanza, G. M.; Wickline, S. A. Perfluorocarbon Nanoemulsions for Quantitative Molecular Imaging and Targeted Therapeutics. *Ann. Biomed. Eng.* **2009**, *37* (10), 1922–1933. https://doi.org/10.1007/s10439-009-9643-z.

(103) Fu, C.; Zhang, C.; Peng, H.; Han, F.; Baker, C.; Wu, Y.; Ta, H.; Whittaker, A. K. Enhanced Performance of Polymeric ^{19} F MRI Contrast Agents through Incorporation of Highly Water-Soluble

Monomer MSEA. *Macromolecules* **2018**, *51* (15), 5875–5882. https://doi.org/10.1021/acs.macromol.8b01190.

(104) *Superhydrophilic fluorinated polymer and nanogel for high-performance 19F magnetic resonance imaging | Elsevier Enhanced Reader*. https://doi.org/10.1016/j.biomaterials.2020.120184.

(105) Fu, C.; Herbst, S.; Zhang, C.; Whittaker, A. K. Polymeric 19F MRI Agents Responsive to Reactive Oxygen Species. *Polym. Chem.* **2017**, *8* (31), 4585–4595. https://doi.org/10.1039/C7PY00986K.

(106) Maki, J.; Masuda, C.; Morikawa, S.; Morita, M.; Inubushi, T.; Matsusue, Y.; Taguchi, H.; Tooyama, I. The MR Tracking of Transplanted ATDC5 Cells Using Fluorinated Poly-L-Lysine-CF3. *Biomaterials* **2007**, *28* (3), 434–440. https://doi.org/10.1016/j.biomaterials.2006.08.050.

(107) Hill, L. K.; Frezzo, J. A.; Katyal, P.; Hoang, D. M.; Ben Youss Gironda, Z.; Xu, C.; Xie, X.; Delgado-Fukushima, E.; Wadghiri, Y. Z.; Montclare, J. K. Protein-Engineered Nanoscale Micelles for Dynamic ^{19} F Magnetic Resonance and Therapeutic Drug Delivery. *ACS Nano* **2019**, *13* (3), 2969–2985. https://doi.org/10.1021/acsnano.8b07481.

(108) Papeo, G.; Giordano, P.; Brasca, M. G.; Buzzo, F.; Caronni, D.; Ciprandi, F.; Mongelli, N.; Veronesi, M.; Vulpetti, A.; Dalvit, C. Polyfluorinated Amino Acids for Sensitive ^{19} F NMR-Based Screening and Kinetic Measurements. *J. Am. Chem. Soc.* **2007**, *129* (17), 5665–5672. https://doi.org/10.1021/ja069128s.

(109) Tressler, C. M.; Zondlo, N. J. Perfluoro- *Tert* -Butyl Hydroxyprolines as Sensitive, Conformationally Responsive Molecular Probes: Detection of Protein Kinase Activity by ^{19} F NMR. *ACS Chem. Biol.* **2020**, *15* (4), 1096–1103. https://doi.org/10.1021/acschembio.0c00131.

(110) Taylor, N. G.; Chung, S. H.; Kwansa, A. L.; Johnson III, R. R.; Teator, A. J.; Milliken, N. J. B.; Koshlap, K. M.; Yingling, Y. G.; Lee, Y. Z.; Leibfarth, F. A. Partially Fluorinated Copolymers as Oxygen Sensitive 19F MRI Agents. *Chem. – Eur. J.* **2020**, *26* (44), 9982–9990. https://doi.org/10.1002/chem.202001505.

(111) Buer, B. C.; Levin, B. J.; Marsh, E. N. G. Perfluoro- *Tert* -Butyl-Homoserine as a Sensitive ^{19} F NMR Reporter for Peptide-Membrane Interactions in Solution: A SENSITIVE ^{19} F NMR REPORTER FOR PEPTIDE-MEMBRANE INTERACTIONS. *J. Pept. Sci.* **2013**, *19* (5), 308–314. https://doi.org/10.1002/psc.2501.

(112) Tada, N.; Horibe, T.; Haramoto, M.; Ohara, K.; Kohno, M.; Kawakami, K. A Single Replacement of Histidine to Arginine in EGFR-Lytic Hybrid Peptide Demonstrates the Improved Anticancer Activity. *Biochem. Biophys. Res. Commun.* **2011**, *407* (2), 383–388. https://doi.org/10.1016/j.bbrc.2011.03.030.

(113) Hossein-Nejad-Ariani, H.; Althagafi, E.; Kaur, K. Small Peptide Ligands for Targeting EGFR in Triple Negative Breast Cancer Cells. *Sci. Rep.* **2019**, *9* (1), 2723. https://doi.org/10.1038/s41598-019-38574-y.

(114) Kilic, O.; Matos de Souza, M. R.; Almotlak, A. A.; Wang, Y.; Siegfried, J. M.; Distefano, M. D.; Wagner, C. R. Anti-EGFR Fibronectin Bispecific Chemically Self-Assembling Nanorings (CSANs) Induce Potent T Cell-Mediated Antitumor Responses and Downregulation of EGFR Signaling and PD-1/PD-L1 Expression. *J. Med. Chem.* **2020**, *63* (18), 10235–10245. https://doi.org/10.1021/acs.jmedchem.0c00489.

(115) Molecular Imaging: Current Status and Emerging Strategies. *Clin. Radiol.* **2010**, *65* (7), 500–516. https://doi.org/10.1016/j.crad.2010.03.011.

(116) Katti, G.; Ara, S.; Shireen, D. Magnetic Resonance Imaging (MRI) - A Review. *Intl J Dent. Clin* **2011**, *3*.

(117) Maly, T.; Debelouchina, G. T.; Bajaj, V. S.; Hu, K.-N.; Joo, C.-G.; Mak–Jurkauskas, M. L.; Sirigiri, J. R.; van der Wel, P. C. A.; Herzfeld, J.; Temkin, R. J.; Griffin, R. G. Dynamic Nuclear Polarization at High Magnetic Fields. *J. Chem. Phys.* **2008**, *128* (5), 052211. https://doi.org/10.1063/1.2833582.

(118) Webb, A. G. Microcoil Nuclear Magnetic Resonance Spectroscopy. *J. Pharm. Biomed. Anal.* **2005**, *38* (5), 892–903. https://doi.org/10.1016/j.jpba.2005.01.048.

(119) Grant, S. C.; Aiken, N. R.; Plant, H. D.; Gibbs, S.; Mareci, T. H.; Webb, A. G.; Blackband, S. J. NMR Spectroscopy of Single Neurons. *Magn. Reson. Med.* **2000**, *44* (1), 19–22. https://doi.org/10.1002/1522-2594(200007)44:1<19::AID-MRM4>3.0.CO;2-F.

(120) Freeman, R.; Kupče, E. New Methods for Fast Multidimensional NMR. *J. Biomol. NMR* **2003**, *27* (2), 101–114. https://doi.org/10.1023/A:1024960302926.

(121) Mishkovsky, M.; Frydman, L. Principles and Progress in Ultrafast Multidimensional Nuclear Magnetic Resonance. *Annu. Rev. Phys. Chem.* **2009**, *60* (1), 429–448. https://doi.org/10.1146/annurev.physchem.040808.090420.

(122) Brünjes, R.; Hofmann, T. Anthropogenic Gadolinium in Freshwater and Drinking Water Systems. *Water Res.* **2020**, *182*, 115966. https://doi.org/10.1016/j.watres.2020.115966.

(123) McDonald, R. J.; McDonald, J. S.; Kallmes, D. F.; Jentoft, M. E.; Murray, D. L.; Thielen, K. R.; Williamson, E. E.; Eckel, L. J. Intracranial Gadolinium Deposition after Contrast-Enhanced MR Imaging. *Radiology* **2015**, *275* (3), 772–782. https://doi.org/10.1148/radiol.15150025.

(124) Kanda, T.; Fukusato, T.; Matsuda, M.; Toyoda, K.; Oba, H.; Kotoku, J.; Haruyama, T.; Kitajima, K.; Furui, S. Gadolinium-Based Contrast Agent Accumulates in the Brain Even in Subjects without Severe Renal Dysfunction: Evaluation of Autopsy Brain Specimens with Inductively Coupled Plasma Mass Spectroscopy. *Radiology* **2015**, *276* (1), 228–232. https://doi.org/10.1148/radiol.2015142690.

(125) Blumfield, E.; Swenson, D. W.; Iyer, R. S.; Stanescu, A. L. Gadolinium-Based Contrast Agents — Review of Recent Literature on Magnetic Resonance Imaging Signal Intensity Changes and Tissue Deposits, with Emphasis on Pediatric Patients. *Pediatr. Radiol.* **2019**, *49* (4), 448–457. https://doi.org/10.1007/s00247-018-4304-8.

(126) Chalmers, K. H.; Kenwright, A. M.; Parker, D.; Blamire, A. M. 19F-Lanthanide Complexes with Increased Sensitivity for 19F-MRI: Optimization of the MR Acquisition. *Magn. Reson. Med.* **2011**, *66* (4), 931–936. https://doi.org/10.1002/mrm.22881.

(127) Srinivas, M.; Heerschap, A.; Ahrens, E. T.; Figdor, C. G.; Vries, I. J. M. D. 19F MRI for Quantitative in Vivo Cell Tracking. *Trends Biotechnol.* **2010**, *28* (7), 363–370. https://doi.org/10.1016/j.tibtech.2010.04.002.

(128) Fu, C.; Yu, Y.; Xu, X.; Wang, Q.; Chang, Y.; Zhang, C.; Zhao, J.; Peng, H.; Whittaker, A. K. Functional Polymers as Metal-Free Magnetic Resonance Imaging Contrast Agents. *Prog. Polym. Sci.* **2020**, *108*, 101286. https://doi.org/10.1016/j.progpolymsci.2020.101286.

(129) Yu, W.; Yang, Y.; Bo, S.; Li, Y.; Chen, S.; Yang, Z.; Zheng, X.; Jiang, Z.-X.; Zhou, X. Design and Synthesis of Fluorinated Dendrimers for Sensitive ^{19}F MRI. *J. Org. Chem.* **2015**, *80* (9), 4443–4449. https://doi.org/10.1021/acs.joc.5b00294.

(130) Wang, Y.; Kilic, O.; Csizmar, C. M.; Ashok, S.; Hougland, J. L.; Distefano, M. D.; Wagner, C. R. Engineering Reversible Cell–Cell Interactions Using Enzymatically Lipidated Chemically Self-Assembled Nanorings. *Chem. Sci.* **2021**, *12* (1), 331–340. https://doi.org/10.1039/D0SC03194A.

(131) Salwiczek, M.; K. Nyakatura, E.; M. Gerling, U. I.; Ye, S.; Koksch, B. Fluorinated Amino Acids : Compatibility with Native Protein Structures and Effects on Protein – Protein Interactions. *Chem. Soc. Rev.* **2012**, *41* (6), 2135–2171. https://doi.org/10.1039/C1CS15241F.

(132) Csizmar, C. M.; Petersburg, J. R.; Perry, T. J.; Rozumalski, L.; Hackel, B. J.; Wagner, C. R. Multivalent Ligand Binding to Cell Membrane Antigens: Defining the Interplay of Affinity, Valency, and Expression Density. *J. Am. Chem. Soc.* **2019**, *141* (1), 251–261. https://doi.org/10.1021/jacs.8b09198.

(133) Wang, J.; Iwasaki, H.; Krivtsov, A.; Febbo, P. G.; Thorner, A. R.; Ernst, P.; Anastasiadou, E.; Kutok, J. L.; Kogan, S. C.; Zinkel, S. S.; Fisher, J. K.; Hess, J. L.; Golub, T. R.; Armstrong, S. A.; Akashi, K.; Korsmeyer, S. J. Conditional MLL-CBP Targets GMP and Models Therapy-Related Myeloproliferative Disease. *EMBO J.* **2005**, *24* (2), 368–381. https://doi.org/10.1038/sj.emboj.7600521.

(134) Perell, G. T.; Staebell, R. L.; Hairani, M.; Cembran, A.; Pomerantz, W. C. K. Tuning Sulfur Oxidation States on Thioether-Bridged Peptide Macrocycles for Modulation of Protein Interactions. *ChemBioChem* **2017**, *18* (18), 1836–1844. https://doi.org/10.1002/cbic.201700222.

Chapter 5

Appendix

5.1 Spectral Characterization

5.1.1 Fluorous Liquids for Magnetic Resonance-based Thermometry with Enhanced Responsiveness and Environmental Degradation

pentafluorophenyl sulfone

^{19}F NMR, 471 MHz, Chloroform-*d*

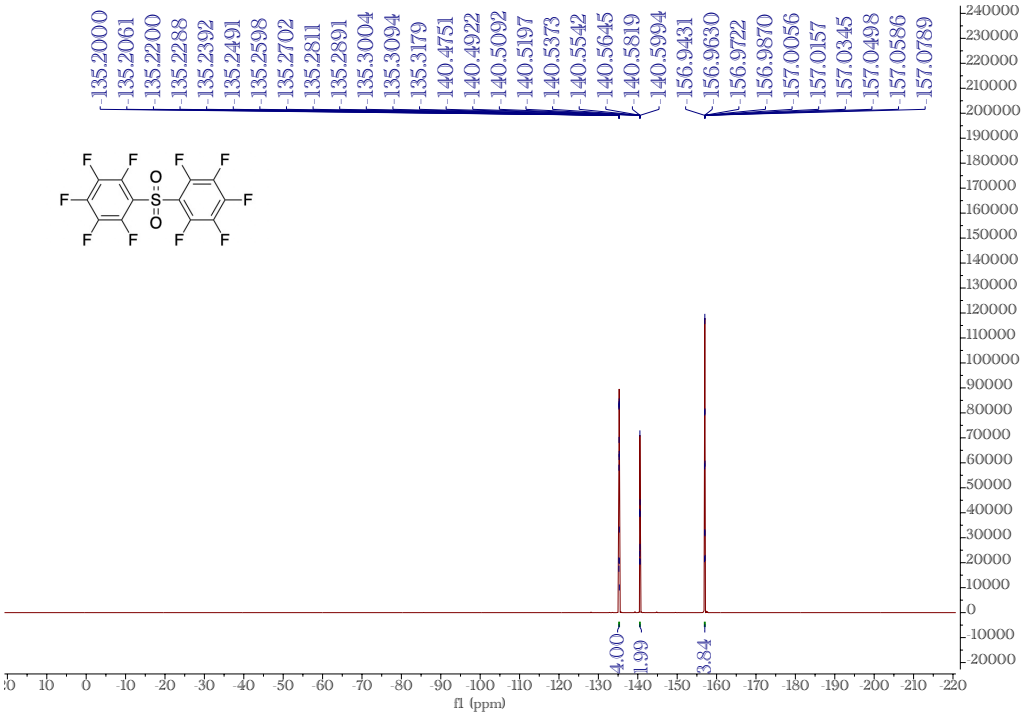

^{13}C NMR, 126 MHz, Chloroform-*d*

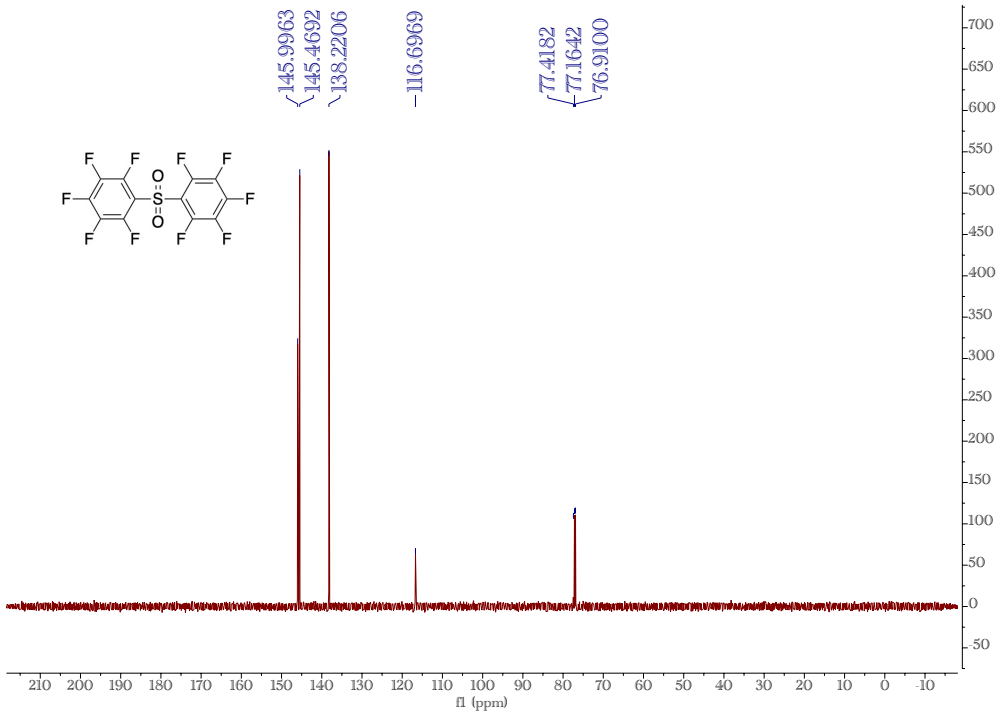

perfluoro-1,4-phenylene)bis((4,4,5,5,5-pentafluoropentyl)sulfane (DD-1)

^{1}H NMR, 500 MHz, Chloroform-*d*

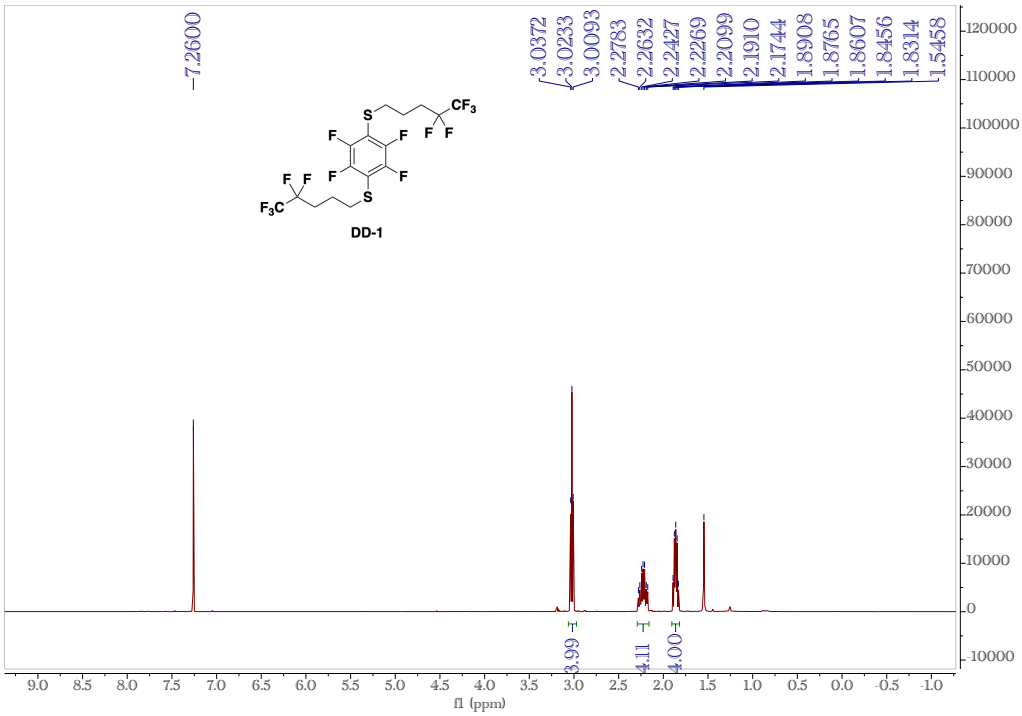

^{13}C NMR, 126 MHz, THF-d_8

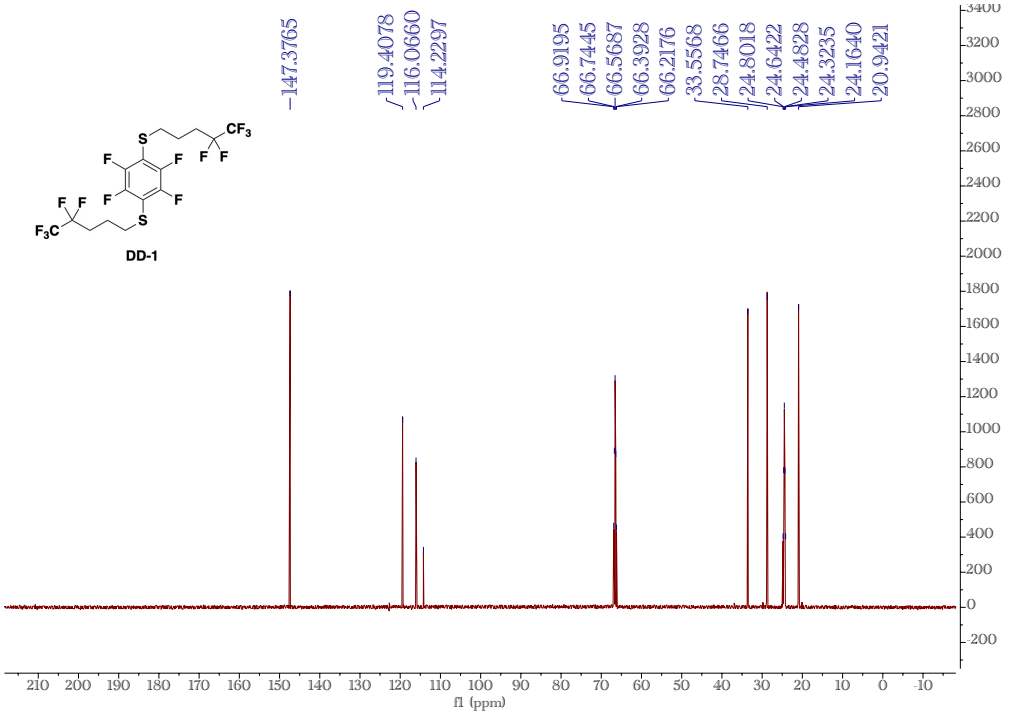

^{19}F NMR, 471 MHz, Chloroform-d

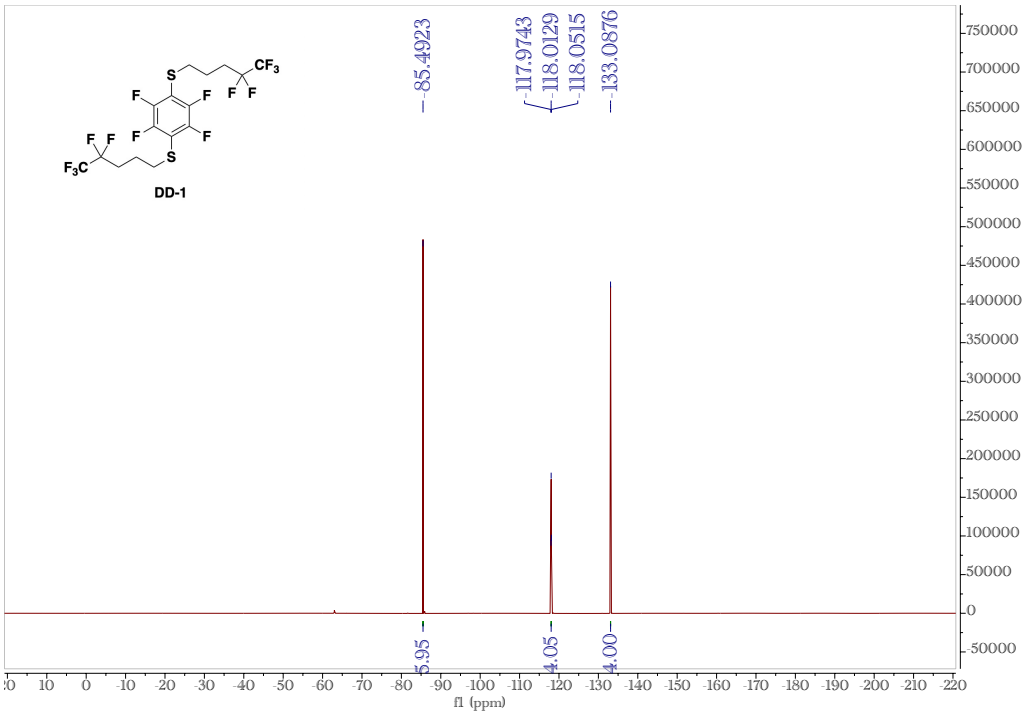

1,2,4,5-tetrafluoro-3,6-bis((4,4,5,5,5-pentafluoropentyl)sulfonyl)benzene (DD-2)

^{1}H NMR, 500 MHz, THF-d_8

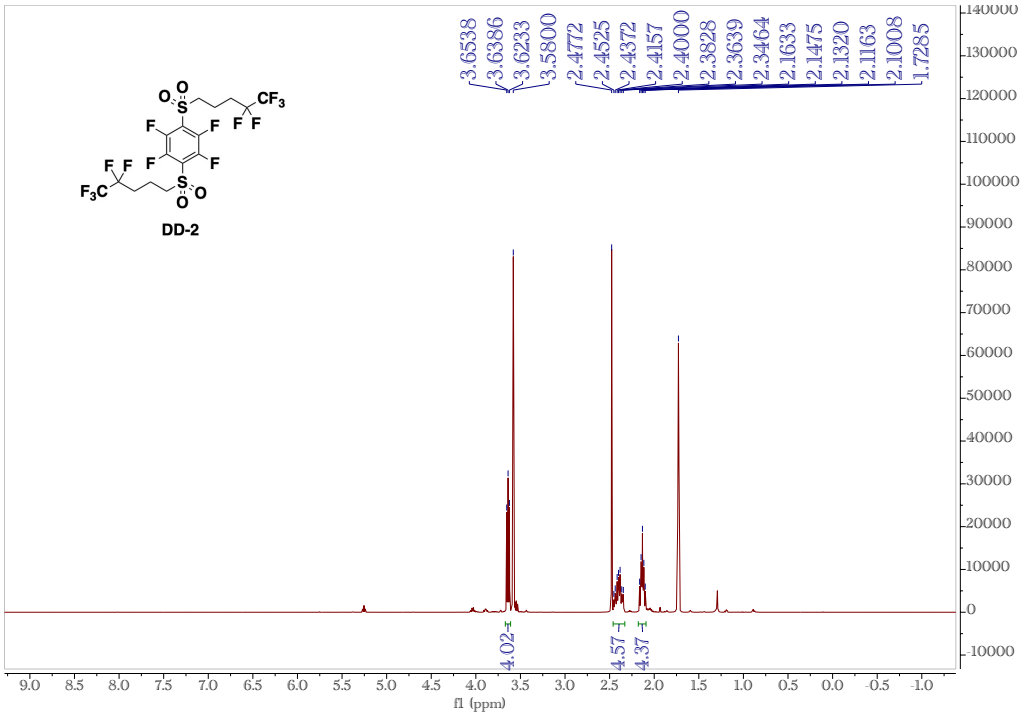

^{13}C NMR, 126 MHz, THF-d_8

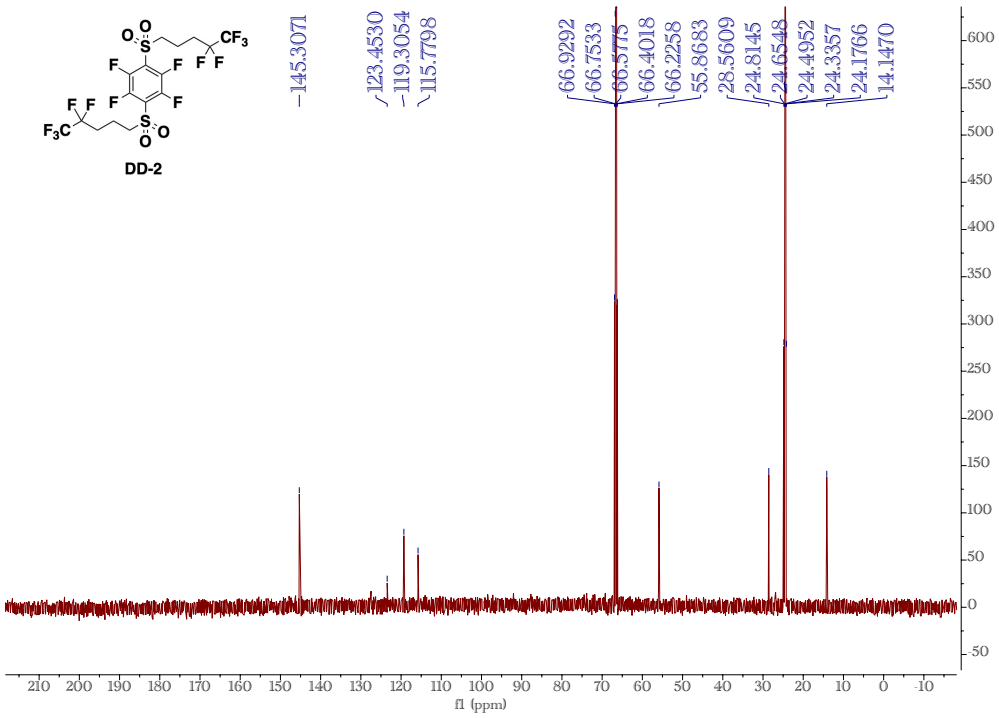

^{19}F NMR, 471 MHz, THF-d_8

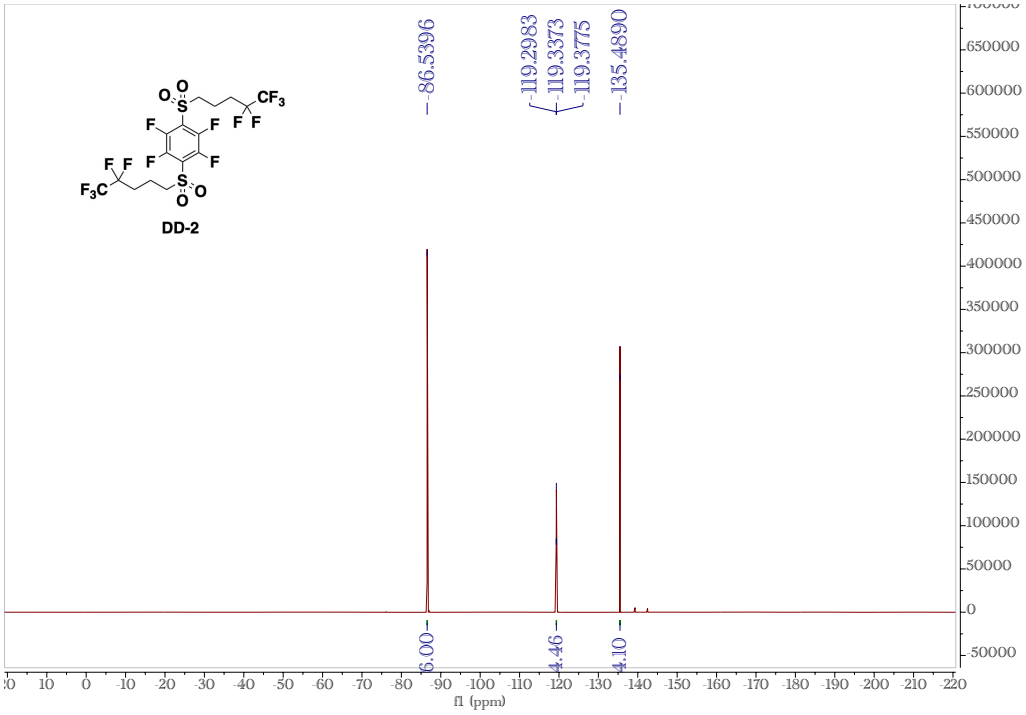

perfluoro-[1,1'-biphenyl]-4,4'-diyl)bis((4,4,5,5,5-pentafluoropentyl)sulfane (DD-3)

^{1}H NMR, 500 MHz, Chloroform-*d*

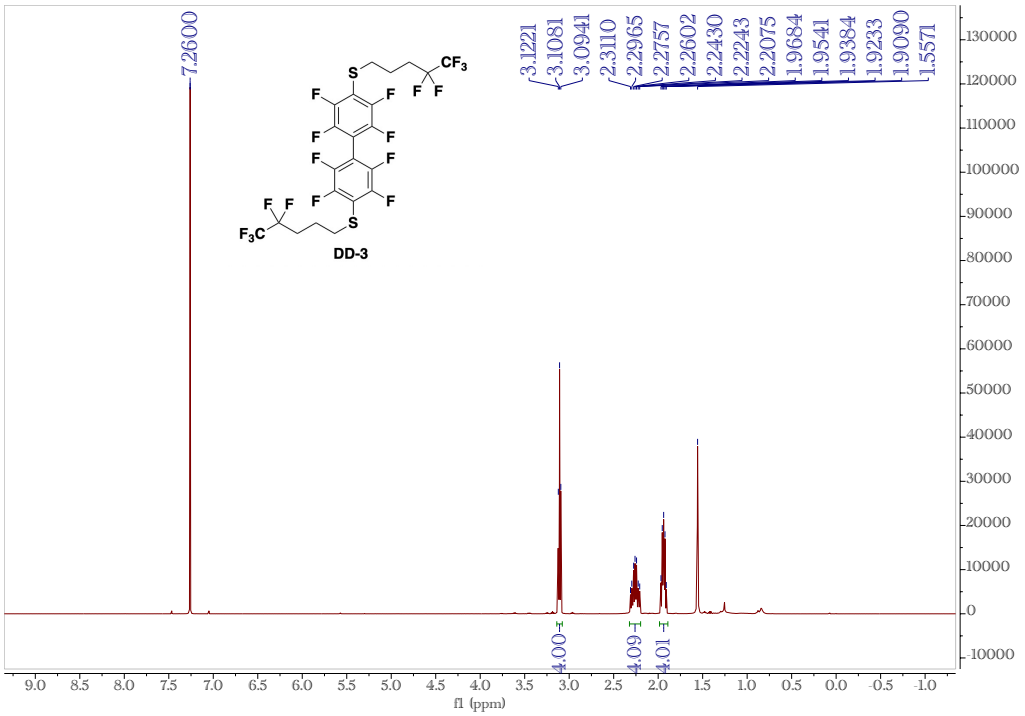

^{13}C NMR, 126 MHz, THF-d_8

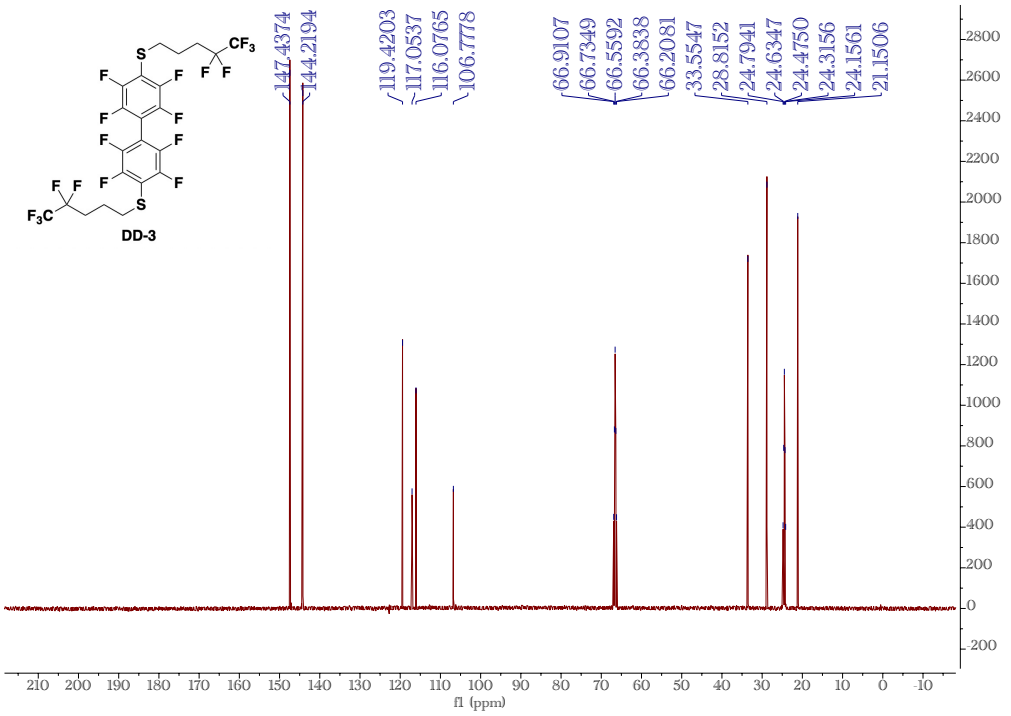

^{19}F NMR, 471 MHz, Chloroform-d

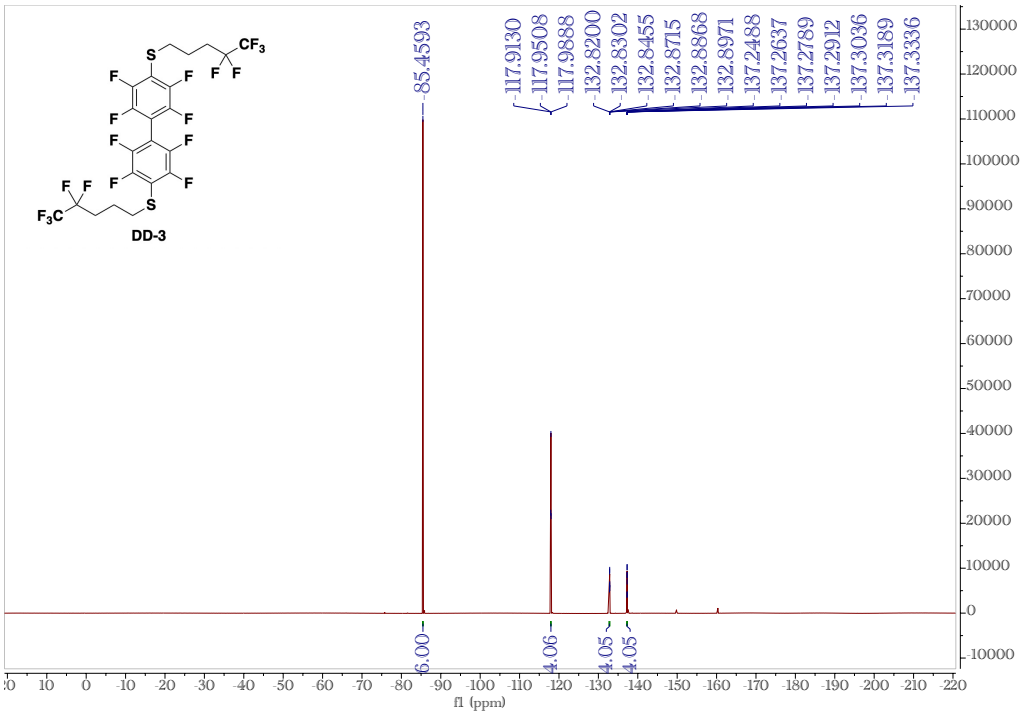

2,2',3,3',5,5',6,6'-octafluoro-4,4'-bis((4,4,5,5,5-pentafluoropentyl)sulfonyl)-1,1'-biphenyl (DD-4)

^{1}H NMR, 500 MHz, THF-d_8

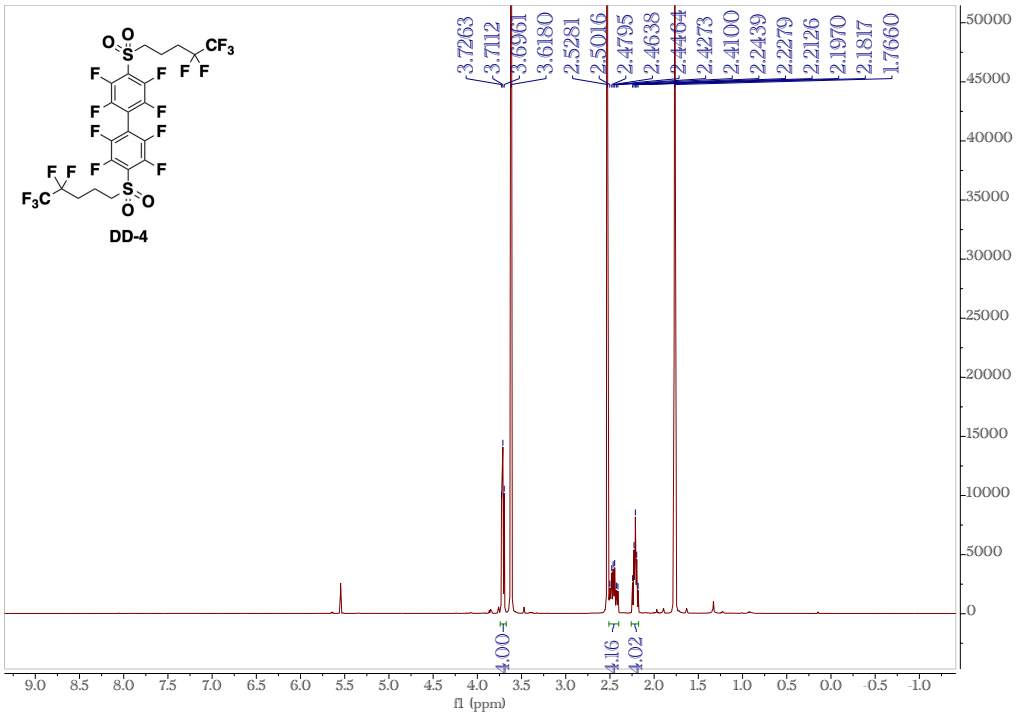

^{13}C NMR, 126 MHz, THF-d_8

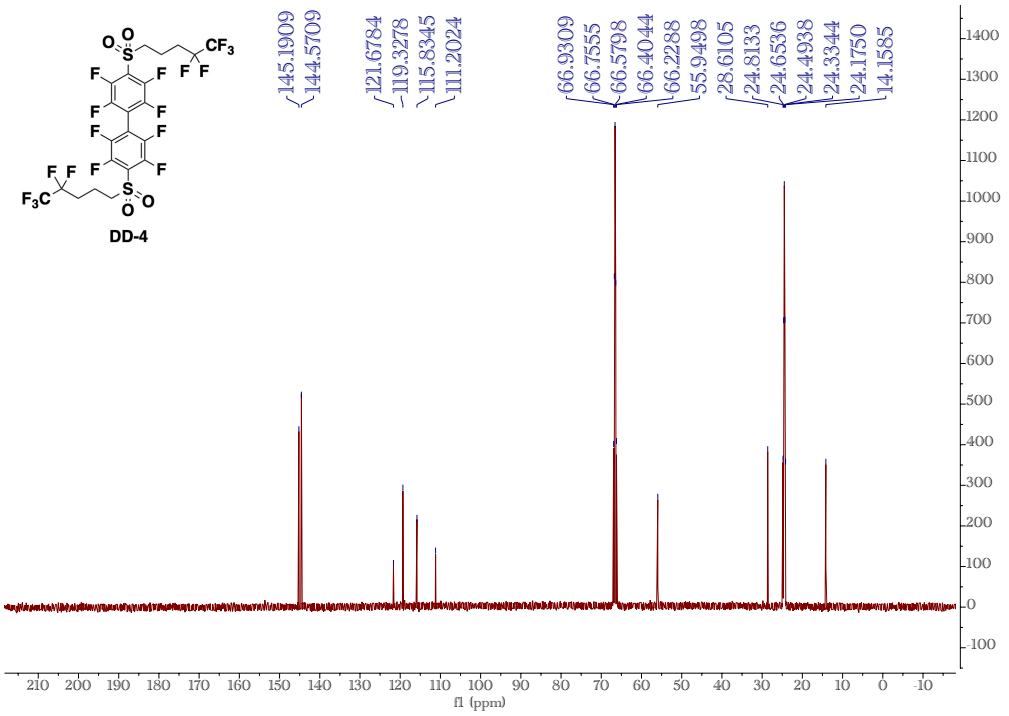

^{19}F NMR, 471 MHz, THF-d_8

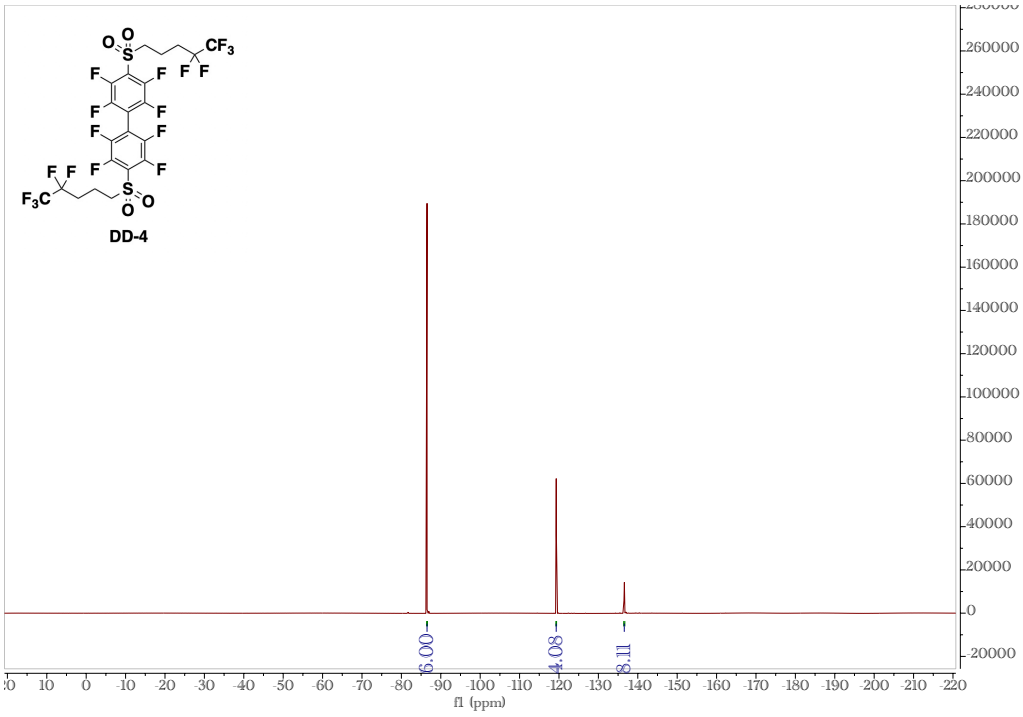

bis(2,3,5,6-tetrafluoro-4-((4,4,5,5,5-pentafluoropentyl)thio)phenyl)sulfane (DD-5)

^{1}H NMR, 500 MHz, THF-d_8

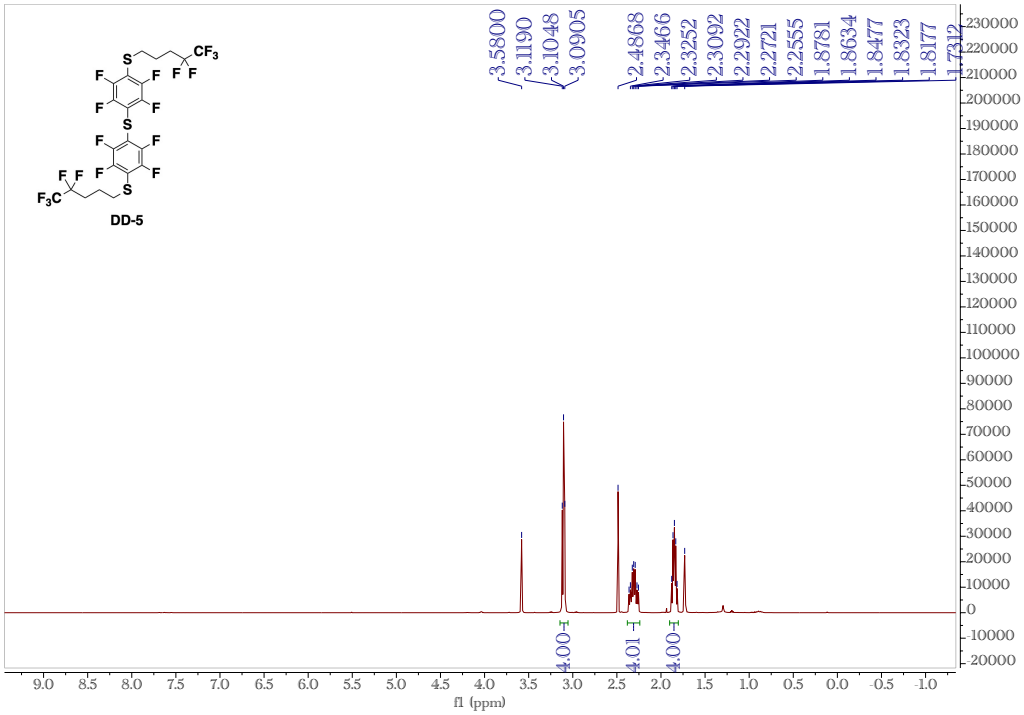

^{13}C NMR, 126 MHz, THF-d_8

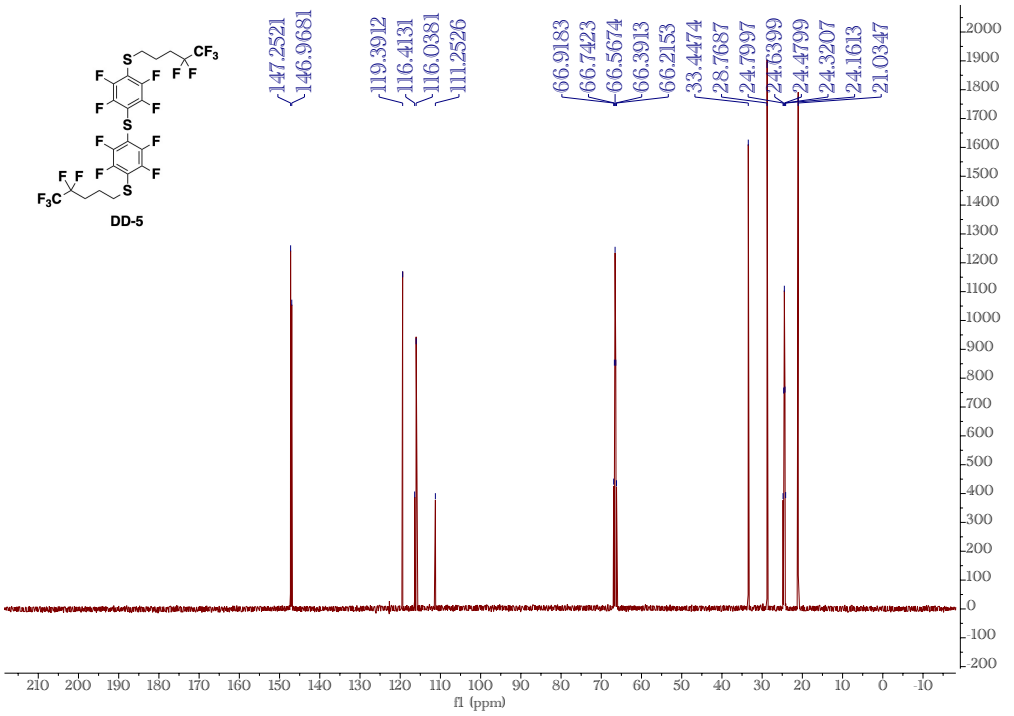

^{19}F NMR, 471 MHz, THF-d_8

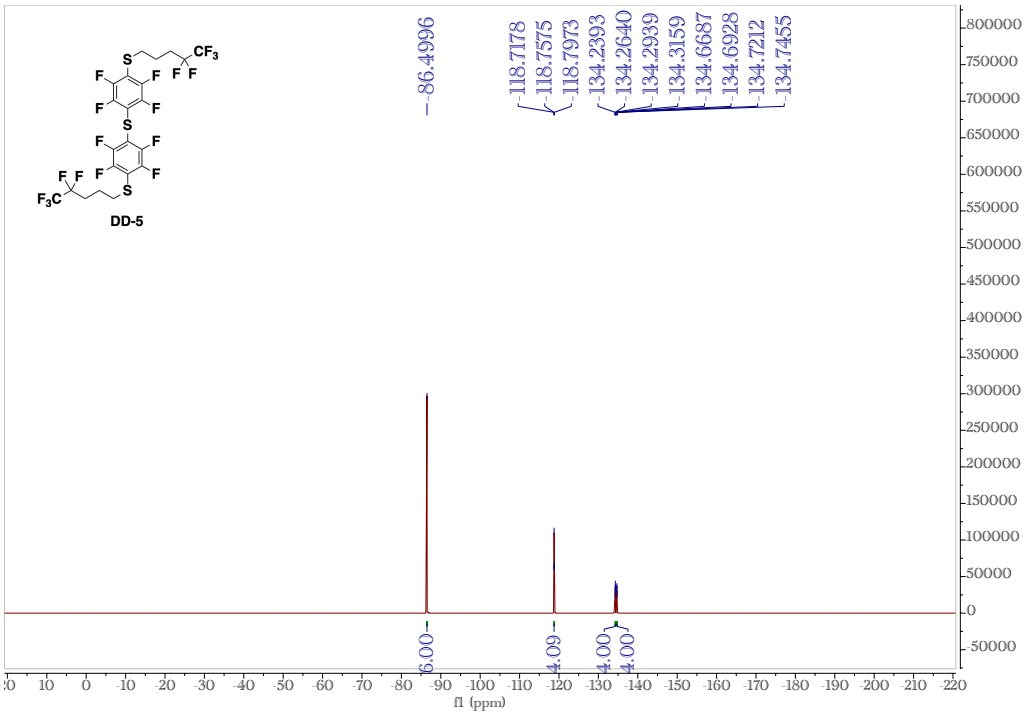

sulfonylbis(2,3,5,6-tetrafluoro-4,1-phenylene))bis((4,4,5,5,5-pentafluoropentyl)sulfane (DD-6)

^{1}H NMR, 500 MHz, Chloroform-*d*

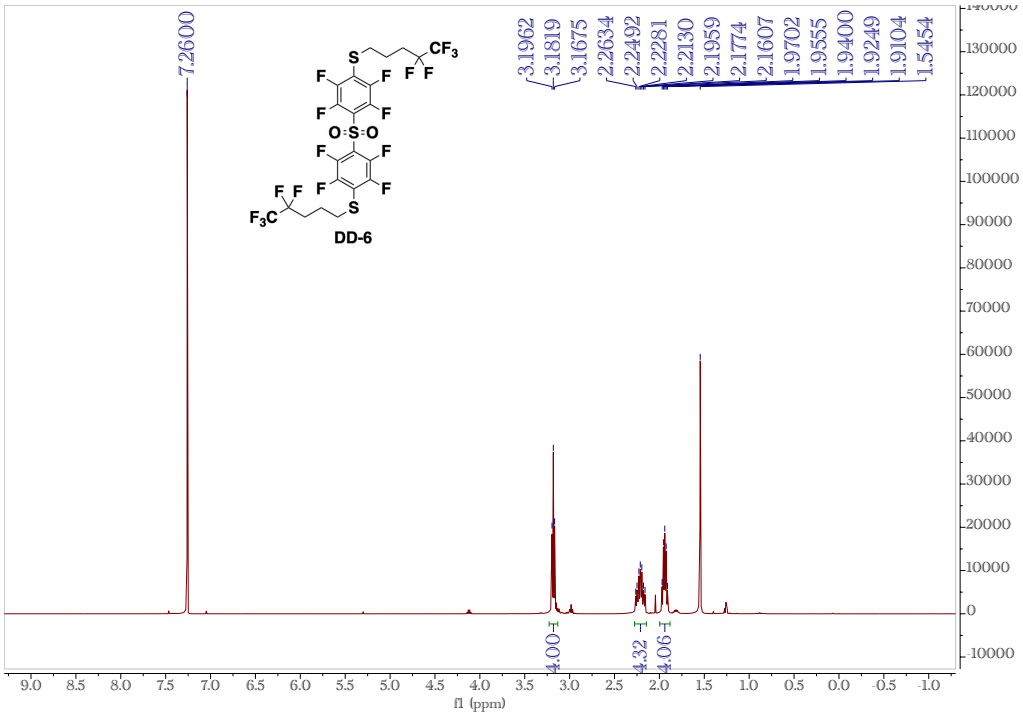

^{13}C NMR, 126 MHz, THF-d_8

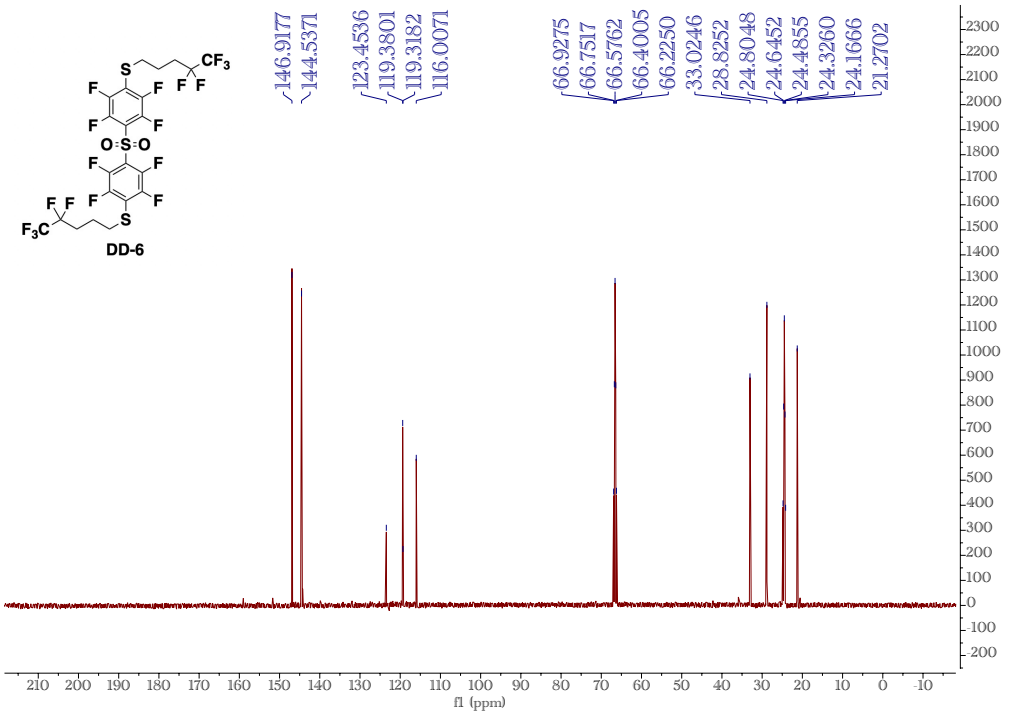

^{19}F NMR, 471 MHz, Chloroform-d

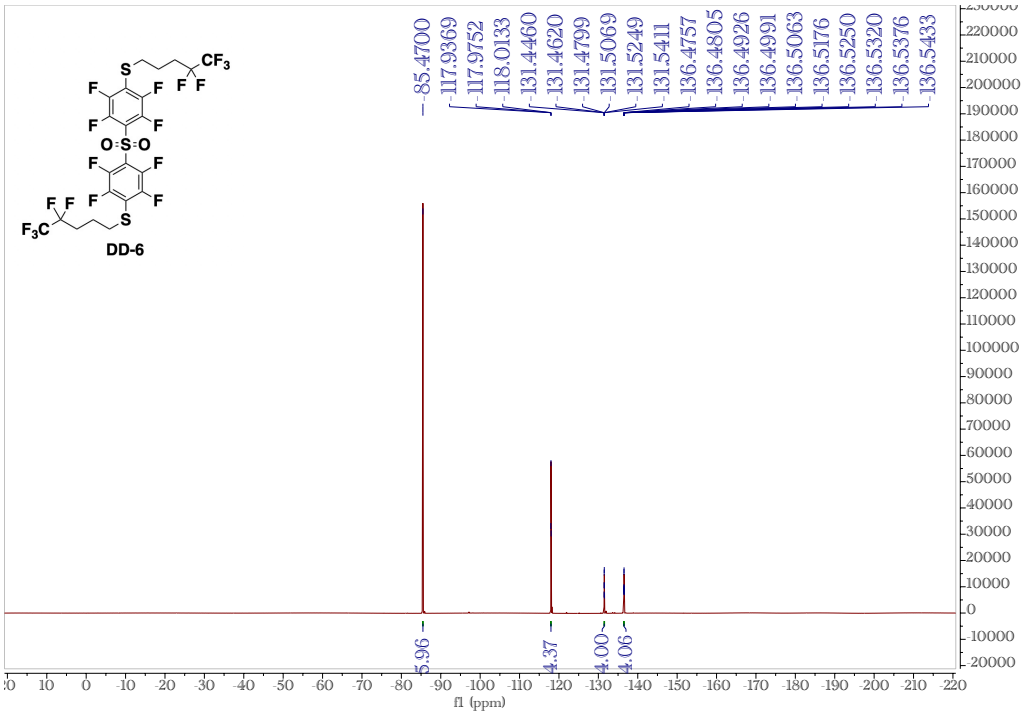

sulfonylbis(2,3,5,6-tetrafluoro-4,1-phenylene))bis((3,3,4,4,5,5,6,6,7,7,8,8,9,9,10,10,10-heptadecafluorodecyl)sulfane (DD-7)

^{1}H NMR, 500 MHz, THF-d_8

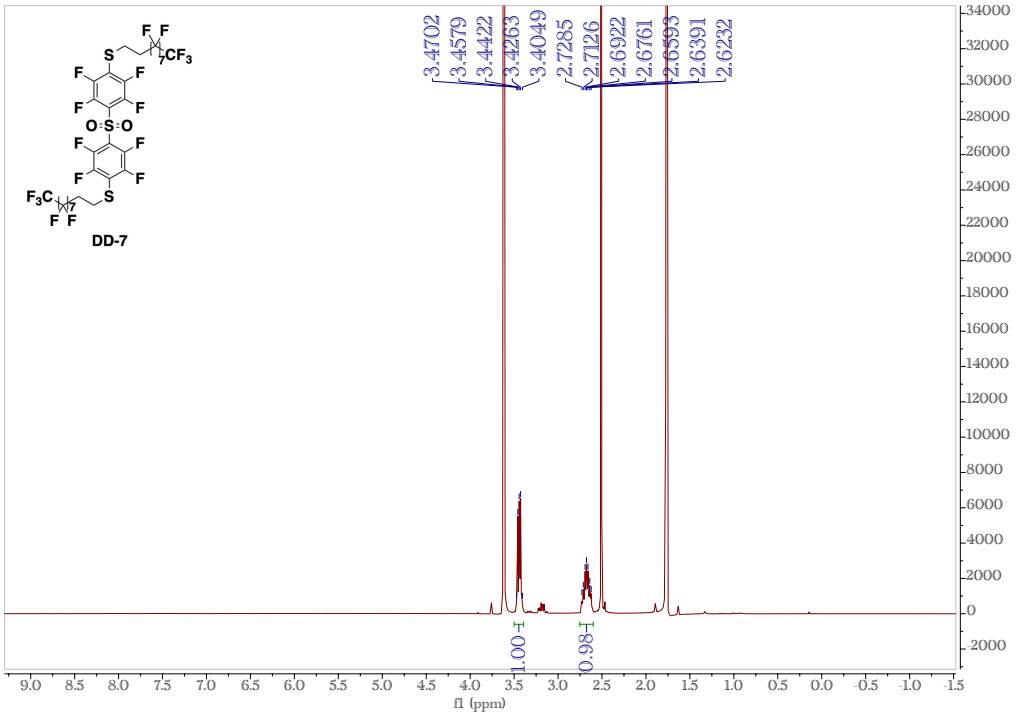

^{13}C NMR, 126 MHz, THF-d_8

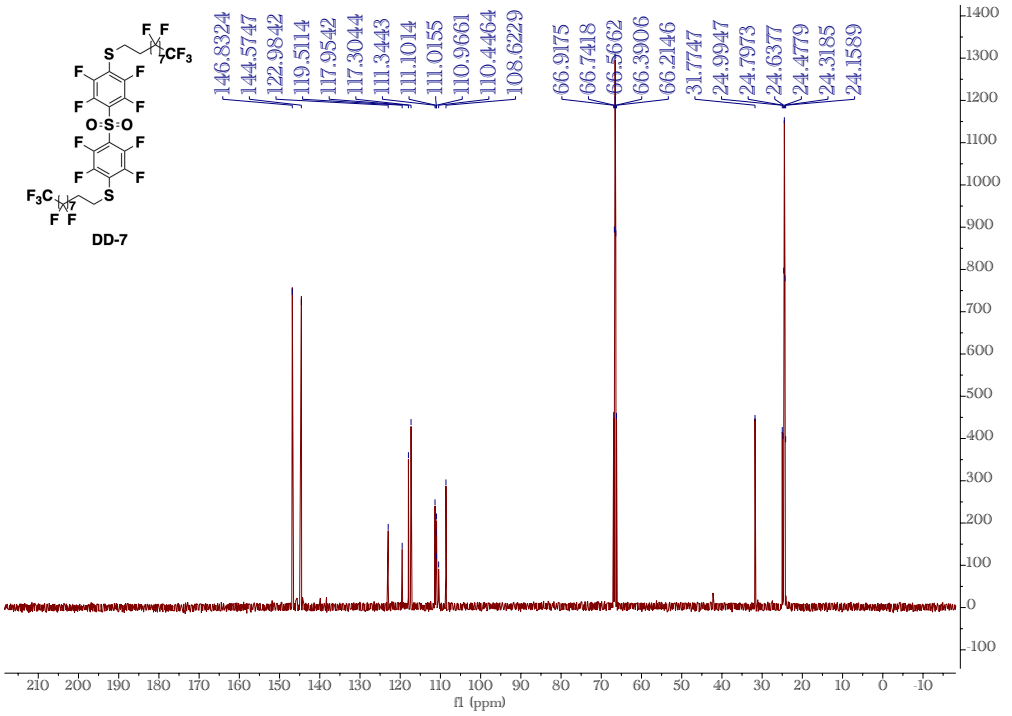

^{19}F NMR, 471 MHz, THF-d_8

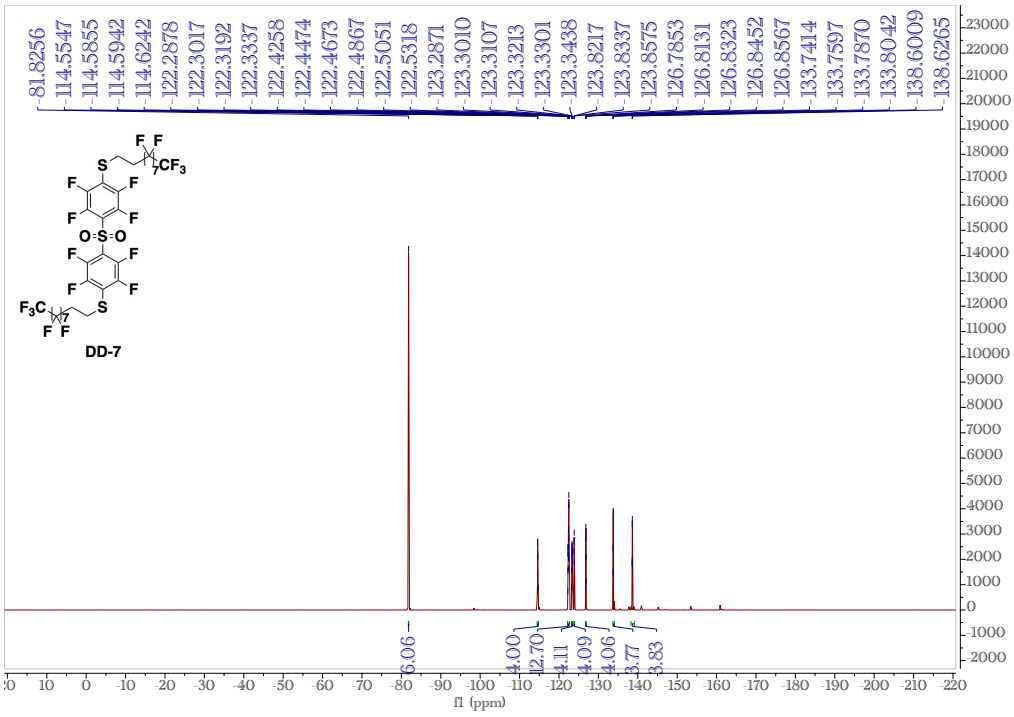

5.1.2 Design of Highly Fluorinated Peptides for Cell-based ^{19}F NMR

methyl (((*9H*-fluoren-9-yl)methoxy)carbonyl)-*L*-cysteinate ($C^{F}a$)

^{1}H NMR, 500 MHz, Chloroform-*d*

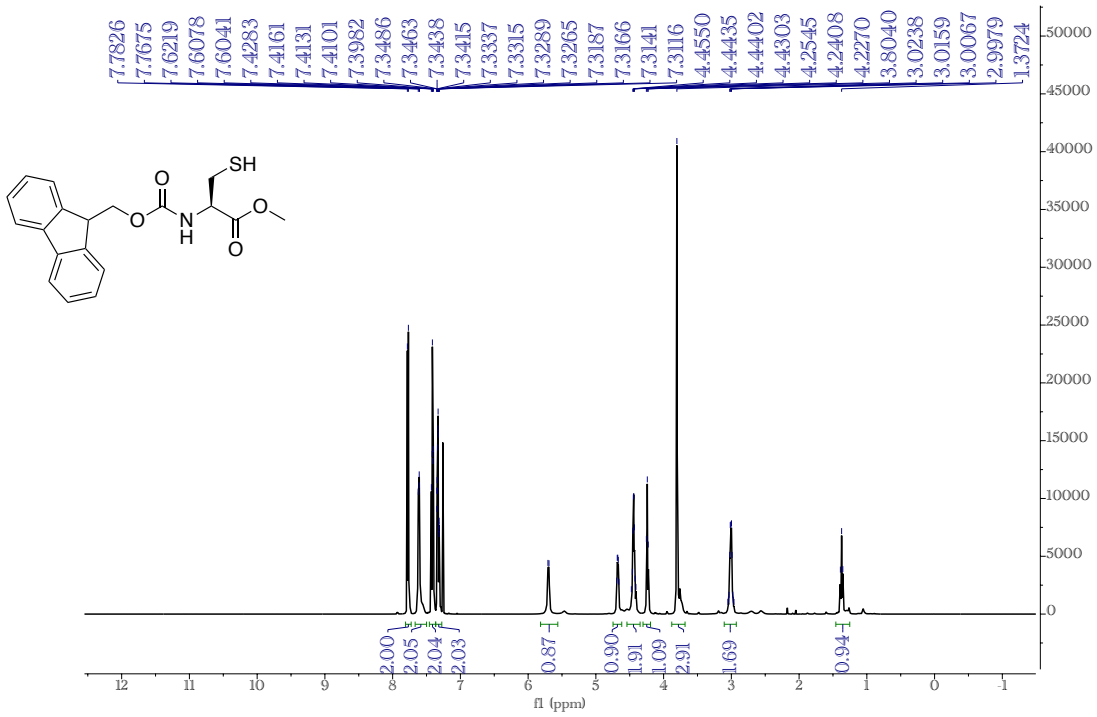

^{13}C NMR, 126 MHz, $CDCl_3$

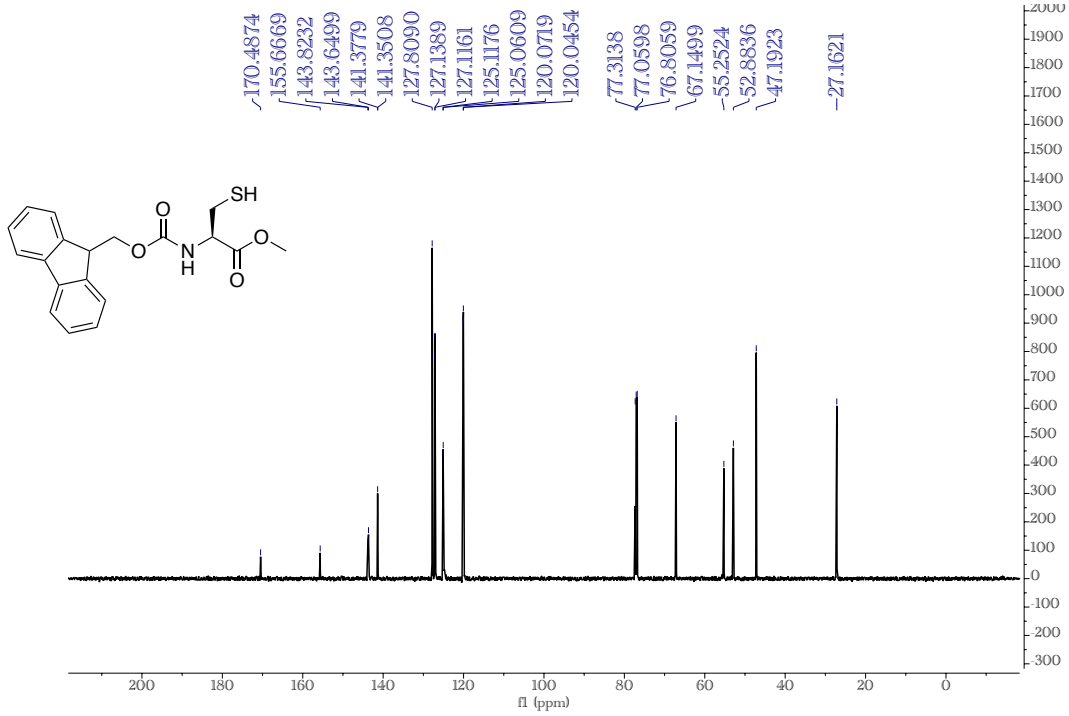

methyl *N*-(((9*H*-fluoren-9-yl)methoxy)carbonyl)-*S*-(3-bromopropyl)-*L*-cysteinate (C^Fb)

^{1}H NMR, 500 MHz, Chloroform-*d*

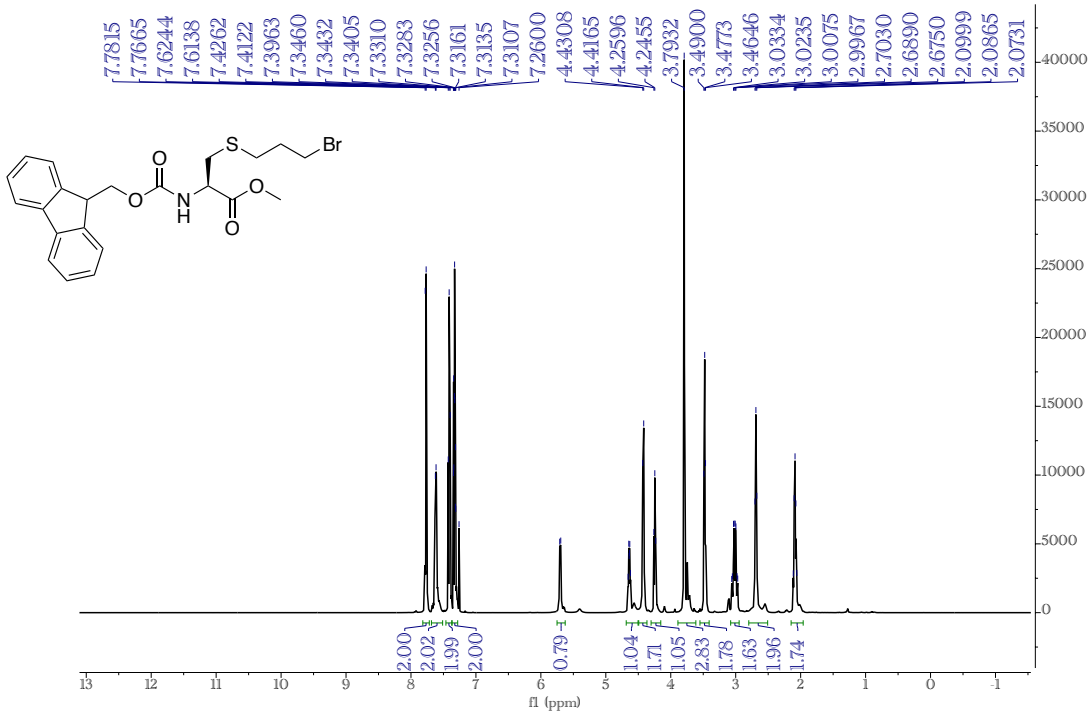

^{13}C NMR, 126 MHz, $CDCl_3$

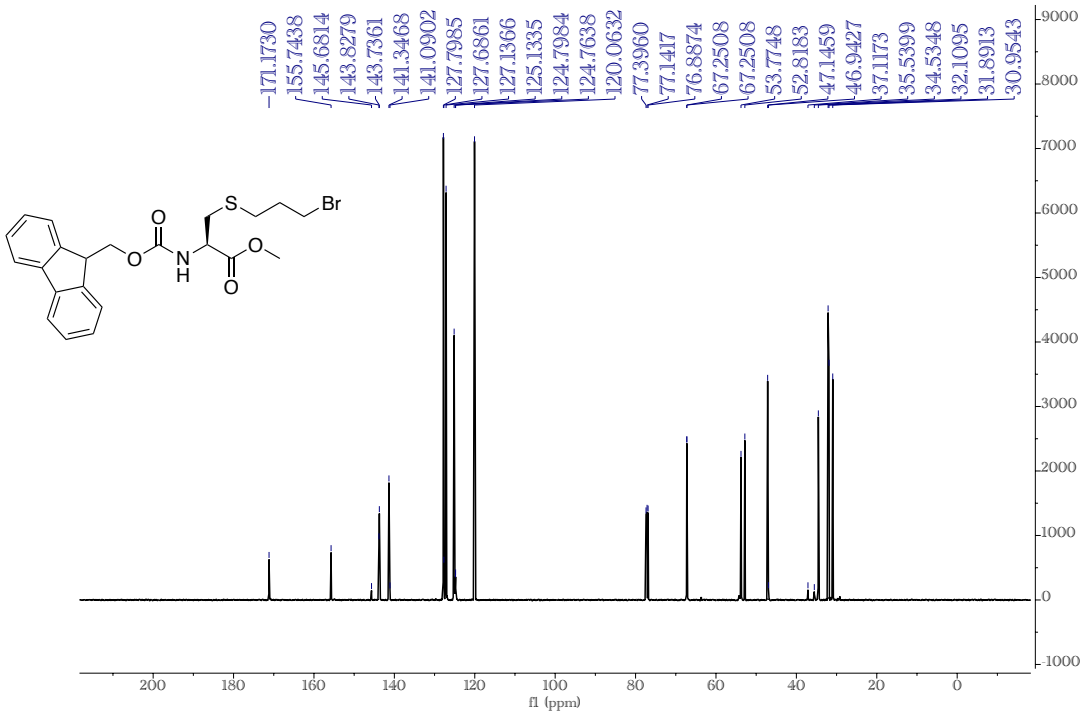

N-(((9*H*-fluoren-9-yl)methoxy)carbonyl)-*S*-(3-((1,1,1,3,3,3-hexafluoro-2-(trifluoromethyl)propan -2-yl)oxy)propyl)-*L*-cysteinate (C^Fc)

^{1}H NMR, 500 MHz, Chloroform-*d*

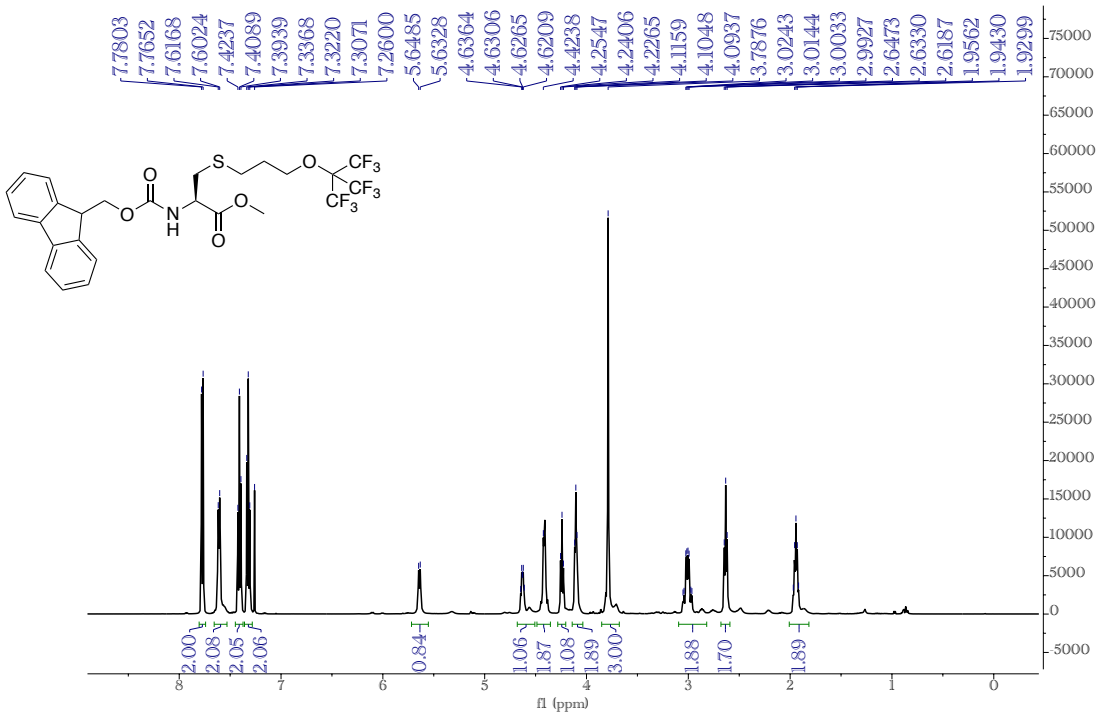

^{13}C NMR, 126 MHz, $CDCl_3$

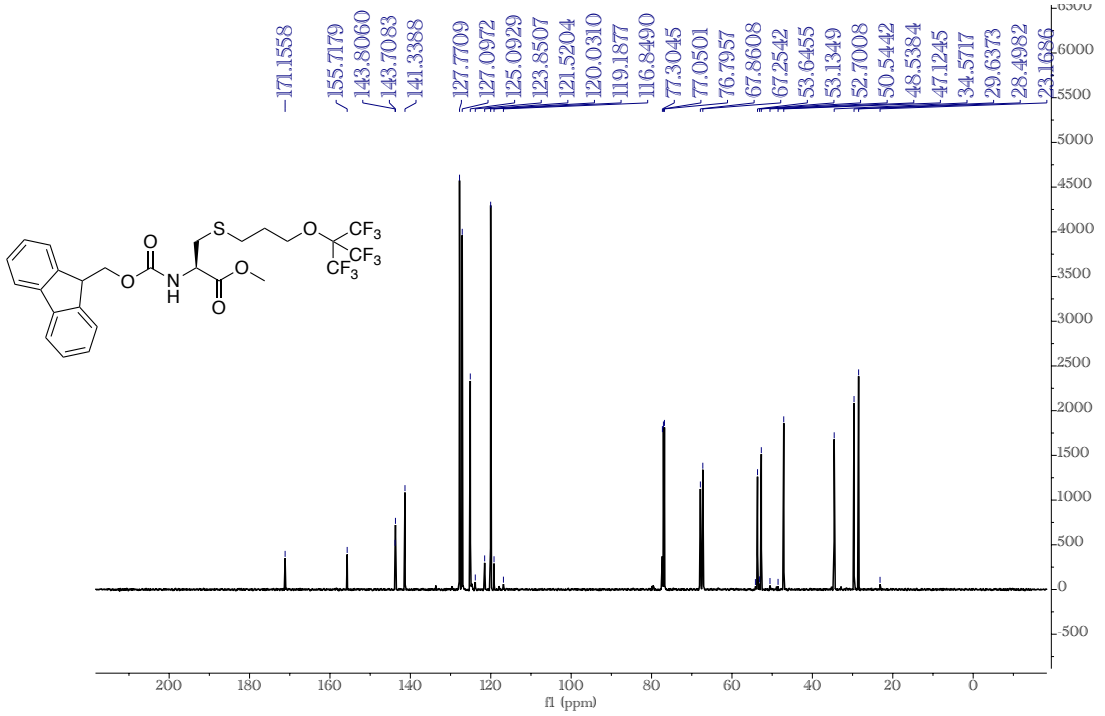

^{19}F NMR, 471 MHz, $CDCl_3$

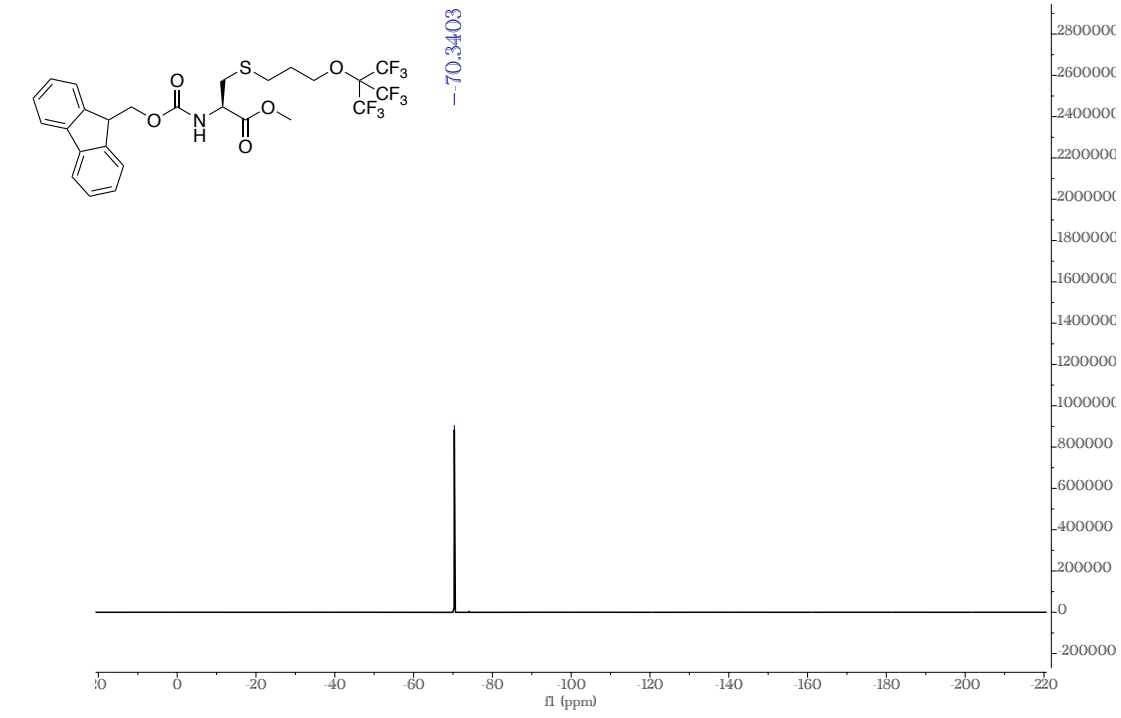

N-(((9*H*-fluoren-9-yl)methoxy)carbonyl)-*S*-(3-((1,1,1,3,3,3-hexafluoro-2-(trifluoromethyl) propan-2-yl)oxy)propyl)-*L*-cysteine (C^F)

^{1}H NMR, 500 MHz, Chloroform-*d*

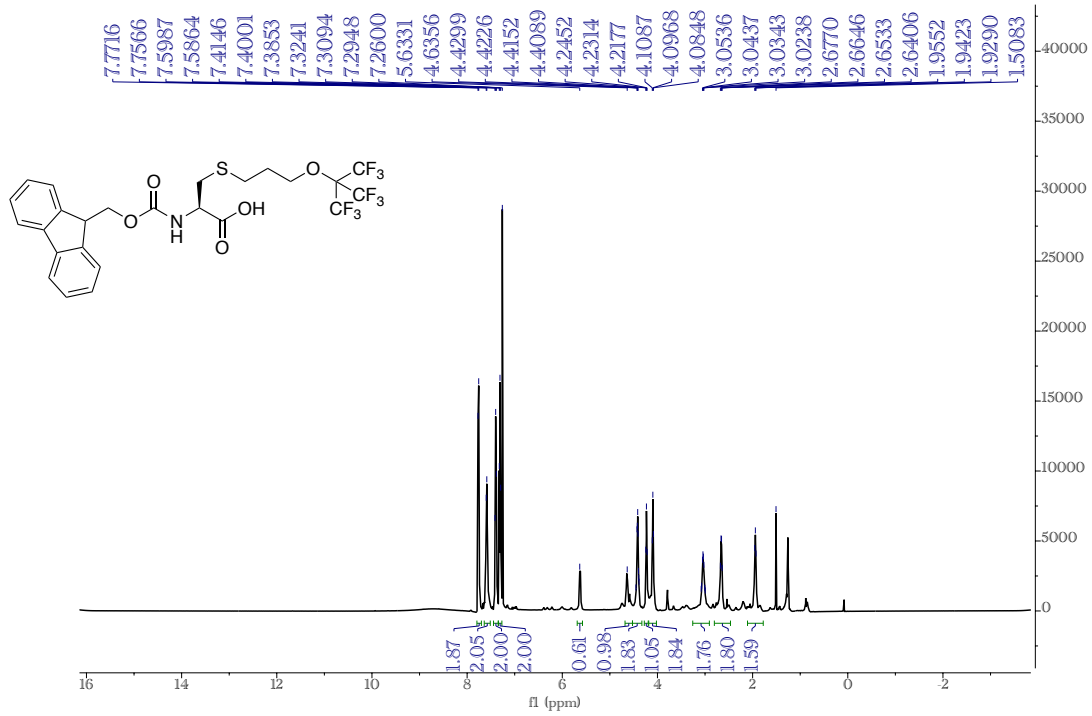

^{13}C NMR, 126 MHz, $CDCl_3$

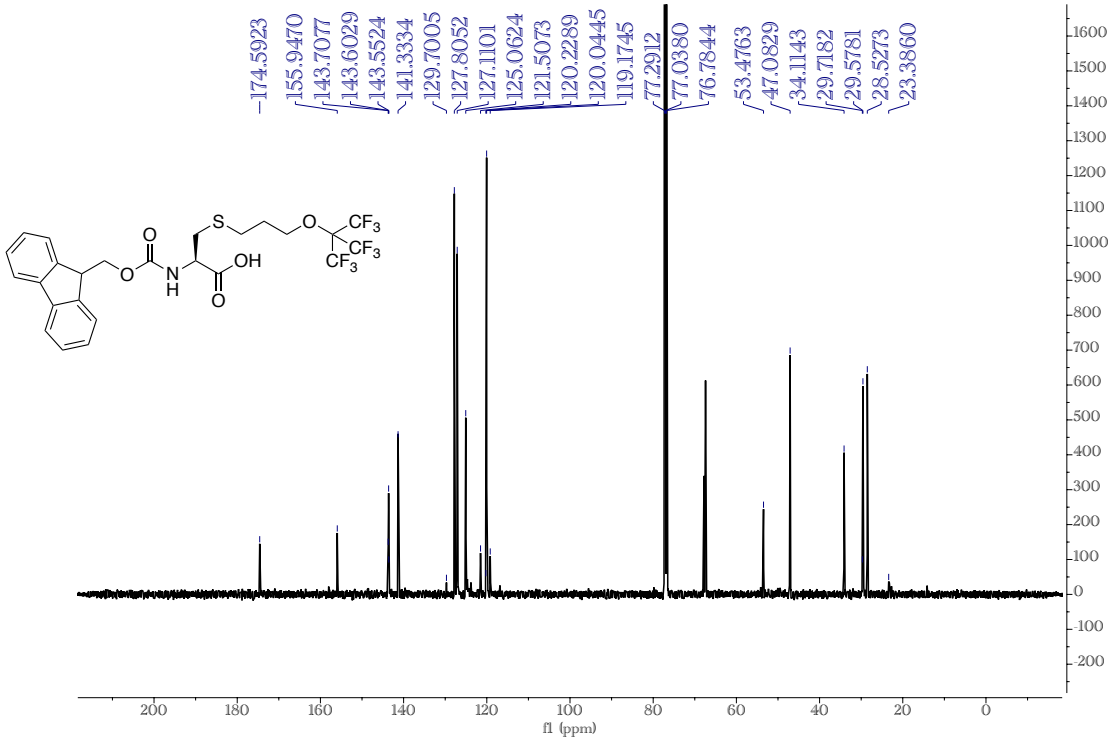

^{19}F NMR, 471 MHz, $CDCl_3$

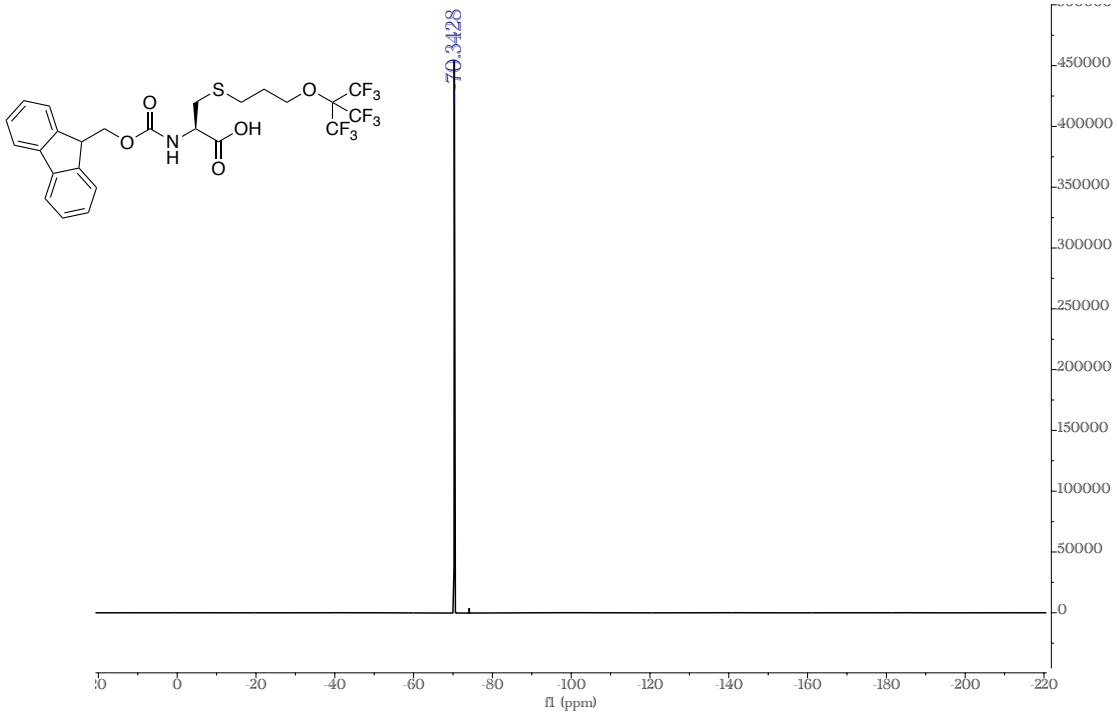

methyl (((9*H*-fluoren-9-yl)methoxy)carbonyl)-*L*-lysinate (K^Fa)

^{1}H NMR, 500 MHz, MeOD

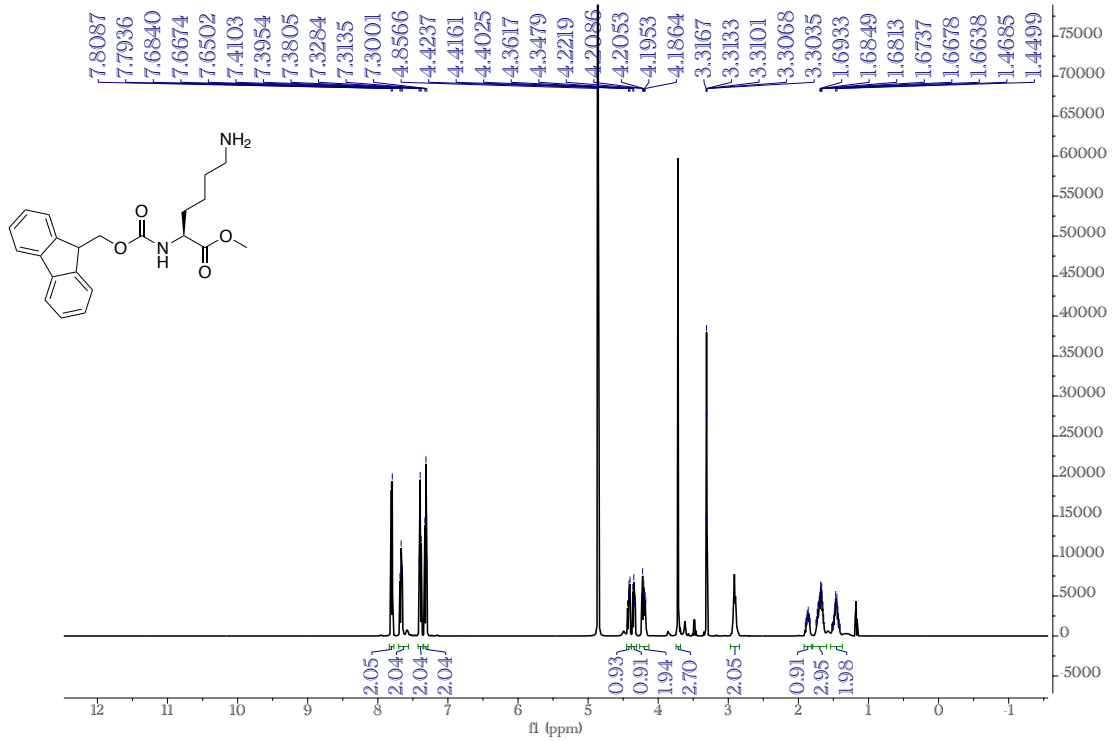

^{13}C NMR, 126 MHz, MeOD

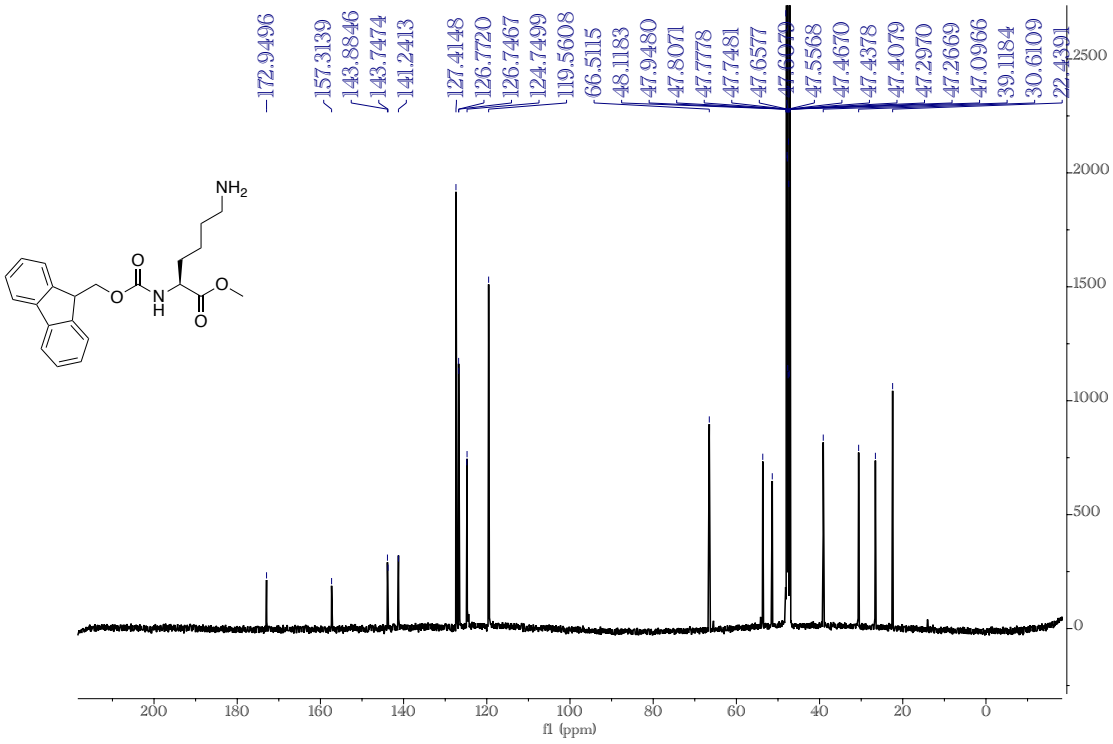

methyl N^2-(((9*H*-fluoren-9-yl)methoxy)carbonyl)-N^6-(3,5-bis(trifluoromethyl)benzyl)-*L*-lysinate (K^Fb)

^{1}H NMR, 500 MHz, Chloroform-*d*

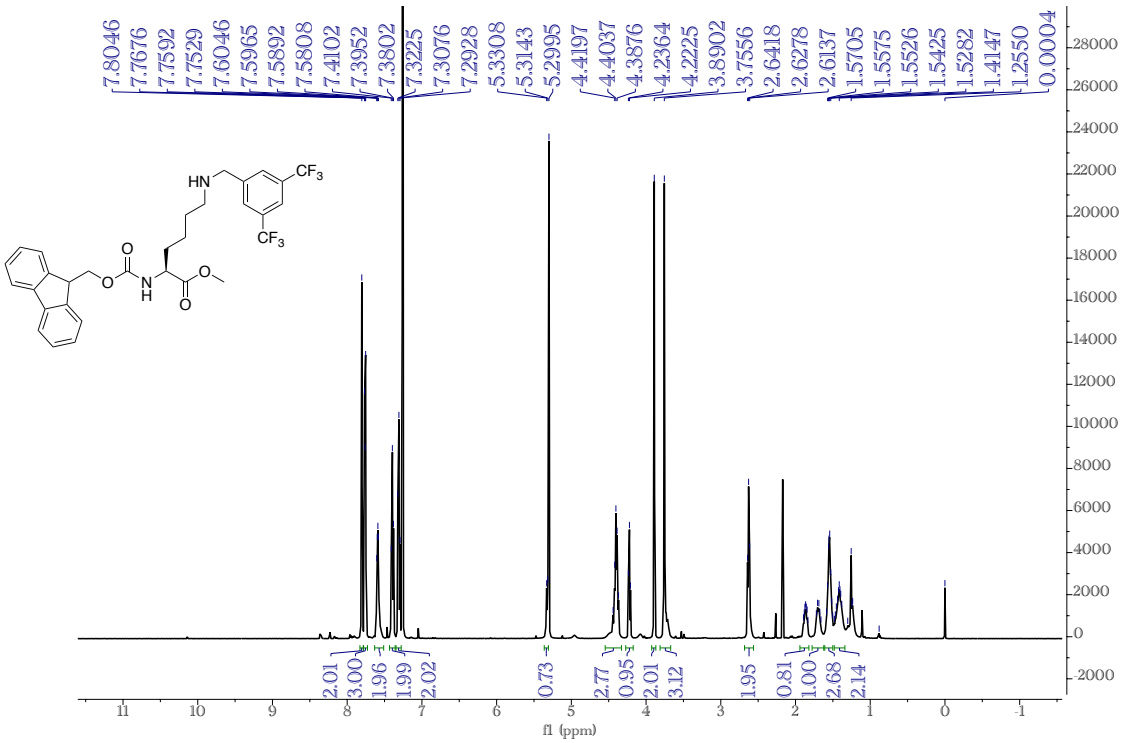

^{13}C NMR, 126 MHz, $CDCl_3$

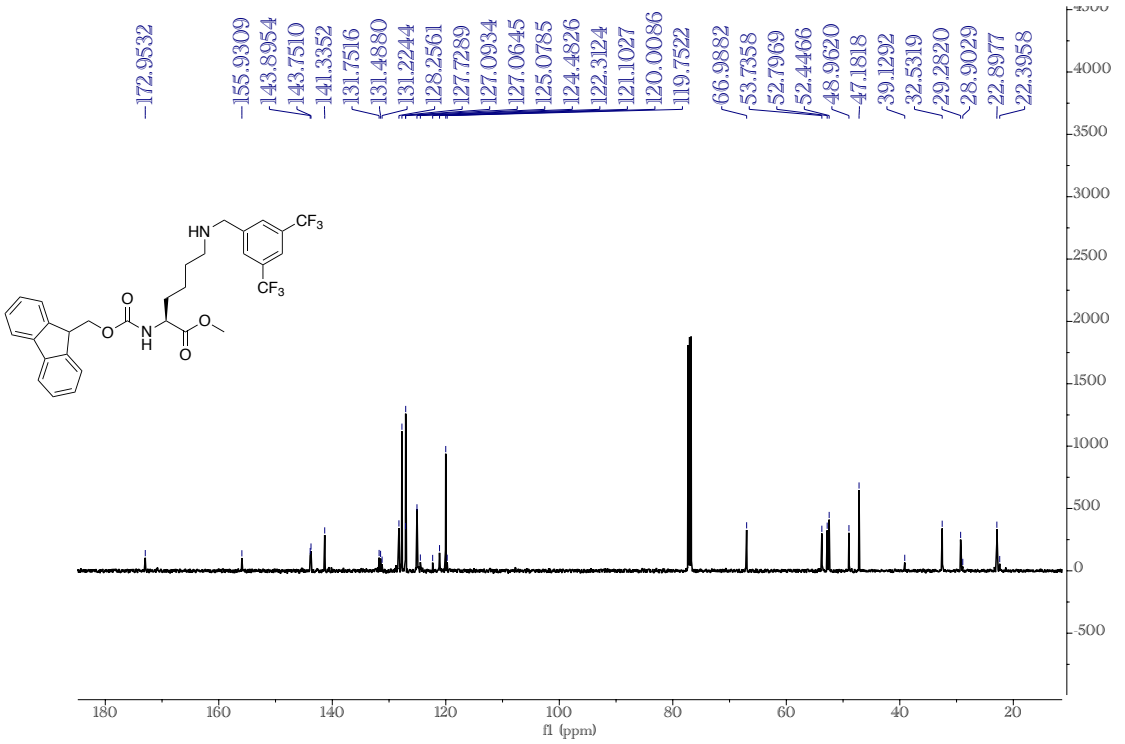

^{19}F NMR, 471 MHz, $CDCl_3$

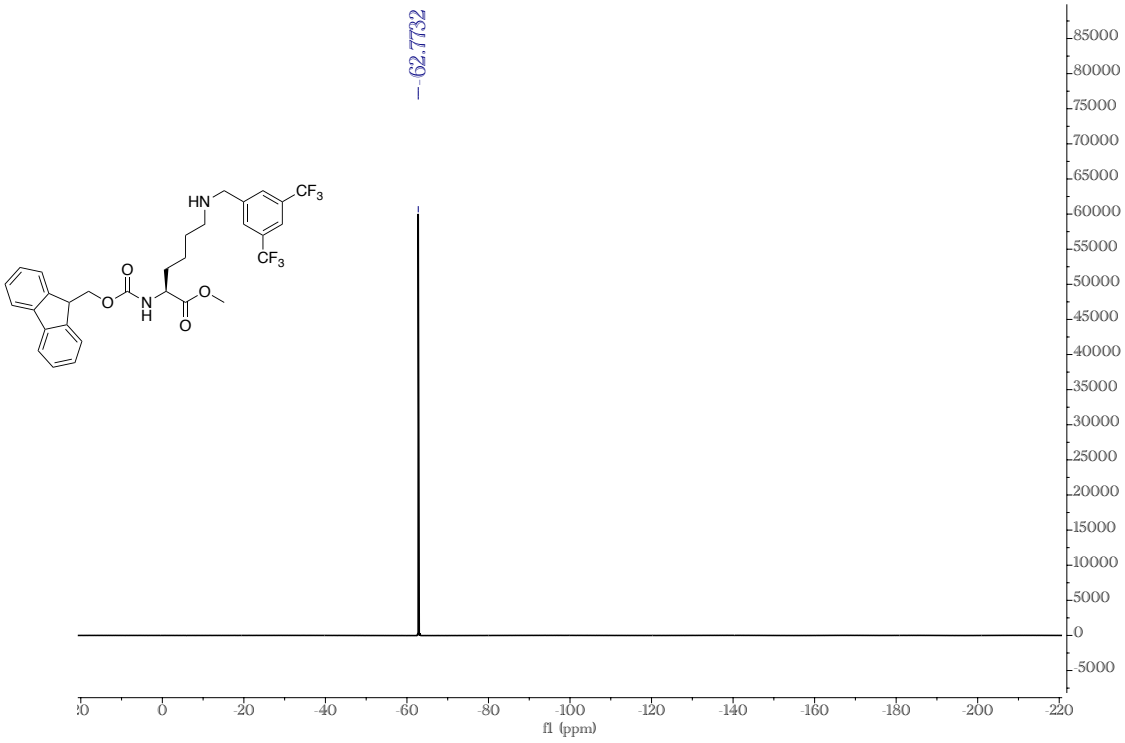

methyl N^2-(((9*H*-fluoren-9-yl)methoxy)carbonyl)-N^6-(3,5-bis(trifluoromethyl)benzyl)-N^6-(*tert*-butoxycarbonyl)-*L*-lysinate (K^Fc)

^{1}H NMR, 500 MHz, DMSO-d_6

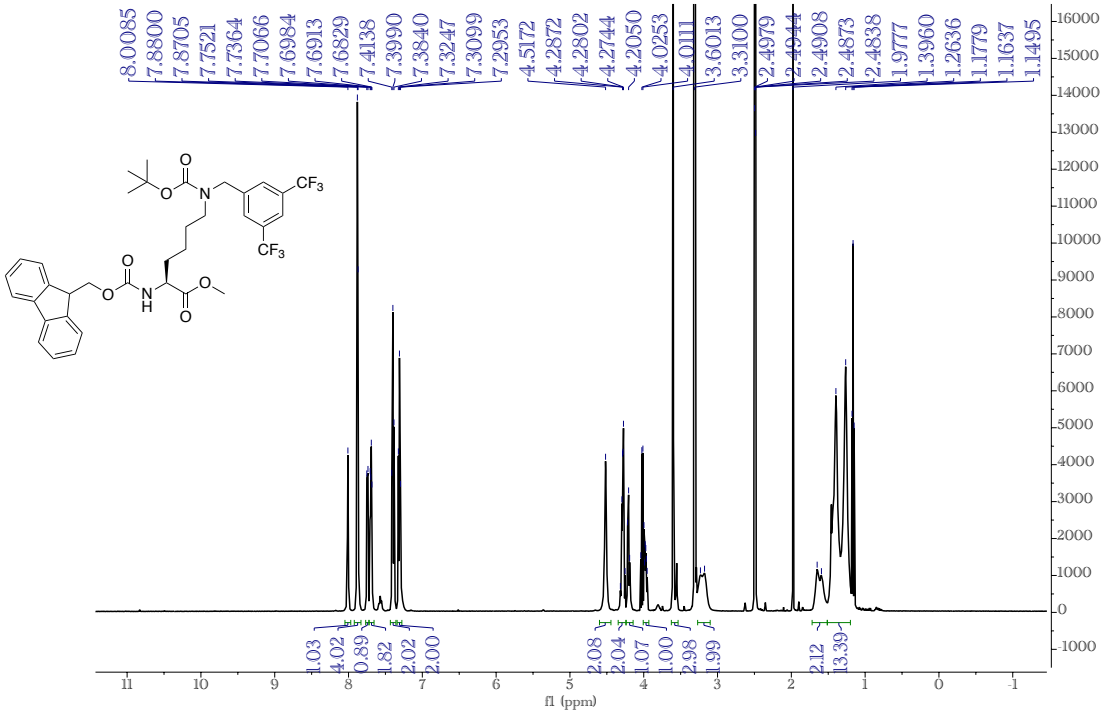

^{13}C NMR, 126 MHz, DMSO

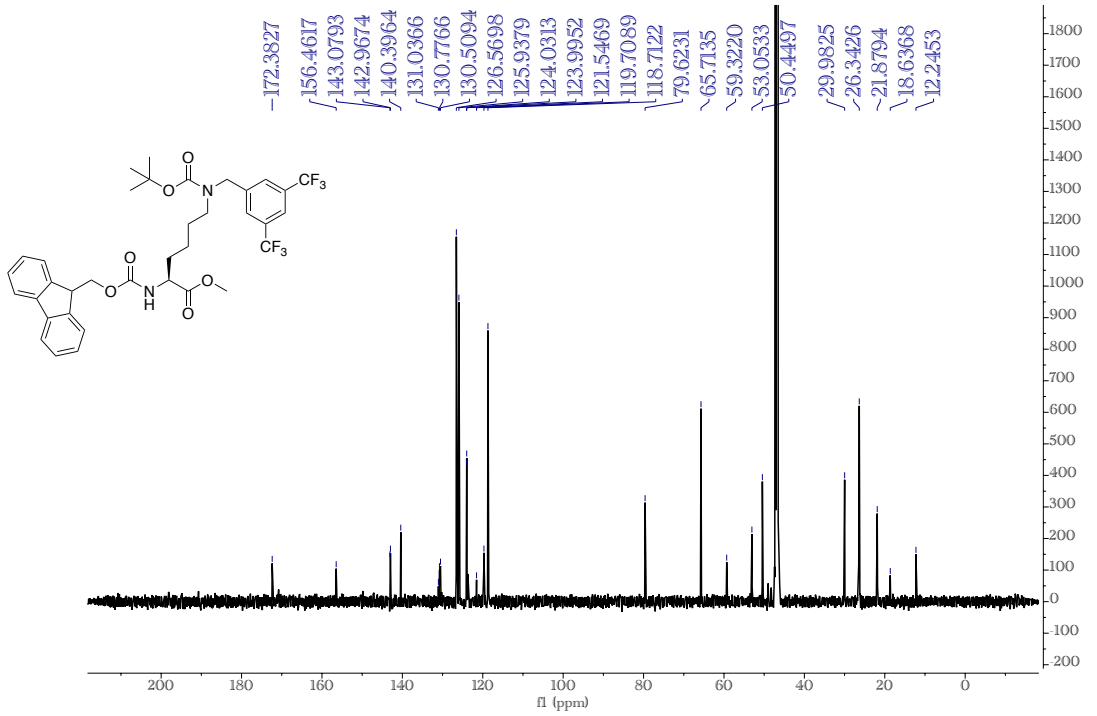

^{19}F NMR, 471 MHz, DMSO

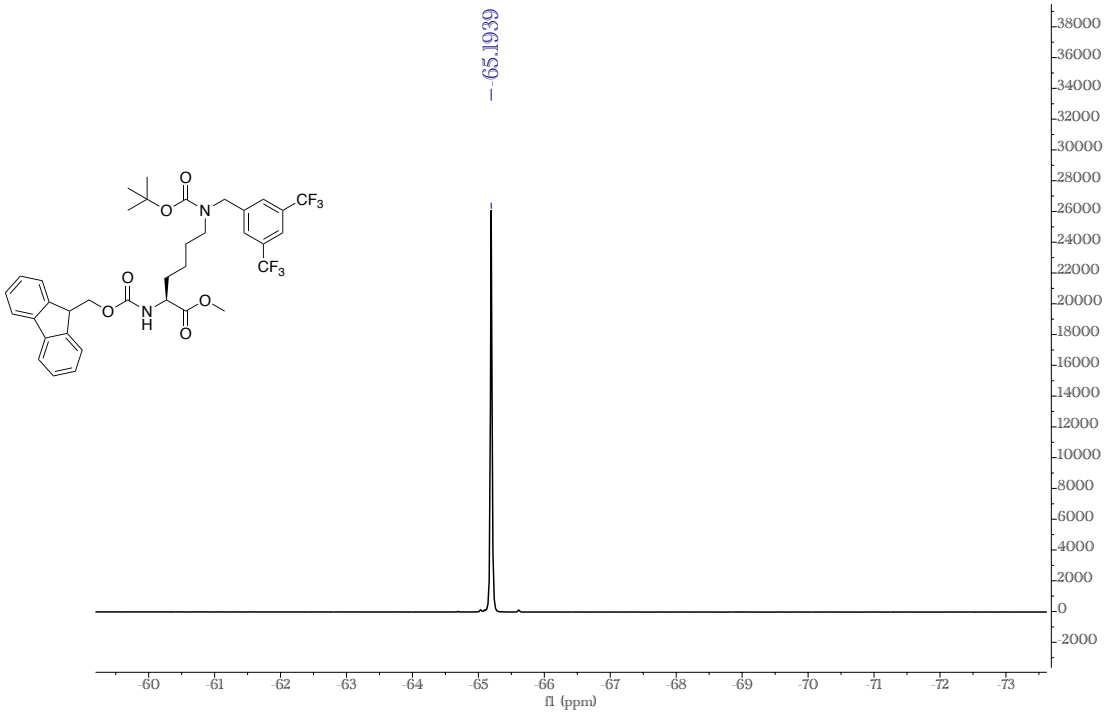

N^2-(((9*H*-fluoren-9-yl)methoxy)carbonyl)-N^6-(3,5-bis(trifluoromethyl)benzyl)-N^6-(*tert*-butoxycarbonyl)-*L*-lysine (K^F)

^{1}H NMR, 500 MHz, Chloroform-*d*

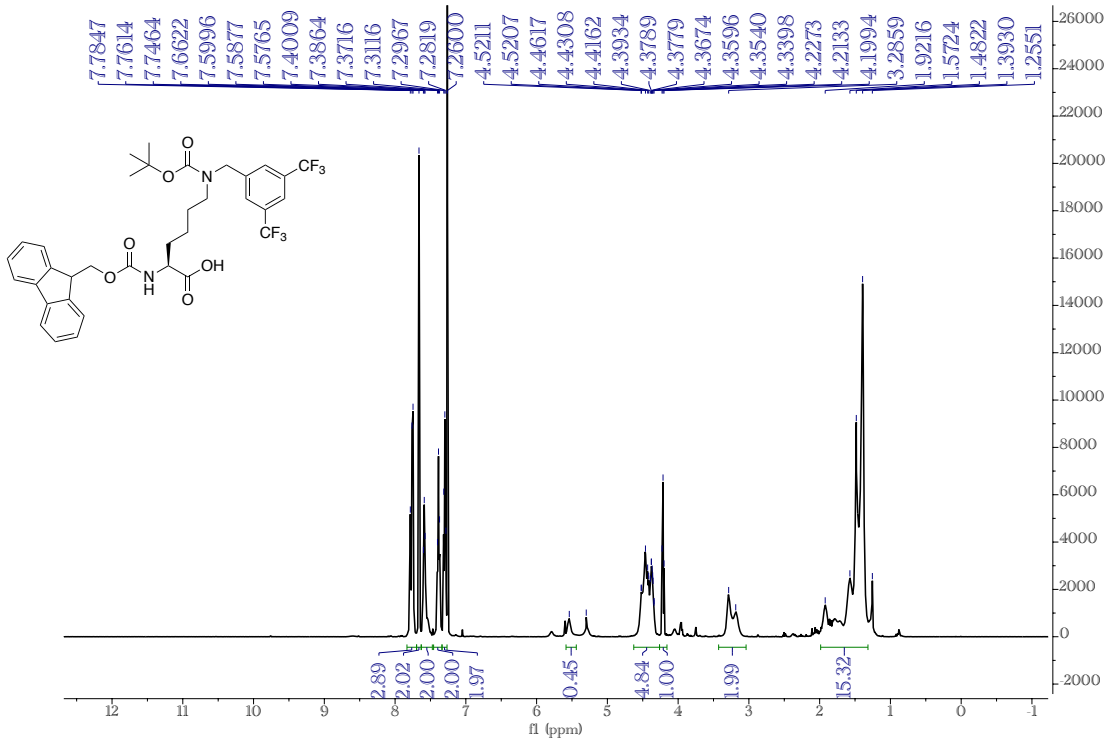

^{13}C NMR, 126 MHz, $CDCl_3$

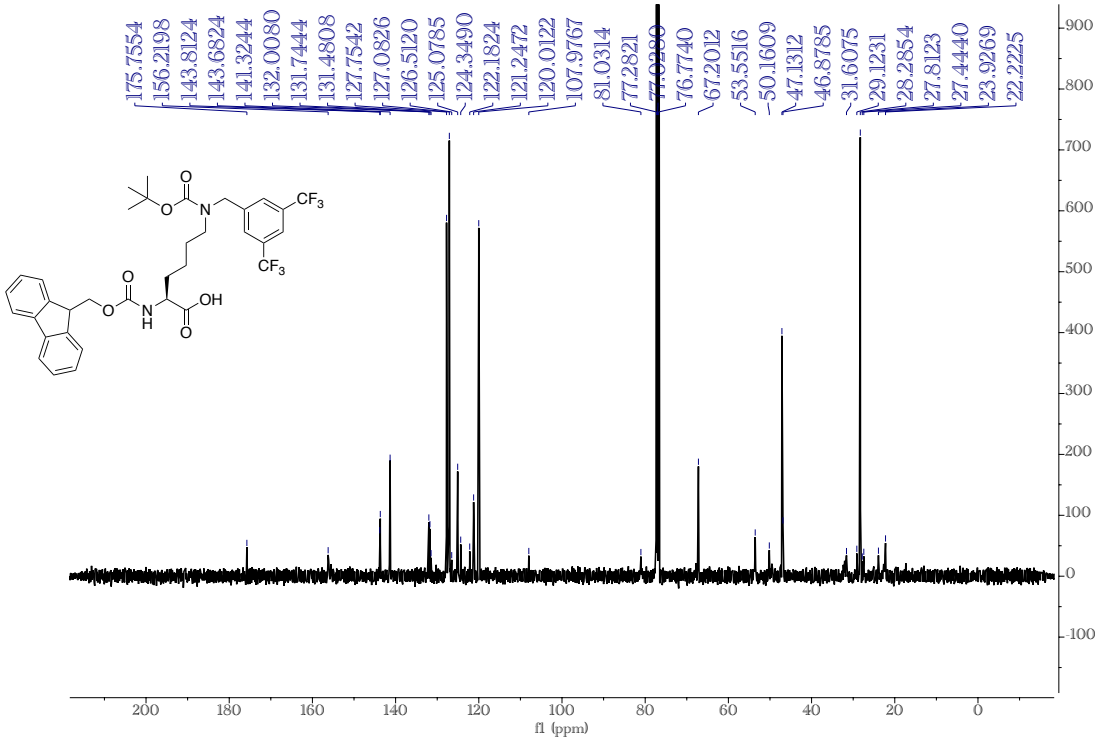

^{19}F NMR, 471 MHz, $CDCl_3$

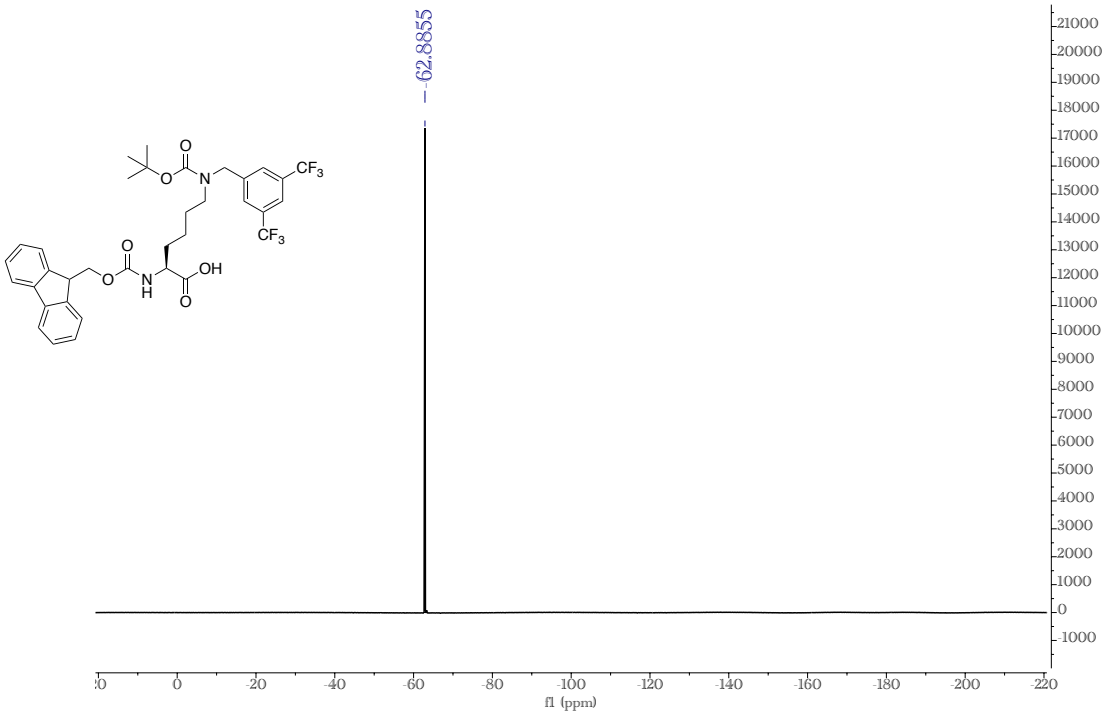

tert-butyl N^2-(((9*H*-fluoren-9-yl)methoxy)carbonyl)-N^6,N^6-bis(3,5-bis(trifluoromethyl)benzyl)-*L*-lysinate ($K^{FF}a$)

^{1}H NMR, 500 MHz, Chloroform-*d*

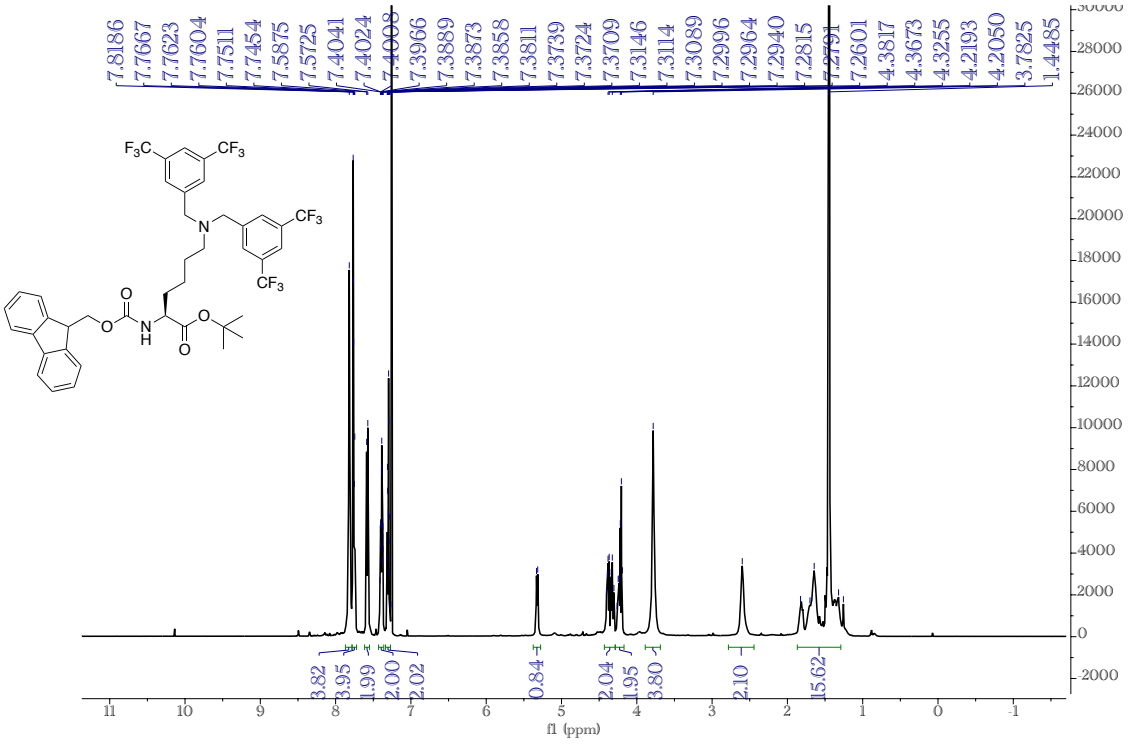

^{13}C NMR, 126 MHz, $CDCl_3$

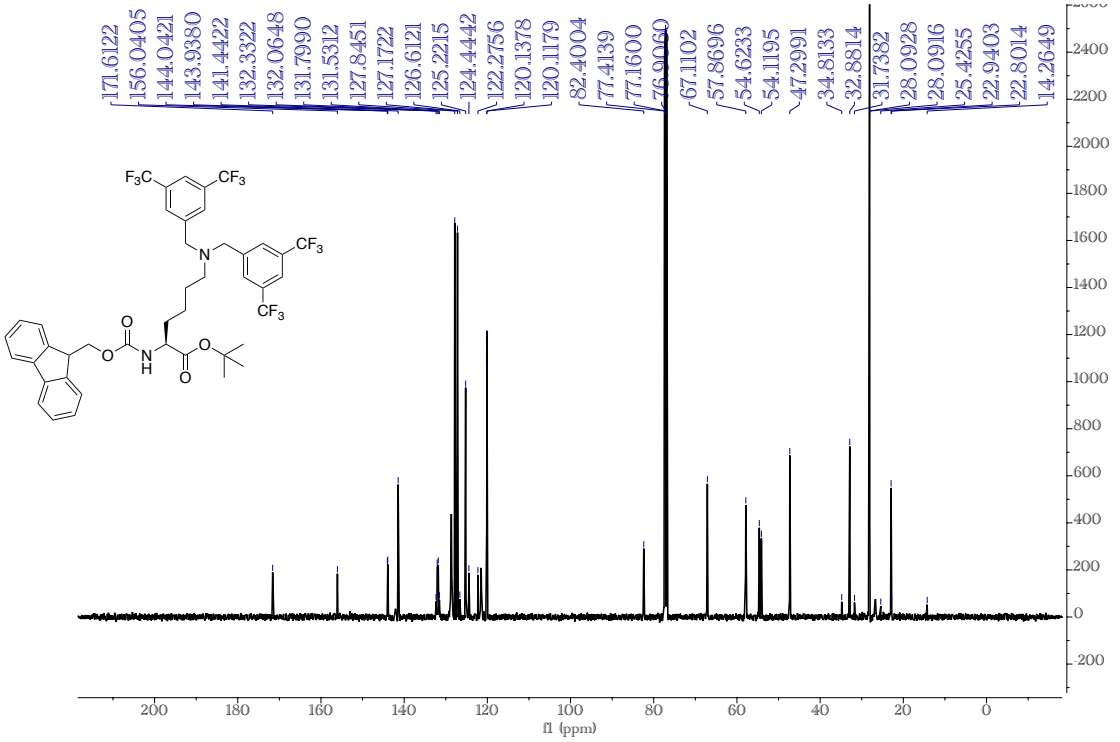

^{19}F NMR, 471 MHz, Chloroform-*d*

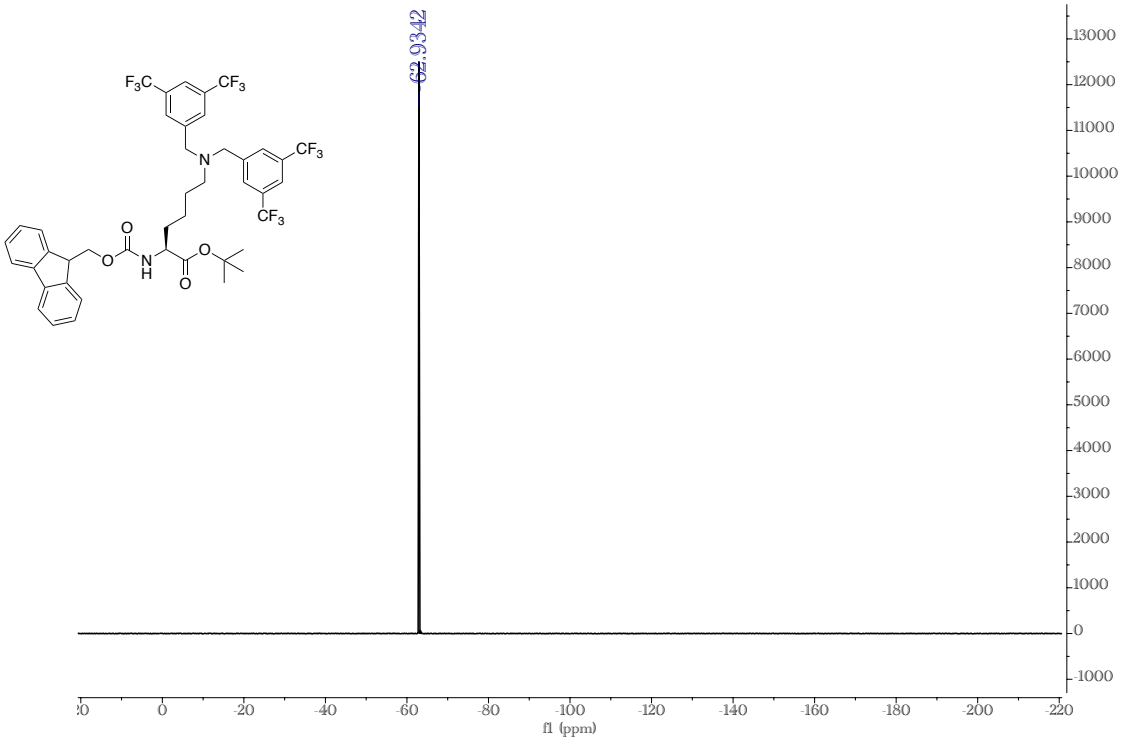

N^2-(((*9H*-fluoren-9-yl)methoxy)carbonyl)- N^6, N^6-bis(3,5-bis(trifluoromethyl)benzyl)-*L*-lysine (K^{FF})

^{1}H NMR, 500 MHz, Chloroform-*d*

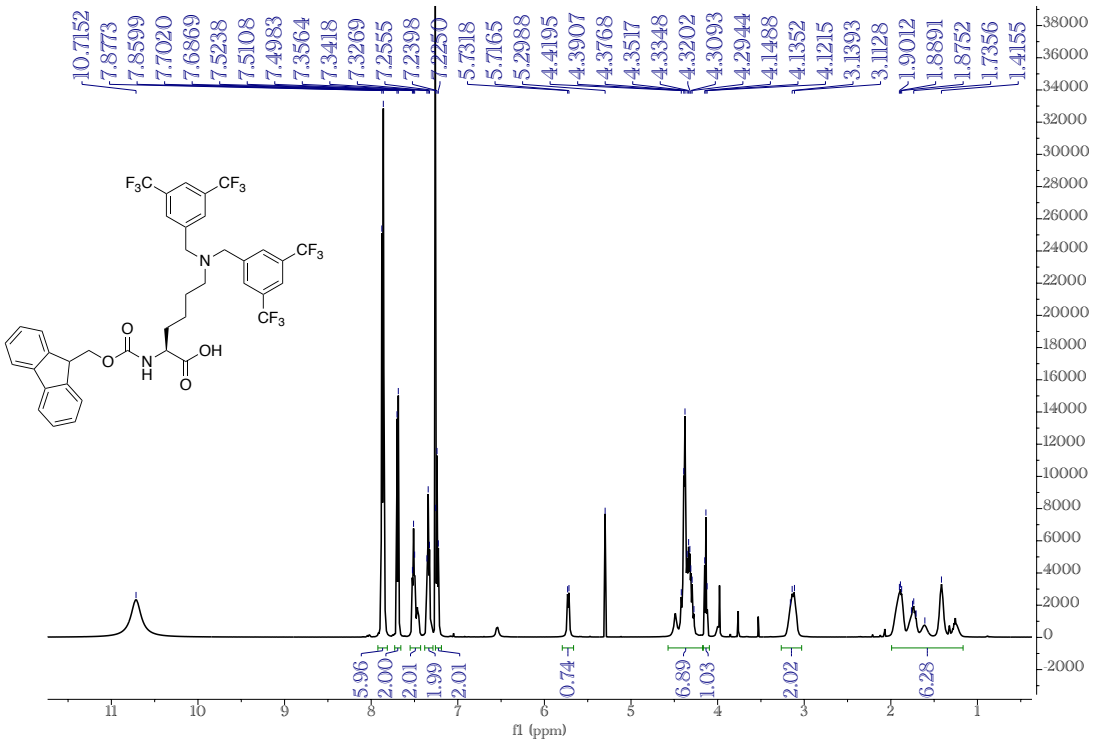

^{13}C NMR, 126 MHz, $CDCl_3$

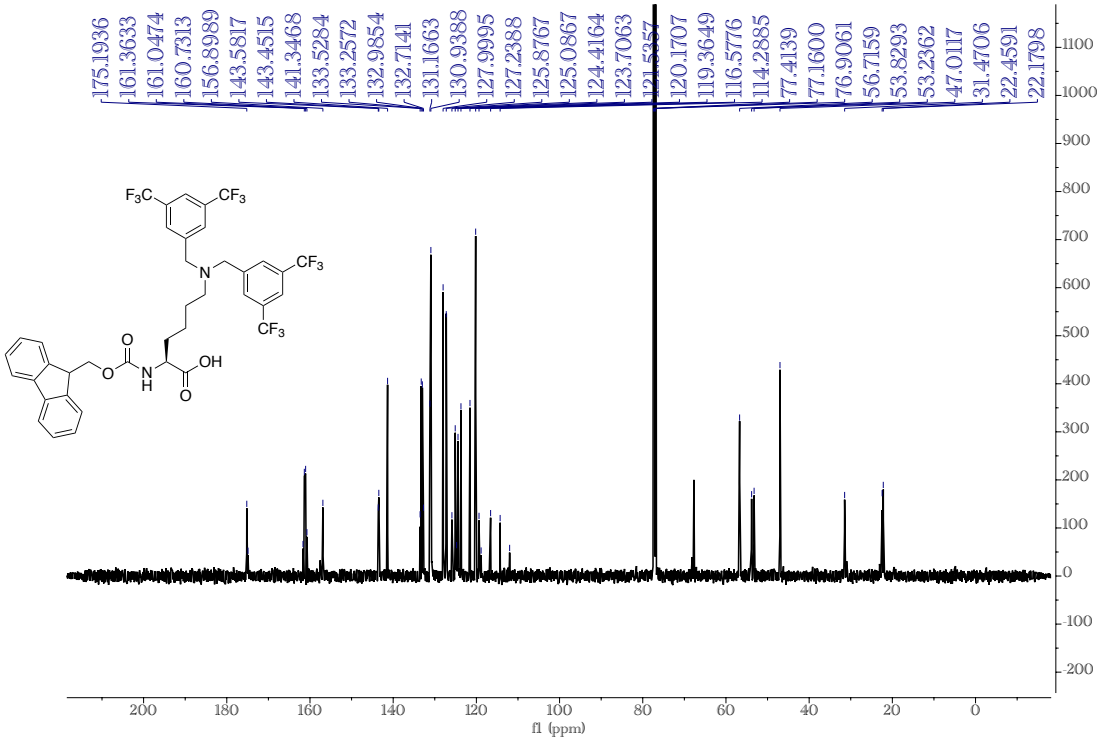

^{19}F NMR, 471 MHz, $CDCl_3$

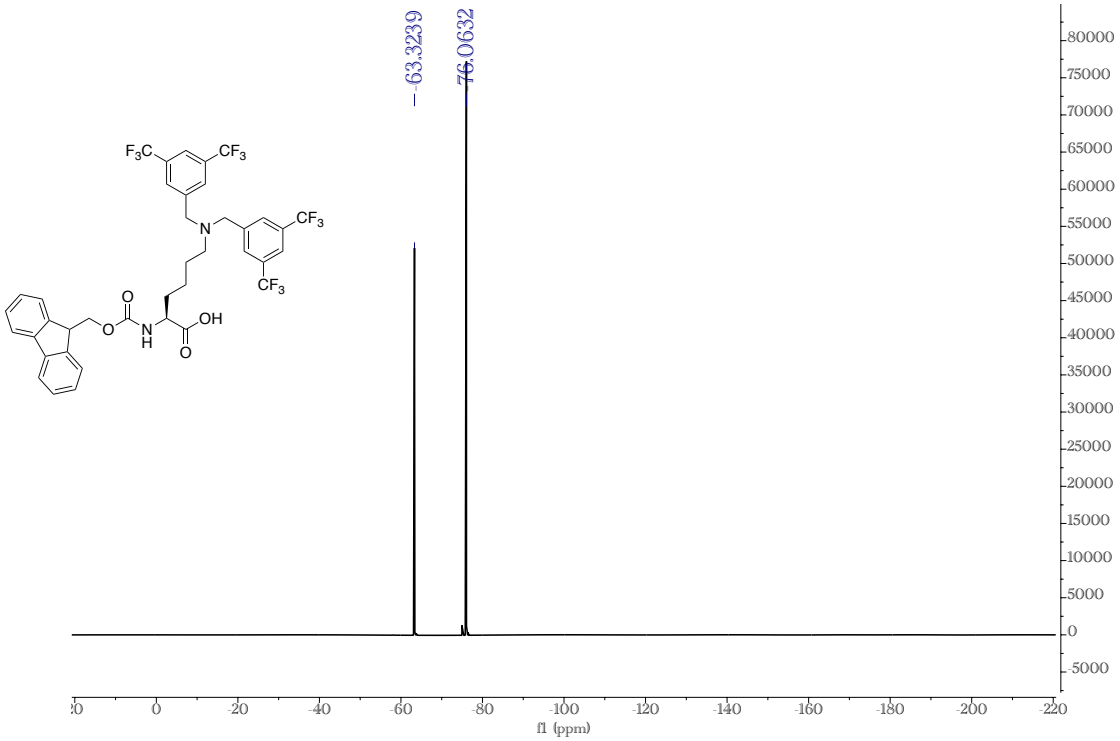

tert-butyl (*S*)-2-((((9*H*-fluoren-9-yl)methoxy)carbonyl)amino)-5-hydroxypentanoate (E^Fa)

^{1}H NMR, 500 MHz, Chloroform-*d*

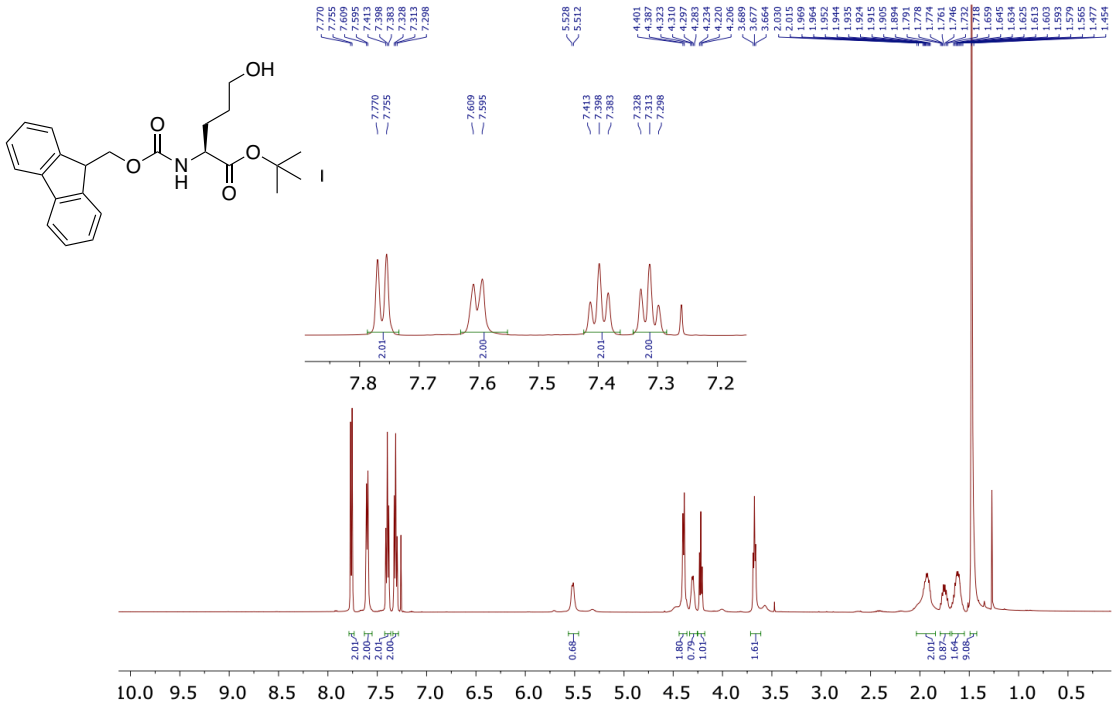

^{13}C NMR, 126 MHz, Chloroform-*d*

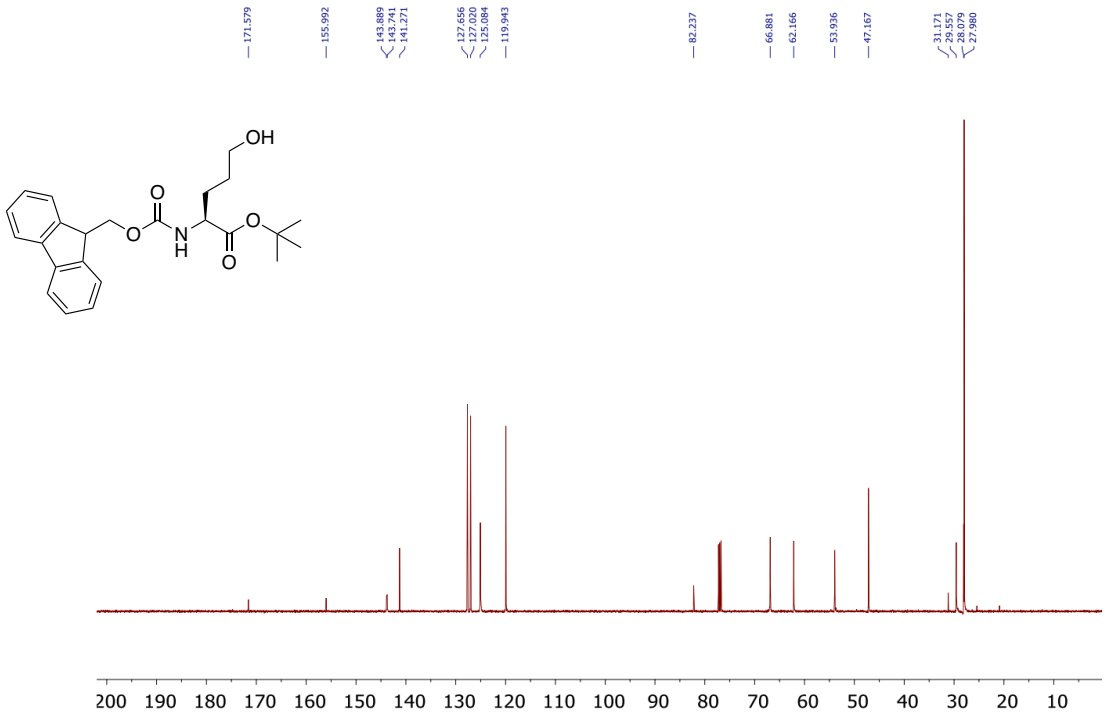

tert-butyl (*S*)-2-((((9*H*-fluoren-9-yl)methoxy)carbonyl)amino)-5-iodopentanoate (E^Fb)

^{1}H NMR, 500 MHz, Chloroform-*d*

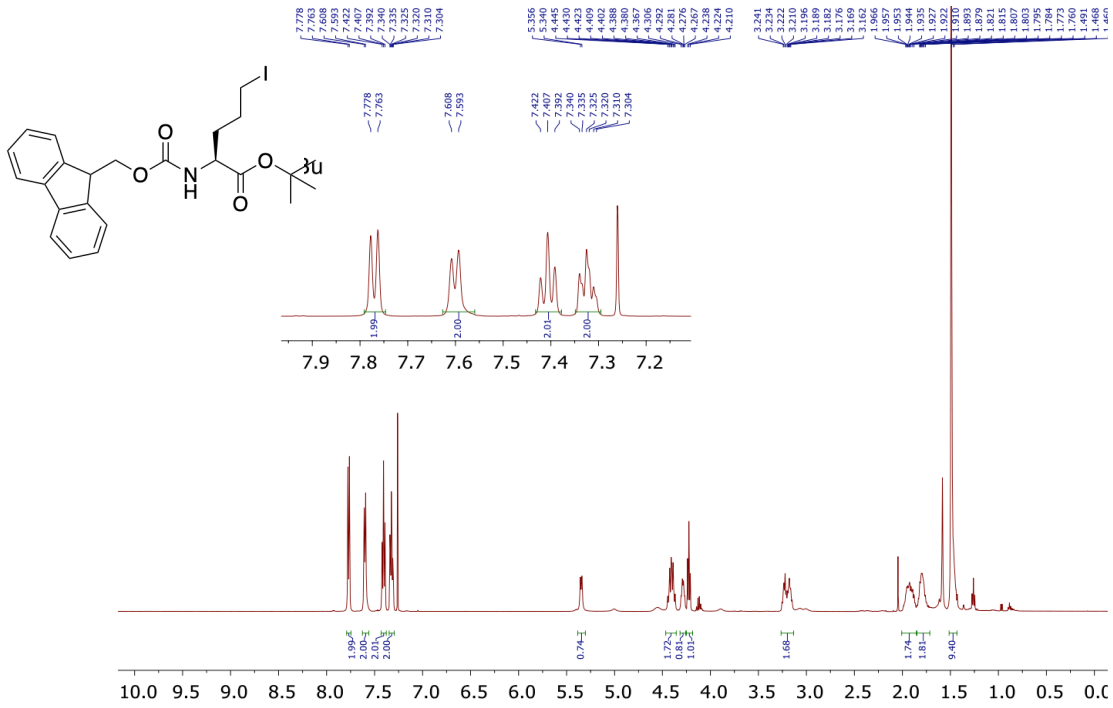

^{13}C NMR, 126 MHz, Chloroform-*d*

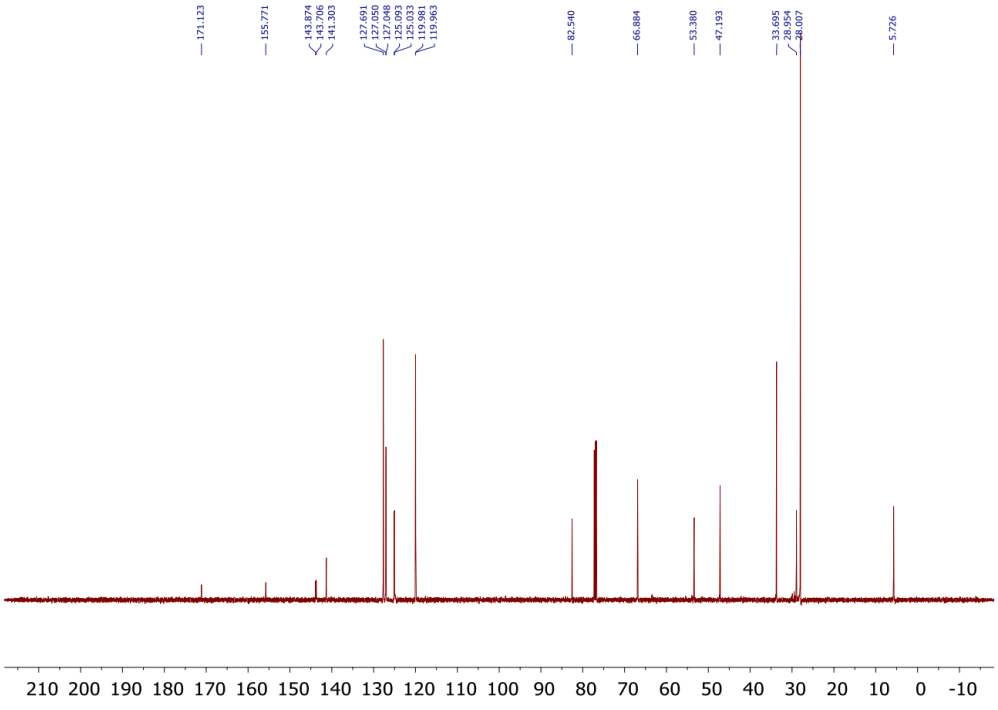

tert-butyl (*S*)-2-((((9*H*-fluoren-9-yl)methoxy)carbonyl)amino)-5-((1,1,1,3,3,3-hexafluoro-2-(trifluoromethyl)propan-2-yl)oxy)pentanoate (E^Fc)

^{1}H NMR, 500 MHz, Chloroform-*d*

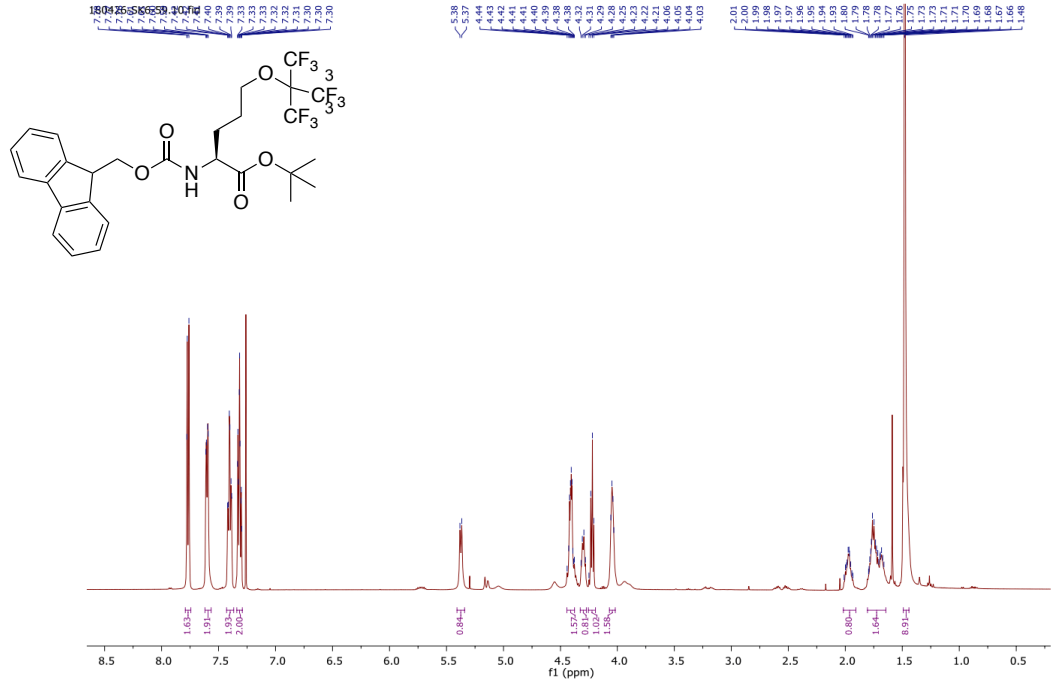

^{13}C NMR, 126 MHz, Chloroform-*d*

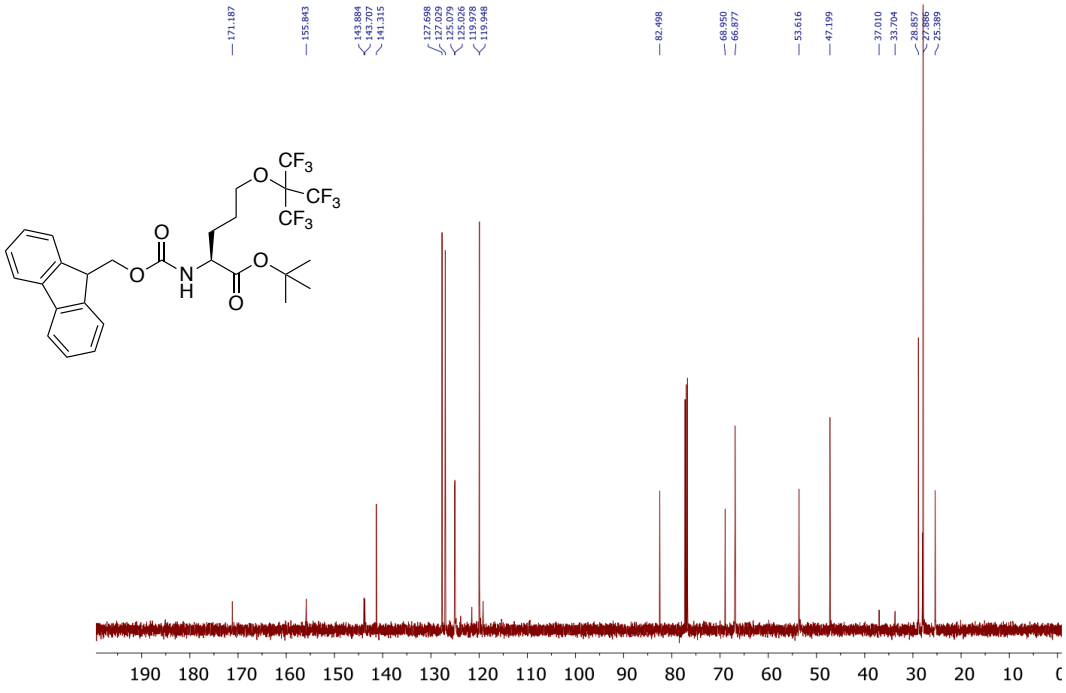

^{19}F NMR, 471 MHz, Chloroform-*d*

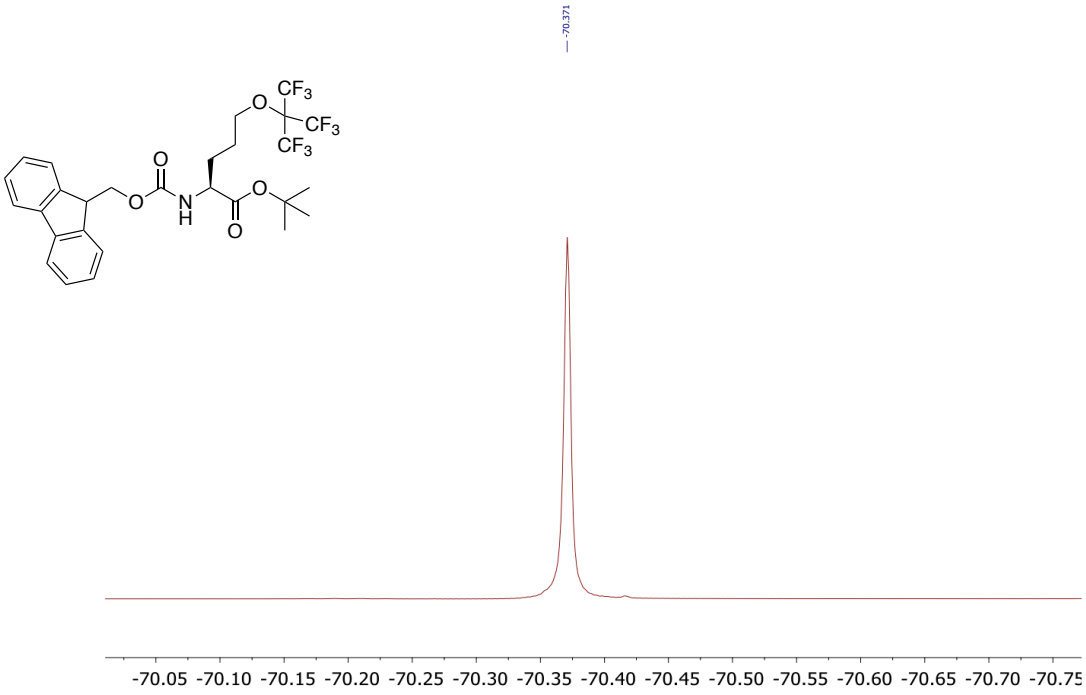

(*S*)-2-((((9*H*-fluoren-9-yl)methoxy)carbonyl)amino)-5-((1,1,1,3,3,3-hexafluoro-2-(trifluoromethyl) propan-2-yl)oxy)pentanoic acid (E^F)

^{1}H NMR, 500 MHz, DMSO-*d*6

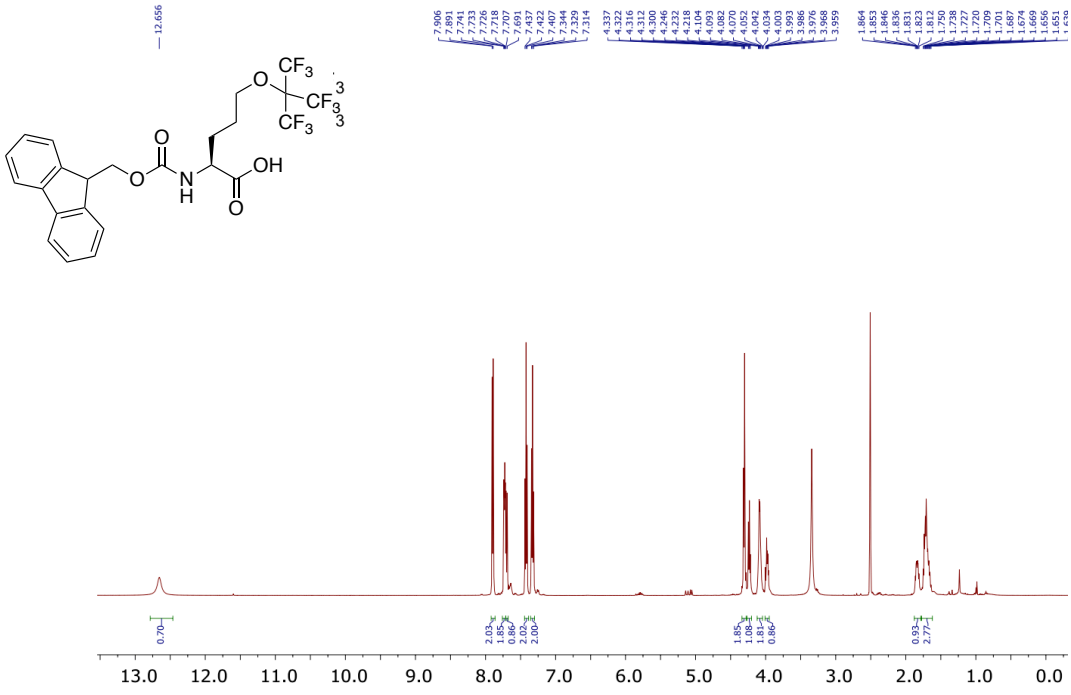

^{13}C NMR, 126 MHz, DMSO-*d*6

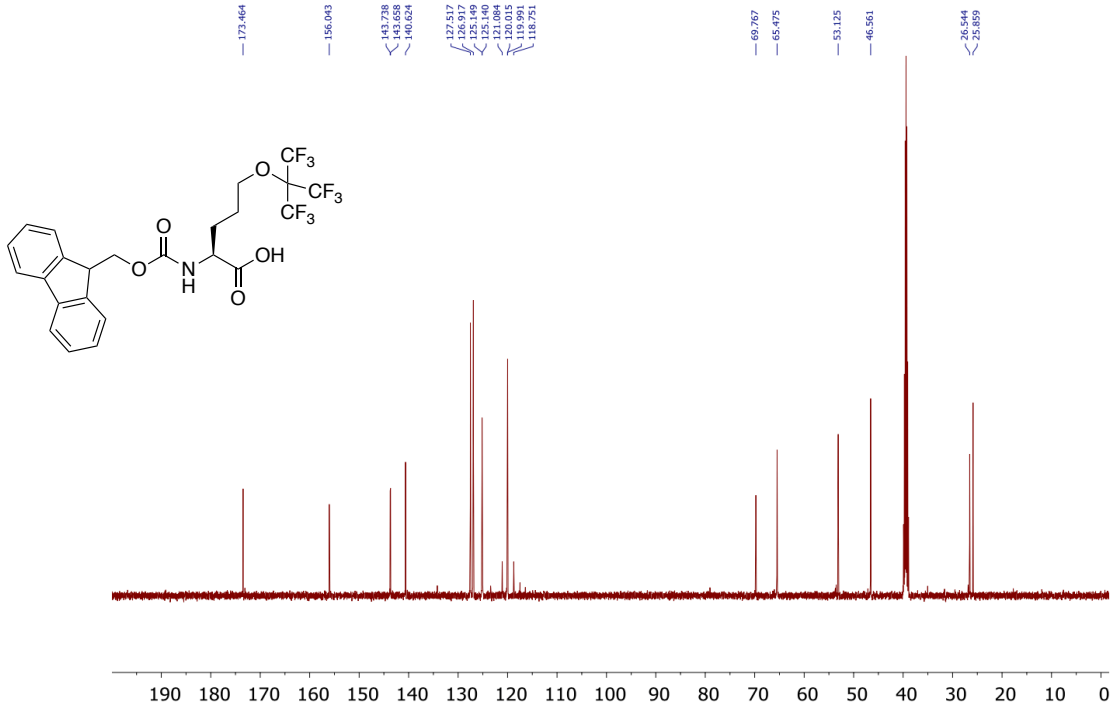

^{19}F NMR, 471 MHz, DMSO-*d*6

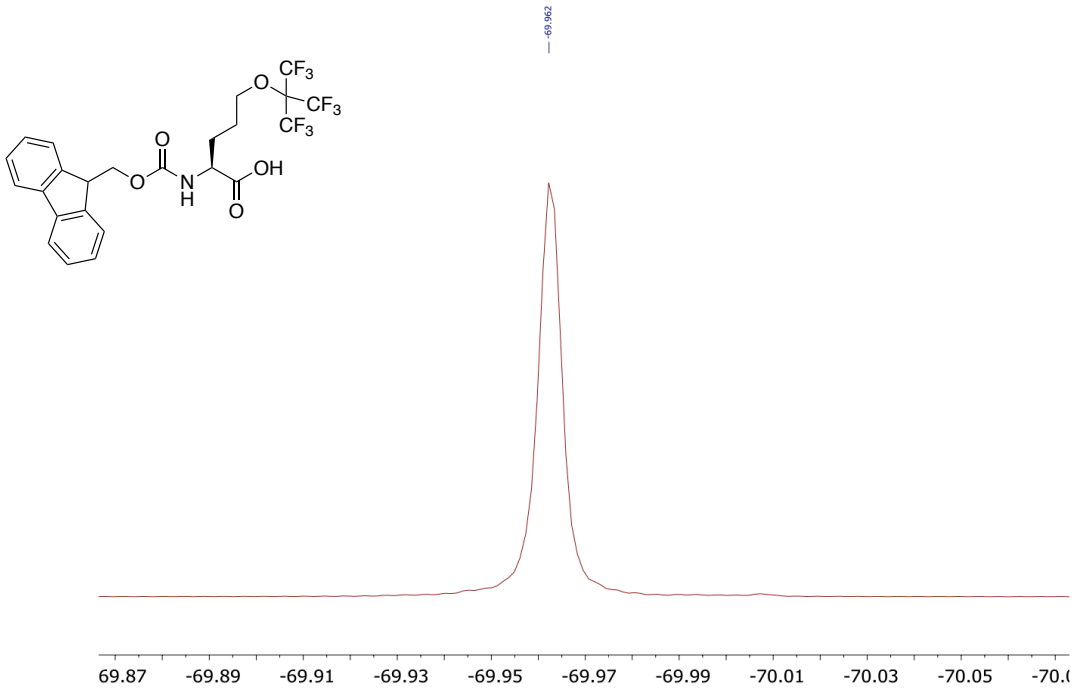

HPLC chromatogram of 1. Gradient of 10:90 CH3CN:H2O (0.1% TFA) to 60: 40 CH3CN:H2O (0.1% TFA) over 50 minutes with a 5 minute equilibration and 5 minute flush (95% CH3CN). λ = 220 nm

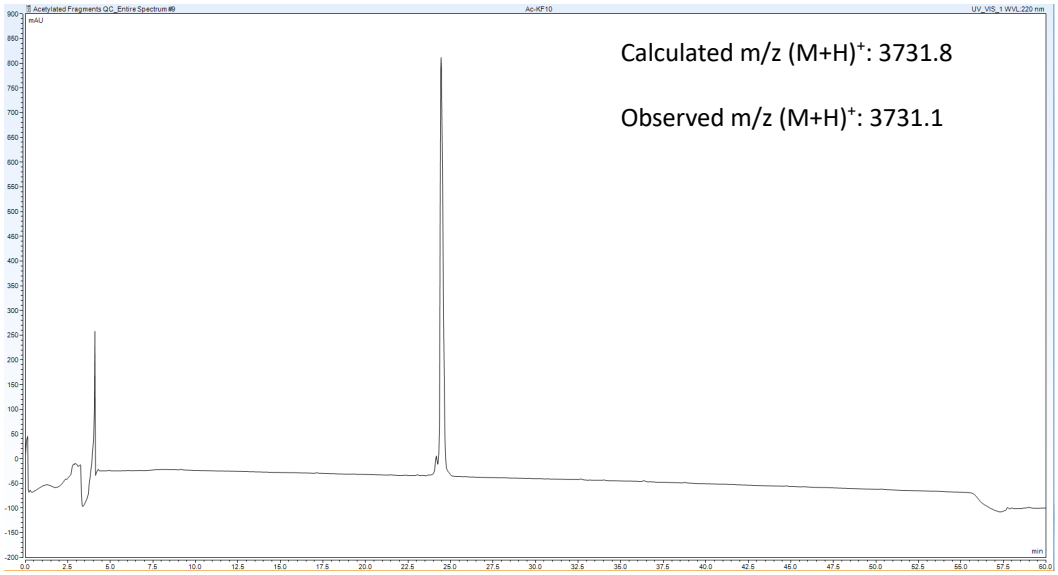

HPLC chromatogram of TB-1. Gradient of 10:90 $CH_3CN:H_2O$ (0.1% TFA) to 60:40 $CH_3CN:H_2O$ (0.1% TFA) over 50 minutes with a 5 minute equilibration and 5 minute flush (95% CH_3CN). λ = 220 nm

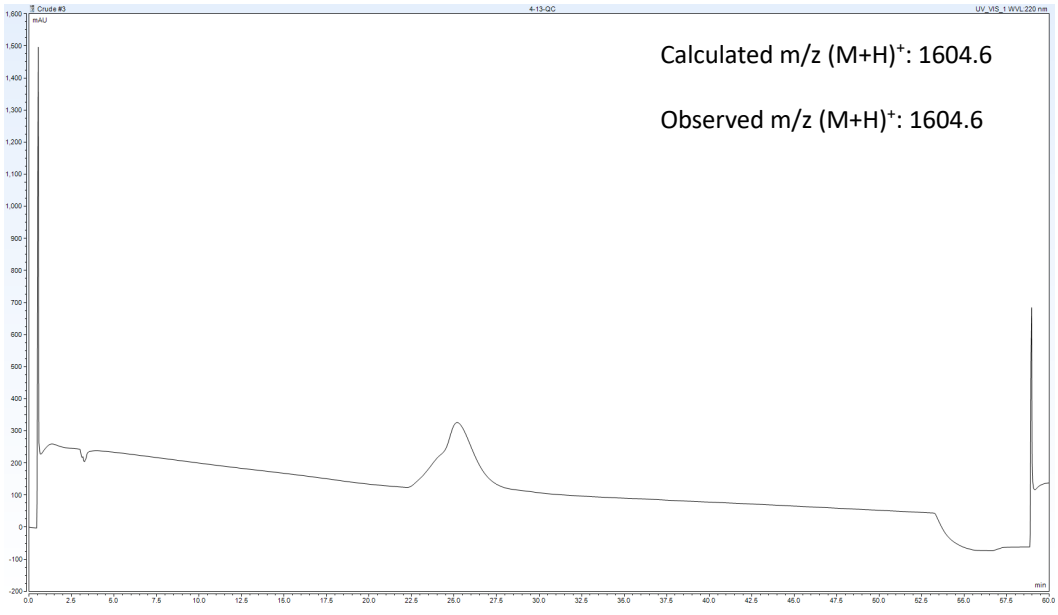

HPLC chromatogram of TB-2. Gradient of 10:90 $CH_3CN:H_2O$ (0.1% TFA) to 60:40 $CH_3CN:H_2O$ (0.1% TFA) over 50 minutes with a 5 minute equilibration and 5 minute flush (95% CH_3CN). λ = 220 nm

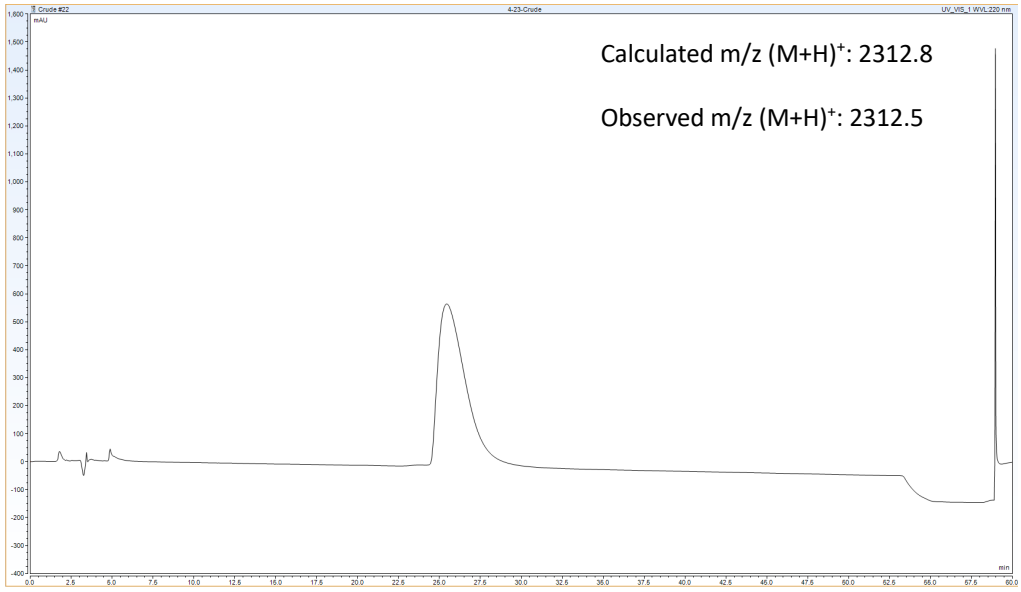

HPLC chromatogram of TB-3. Gradient of 30:70 $CH_3CN:H2O$ (0.1% TFA) to 60:40 $CH_3CN:H_2O$ (0.1% TFA) over 50 minutes with a 5 minute equilibration and 5 minute flush (95% CH_3CN). λ = 220 nm

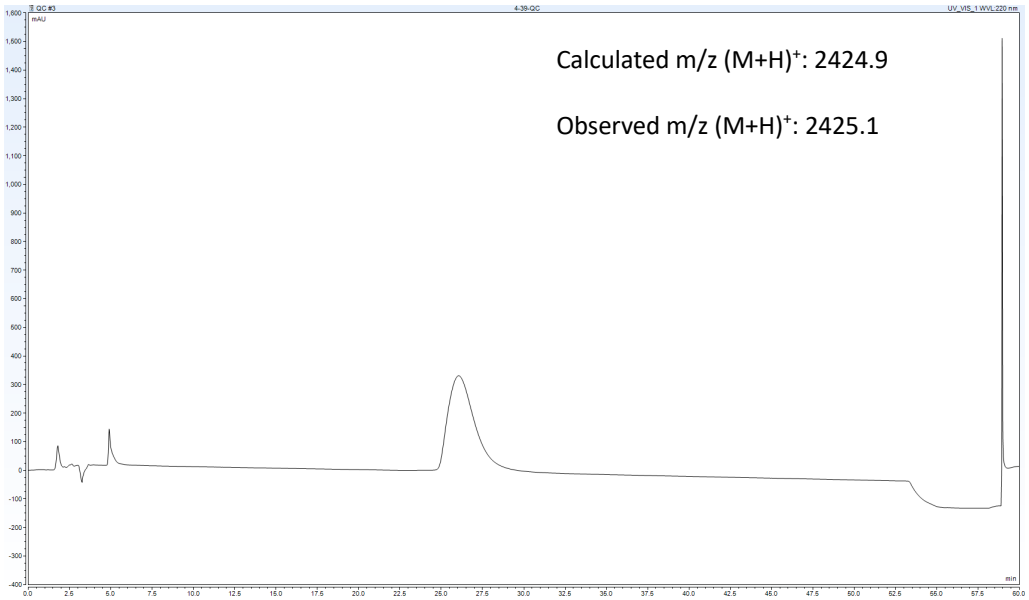

HPLC chromatogram of TB-4. Gradient of 10:90 $CH_3CN:H_2O$ (0.1% TFA) to 40:60 $CH_3CN:H_2O$ (0.1% TFA) over 40 minutes with a 5 minute equilibration and 5 minute flush (95% CH_3CN). λ = 220 nm

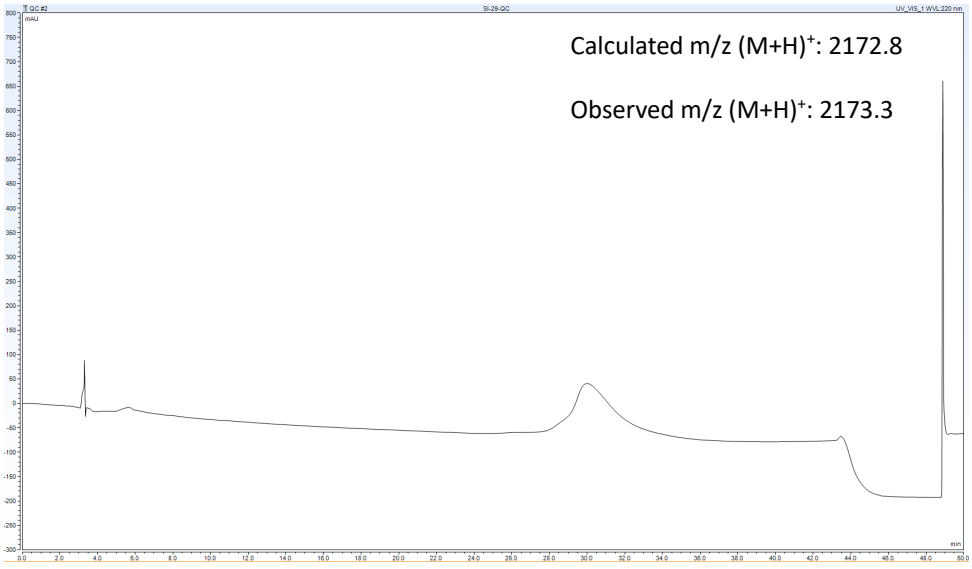

HPLC chromatogram of TB-5.Gradient of 10:90 CH_3CN :H_2O (0.1% TFA) to 60:40 $CH_3CN:H_2O$ (0.1% TFA) over 50 minutes with a 5 minute equilibration and 5 minute flush (95% CH_3CN). λ = 220 nm

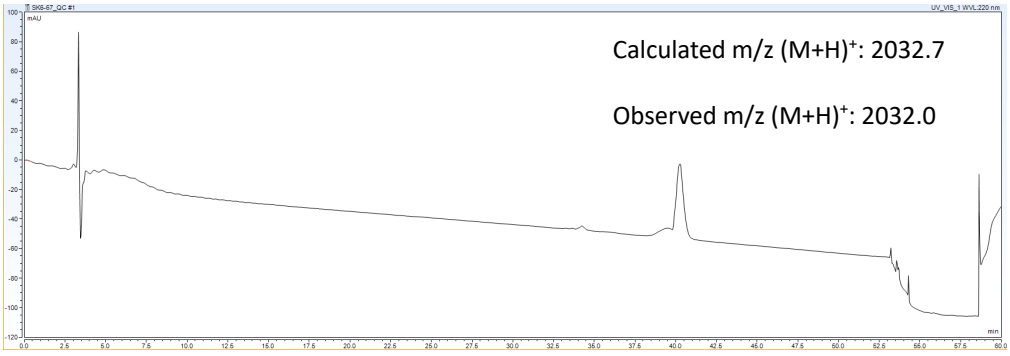

HPLC chromatogram of TB-6. Gradient of 20:80 $CH_3CN:H_2O$ (0.1% TFA) to 75:25 $CH_3CN:H_2O$ (0.1% TFA) over 50 minutes with a 5 minute equilibration and 5 minute flush (95% CH_3CN). λ = 220 nm

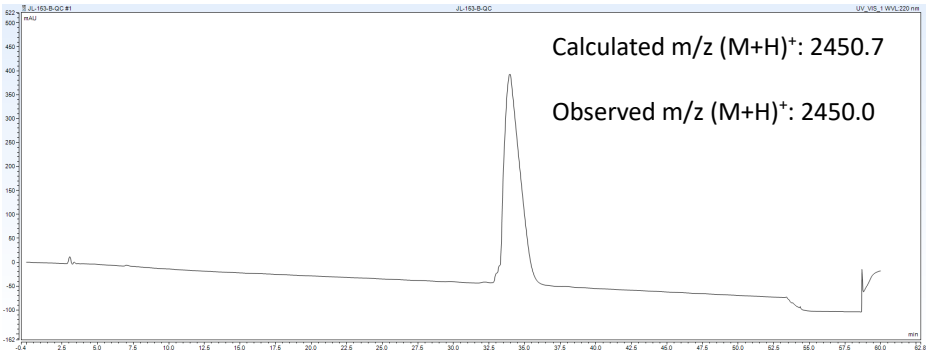

HPLC chromatogram of TB-7. Gradient of 20:80 $CH_3CN:H_2O$ (0.1% TFA) to 75:25 $CH_3CN:H_2O$ (0.1% TFA) over 50 minutes with a 5 minute equilibration and 5 minute flush (95% CH_3CN). λ = 220 nm

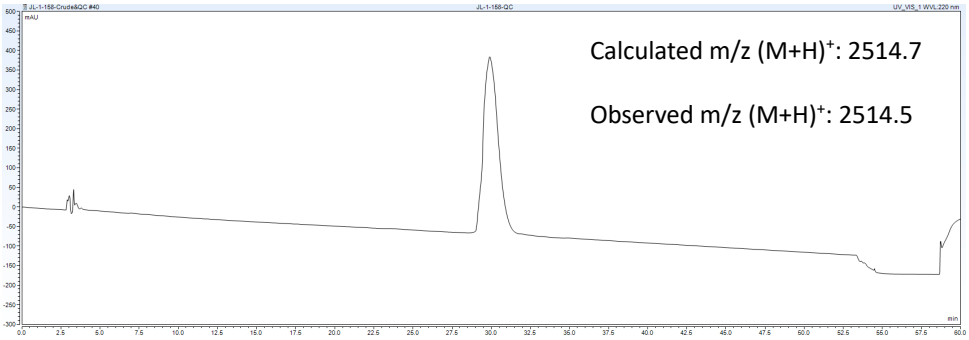

HPLC chromatogram of TB-8. Gradient of 20:80 $CH_3CN:H_2O$ (0.1% TFA) to 60:40 $CH_3CN:H_2O$ (0.1% TFA) over 70 minutes with a 5 minute equilibration and 5 minute flush (95% CH_3CN). λ = 220 nm

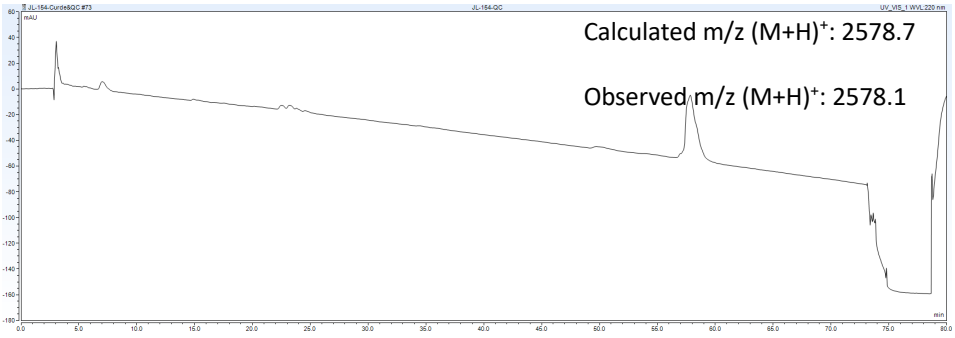

HPLC chromatogram of TB-9. Gradient of 0:100 $CH_3CN:H_2O$ (0.1% TFA) to 50: 50 $CH_3CN:H_2O$ (0.1% TFA) over 30 minutes with a 5 minute equilibration and 5 minute flush (95% CH_3CN). λ = 220 nm

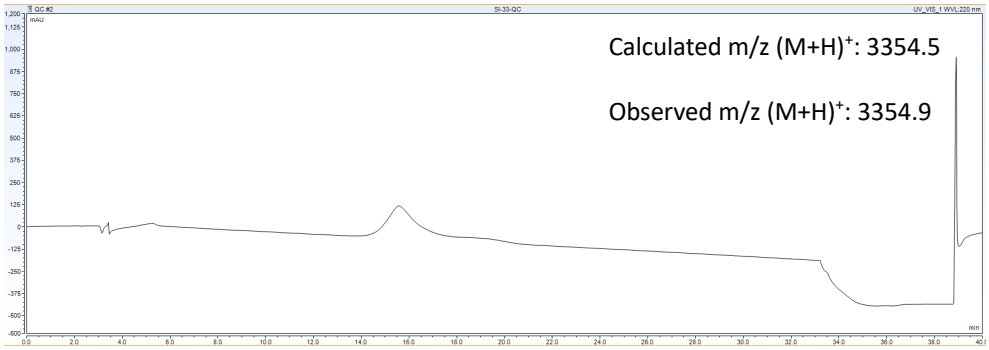

HPLC chromatogram of FAM-1. Gradient of 10:90 $CH_3CN:H_2O$ (0.1% TFA) to 30:70 $CH_3CN:H_2O$ (0.1% TFA) over 50 minutes with a 5 minute equilibration and 5 minute flush (95% CH_3CN). λ = 220 nm

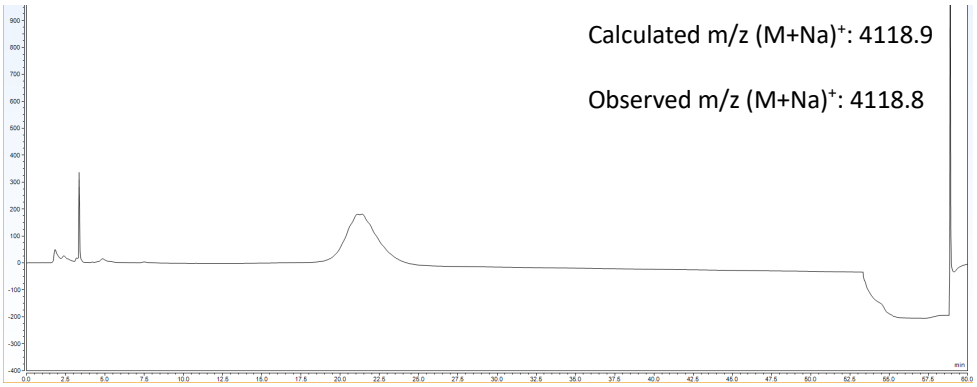

HPLC chromatogram of FAM-TB-1. Gradient of 10:90 $CH_3CN:H_2O$ (0.1% TFA) to 30:70 $CH_3CN:H_2O$ (0.1% TFA) over 50 minutes with a 5 minute equilibration and 5 minute flush (95% CH_3CN). λ = 220 nm

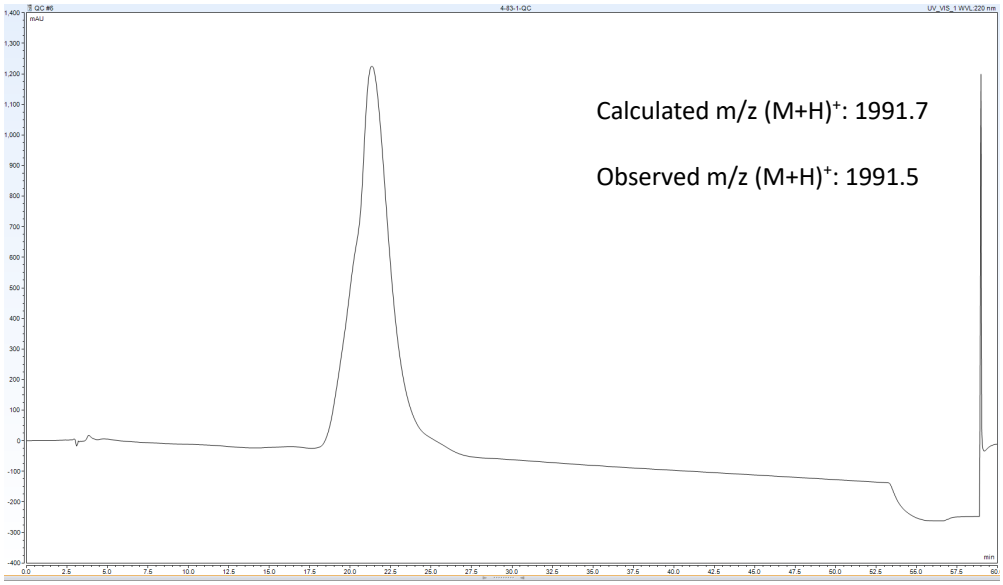

HPLC chromatogram of FAM-TB-4. Gradient of 20:80 $CH_3CN:H_2O$ (0.1% TFA) to 45:55 $CH_3CN:H_2O$ (0.1% TFA) over 50 minutes with a 5 minute equilibration and 5 minute flush (95% CH_3CN). λ = 220 nm

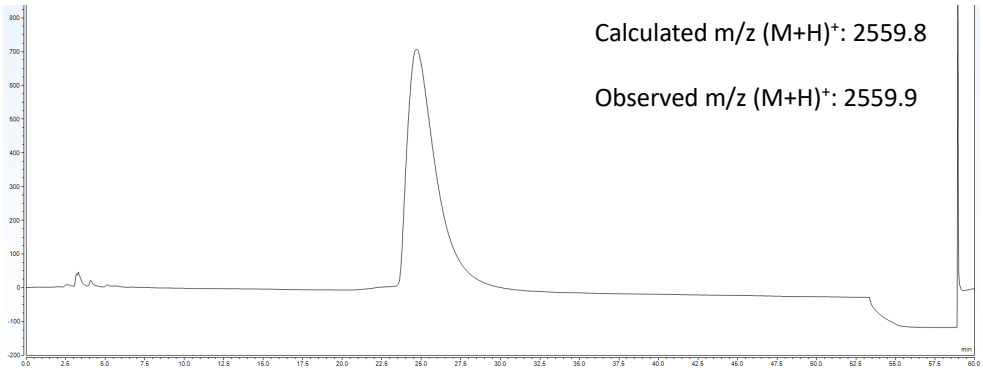

HPLC chromatogram of FAM-TB-9. Gradient of 10:90 $CH_3CN:H_2O$ (0.1% TFA) to 30:70 $CH_3CN:H_2O$ (0.1% TFA) over 50 minutes with a 5 minute equilibration and 5 minute flush (95% CH_3CN). λ = 220 nm

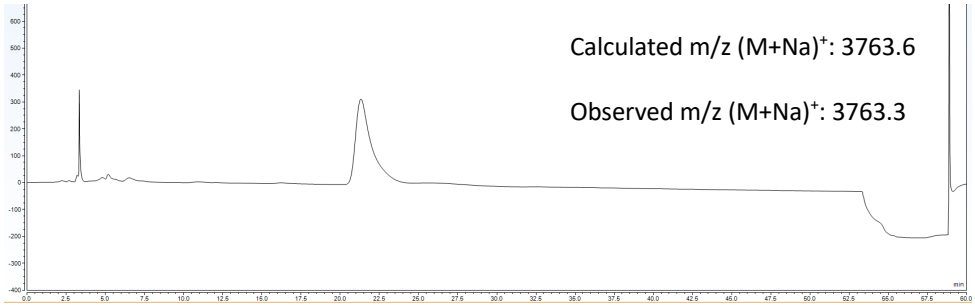

HPLC chromatogram of Mal-TB-9. Gradient of 0:100 $CH_3CN:H_2O$ (0.1% TFA) to 30:70 $CH_3CN:H_2O$ (0.1% TFA) over 30 minutes with a 5 minute equilibration and 5 minute flush (95% CH_3CN). λ = 220 nm

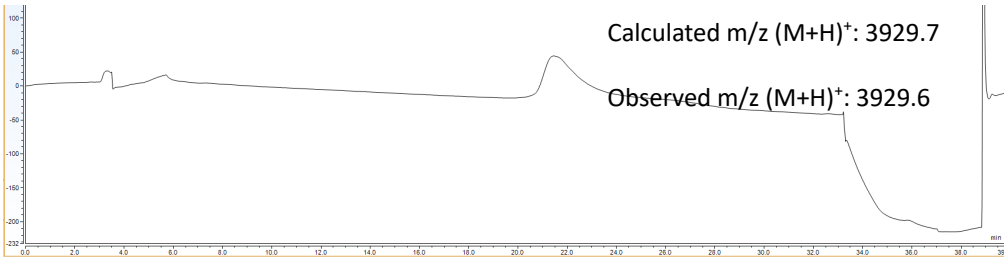

HPLC chromatogram of fluorinated peptide $KKK^{FF}KK^{\beta}AYHWYGYTPENVI$. Gradient of 10:90 $CH_3CN:H_2O$ (0.1% TFA) to 30:70 $CH_3CN:H_2O$ (0.1% TFA) over 30 minutes with a 5 minute equilibration and 5 minute flush (95% CH_3CN). λ = 220 nm

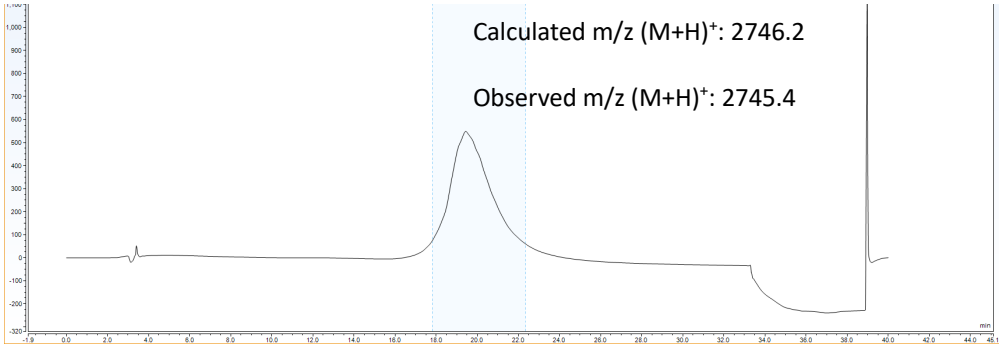

5.1.3 Multivalent Highly-Fluorinated-Peptide-Bioconjugated Nanorings for On-Cell ^{19}F NMR

HPLC chromatogram of 1. Gradient of 0:100 $CH_3CN:H_2O$ (0.1% TFA) to 30:70 $CH_3CN:H_2O$ (0.1% TFA) over 30 minutes with a 5 minute equilibration and 5 minute flush (95% CH_3CN). λ = 220 nm

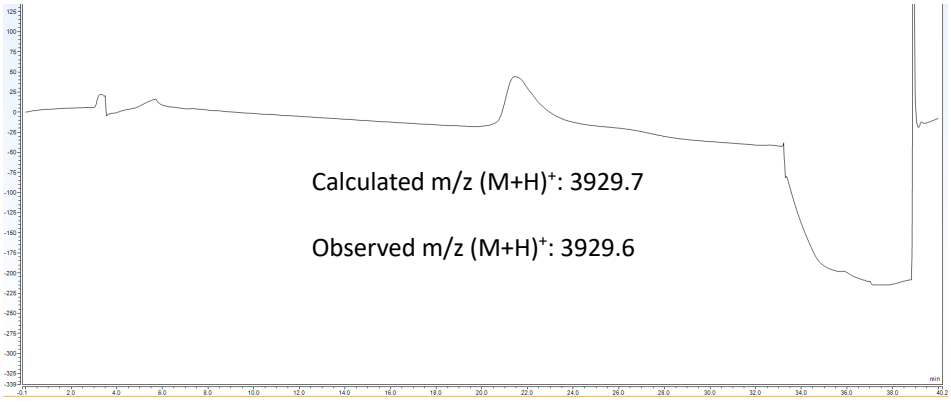

HPLC chromatogram of 2. Gradient of 0:100 $CH_3CN:H_2O$ (0.1% TFA) to 20:80 $CH_3CN:H_2O$ (0.1% TFA) over 30 minutes with a 5 minute equilibration and 5 minute flush (95% CH_3CN). λ = 220 nm

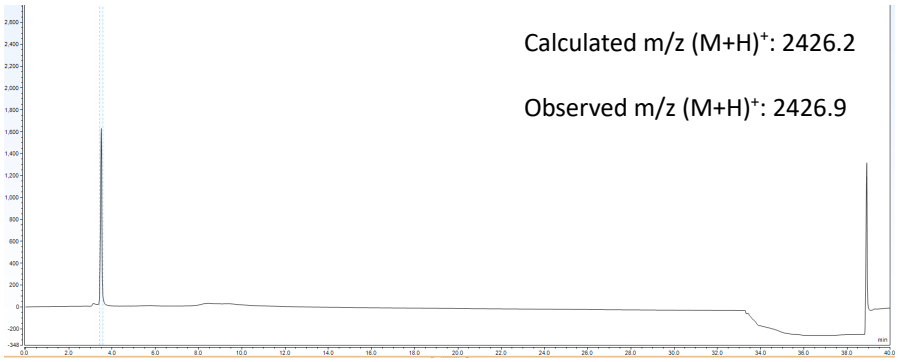

HPLC chromatogram of 3. Gradient of 0:100 $CH_3CN:H_2O$ (0.1% TFA) to 30:70 $CH_3CN:H_2O$ (0.1% TFA) over 50 minutes with a 5 minute equilibration and 5 minute flush (95% CH_3CN). $\lambda = 220$ nm

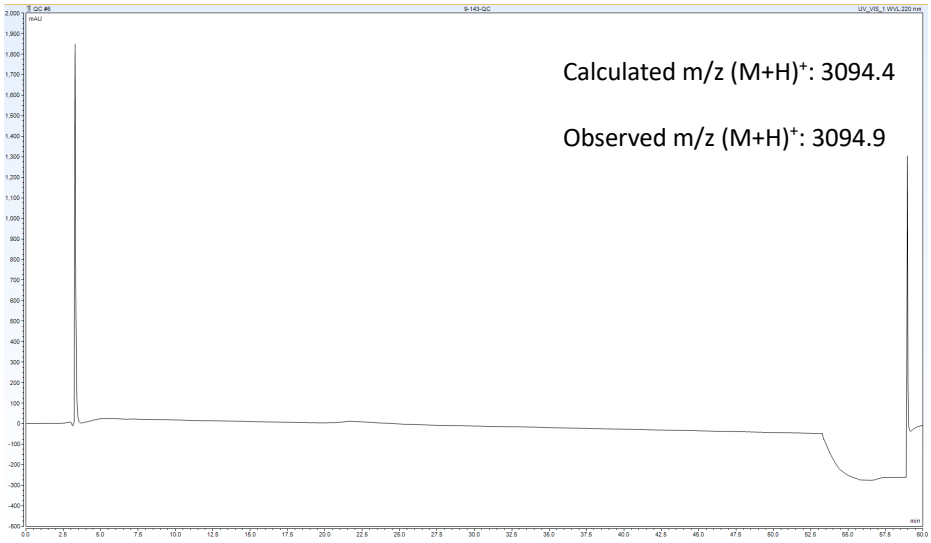

HPLC chromatogram of 4. Gradient of 10:90 $CH_3CN:H_2O$ (0.1% TFA) to 60:40 $CH_3CN:H_2O$ (0.1% TFA) over 50 minutes with a 5 minute equilibration and 5 minute flush (95% CH_3CN). $\lambda = 220$ nm

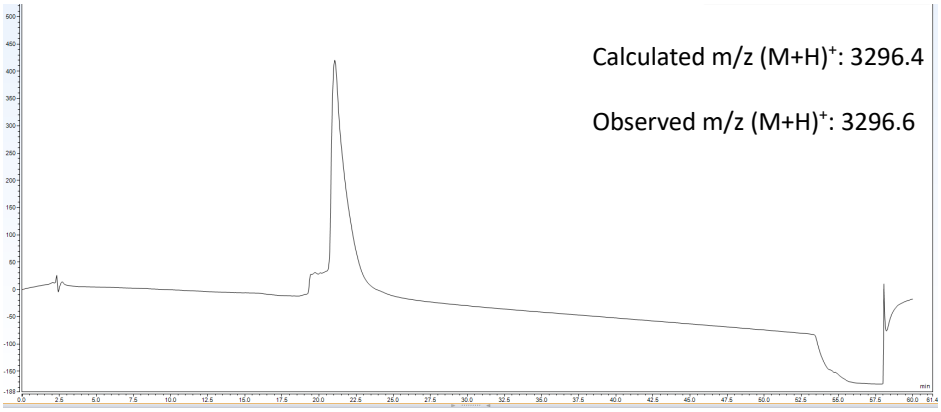

HPLC chromatogram of 5. Gradient of 10:90 $CH_3CN:H_2O$ (0.1% TFA) to 70:30 $CH_3CN:H_2O$ (0.1% TFA) over 30 minutes with a 5 minute equilibration and 5 minute flush (95% CH_3CN). $\lambda = 220$ nm

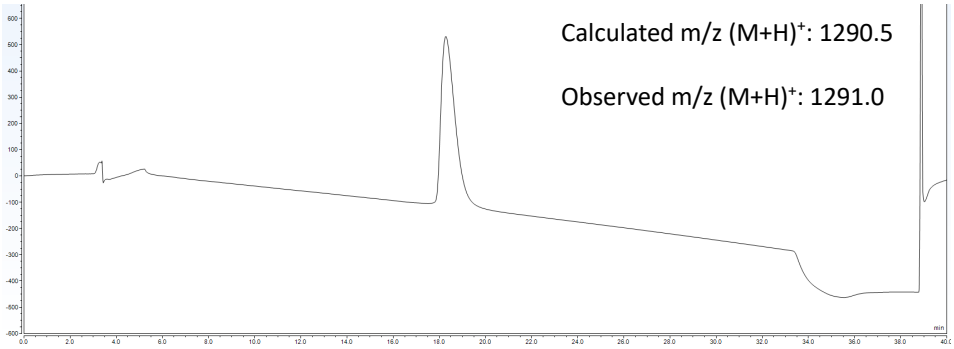

HPLC chromatogram of 6. Gradient of 10:90 $CH_3CN:H_2O$ (0.1% TFA) to 70:30 $CH_3CN:H_2O$ (0.1% TFA) over 30 minutes with a 5 minute equilibration and 5 minute flush (95% CH_3CN). $\lambda = 220$ nm

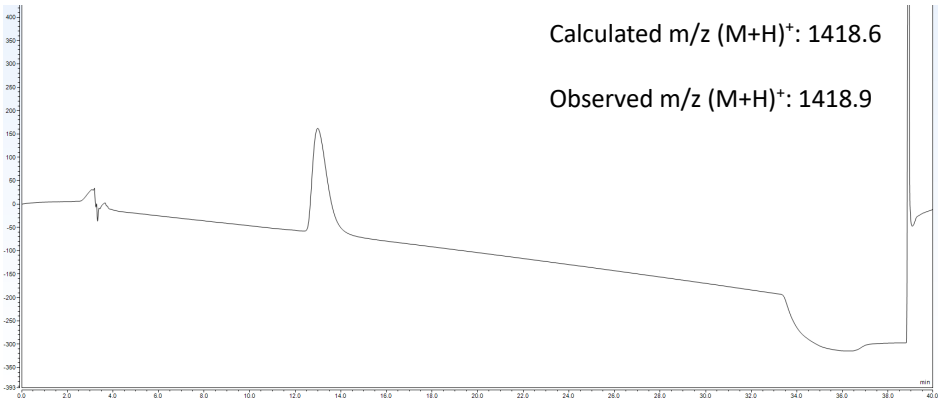

HPLC chromatogram of 7. Gradient of 10:90 $CH_3CN:H_2O$ (0.1% TFA) to 60:40 $CH_3CN:H_2O$ (0.1% TFA) over 30 minutes with a 5 minute equilibration and 5 minute flush (95% CH_3CN). $\lambda = 220$ nm

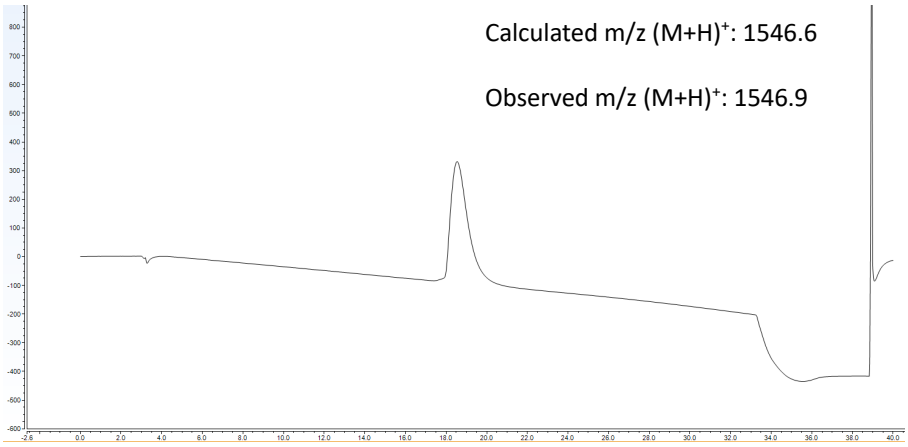

HPLC chromatogram of 8. Gradient of 10:90 $CH_3CN:H_2O$ (0.1% TFA) to 50:50 $CH_3CN:H_2O$ (0.1% TFA) over 30 minutes with a 5 minute equilibration and 5 minute flush (95% CH_3CN). $\lambda = 220$ nm

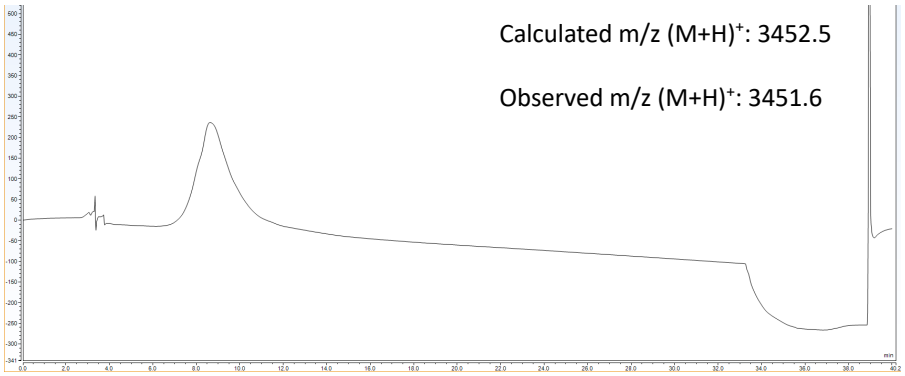

5.2 Genetically-Encoded Discovery of Perfluoroaryl-Macrocycles that Bind to Albumin and Exhibit Extended Circulation in-vivo

'Genetically-Encoded Discovery of Perfluoroaryl-Macrocycles that Bind to Albumin and Exhibit Extended Circulation in-vivo'

Jeffrey Y.K. Wong, Arunika I. Ekanayake, Serhii Kharchenko, Steven E. Kirberger, Ryan Qiu, Payam Kelich, Susmita Sarkar, Jianqian Li, Kleinberg X. Fernandez, Edgar R. Alvizo-Paez, Jiayuan Miao, Shiva Kalhor-Monfared, John, J. Dwyer, Hongsuk Kang, Hwanho Choi, John M. Nuss, John C. Vederas, Yu-Shan Lin, Matthew S. Macauley, Lela Vukovic, William C.K. Pomerantz and Ratmir Derda*

Nature Communication Resubmitted

5.2.1 Introduction

Sufficient circulation lifetime of drugs such as peptides is important in therapeutic applications. With limited peptides exhibiting a naturally extended circulation lifetime, multiple strategies have been studied to tune such lifetime. Apart from covalent linkage to moieties such as macromolecules or long-living serum proteins, non-covalent binding serum proteins such as albumin is an alternative strategy. Albumin is the most abundant protein in plasma with an average half-life of 19 days in humans. In addition to the favorable lifetime, albumin also features the interaction with hydrophobic small molecule drugs, which enhances the pharmacokinetic properties. Albumin-binding peptide moiety can be further developed through being incorporated in tandem to other moiety for various therapeutic applications. However, there's limited human serum albumin (HSA)-binding peptides known to date. Hence, it's necessary to develop small peptide-based albumin-binding ligands with lower molecular weight.

5.2.2 Results and discussion

In collaboration with Ratmir Derda's group, I focused on validation of the macrocyclized albumin binder, which were discovered through phage selection. ^{19}F NMR was used to determine the apparent binding affinity of those macrocyclized peptides to HSA. Previous studies indicated that the discovered peptide sequence 14c (PFS-SICRFFCGGG) played a major role in affinity determination, alanine scans of 14c were conducted to reinforce this observation. It was observed that R4A or F5A in 14c would ablate the binding between macrocyclized peptide and HSA **(Fig. 5-1** and **5-2)**. In contrast, S1A and I2A in 14c resulted in a 3- and 10-fold loss in binding affinity respectively **(Fig. 5-1** and **5-2)**. This result indicated that the changes in any of four amino acids in SXCXXXC fragment would negatively affect the binding characteristics between macrocyclized peptide and HSA.

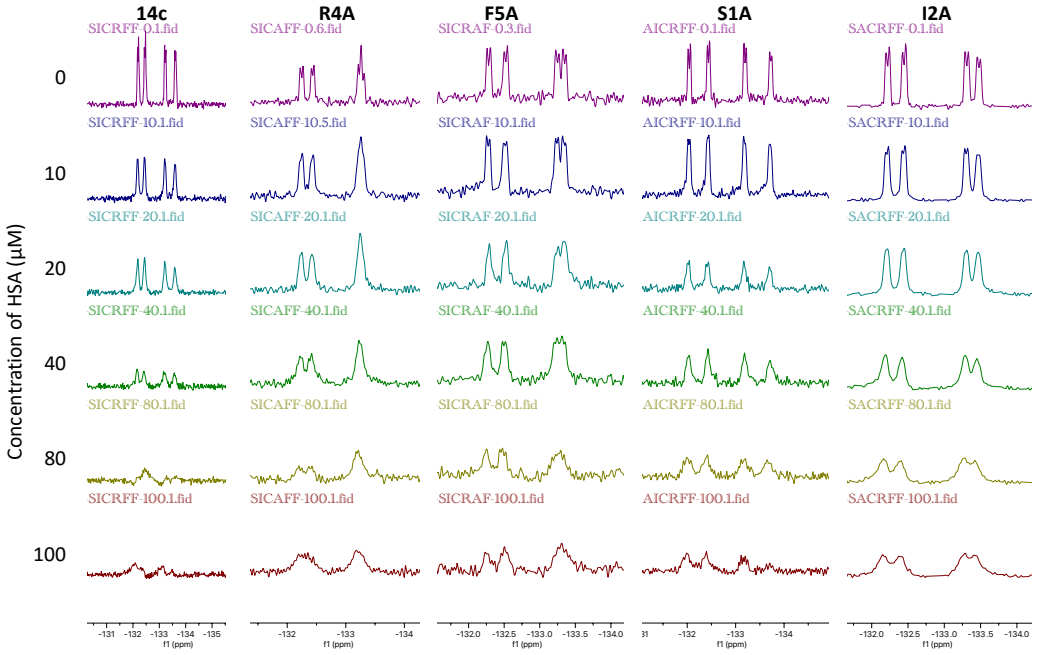

Figure 5-1. ^{19}F NMR measurement of interaction between macrocyclized peptides and albumin. Peptides were at concentration of 20 μM and HSA were at the concentration ranging from 0 μM to 100 μM.

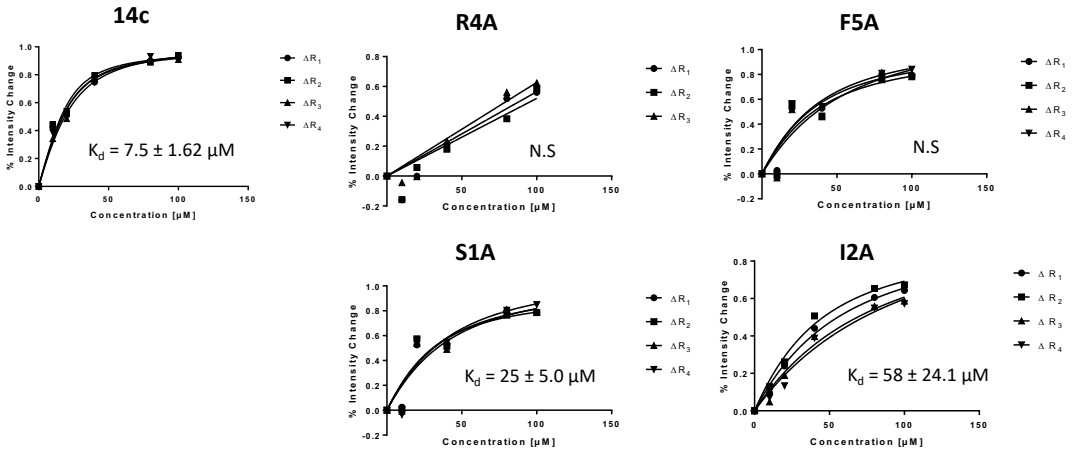

Figure 5-2. Affinity determination of peptides to HSA under ^{19}F NMR measurement.

5.2.3 Supplementary Information

^{19}F NMR binding experiment

^{19}F NMR binding experiments to determine the apparent Kd were performed on the Bruker 600-MHz Avance NEO (6001), equipped with a 5-mm triple resonance cryoprobe (7400:1 S/N) at the University of Minnesota. Human serum albumin (HSA) was dissolved in 10:90 D2O:phosphate buffer (50 mM phosphate, 100 mM NaCl, pH 7.4). PFS-peptides in a DMSO stock solution were then added to HSA solution to a final concentration of 0 μM, 10 μM, 20 μM, 40 μM, 80 μM, 100 μM HSA with a constant concentration of 0.5% DMSO and 20 μM peptide. Qualitative binding experiments used 50 μM peptide. Parameters used for each experiment are as follows: number of scans of 2000, receiver gain of 101, acquisition time of 0.05 s, relaxation delay of 1.00 sec, temperature of 297 K. The change in intensity of the peptide fluorine resonance (ΔI) was plotted as a function of protein concentration to generate binding isotherms using eq 1 where ΔImax is the maximum change in fluorine resonance intensity, [L] is the concentration of the protein, and [P] is the concentration of the peptide, and [PL] is the concentration of bound complex. All titrations were performed in a single replicate unless otherwise specified. Binding affinity was determined based on all resonances.

$$\Delta I = \Delta I_{max} \times \frac{(K_d+[L]+[P]) - \sqrt{(K_d+[L]+[P])^2-4[PL]}}{2[PL]} \qquad \text{Eq. 1}$$

Table 5-1. Titration experiment conditions for HSA for apparent K_d determination

1 mM HSA (μL)	4 mM **PFS**-peptide (μL)	D_2O (μL)	PBS Buffer (μL)
0	2.5	50	447.5
5	2.5	50	442.5
10	2.5	50	437.5
20	2.5	50	427.5
40	2.5	50	407.5
50	2.5	50	397.5

5.3 Macrocyclized MLL fragments for Modulation of Protein Interactions

5.3.1 Introduction

Exploration of macrocyclized peptides as protein-protein interaction (PPI) inhibitors has been an emerging area of research in medicinal chemistry. It has been shown that peptide macrocyclization can benefit the cellular uptake, proteolytic stability, and binding. Cysteine-mediated macrocycle formation is one widely used strategy for macrocyclization due to the reactivity of thiol group and its genetically encodability.

The kinase-inducible domain interacting (KIX) domain serves as a docking site for the formation of heterodimers between the coactivator and specific transcription factors including the transcriptional activation domains of MLL. The transcriptional activation domain of MLL would fold into an α-helical structure upon binding to KIX and the transcription factor-coactivator complex would form subsequently. It is known that the aberrant levels of MLL-mediated transcription would lead to cancer cell growth.[1] However, with the MLL-KIX interacting being dictated by a dynamic, hydrophobic region, targeting is very challenging. Previous studies in our group used MLL as a model to explore the KIX PPIs through using sulfur-containing side chains for macrocyclization.[2] Here we attempted to expand the side chain to perfluoro-aromatic moieties for macrocyclization to investigate the KIX PPIs.

5.3.2 Results and discussion

Macrocyclization was attempted on MLL fragment (SDIMDFVLKNTY) variants (**Table 5-2**). We substituted specific amino acids to either lysine or cysteine at *i* and *i+7* position for macrocyclization. Perfluoro-aromatic moieties included decafluorobiphenol, pentafluorophenyl sulfide, and pentafluorophenyl sulfone. In addition to cysteine-mediated macrocyclization, lysine-mediated and lysine-cysteine-mediated macrocyclization were observed as well when using a pentafluorophenyl sulfone moiety (**Fig. 5-3**). The macrocyclization results were very encouraging as it would allow for more macrocyclized peptide candidates. Future work would focus on the studies on those peptides in their binding affinities, proteolytic stability, and cellular permeability.

Table 5-2. MLL fragment variants for macrocyclization.

Peptide Sequence
Ac-SKICDFVLKNCY
Ac-SKICDFVLKNCY
Ac-SKIMDFVLKNTY
Ac-SCTNDFVLKNTY

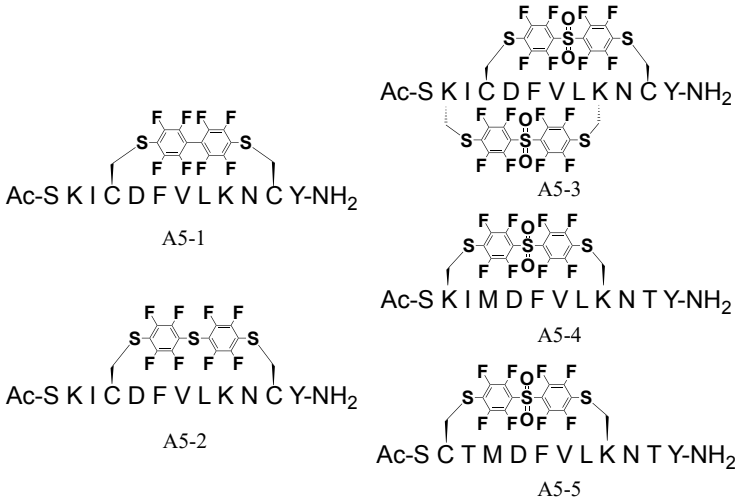

Figure 5-3. Structures of macrocyclized peptides.

5.3.3 Supplementary Information

Macrocyclization

1.424 μmol of the peptide was dissolved in 0.6 mL of DMF. 30 μL of 100 mM fluorinated small molecule solution was added to the peptide followed with 300 μL of 50 mM Tris Base solution in DMF. Reaction mixture was stirred at room temperature for 4.5 hours. Reaction was quenched with 1.2mL of 0.1 % TFA in H_2O and was purified with RP-HPLC.

HPLC chromatogram of A5-1.Gradient of 10:90 $CH_3CN:H_2O$ (0.1% TFA) to 60:40 $CH_3CN:H_2O$ (0.1% TFA) over 30 minutes with a 5 minute equilibration and 5 minute flush (95% CH_3CN). λ = 220 nm.

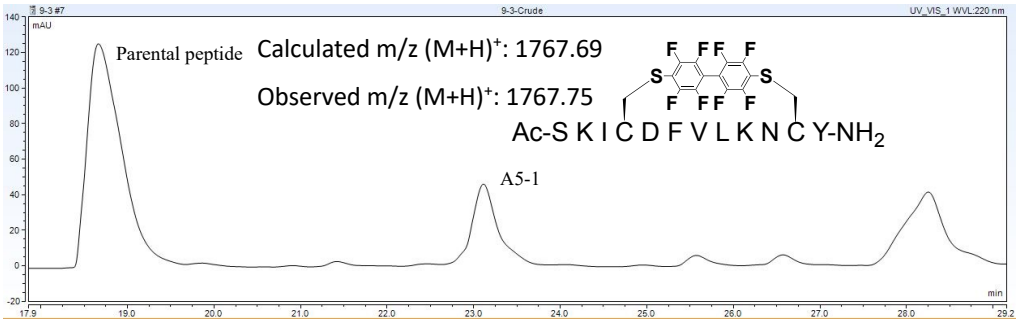

HPLC chromatogram of A5-2.Gradient of 10:90 $CH_3CN:H_2O$ (0.1% TFA) to 60:40 $CH_3CN:H_2O$ (0.1% TFA) over 30 minutes with a 5 minute equilibration and 5 minute flush (95% CH_3CN). λ = 220 nm

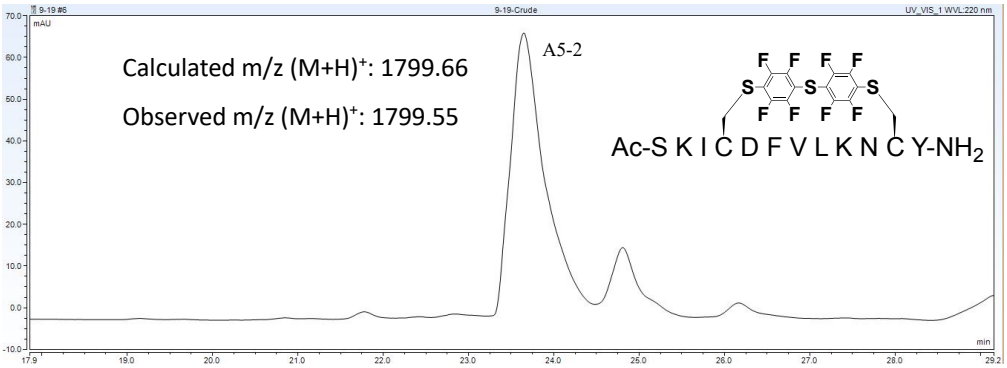

HPLC chromatogram of A5-3.Gradient of 10:90 $CH_3CN:H_2O$ (0.1% TFA) to 60:40 $CH_3CN:H_2O$ (0.1% TFA) over 30 minutes with a 5 minute equilibration and 5 minute flush (95% CH_3CN). λ = 220 nm

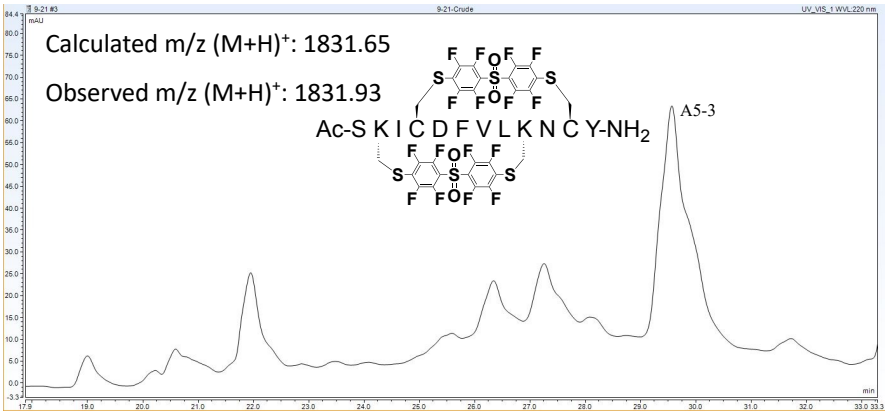

HPLC chromatogram of A5-4.Gradient of 40:60 $CH_3CN:H_2O$ (0.1% TFA) to 70:30 $CH_3CN:H_2O$ (0.1% TFA) over 30 minutes with a 5 minute equilibration and 5 minute flush (95% CH_3CN). λ = 220 nm

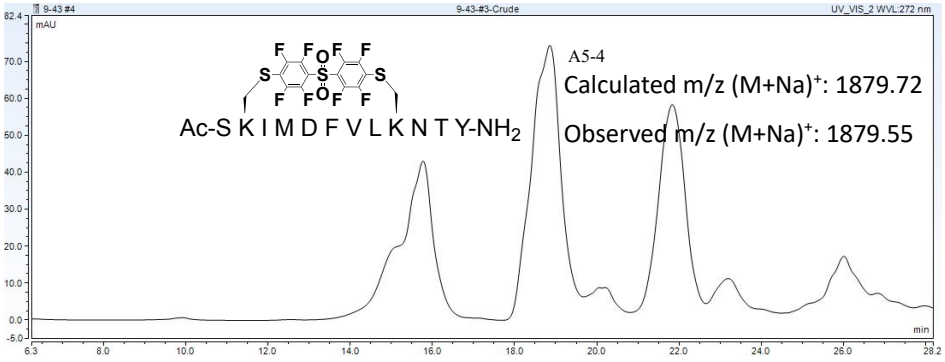

HPLC chromatogram of A5-5.Gradient of 10:90 $CH_3CN:H_2O$ (0.1% TFA) to 60:40 $CH_3CN:H_2O$ (0.1% TFA) over 40 minutes with a 5 minute equilibration and 5 minute flush (95% CH_3CN). λ = 220 nm